GRAFTING MODIFICATION OF CHITOSAN BIOPOLYMER FOR STABILIZED GOLD AND SILVER NANOPARTICLES AND THEIR POTENTIAL APPLICATIONS

PAKAWAT CHITTRATAN

A THESIS SUBMITTED IN FULFILLMENT OF THE REQUIREMENT FOR THE DEGREE OF DOCTOR OF PHILOSOPHY IN APPLIED CHEMISTRY

DEPARTMENT OF CHEMISTRY SCHOOL OF SCIENCE
KING MONGKUT'S INSTITUTE OF TECHNOLOGY LADKRABANG

2024

KMITL-2024-SC-D-012-021

Thesis Title	Grafting Modification of Chitosan Biopolymer for Stabilized Gold and Silver Nanoparticles and Their Potential Applications
Student Name	Pakawat Chittratan
Student ID	59605103
Degree	Doctor of Philosophy (Applied Chemistry)
Department	Chemistry
Year	2024
Thesis Advisor	Assoc. Prof. Dr. Pathavuth Monvisade
Thesis Co-advisor	Assoc. Prof. Dr. Ekarat Detsri

Abstract

Modified-chitosan coated on metallic nanoparticle have been synthesized and characterized for the design of antimicrobial materials. Chitosan-grafted-thymol (CST) and chitosan-grafted-chloroxylenol (CSX) were synthesized *via* the Mannich reaction. The solubility of CSX was enhanced through the Michael reaction to overcome limitations in conditions with pH greater than 6. ^{1}H NMR confirmed the successful substitution of thymol onto the side chain of HCS with $\%DS_{NMR}$ of 10.0%. Similarly, grafting chloroxylenol onto the side chain of HCS and LCS produced a $\%DS_{NMR}$ of 9.3% and 15.8%, respectively. Moreover, grafting acrylic acid onto side chain of HCSX and LCSX produced a $\%DS_{AA}$ of 45.0 and 33.0, respectively. The appropriate concentration of CST for AuNP synthesis was found to be 0.020% w/v. A red-wine colloidal AuNP solution with a particle size ranging from 2.41-3.30 nM was exhibited a strong surface plasmon resonance at 520 nm, displaying negative charges at pH = 9 of -36.37 mV. For AgNP synthesis, the appropriate concentration of HCECSX and LCECSX was found to be 0.005 % w/v. HCECSX-AgNP and LCECSX-AgNP yielded clear-yellow colloidal solutions with particle size of 0.80-14.40 nM, showing strong surface plasmon resonance at 400 and 411 nm, respectively, with negative charges at pH 9 of -26.70 and -20.97 mV, respectively. These results evidenced that the AgNPs and AuNPs showed electrostatic repulsion, with modified-CS acting as a capping agent to ensure good dispersion and stability. The average minimum inhibitory concentration values

(MIC) of CST-AuNPs against *S. mutans* ATCC 25175 and *S. sobrinus* ATCC 33402 were found to be 25 and 100 mg/L, respectively. In case of CECSX-AgNPs, the MIC of HCECSX-AgNPs against *S. aureus* (ATCC25923), and *A. baumanii* (ATCC19606) were found to be 25 and 3.125 mg/L, whereas the MIC of LCECSX-AgNPs against *E. coli* (ATCC25922), *S. aureus* (ATCC25923), and *A. baumanii* (ATCC19606) were found to be 25, 12.5 and 1.56 mg/L, respectively. Remarkably, CECSX-AgNPs coated surgical sutures materials exhibited the highest bacterial reduction of 99.99 %. These findings underscore the efficacy of the modified-CSs as a high-performance stabilizing agent for AuNPs and AgNPs production, modified-CS coated on nanoparticles providing outstanding antibacterial activity and can be applied to antimicrobial materials.

Keywords: Antimicrobial suture, Chitosan, Gold Nanoparticle, Metallic Nanoparticle, Modified Chitosan, Nanoparticle mouthwash, Silver nanoparticle

Acknowledgements

First of all, I would like to thank my advisor, Assoc. Prof. Dr. Pathavuth Monvisade and Assoc. Prof. Dr. Ekarat Detsri, for their guidance through my Ph.D. research. I appreciate your precious time and valuable advice on my research and thesis.

I am very grateful to have his helpful suggestions during my research. Also, I would like to thank the valuable comments by examination committees Assoc. Prof. Dr. Thanida Trakulsujaritchok, Assoc. Prof. Dr. Karoon Sadorn, Assoc. Prof. Dr. Punnama Siriphannon and Asst. Prof. Dr. Chonlada Ritvirulh. I would like to thank Polymer Synthesis and Functional Materials Research Unit at King Mongkut's Institute of Technology Ladkrabang for workplace and facility. I also thank all the staff members of the School of Science at King Mongkut's Institute of Technology Ladkrabang.

At last, I would like to thank my family for their encouragement and support. I dedicate this work to my family with love because I could not have done it without you.

Mr. Pakawat Chittratan

Table of contents

Page

Table of contents (Continued)

Page

Table of contents (Continued)

Page

Table of contents (Continued)

Page

Table of contents (Continued)

Page

List of Tables

List of Figures

Figure **Page**

List of Figures (Continued)

Figure **Page**

List of Figures (Continued)

Figure **Page**

List of Figures (Continued)

Figure **Page**

List of Figures (Continued)

Figure **Page**

Abbreviations/Symbol

Abbreviations/Symbol	Descriptions
UV-vis spectrophotometer	Ultraviolet-visible spectrophotometer
IR	Infrared Spectrophotometer
ATR-FTIR	Attenuated Total Reflection - Fourier Transform Spectrophotometer
NMR	Nuclear magnetic resonance spectroscopy
XRD	X-ray Diffractometer
Zeta potential	Zeta Potential Analyzer
pH	Potential of Hydrogen ion
nm	Nanometer
HCS	High molecular weight chitosan
HCST	High Mw Chitosan-grafted-Thymol
HCSX	High Mw Chitosan-grafted-Chloroxylenol
LCS	Low molecular weight chitosan
LCST	Low Mw Chitosan-grafted-Thymol
LCSX	Low Mw Chitosan-grafted-Chloroxylenol
AgNPs	Silver Nanoparticals
AuNPs	Gold Nanoparticles
Au-CST	Gold Nanoparticles stabilized by Chitosan-grafted-Thymol
Au-CSX	Gold Nanoparticles stabilized by Chitosan-grafted-Chloroxylenol
DI	Deionized water

Chapter 1
Introduction

1.1 Research Motivation

The major problem of inflammation and infections in the human body, including the oral cavity, is primarily caused by bacteria [1]. Oral infections, including cavities, gingivitis, and periodontal disease, are the most common oral infections caused by the bacteria *Streptococcus mutans (S. mutans)* and *Streptococcus sobrinus (S. sobrinus)*, one of the principal cariogenic dental biofilm inhabitants that feed on sugary, sticky foods, and beverages. Bacteria found in surgical site infections can vary depending on the type of surgery and the specific circumstances of the patient. However, some common bacteria that may be present in surgical sites include *Escherichia coli (E. coli)* and *Staphylococcus aureus (S. aureus)*. Additionally, *Acinetobacter baumannii (A. baumannii)* is notable for its ability to survive on environmental surfaces for extended periods and its tendency to cause infections in hospitalized patients.

To prevent the infection, a variety of antibacterial agents are used. Three different types of clinically used and most frequently studied antiplaque agents in oral cavity are sodium fluoride, ampicillin, and chlorhexidine. However, some inherent issues of these antiplaque agents could not be avoided such as brown staining of the teeth and tongue, an unpleasant taste, enhanced supragingival calculus formation, and rarely painful desquamations of the oral mucosa. In terms of surgical-site infection, suture functionalization with antibacterial agents is regarded as an alternate control strategy that counteracts cross–contamination and microbial proliferation. A variety of antibacterial agents are used in suture functionalization, including triclosan [2], chlorohexidine [3], and iodine [4]. Despite their effectiveness, these antimicrobial medications may induce allergies, skin irritation, and staining of surrounding tissues or clothing, particularly with iodine-containing solutions.

In recent years, metallic nanoparticles [5] have shown great potential for use in the fields of chemistry, physics, biology, and medicine. Currently, gold and silver nanoparticles (AuNPs and AgNPs) have been developed as metal nanoparticles that

can be used for a wide range of applications in the medical and pharmaceutical industries, especially in antimicrobial application. The development of AuNPs and AgNPs conjugated with various biomolecules, including antibiotics medicines, genes, peptides, and other targeted ligands in order to enhance the antibacterial abilities, have been proposed as an antimicrobial agent to prevent the infections and inflammation of human body. Nanoparticles conjugated with small molecules as stabilizing agents are more effective at inhibiting growth of microorganisms than isolated nanoparticles and molecules [5].

Chitosan (CS) is one of the most desirable biomolecules to use as stabilizing agents in AgNPs and AuNPs synthesis due to its antimicrobial properties against a wide range of target organisms [6-11] with excellent properties, e.g., biocompatibility, biodegradability, and nontoxicity. CS contains amino and hydroxyl groups, which allow for electrostatic interactions with negatively charged nanoparticles, effectively preventing aggregation, and this active group gives CS flexibility in structural improvements. Many chemical modifications at the amino group were chosen to improve the antimicrobial properties by increasing the potential of electrostatic charge binding to the surface of microorganism. The introducing of active molecules such as, catechol , N-halamine [12], and phenolic acid [13] bring chitosan a better antibacterial activity and expand its application as well with various microorganism. Moreover, in some cases, it can also be improved solubility at the same time enhancing antimicrobial activity both in acidic and alkaline conditions. Nowadays, there are several reports in the literature about modification of CS using Mannich reaction [14-16]. Derivatives of CS along with various chemical functionalities make them applied for various applications such as pharmaceutical, medicinal, environmental, drug delivery, and biotechnology applications. Among the antimicrobial chemicals, phenolic compounds with free ortho position were chosen to be modified with CS. Formaldehyde can be attached to the aromatic ring as a carbonyl group *via* electrophilic aromatic substitution at the ortho position. Thymol and chloroxylenol with activated hydroxyl group are the potential candidates as precursor for CS derivative with antimicrobial application.

Thymol, a major phenolic component of thyme essential oil, is a natural substance that can inhibit the growth of microorganisms. As reported in many studies [17], the use of natural antibacterial agents provides a potential way to inhibit a wide

range of microorganisms without compromising consumer health. The World Health Organization has pointed out that thymol does no harm to consumers. Thymol has promising characteristics for treatment of root caries and oral therapy [18]. It has been reported that thymol was effective for the control of Staphylococcus aureus, Staphylococcus epidermidis, Pseudomonas aeruginosa, Shigella sonnei, Shigella flexneri and oral pathogens.

Chloroxylenol, a high efficiency antimicrobial phenolic compound, is an antiseptic and disinfectant which is used in personal care products, and together with alcohol for cleaning surgical instruments. It is also used within a number of household disinfectants and wound cleaners. Chloroxylenol has significantly increased the consumption of antibacterial products worldwide due to coronavirus disease 2019 (COVID-19) pandemic [19]. It has been reported that chloroxylenol is effective for control of gram-positive bacteria.

Accordingly, this thesis focuses on the development of a new antimicrobial agent by incorporating AuNPs or AgNPs with CS derivatives. The strong antimicrobial effect of the CS-modified AgNPs can be enhanced by altering the surface charges of AuNPs and AgNPs to achieve stronger attractive force. The study divided into 2 parts: **Part 1:** The objective of this part is to be focused on antimicrobial AuNPs for oral application. Firstly, thymol was covalently bonded to the CS backbone yielding chitosan-grafted thymol (CST). The incorporation of thymol as hydrophobic active functional groups onto the CS backbone represents a strategic enhancement to the antimicrobial activity of the materials. Subsequently, a novel CST antimicrobial compound was utilized as a stabilizer in the synthesis of AuNPs, resulting in a highly stable colloidal CST-AuNPs solution [20]. This solution was developed to control bacterial growth in oral applications. These modifications bring chitosan a better antibacterial activity and expand its application as well with *S. mutans ATCC 25175* and *S. sobrinus ATCC 33402.* **Part 2:** Chloroxylenol as hydrophobic active functional groups was incorporated with CS backbone yielding chitosan-grafted chloroxylenol (CSX). Secondly, hydrophilic acrylic acid was introduced to CSX to obtain carboxyethyl chitosan-grafted chloroxylenol (CECSX). The modification of acrylic acid brings CSX better water solubility affecting the higher antibacterial activity under neutral and basic conditions (pH 7–12) against pathogenic bacteria. Additionally, a novel CECSX antimicrobial compound was employed as a stabilizer in the synthesis of AgNPs,

producing a highly stable CECSX-AgNPs colloidal solution [21]. This solution was applied on surgical suture surfaces by Layer-by-Layer method. The resulting CECSX-AgNPs coated surgical suture surfaces demonstrated outstanding antimicrobial properties against *E. coli* (ATCC25922), *S. aureus* (ATCC25923), and *A. baumanii* (ATCC19606), thereby highlighting the potential of this innovative approach to advance the field of medical materials and infection control.

1.2 New chitosan-grafted thymol coated on gold nanoparticles for control of cariogenic in the oral cavity (CST-AuNPs)

Objectives

1) To develop antimicrobial AuNPs for controlling cariogenic bacterial in oral application.
2) To modify CS backbone with thymol as hydrophobic region, resulting in chitosan-grafted thymol (CST) via Mannich reaction to enhance the antimicrobial activity of the CS.
3) To optimize concentration of CST to produce highly stable colloidal CST-AuNPs solution by chemical reduction method.
4) To study antimicrobial properties of the CS, CST, and CST-AuNPs with oral bacteria e.g., *S. mutans* and *S. sobrinus.*

Scopes of study

1) Develop antimicrobial AuNPs for controlling cariogenic bacterial in oral applications.
2) Synthesize CST *via* Mannich reaction and characterize it to confirm the covalent bonding of thymol to the CS backbone.
3) Synthesize CST-AuNPs by chemical reduction method and characterize them to determine the optimal ratio of CST in the AuNPs synthesis.
4) Study factors affecting the stability of nanoparticles such as pH, ionic strength, and time.
5) Study the antimicrobial activity of CS, CST and CST-AuNPs against oral bacteria, including *S. mutans* and *S. sobrinus.*

1.3 Antimicrobial nanolayer films of chloroxylenol-carboxyethylchitosan -modified silver nanoparticles for enhanced surgical suture performance (CECSX-AgNPs)

Objectives

1) To develop AgNP antimicrobial coatings for suture materials e.g., cotton, polyamide and polypropylene.
2) To modify CS backbone with chloroxylenol and acrylic acid, resulting in carboxyethyl chitosan-grafted-chloroxylenol (CECSX) to improve antimicrobial properties in both acidic and alkaline conditions.
3) To optimize concentration of CECSX to produce highly stable colloidal CECSX-AgNPs solution by chemical reduction method.
4) To study the fabrication of nanoparticles onto suture materials by layer-by-layer deposition method.
5) To study antimicrobial properties of the CS, CSX, CECSX, CECSX-AgNPs and CECSX-AgNPs coated on suture materials against *E. coli* (ATCC25922), *S. aureus* (ATCC25923), and *A. baumanii* (ATCC19606).

Scopes of Study

1) Develop AgNP antimicrobial coatings for suture materials e.g., cotton, polyamide and polypropylene.
2) Synthesize and characterize CSX and CECSX, and study their solubility properties in various pH conditions.
3) Synthesize CECSX-AgNPs by chemical reduction and characterize them to determine the optimal ratio of CECSX in the AgNPs synthesis.
4) Study the fabrication and the factors affecting the coating of AgNPs onto suture materials using the Layer-by-Layer deposition method.
5) Study the antimicrobial activity of CS, CECSX, and CECSX-AgNPs using microdilution methods and investigate the bacterial reduction of AgNP coatings on various suture materials by time-kill-study methods against *E. coli* (ATCC 25922), *S. aureus* (ATCC 25923), and *A. baumannii* (ATCC 19606).

Chapter 2
Theory and Literature Reviews

2.1 Metallic Nanoparticles

2.1.1 Methods of metallic nanoparticle preparation

The preparation metallic nanoparticles involve a multitude of techniques, broadly categorized into two approaches: bottom-up and top-down, as illustrated in Figure 2.1. These approaches primarily differ in terms of the initial materials used for nanoparticle preparation. In the top-down methods, nanoparticles are generated from bulk materials, which are systematically reduced to nanoparticle sizes through a combination of physical, chemical, and mechanical processes. For the example in this method include mechanical milling, laser ablation and sputtering.

Mechanical milling [22] is a top-down approach used to prepare metallic nanoparticles by subjecting bulk metallic materials to high-energy ball mills or attritor mills. In this method, the precursor material, typically a ductile metal such as iron, aluminum, copper, or alloy, is loaded into the milling chamber along with milling balls made of hard materials such as steel or tungsten carbide. As the milling chamber rotates, the milling balls impact the precursor material, causing deformation, fracture, and ultimately particle size reduction.

Laser ablation is a method used to prepare metallic nanoparticles by irradiating a bulk metallic target with a high-energy laser beam in a liquid medium. The laser beam vaporizes the surface of the target, generating a plasma plume containing metal atoms and ions. Rapid cooling of the plasma in the surrounding liquid leads to the nucleation and growth of metallic nanoparticles.

Ion sputtering is a method utilized for the preparation of metallic nanoparticles by bombarding a solid metallic target with high-energy ions in a vacuum environment. During the sputtering process, energetic ions impinge on the surface of the target material, causing atoms to be ejected from the surface. These ejected atoms form a flux of metal atoms in the surrounding environment, which then condense and aggregate to form metallic nanoparticles on a substrate placed nearby.

Conversely, the bottom-up methods commence with atoms or molecules as the foundational materials, which are then assembled or synthesized to form nanoparticles [23]. For the example in this method include solid state methods, liquid state synthesis methods, gas phase methods and green synthesis method. The chemical reduction method was widely chosen for the preparation metallic nanoparticles because it is the simplest method which can create metallic nanoparticles of various sizes and forms by changing the ingredients and concentrations with high yield in synthesis and ease of application.

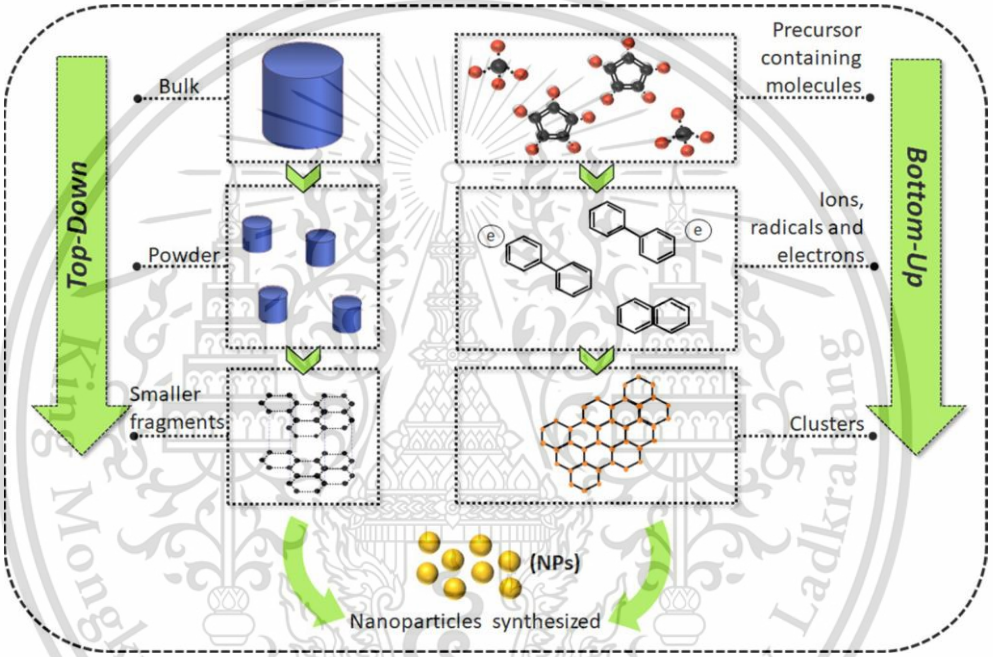

Figure 2.1 Diagrammatic representation of top-down and bottom-up approaches for synthesis of metal NPs [24].

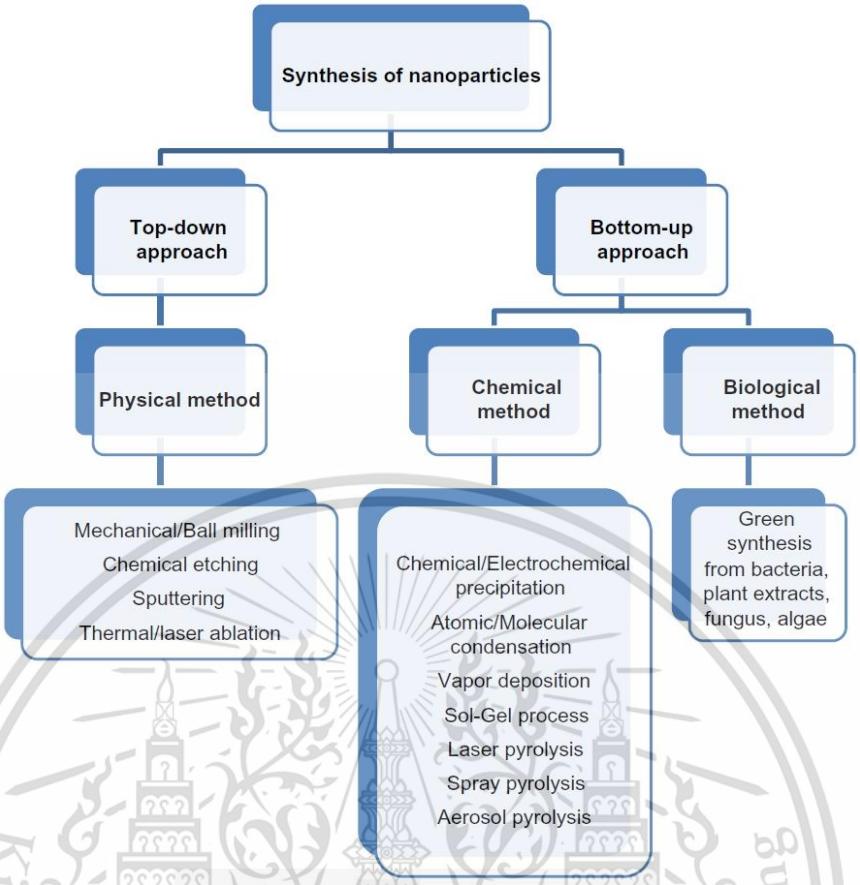

Figure 2.2 Top-down methods and bottom-up methods of nanoparticle preparation.

2.1.2 Chemical reduction synthesis

The principle of chemical reduction method is that Au^{3+} is reduced to Au^{0} by receiving electrons from a reducing agent. In this method, nanoparticle size can be controlled by changing the ingredients and concentration. Ascorbic acid, sodium citrate, sodium borohydride, and other substances are common reducing agents. Some reducing agents can also act as stabilizers. Numerous studies on metal nanoparticles have focused on their functionalization using diverse stabilizing agents such as proteins, drugs, genes, peptides, or biomolecules [25]. This functionalization aims to enhance their colloidal stability, biocompatibility, safety, and overall effectiveness. When metal nanoparticles are conjugated with antibiotics or drugs, they demonstrate enhanced antibacterial or antiviral activities compared to the standalone antibiotics or drugs [26]

Occasionally, stabilizing agents are also combined with the reducing agents to enhance the process. Agglomeration of the nanoparticles can be efficiently prevented by stabilizers and surfactants. Additionally, surfactants can also control their growth. The most typical chemical reduction methods are sodium citrate reduction and the

Brust–Schiffrin method. The preparation of AuNPs with various chemical reduction methods is shown in Figure 2.3.

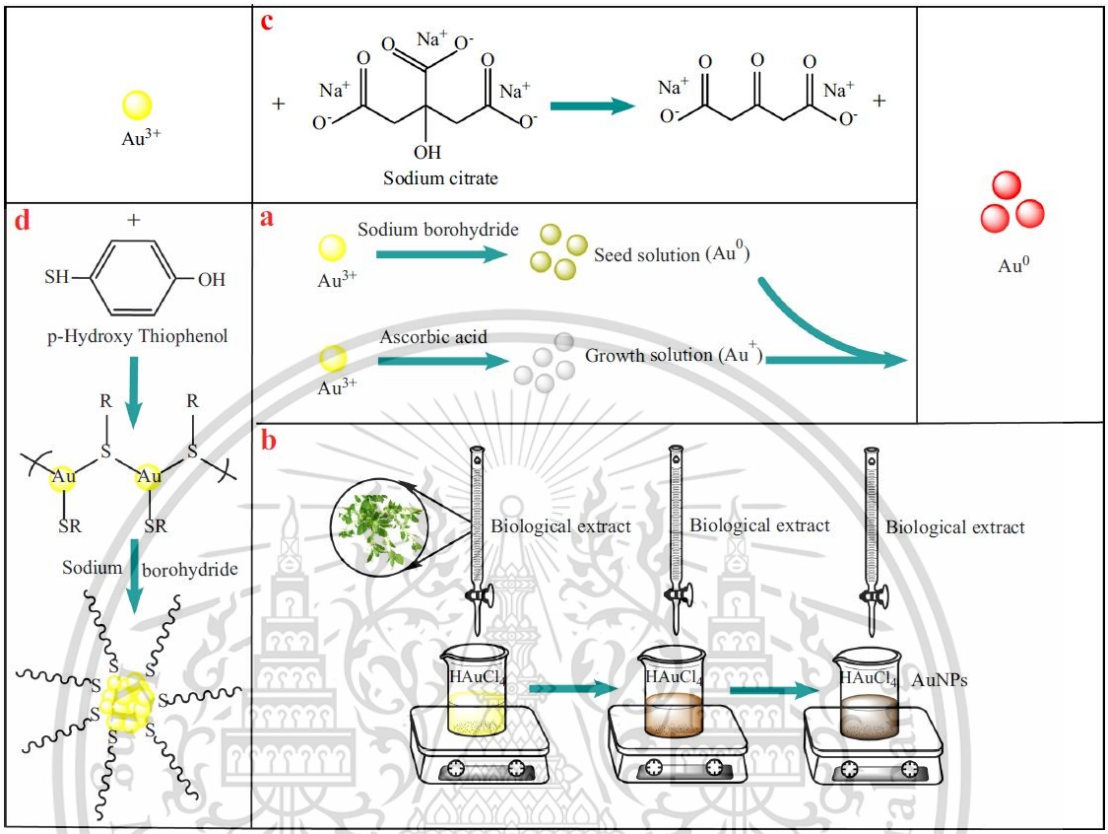

Figure 2.3 Preparation of gold nanoparticles (AuNPs). (a) The seed growth method. (b) biological extract synthesis. (c) the sodium citrate reduction method. (d) the Brust–Schiffrin method.

- Chemical reduction method (Chitosan-Mediated Synthesis)

Huang et. al. [27] prepared AuNPs by using only medium molecular weight CS (400,000 g/mol) or low molecular weight CS (5400 g/mol). In this research, CS functioned as both a reducing and stabilizing agent. A solution of $HAuCl_4$ (1 mL, 1 mM) was combined with a diluted CS solution (3 mL). This mixture was then heated to 70°C and magnetically stirred for a duration of 2 hr. The results indicated that the molecular weight and concentration of CS had an impact on the form and size distribution of gold nanoparticles.

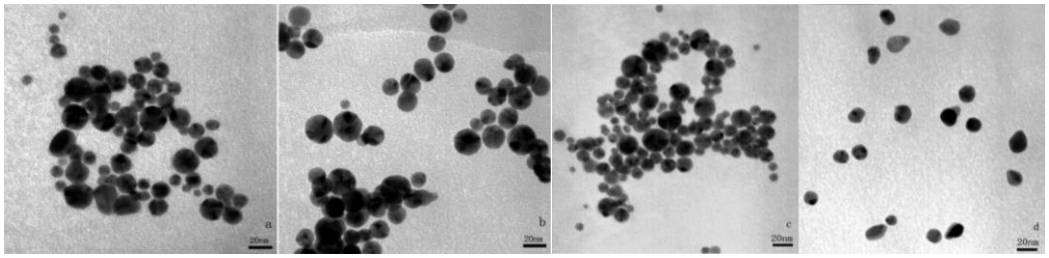

Figure 2.4 TEM images of gold nanoparticles prepared by 0.05% (A) and 0.25% (B) medium molecular weight CS and 0.05% (C) and 0.25% (D) lower molecular weight CS [27].

- The seed growth method

The seed growth method can also be formulated in a number of geometries and shape such as rods. This method is based on the fundamental principle which involves first synthesizing seed particles by reducing gold salts. This reaction is done in the presence of reducing agents like $NaBH_4$. The next step involves the transferring of the seed particles to a metal salt and a weak reducing agent like ascorbic acid which prevents further nucleation and speeds up the synthesis of AuNPs of rod shape. Shape and geometry of gold nanoparticles depends on the concentration of reducing agents and seeds.

Emam et. al. [28] used Arabic gum as a biosynthetic agent to produce Ag–Au bimetallic nanoscale composite particles using seed-mediated growth techniques, as shown in Figure 2.5. Acacia gum can be used as both a reducing agent for metal ions in producing nanoscale structures and as a crystal growth modifier for nanocomposites. Silver nitrate, gold chloride and sodium hydroxide are added to the prepared Arabic gum with stirring at room temperature or 70 °C. The order of addition of the alkali and metal salts, the concentration of the glue and the reaction temperature all affect the particle size generated. Increasing the reaction temperature reduces the average size of the bimetallic particles from 6.5 to 3.1 nm. Adding alkali after the metal salt increases the size of Ag–Au composite particles from 3.1 to 12.7 nm.

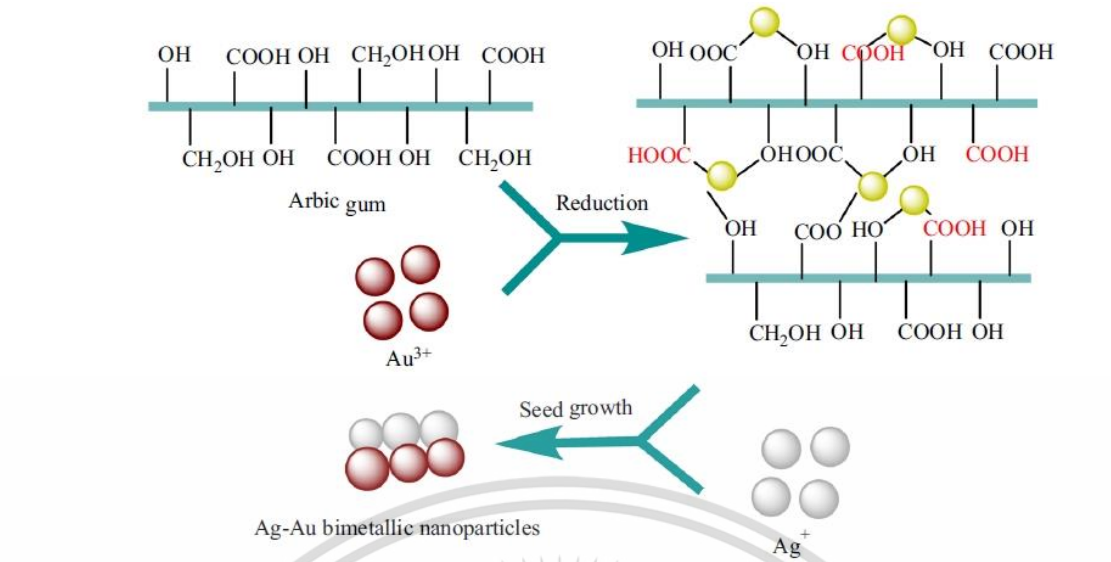

Figure 2.5 The seed growth method [28].

- Biological extract synthesis

Biological extract synthesis involves the use of biological organisms or biomolecules. The biological extract is obtained through a series of treatments such as washing, water bath heating and paper filtration. Reducing substances such as vitamins, sugars and hydroxyl groups are extracted in this way from grapefruit skins and used as reducing agents and stabilizers [29]. This method is eco-friendly and offers biocompatible nanoparticles for various biomedical applications.

- The sodium citrate reduction method

The sodium citrate reduction method, also known as the Turkevich method, involves the reduction of metal salts by a reducing agent, typically sodium citrate, under controlled conditions to form nanoparticles. Citrate ions in the solution serve as both reducing and stabilizing agents. Sodium citrate reduction is the most convenient and the most commonly used in chemical reduction methods. It can generate spherical gold particles between 10 and 50 nm in diameter.

Franconetti et. al. synthesized AuNPs capped with citrate by modifying the traditional Turkevich method. In their procedure, an aqueous solution of $HAuCl_4$ (97mL, 0.01%) was heated to 90 °C. Subsequently, sodium citrate (3 mL, 38.8 mM) was added to the heated solution, and the mixture was further heated for 10 minutes. The resulting synthesized nanoparticles exhibited a particle size of 15 ± 2 nm.

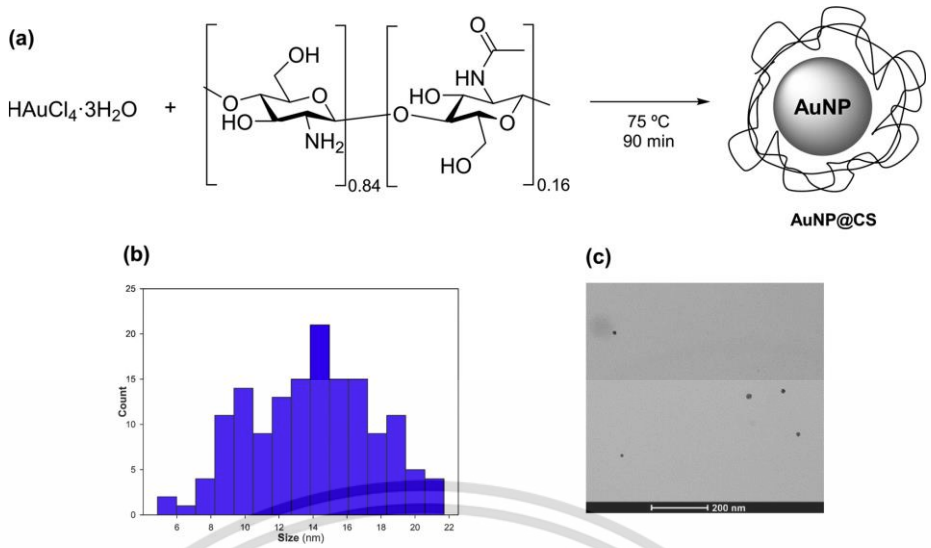

Figure 2.6 Synthesis and characterization of AuNPs-CS: (a) schematic representation of synthesized NP; (b) Histogram of the size distribution of the colloidal system and (c) TEM image used for measuring the average size [AuNPs-CS] =3.1×10^{-9} M.

- The Brust–Schiffrin method

The Brust–Schiffrin method utilizes strong reducing agents such as phosphines or amines to rapidly reduce metal salts and form nanoparticles. Ligands attached to the metal surface play a crucial role in stabilizing the nanoparticles and controlling their size and shape.

The Brust–Schiffrin method [30], also dubbed the two-phase method, involves dissolving chloroauric acid solution and p-mercaptophenol in methanol. Acetic acid is employed to stop p-mercaptophenol from being protonated. Tetraoctylammonium bromide functions as a phase transfer agent that assists transfer $HAuCl_4$ from the aqueous phase into the organic phase. The solution rapidly turns brown in the presence of dodecyl mercaptan upon the addition of sodium borohydride, a strong reducing agent, signifying the creation of gold clusters. The ratio of gold to dodecyl mercaptan affects the size of the particles. As a surfactant, dodecyl mercaptan is amphiphilic, which allows it to adsorb onto the surface of the particles. This surfactant-coated nanoparticle provides long durations of stability in both a liquid and solid form. Although the procedure shown in Figure 2.3 (d) produces small and highly stable AuNPs, the disadvantage is its complexity.

2.1.3 Stabilization of Metallic Nanoparticles

A stabilizing agent plays a crucial role in maintaining repulsive forces in nanoparticle solutions, effectively countering Van der Waals forces to prevent nanoparticle agglomeration. In the chemical synthesis of AuNPs, compounds such as sodium borohydride, sodium hydride, sodium citrate, or ascorbic acid can serve dual functions as both capping and stabilizing agents. The stability of nanoparticles can be accomplished during the biological synthesis of AuNPs, however, by utilizing the biomaterial, which is rich in antioxidant characteristics. In the synthesis and stabilization processes, the biomass contains a wide range of reactive chemicals. Gold nanoparticles (AuNPs) are highly stable, largely due to their high surface charge which helps prevent them from agglomeration. This stability is indicated by their high zeta potential values. Research has shown that substances like proteins, nicotinamide adenine dinucleotide, terpenoids, and phenolic compounds can act as stabilizers and capping agents in the biological creation of AuNPs. Additionally, the size and shape of these nanoparticles can be manipulated by adjusting factors such as the temperature, pH, and the concentration of gold salt used in the reaction. The process of stabilizing metallic nanoparticles, including AuNPs, is comprehensively described by the Derjaguin Landau Verwey Overbeek (DLVO) theory.

The DLVO theory posits that the stability of colloidal systems depends on the balance between attractive van der Waals forces and repulsive electrostatic forces. In nanoparticle solutions, stabilizing agents play a crucial role in maintaining repulsive electrostatic forces, effectively countering the attractive van der Waals forces that promote nanoparticle agglomeration.

Three types of stabilization of NPs employing various capping agents can be distinguished: steric stabilization, electrostatic stabilization, and unification of steric and electrostatic stability [31].

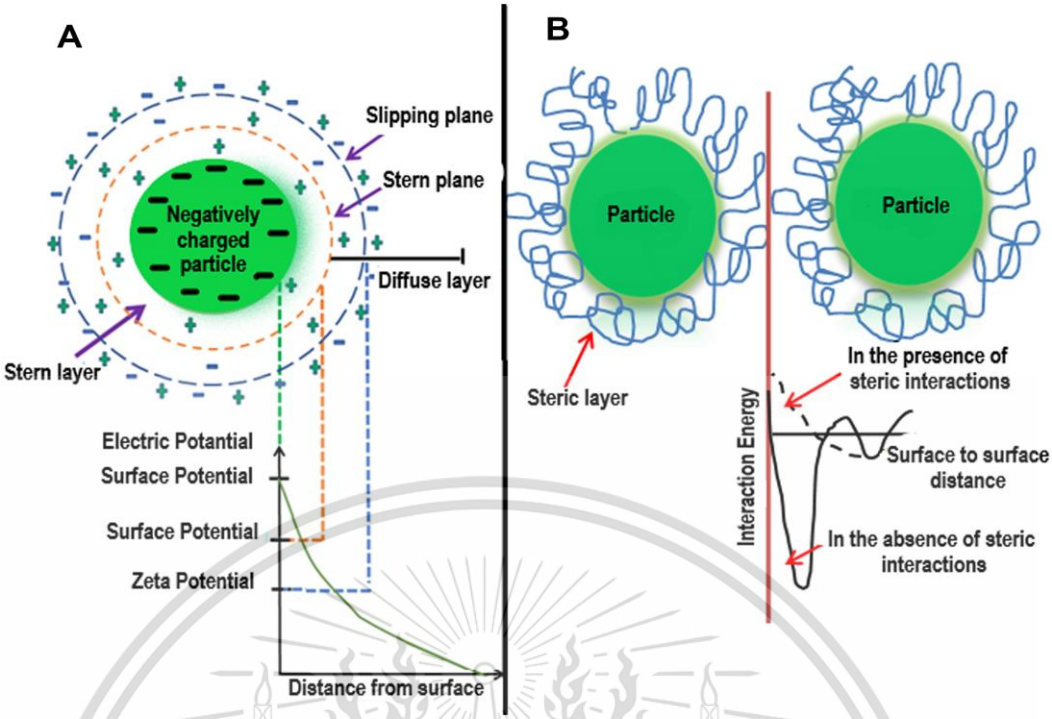

Figure 2.7 (a) Electrostatic stabilization of metallic nanoparticles. (b) Steric stabilization of metallic nanoparticles[31].

2.1.3.1 Electrostatic Stabilization

Ionic groups in the liquid dispersion medium can adhere to the surface of a colloidal nanoparticle, creating a charged layer around it. As a result, equal numbers of ions with opposing charges will surround the colloidal nanoparticles, creating double layers that are overall electro-neutral. As a result, double layers that are electro-neutral overall will be formed by an equal number of ions with opposing charges surrounding the colloidal nanoparticles. As shown in Figure 2.7 (a) this stabilization process is based on the formation of an electric double layer around the nanoparticles, involving both repulsive and attractive forces. This balance is influenced by various ionic compounds present in the solution. The aggregation of nanoparticles in a liquid is prevented by the electrostatic repulsion force between them. Electrostatic stabilization is controlled by the regulation of several significant factors, including pH, concentration, and temperature.

2.1.3.2 Steric Stabilization

Steric stabilization is a crucial method used in nanoparticle synthesis to prevent the uncontrolled aggregation or coalescence of metal nanoparticles. This stabilization technique utilizes molecules with bulky, long, and flexible chains, such as surfactants, polymers, or biomolecules, which adsorb onto the surface of nanoparticles during their formation. These molecules create a physical barrier or protective coating around the nanoparticles, hindering their movement and preventing them from coming into close contact with each other as shown in Figure 2.7 (b).

The functional groups present in these stabilizing molecules, such as hydroxyl groups (-OH) in surfactants or polymer chains, play a key role in providing steric hindrance. When nanoparticles are synthesized in the presence of these stabilizers, the molecules adsorb onto the nanoparticle surface via non-covalent interactions, such as hydrogen bonding or van der Waals forces. The long and flexible chains of the stabilizer molecules extend outward into the surrounding solution, forming a dense layer around each nanoparticle.

This protective coating effectively shields the nanoparticles from interacting with each other by creating repulsive forces and steric hindrance. The nanoparticles become "sterically stabilized," meaning they are unable to approach each other due to the presence of the surrounding macromolecules. As a result, the nanoparticles remain well-dispersed and isolated from each other in the solution, preventing aggregation and maintaining their stability.

2.1.3.3 Unification of steric and electrostatic stability

Although electrostatic stabilization is easier to maintain in colloidal media, there are certain limitations to it. Firstly, electrostatic stabilization cannot be achieved in electrolyte sensitive media. Additionally, due to strong forces of interactions between oppositely charged ions it is impossible to separate agglomerated particles. Moreover, it cannot be applied to multiple phase systems as different solids establish distinct surface charge and surface potential. As compared to the electrostatic stabilization, which is a kinetic stabilization method, steric stabilization is a thermodynamic stabilization

method; therefore, particles can be redispersed. It is also not sensitive to electrolytes and can be applied to multiple phase systems.

Unified stabilization combines both steric and electrostatic mechanisms offers a comprehensive and versatile approach to nanoparticle stabilization, addressing the limitations of individual stabilization methods while providing enhanced stability, redispersion capability, and applicability across diverse environmental conditions.

2.1.4 Antimicrobial Mechanism of Metallic Nanoparticles [32, 33]

Metallic nanoparticles can produce by various modification methods. The different methods were affecting the antibacterial properties of metallic nanoparticles. The antimicrobial mechanisms of metallic nanoparticles are also unclear [33]. For example, The antimicrobial action of AgNPs is linked to four main mechanisms: (i) attraction to bacterial surface, (ii) destabilization of bacterial cell wall and membrane with change in its permeability, (iii) induction of toxicity and oxidative stress by generation of ROS and free radicals, and (iv) modulation of signal transduction pathways

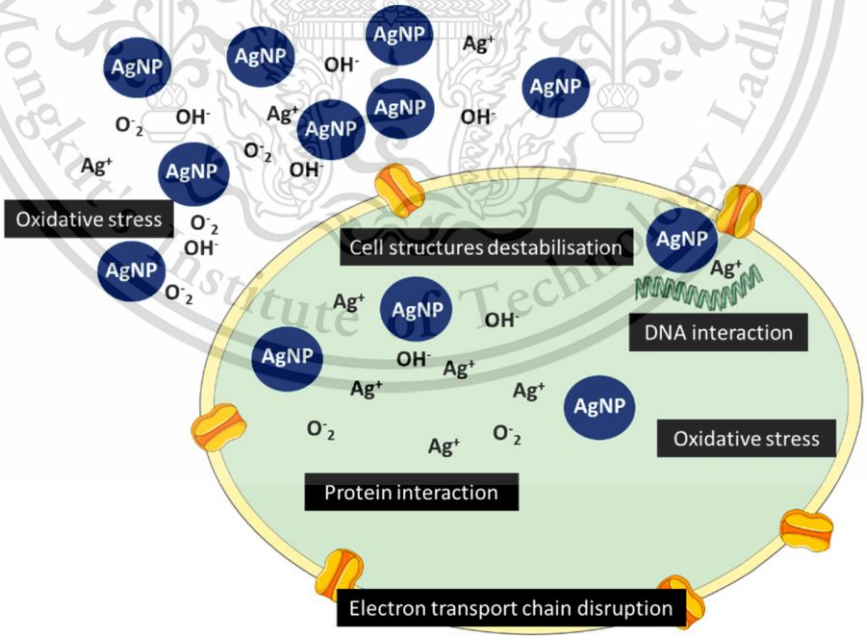

Figure 2.8 Schematic representation of AgNPs mechanism of antibacterial activity [32].

Adhesion of AgNPs onto the surface of bacteria is described by many authors as the first step of a complex mechanism of bacterial inhibition. AgNPs adhesion is highly influenced by their size, but also by their zeta potential. Depending on the method for their synthesis, AgNPs may have a positive, neutral, or negative surface charge.

Abbaszadegan et al [34]. demonstrated that by varying the surface charge of nanoparticles, a marked fluctuation of the antibacterial activity occurs. Since bacterial surface shows a slightly negative charge, positively charged AgNPs are strongly attracted to the surface of the bacteria, resulting in increased antibacterial activity. On the other hand, neutral or negatively charged nanoparticles have a significantly decreased antibacterial effect. However, an increase in the concentration of AgNPs allows the attenuation of electrostatic repulsion through a bacterial surface saturation method.

Upon adhesion to the bacterial surface, AgNPs engage with cells through two distinct mechanisms. Smaller AgNPs directly penetrate the cell, while larger ones remain outside the bacteria. Regardless of size, AgNPs continually release silver ions (Ag^+). These ions interact with cell membrane structures, leading to membrane potential destabilization and proton leakage. Consequently, bacterial cell wall destabilization significantly enhances permeability, facilitating the entry of larger AgNPs into the cell. After entering the cell, both silver nanoparticles (AgNPs) and silver ions (Ag^+) interact with various structures and biomolecules such as proteins, lipids, and DNA, leading to cellular dysfunction. AgNPs are well known by their high capacity to produce reactive oxygen species (ROS) and free radicals as hydrogen peroxide (H_2O_2), superoxide anion (O_2^-), and hydroxyl radical (OH^-).

While reactive oxygen species (ROS) naturally arise in bacteria during cellular respiration, bacteria typically possess defense mechanisms to mitigate their harmful effects. These defense mechanisms include antioxidant enzymes like glutathione (GSH), superoxide dismutase, and catalase, which function to neutralize ROS and eliminate these toxic species.

High concentrations of Ag^+ released by AgNPs produce extreme levels of oxidative stress (Figure 2.8). Even though antioxidant enzymes remove some of the released ions, these are not enough to neutralize the AgNPs amount. These ions interact with respiratory chain proteins on the cell membrane, deactivating enzymes because they strongly bind to phosphates, thiols, and carboxyl groups. Their

attachment to phosphate groups prevents protein phosphorylation, a crucial step in activating enzymes, ultimately leading to the inhibition of bacterial growth.

Tyrosine residue dephosphorylation within proteins has been associated with the disturbance of exopolysaccharide and capsular polysaccharide biosynthesis and transport to the membrane, leading to cell cycle disruption. Furthermore, Ag^{+} can intercalate DNA strands forming complexes with nucleic acids between the purine and pyrimidine base pairs, disrupting H-bonds between them.

2.2 Chitosan

2.2.1 Structure

CS is a natural polymer derived from deacetylation reaction of chitin. Its structure has one amino group and two hydroxyl groups in the repeating glycosidic residue. Each unit is linked by (1⟶4)-β-glycosidic bonds, which is similar to cellulose. However, the hydroxyl group at C_2 is replaced by acetylamino or amino group, providing units so called N-acetyl-2-amino-2-deoxy-D-glucopyranose (N-acetylglucosamine, D-GlcNAc) and 2-amino-2-deoxy-D-glucopyranose (Glucosamine, D-GlcN). The structure of chitin and CS is depicted in Figure 2.9. The degree of deacetylation (DD) of CS, giving indication of the number of amino groups along the chains, is calculated as the ratio of glucosamine unit to N-acetylglucosamine unit. To be named as CS, the degree of deacetylation has to over than 0.65 [35].

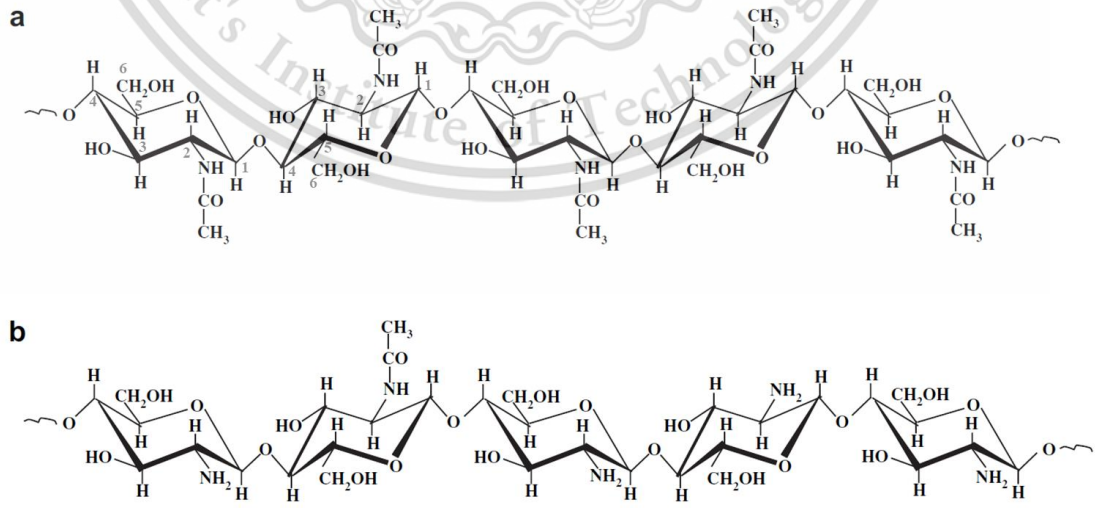

Figure 2.9 Primary structure of (a) chitin, and (b) chitosan [35].

2.2.2 Synthesis

As discussed above, CS can be derived by deacetylation reaction of chitin. Chitin is a natural polymer obtained from crustacean shells (especially from shrimp, squid, shell, and crab) and cell walls of fungi. To begin with, crustacean shell or fungi was demineralized to remove $CaCO_3$ by treating with HCl. After that, it was deproteinized by treating with NaOH. The resulting product was deacetylated using 40% NaOH at 120 ^{o}C for 1-3 h to obtain deacetylated CS. The simplified flowsheet for CS preparation demonstrated in Figure 2.10

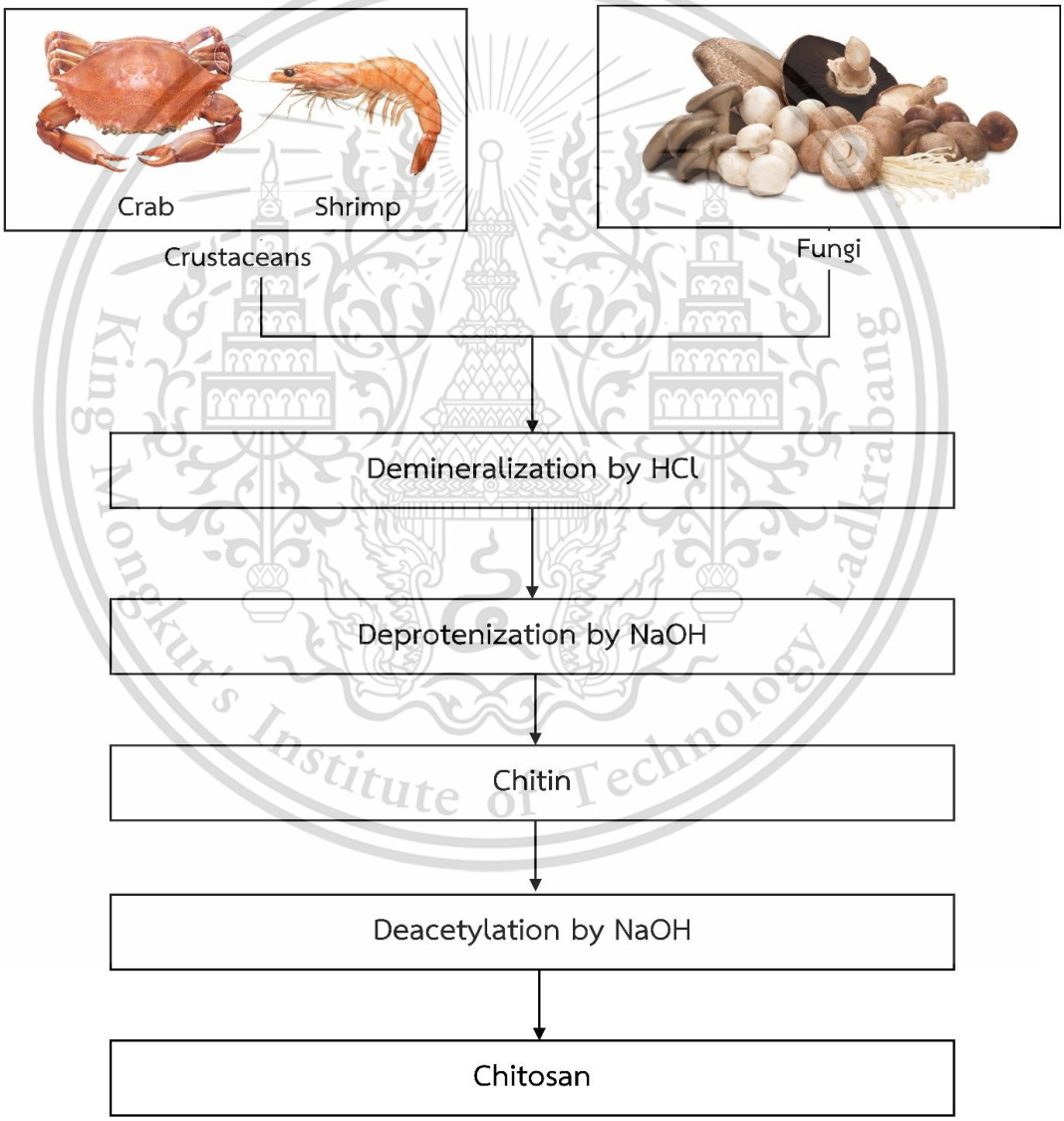

Figure 2.10 Synthesis of chitin/chitosan.

2.2.3 Properties of chitosan

Solubility: CS is soluble in dilute acidic solution below pH 6.0. In acidic solution, amines in CS get protonated and turn to positive charge which can dissolve in water in form of water-soluble cationic polyelectrolyte (Figure 2.11). The quaternary nitrogen salt is obtained by dissolving CS in acetic, formic, lactic, hydrochloric, nitric acid solutions. 1% w/v acetic acid (pH=4) is the most popular solvent for dissolving CS. However, CS can be depolymerized when using concentrated acetic acid solutions as solvents at high temperature. When pH increases above 6, amine groups in CS are deprotonated and CS loses its charges and becomes insoluble. The soluble-insoluble transition takes place at its pK_a value around pH between 6 and 6.5. In fact, the solubility of CS is very hard to control owing to many parameters affecting its solubility such as degree of deacetylation, ionic concentration, pH, nature of acid used for protonation, distribution of acetyl group along the chain, and conditions of isolation and drying of the CS.

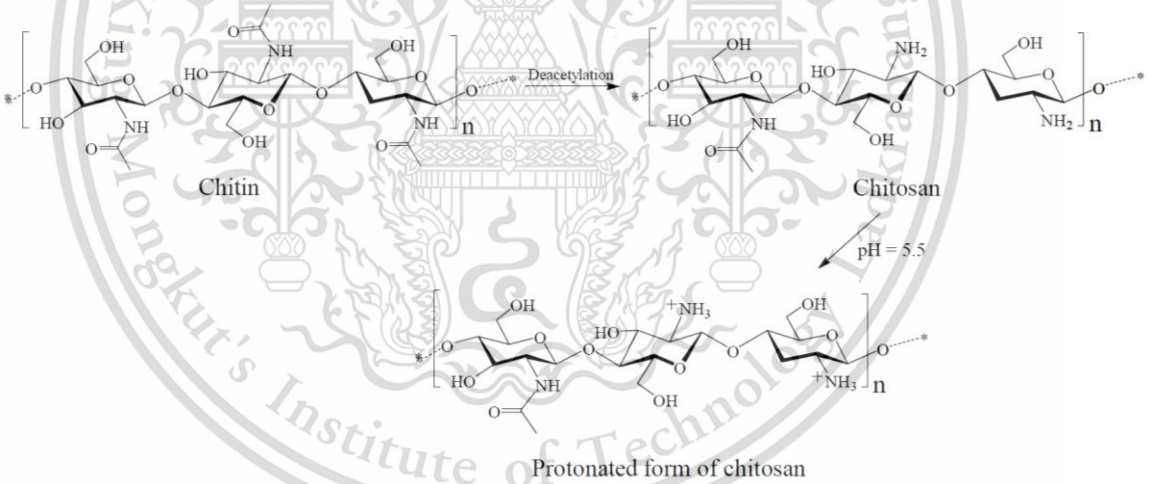

Figure 2.11 Structure of chitin, chitosan and the protonated form of chitosan [36].

Antimicrobial properties: CS has been extensively studied as an antimicrobial material targeting a wide range of organisms such as algae, bacteria, yeasts, and fungi in various forms including solutions, films, and composites. Generally, CS is considered to be either bactericidal (killing live bacteria or a portion thereof) or bacteriostatic (inhibiting bacterial growth without necessarily killing them). While the precise mechanism underlying the antibacterial activity of CS remains incompletely

understood, several mechanisms have been proposed. These antimicrobial mechanisms of CS are illustrated in Figure 2.12, and four models have been suggested to explain its antibacterial mechanism.

Model 1 depends on the electrostatic interaction between protonated NH_3^+ groups and negative residues. This interaction is thought to compete with Ca^{2+} for electronegative sites on the membrane surface, resulting in two main effects: (i) Inducing changes in membrane wall permeability, leading to internal osmotic imbalances that inhibit the growth of microorganisms. (ii) Hydrolyzing the peptidoglycans in the microorganism wall, causing leakage of intracellular electrolytes such as potassium ions and other low molecular weight proteinaceous constituents (e.g., proteins, nucleic acids, glucose, and lactate dehydrogenase).

Model 2 depends on the forming of polymer membrane by CS on the surface of the bacteria, which prevents nutrients from entering the cell. In this mechanism, CS is not necessary attached to the surface and independently of the bacteria type. Adjustments on pH can be decisive for a good solubility and keep the chains apart from each other.

Model 3 involves the binding of CS with microbial DNA, resulting in the inhibition of mRNA and protein synthesis. This occurs through the penetration of CS into the nuclei of microorganisms. It is hypothesized that CS molecules can traverse the bacterial cell wall, composed of multilayers of cross-linked murein, to reach the plasma membrane.

Model 4 involves the chelation of metals, suppression of spore elements, and binding to essential nutrients required for microbial growth. CS exhibits excellent metal-binding capacities, with the amine groups in CS molecules responsible for the uptake of metal cations through chelation. This mechanism is particularly efficient at high pH levels, where positive ions are bound to CS, as the amine groups are unprotonated, allowing the electron pair on the amine nitrogen to be available for donation to metal ions.

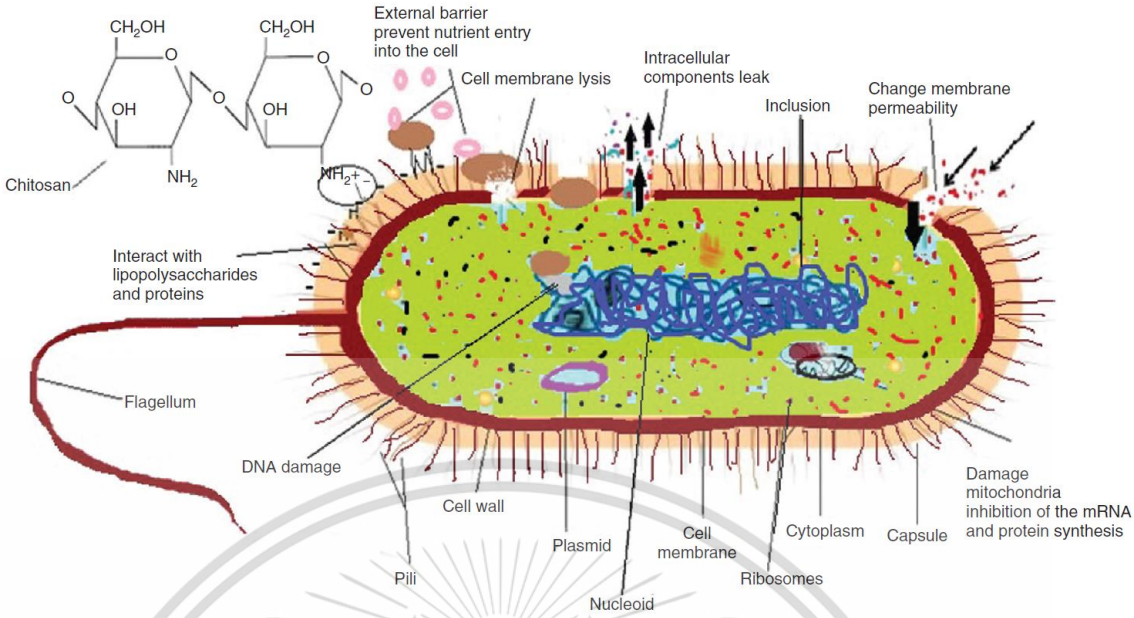

Figure 2.12 Various antimicrobial mechanisms of chitosan [37].

Generally, the mechanisms of inhibitory activity differ of CS depends on many factors include molecular weight [38], deacetylation, pH and the concentration of active compounds connected to CS and bacteria type [39] .

- Molecular weight and Deacetylation: Several studies have shown that the biological activity of CS depends significantly on its molecular weight (MW) and degree of deacetylation (DD). Both parameters independently affect the antimicrobial activity of CS, although it has been suggested that the influence of MW on the antimicrobial activity is greater than the influence of DD. The mobility, attraction and ionic interaction of smaller chains are easier than those of larger ones, facilitating the adoption of an extended conformation and effective binding to the membrane surface. Similarly, but to a varying degree, CS antimicrobial effectiveness improves with higher DD. Solubility and charge depend on DD, where the $-NH_2$, –OH groups in the CS molecule are considered as the dominant reactive sites. As the DD increases, the number of free amino groups in CS also increases, resulting in higher antimicrobial activity [11].

- pH of media solution: The antimicrobial efficacy of CS is predominantly observed at pH levels below 6, limiting its applicability and bioactivity studies under neutral and physiological conditions. To address this constraint, CS has been chemically modified to produce derivatives with enhanced activity and better aqueous solubility. Among the most prevalent functional groups found in antimicrobial CS derivatives are quaternary ammoniumyl, guanidinyl, carboxyalkyl, hydroxyalkyl, thiol-containing groups, and hydrophobic groups like long alkyl chains, substituted phenyl, and benzyl rings [36].

- Bacteria type: The mechanisms of the antimicrobial activity of CS are different between gram-positive and negative bacteria. Since CS can adsorb the electronegative substance in the cell and flocculate them, the dominant mechanism of gram-negative bacterial depends on low MW CS as model 1, it disturbs the physiological activities of the bacteria and kills them. But for gram-positive bacteria, the dominant mechanism depends on High MW CS as model 2. The cell membrane of S. aureus was weakened or ruptured, whereas the cytoplasm of E. coli appeared to be concentrated and the intercellular spaces were noticeably enlarged. Furthermore, the antimicrobial mechanism of CS may vary from that of other polysaccharides due to the presence of positive charges on its surface [38].

2.2.4 Modification of Chitosan

In general, CS contains three primary functional groups: C_2–NH_2, C_3–OH, and C_6–OH (Fig. 2.13). While modifications at the C_2–NH_2 or C_6–OH sites are relatively straightforward, altering CS at the C_3–OH position can be challenging due to significant steric hindrance. Among these functional groups, amino groups are commonly targeted for chemical modifications, primarily owing to the favorable reactivity of the C_2-amino group, which facilitates grafting reactions. Although amino groups exhibit greater reactivity towards nucleophilic reactions compared to hydroxyl groups, both functional groups readily react with electrophilic reagents such as halogenated alkanes, acyl chlorides, and acids, albeit non-selectively. The antimicrobial derivatives of CS typically incorporate functional groups such as quaternary ammoniumyl, guanidinyl, carboxyalkyl, hydroxyalkyl, thiol-containing groups, and hydrophobic moieties like long alkyl chains, substituted phenyl, and benzyl rings [7, 36, 40].

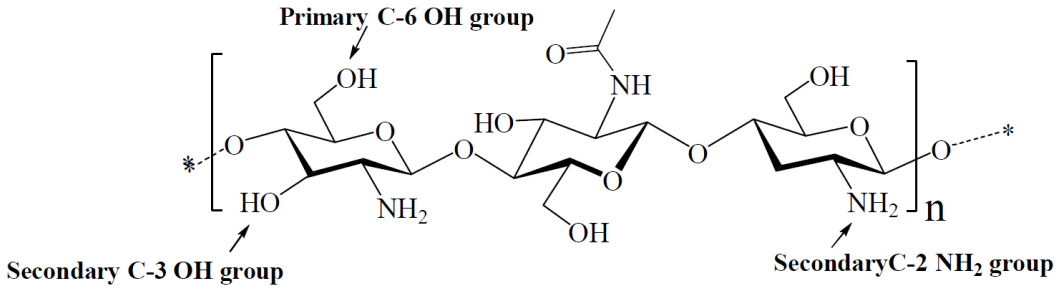

Figure 2.13 Chemical structure and possible reaction sites of chitosan.

Chemical modification reaction

1) Mannich Reaction [41]

The Mannich reaction is an organic reaction which consists of an amino alkylation of an acidic proton placed next to a carbonyl functional group by formaldehyde and a primary or secondary amine or ammonia. The final product is a β-amino-carbonyl compound also known as a Mannich base. Reactions between aldimines and α-methylene carbonyls are also considered Mannich reactions because these imines form between amines and aldehydes. The reaction is named after chemist Carl Mannich.

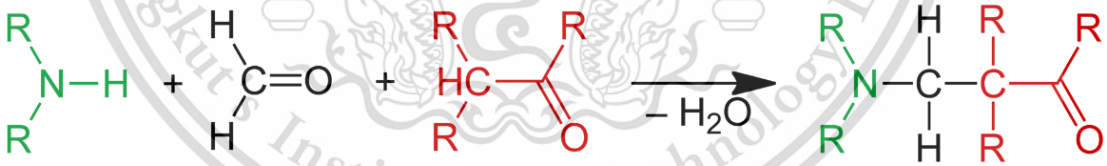

Figure 2.14 Mannich Reaction (Alkylation).

The Mannich reaction involves the nucleophilic addition of an amine to a carbonyl group, forming a Schiff base through dehydration. This Schiff base then reacts in an electrophilic addition with a compound containing an acidic proton, typically an enol. It is categorized as a condensation reaction.

In this reaction, primary or secondary amines, or ammonia, activate formaldehyde. Tertiary amines cannot form the intermediate enamine due to the lack of an N–H proton. Nucleophiles include α-CH-acidic compounds such as carbonyl

compounds, nitriles, acetylenes, aliphatic nitro compounds, α-alkyl-pyridines, or imines. Activated phenyl groups and electron-rich heterocycles like furan, pyrrole, and thiophene can also be used. Indole is notably reactive, yielding gramine derivatives. The Mannich reaction combines features of mixed-Aldol reaction, alcohol dehydration, and conjugate addition of an amine (Michael reaction), all occurring simultaneously. Double Mannich reactions are common and widely used.

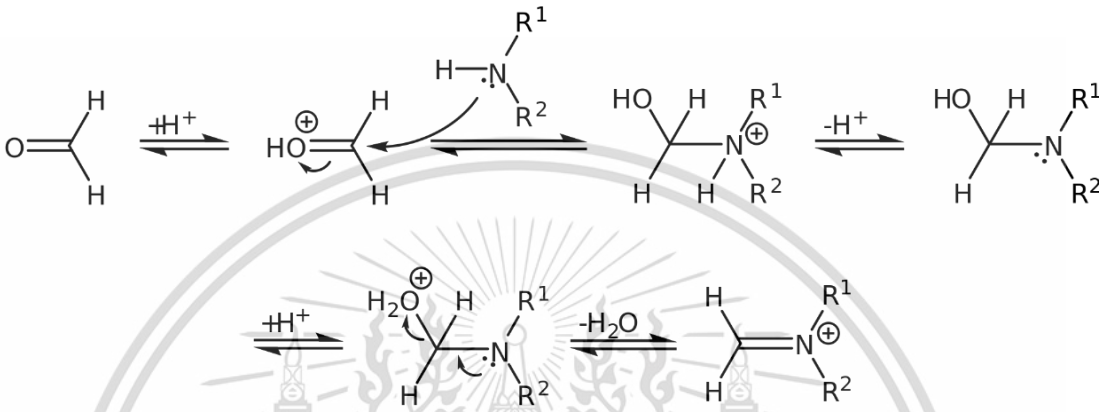

Figure 2.15 The mechanism of the Mannich reaction. (Starts with the formation of an iminium ion from the amine and the formaldehyde).

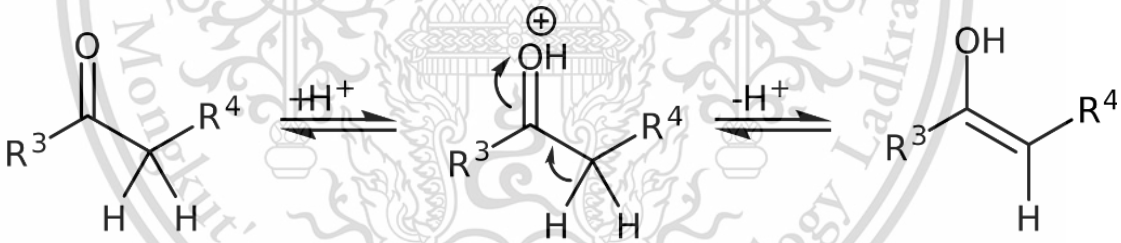

Figure 2.16 The mechanism of the Mannich reaction. (The compound with the carbonyl functional group can tautomerize to the enol form)

https://chem.libretexts.org/Bookshelves/Organic_Chemistry/Supplemental_Modules_(Organic_Chemistry)/Reactions/Organic_Reactions/Mannich_Reaction

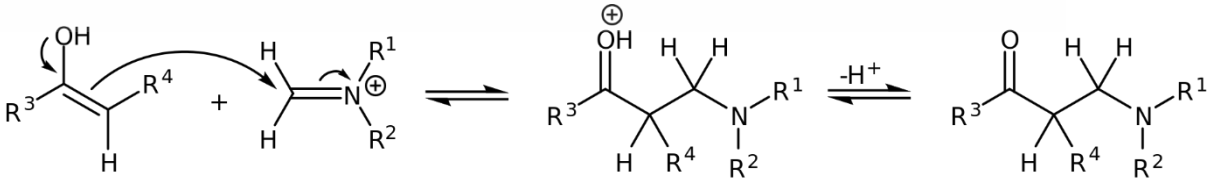

Figure 2.17 The mechanism of the Mannich reaction. (The enol form attacks the iminium ion).

2) Michael addition [42]

The Michael reaction, also known as Michael addition, involves the nucleophilic addition of a carbanion or another nucleophile to an α, β-unsaturated carbonyl compound with an electron-withdrawing group. It belongs to the category of conjugate additions and is widely utilized for the gentle formation of C–C bonds. Numerous asymmetric versions of the reaction have been developed.

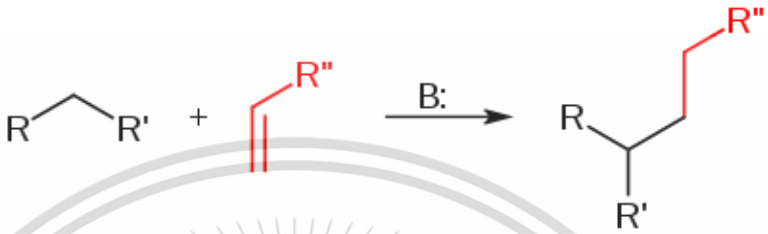

Figure 2.18 Michael addition reaction.

In this scheme, the R and R' groups on the nucleophile (the Michael donor) typically denote electron-withdrawing entities like acyl and cyano groups. These groups render the adjacent methylene hydrogen acidic enough to generate a carbanion upon reaction with the base, B:. The R" substituent on the activated alkene, known as a Michael acceptor, is commonly a ketone, thereby classifying the compound as an enone. However, it can also be a nitro group or a sulfonyl methyl fluoride.

2.3 Thymol

2.3.1 Properties of Thymol

Thymol (2-isopropyl-5-methylphenol, IPMP) is a monoterpene phenol, also known as "hydroxy cymene". Thymol is extracted from Thymus vulgaris (common thyme). Thymol is a natural antibacterial agent that can inhibit the growth of microorganisms. The World Health Organization has pointed out that thymol in food has no harm to consumers. It can be safely used in the food industry to control post-harvest crop rot. The physical properties of thymol are white crystalline substances with low water solubility. It can only be slightly soluble in water at neutral pH, but it is extremely soluble in alcohols and organic solvents. In addition, it is also soluble in strongly alkaline aqueous solutions due to deprotonation of the phenol. Thymol has

a pleasant aromatic odor but low palatability; it has an unpleasant taste with a strong flavor [17, 18, 43].

(a) (b)

Figure 2.19 (a) Structure of Thymol, (b) Thymus vulgaris (common thyme) [44].

2.3.2 Antimicrobial properties of Thymol

Thymol is also known that it is the antimicrobial and antiseptic agent. It is often the active ingredient in disinfectant or antiseptic products such as mouthwash (Listerine). Thymol can inhibit a variety of microorganisms to prevent food rotten and control food quality during storage. The most common use of thymol is in food and oral applications. It has been reported that thymol was effective for the control both the gram-positive and gram-negative bacteria, e.g., *Staphylococcus aureus, Staphylococcus epidermidis, Streptococcus mutans, Escherichia coli, Pseudomonas aeruginosa, Shigella sonnei, Shigella flexneri.*

The antibacterial activity of thymol against gram-positive bacteria; *Streptococcus mutans* (MTCC 890), *Staphylococcus aureus* (MTCC 96) and gram-negative bacteria; *Escherichia coli* using the disk diffusion method and microbroth dilution methods. The results showed that the most weakened microorganism is *Staphylococcus aureus* with a zone of inhibition of 25 mm and a MIC value of 62.5 ppm, followed by Streptococcus *mutans* with a zone of inhibition of 17 mm and a MIC value of 125 ppm. Thymol displayed a lower activity against *Escherichia coli* with inhibition of 13 mm and MIC value of 250 ppm [45]. The mean of zone of inhibition and the MICs values showed that thymol is more active against gram-positive bacteria than gram-negative bacteria. Therefore, thymol is suitable for use in oral application

due to the most important etiological agents of dental plaque and dental caries being gram-positive bacteria, *e.g., Streptococcus mutans and Streptococcus sobrinus* [17, 46].

2.4 Chloroxylenol (para chloro meta xylenol, PCMX)

2.4.1 Properties of Chloroxylenol

Chloroxylenol, commonly known as para-chloro-meta-xylenol (PCMX), is an antiseptic and disinfectant that is used to disinfect skin and surgical instruments when combined with alcohol. The most prevalent products that contain chloroxylenol e.g., antibacterial soaps in health care facilities and restaurants, antiseptics and disinfectants, cosmetics, and topical (externally applied) pharmaceuticals. The physical properties of chloroxylenol are milky white crystalline substances with low water solubility. It can be soluble in alcohols and organic solvents; it may be used mixed with water or alcohol.

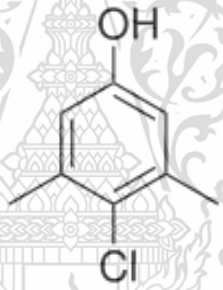

Figure 2.20 Structure of chloroxylenol.

2.4.2 Antimicrobial properties of Chloroxylenol

Chloroxylenol is most effective against gram-positive more than gram-negative bacteria. It works by disruption of the cell wall and stopping the function of enzymes. Chloroxylenol is the active ingredient in Dettol. It comprises 4.8% of Dettol's total admixture, with the rest made up by pine oil, isopropanol, castor oil, soap and water.

The antibacterial activity of chloroxylenol report by Johnson et al. (2002) , The MICs and MBCs of chloroxylenol against Escherichia coli (NCTC 10418) were found to be 200 and 400 mg/L, respectively. The MICs and MBCs of chloroxylenol against and Staphylococcus aureus (SA8) were found to be 75 and 400 mg/L, respectively.

2.5 Related Literature Reviews

Modified chitosan

Chalitangkoon et al [14] modified a novel polymeric dye by grafting phenolphthalein (PHP) onto side chains of CS by one-pot Mannich reaction. PHP was successfully grafted to the CS backbone, confirmed by UV-vis, FT-IR, and ^{1}H NMR techniques. PHP covalently grafted onto CS displayed a pink color under normal circumstances without dye leaking or color fading after a few weeks. Moreover, after heating, the derivatives dissolved in LiOH/urea systems could exhibit a darker pink color. According to the findings, novel CS derivatives with dual pH/thermal dependent coloring properties may be created as pH/thermal responsive biomaterial in a wide range of applications.

Savetsakulanont et al [15] fabricated polysaccharide-based hydrogels on water-soluble CS with dual imine crosslinks (CECS, CECS-g-PHP, and OSA) and host–guest interactions (CECS-g-PHP and β-CD-HDA). The Mannich reaction was used to synthesize the water-soluble guest polymer CECS-g-PHP, which complexed with hexamethylenediamine modified-cyclodextrin (β -CD-HDA), as the host molecule. FT-IR and ^{1}H NMR were used to confirm the chemical structure after modification. The hydrogels show significantly shorter gelation times and higher compressive stresses, compared with the single-crosslinked hydrogels. Thus, these dual-crosslinked hydrogels, which respond to pH and other stimuli, are promising designs for new multifunctional biomaterials.

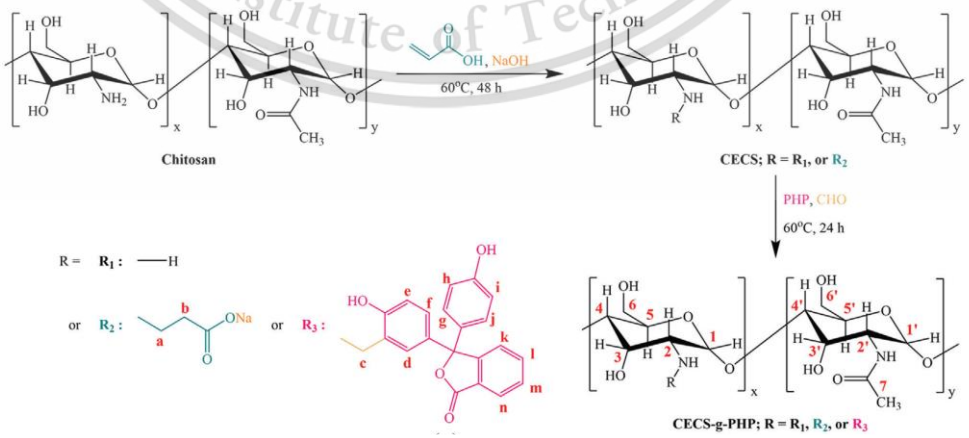

Figure 2.21 Synthesis of CECS-g-PHP [15].

Stabilized metallic nanoparticle with chitosan

Huang et al [47] prepared AuNPs by reducing $HAuCl_4$ with a CS, in the absence/presence of tripolyphosphate (TPP). CS acted as a reducing/stabilizing agent. The AuNPs obtained from the reaction exhibited differences in shape and size distribution when the molecular weight and concentration of chitosan were changed. The obtained AuNPs were characterized with UV-vis spectroscopy and transmission electron microscopy. More interestingly, the gelation of chitosan upon contacting with polyanion (TPP) can also affect the shape and size distribution of gold nanoparticles. By adding TPP to chitosan solution before the reduction of gold salt, gold nanoparticles have a bimodal size distribution, and at the same time, polygonal gold particles were obtained in addition to spherical gold nanoparticles as shown in Figure 2.22.

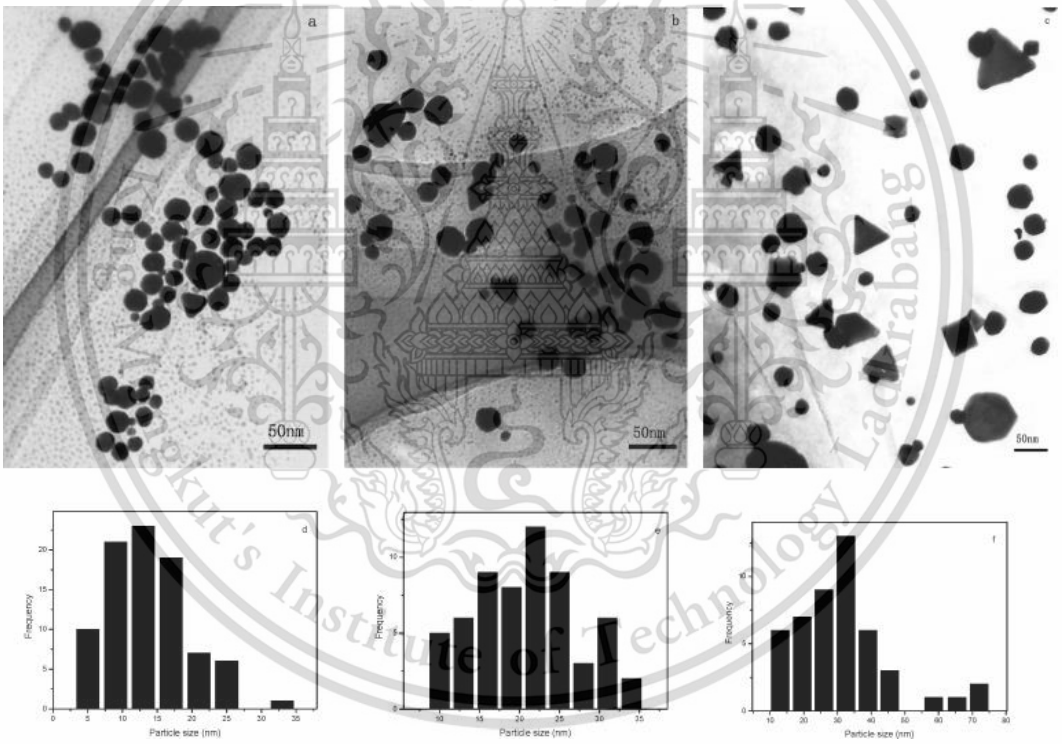

Figure 2.22 TEM images and the histograms of particle size distribution of gold nanoparticles prepared in the presence of various amount of 0.1% TPP: (a, d) 0 μL, (b, e) 500 μL, and (c, f) 1000 μL.

Huang et al [27] prepared various metal–chitosan nanocomposites including silver (Ag), gold (Au), platinum (Pt), and palladium (Pd) in aqueous solutions. Metal nanoparticles were formed by reduction of corresponding metal salts with $NaBH_4$ in

the presence of high molecular weight of CS (400,000 Da, %DD=100). CS adsorbing onto the surface of as-prepared metal nanoparticles formed the corresponding metal–chitosan nanocomposites. TEM images of gold and platinum nanoparticles distributed in Au– and Pt–chitosan nanocomposites was shown in Figure 2.23. Comparison of all the resulting particles size, it shows that silver nanoparticles are much larger than others (Au, Pt and Pd). In addition, the difference in particles size leads to develop different morphologies in the films cast from prepared metal–chitosan nanocomposites. Polarized optical microscopy (POM) images show a batonet-like structure for Ag–chitosan nanocomposites film, while for the films cast from other metal (Au, Pt, and Pd)–chitosan nanocomposites show branched-like structures with a few differences among them were observed, as shown in Figure 2.24.

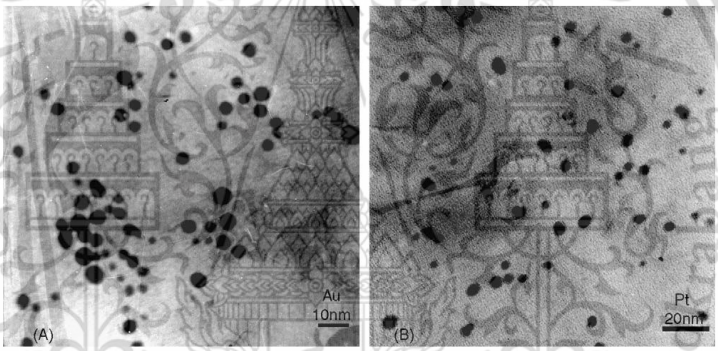

Figure 2.23 TEM images of gold (a) and platinum (b) nanoparticles distributed in Au– and Pt–chitosan nanocomposites.

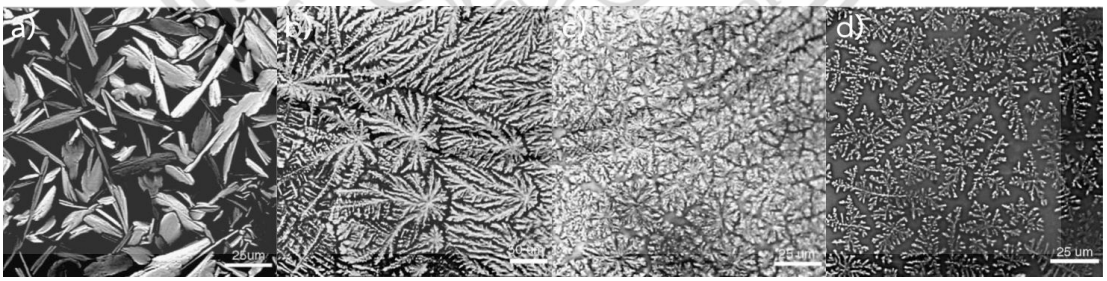

Figure 2.24 POM graphs of the films cast from Ag(a)- Pt(b)- Pd(c)– and Au(d)–chitosan nanocomposite prepared with 20mM $AgNO_3$, H_2PtCl_6, Na_2PdCl_4, and $HAuCl_4$, respectively.

Laghrib et al [48] prepared silver nanoparticles in the presence of CS *via* chemical reduction of $AgNO_3$ in the presented of sodium borohydride at room

temperature. The average size of AgNPs was found at 50 nm, confirmed by X-Ray diffraction analysis. CS stabilized AgNPs on the carbon paste electrode (CS-SNPs/CPE) were used as an electrochemically active material for the determination of *p*-nitroaniline (*p*-NA) in neutral medium by differential pulse voltammetry. The electrochemical analysis revealed that the CS-SNPs/CPE exhibits strong electroanalytic activity that can be used in sensor development and related applications.

Layer by layer deposition method

Layer-by-layer (LbL) deposition is a method for creating thin films by sequentially adsorbing oppositely charged species onto a substrate. This process involves alternating immersion of the substrate in solutions containing positively and negatively charged materials, leading to the formation of a multilayered structure through electrostatic interactions. Each layer adheres to the previous one due to the attraction between opposite charges. Various polyelectrolytes can be used depending on the specific requirements of the application. Some commonly used polyelectrolytes include polycationic species such as Poly(allylamine hydrochloride) (PAH) and Poly(diallyldimethylammonium chloride) (PDADMAC), as well as polyanionic like Poly(sodium 4-styrenesulfonate) (PSS) and Poly(acrylic acid) (PAA). In the case of nanoparticle layer film assembly, the negatively charged NP solution and positively charged PDADMAC were utilized to form a film through electrostatic interactions. Parameters involved in this method, such as solution concentration, pH, and immersion time, were studied to enhance the nanofilm's adhesion ability.

Detsri et al [49] prepared the composite thin films of silver nanoparticles and polyaniline by the Layer-by-Layer (LbL) deposition technique. Anionic polyelectrolyte was prepared by chemical reduction of silver ion using water soluble polyaniline as the stabilizing agent to form anionic AgNPs/polyaniline composite solution. From TEM images, the particle size was found to be less than 20 nm, as shown in figure 2.25 (a). The negatively AgNPs anionic /polyaniline composite solution and positively charged cationic poly(diallyldimethylammonium chloride), (PDADMAC) were utilized to created multilayer thin films using the self-assembled production through electrostatic interactions. The films were shown a striking color due to the nanoparticles adsorption (Fig. 2.25 (b)). The lowest polyaniline-CoPSS capping concentration (0.005 %w/v) was

produced a film that appeared shiny due to the close packing of AgNPs which made the NPs contact one another. This is probably the result of low electrostatic charge and low electrostatic repulsion between particles. This lower electrostatic repulsion between particles has provided higher packing of the particles. On the other hand, when the polyaniline-CoPSS capping concentration is increased (0.1 %w/v and 0.8 %w/v) the films appear orange-red color which matches the optical properties of individual silver nanoparticles in solution. The nanoparticles posses a vivid orange color as a result of the surface plasmon resonance, (SPR) of the conduction electron, their assembly also led to the formation of an orange-colored film. Finally, these films are design to use as optical sensor for the ammonia detection. The silver nanoparticles/polyaniline-CoPSS composite thin films was found to display the strong color changes from orange-red to yellow upon adjunction of ammonia concentration, as shown in Figure 2.26.

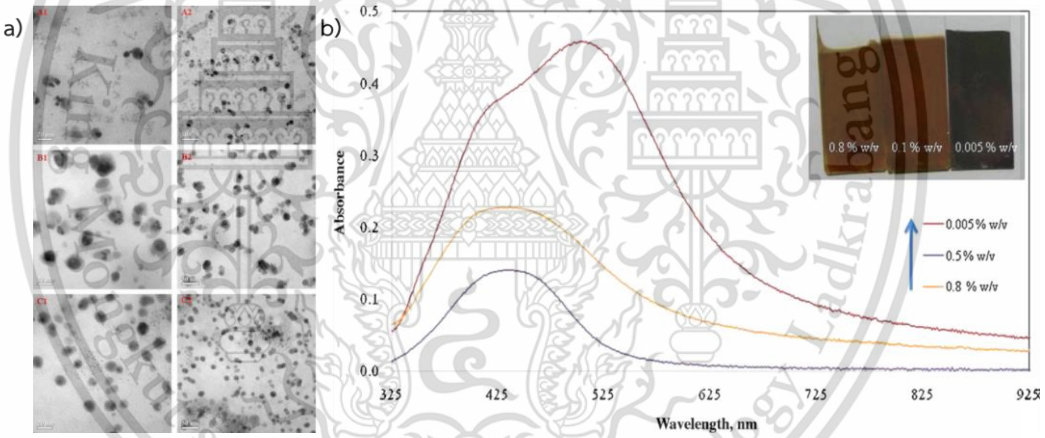

Figure 2.25 (a) TEM images of silver nanoparticles at various concentration of polyaniline-CoPSS stabilizing agent A-0.005, B-0.1, C-0.8 %w/v, (b) the absorbance value of silver nanoparticles as the different polyaniline-CoPSS stabilizing concentration.

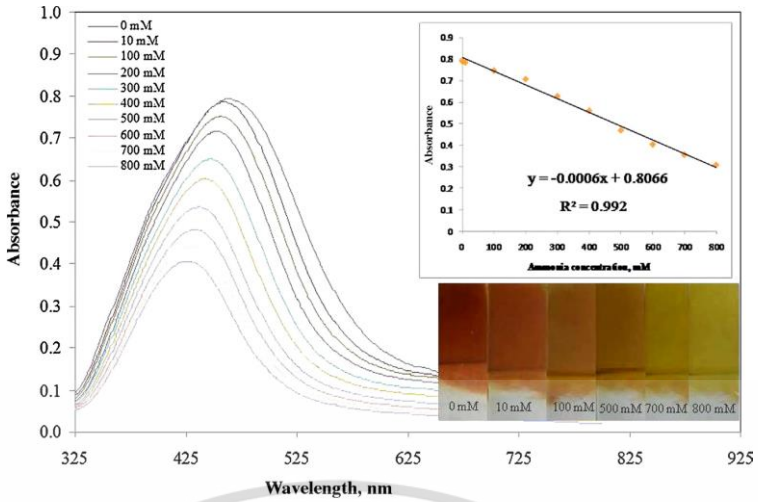

Figure 2.26 UV–visible spectrum of silver nanoparticles/polyaniline-CoPSS/PDADMAC multilayer films exposed to various concentration of ammonia (0, 10, 100, 200, 300, 400,500, 600, 700 and 800 mM).

Antimicrobial textile and suture material

Yunping et al [50] prepared antibacterial cotton fabrics with silver nanoparticles. The average particle size of silver nanoparticles is 2.3 nm with the minimal inhibitory concentration of 7.8 mg/ml. In the synthesis process, sodium citrate acted as a stabilizer to prevent Ag NP agglomeration, while citric acid (CA) served as a binder to fix Ag NPs on the cotton fibers through chemical bonding, as shown in Figure 2.27. The agar diffusion plate and shaking flask methods were used to evaluate the antibacterial capabilities of hybrid textiles. It is discovered that the cotton fabrics coated with Ag NP have outstanding antibacterial properties against both the Gram-positive *Staphylococcus aureus* and the Gram-negative *Escherichia coli*. The percentages of bacterial reduction remained at 91.8% and 98.7% for *S. aureus* and *E. coli*, respectively. The antibiotic performance of the fabrics was also durable after 50 cycles of laundering.

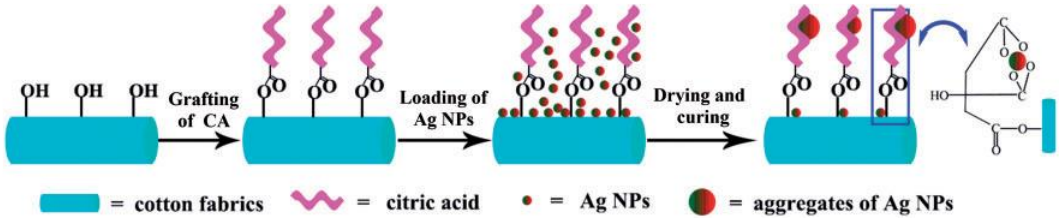

Figure 2.27 Schematic for fabrication of Ag- CA cotton fabrics and the supposed linkage mode between AgNPs and fabrics through CA.

T. Dubas et al [51] prepared antimicrobial textile from nylon and silk by the layer-by-layer deposition method. A colored thin film with antibacterial properties was prepared by sequentially dipping nylon or silk fibers in diluted solutions of poly (diallyl dimethylammonium chloride) (PDADMAC) and silver nanoparticles with poly (methacrylic acid) (PMA). Scanning electron microscopy studies confirmed morphology of silver nanoparticle that coating on the fibers by the layer-by-layer method. 20 PDADMAC/PMAcapAg layers were applied to the fibers. The percentages of bacterial reduction remain at 80% for silk fiber and 50% for nylon fiber. The fibers coated with nanoparticles have antibacterial activity, which makes them valuable for other applications, including water sanitation and antimicrobial fabrics.

Augustine et al [52] synthesis AgNPs stabilized with tri-sodium citrate, with an average particle size of 20 nm. The AgNPs exhibited excellent antimicrobial properties, with MIC values of 10.0 µg/mL against E. coli (ATCC 12228) and 12.5 µg/mL against S. aureus (ATCC6538-P). Furthermore, the nanoparticles were immobilized on surgical gut sutures using alginate as a crosslinking agent. The controlled release of the nanoparticles checked in vitro in Simulated Body Fluid. The successful release of silver nanoparticles under physiological PH depicts the applicability of this novel suture in surgery for the prevention of surgical wound infection and to enhance wound healing.

Chapter 3
Research Methodology

In this research, the operation method is divided into 2 sections:

1) New chitosan-grafted thymol coated on gold nanoparticles for control of cariogenic bacteria in the oral cavity.

2) Antimicrobial nanolayer films of carboxyethyl chitosan–grafted–chloroxylenol modified silver nanoparticles for enhanced surgical suture performance.

Each section consists of 3 experimental steps: Step 1: Synthesis of modified chitosan (Chitosan-grafted thymol and carboxyethyl chitosan–grafted–chloroxylenol) through a mannich reaction and Michael reaction. Step 2: Synthesis of metallic nanoparticle using chemical reduction method. Modified chitosan and sodium borohydride ($NaBH_4$) were used as the stabilizing and reducing agent, respectively. Step 3: Antimicrobial activity of chitosan-grafted thymol and carboxyethyl chitosan–grafted–chloroxylenol coated metallic nanoparticles were investigated against *E. coli* (ATCC25922), *S. aureus* (ATCC25923), and *A. baumanii* (ATCC19606).

3.1 Equipment

1. Glass wares
2. Hot plate and thermostat
3. Magnetic stirrer
4. pH meter
5. Micro pipette
6. Filter paper
7. Buchner funnel and suction flask
8. Vacuum pump filter system
9. Analytical Four digit weighing balance

3.2 Instrument

Instrument	Model	Brand
UV-vis spectrophotometer	UV-1800	Shimadzu
Attenuated total reflectance – FTIR	IRTracer-100	Shimadzu
Nuclear magnetic resonance spectroscopy; NMR	JNM-ECZS	JEOL

Instrument	Model	Brand
Elemental analysis	Thermo FLASH 2000	Thermo Scientific
Zeta potential analysis	SZ-100	Horiba
Transmission Electron Microscope (TEM)	JEM-2010	JEOL
X-ray diffractometer (XRD)	Smartlab SE	RIGAKU
pH Meter	FEP20	Mettler Toledo

3.3 Chemicals

Chemicals	Chemical Formula	Company
High molecular weight chitosan, %DD = 85, Mw = 320,000 Da	$(C_6H_{11}NO_4)_n$	Eland Co., Ltd.
Low molecular weight chitosan, %DD = 85, Mw = 50,000 Da	$(C_6H_{11}NO_4)_n$	Sigma-Aldrich
Thymol	$C_{10}H_{14}O$	Sigma-Aldrich
Chloroxylenol	C_8H_9ClO	Sigma-Aldrich
Acrylic acid	$C_3H_4O_2$	Acros Organics
Gold (III) chloride trihydrate	$HAuCl_43H_2O$	Sigma-Aldrich
Silver nitrate	$AgNO_3$	Sigma-Aldrich
Sodium borohydride	$NaBH_4$	Sigma-Aldrich
Formaldehyde 37% w/w	CH_2O	Carlo Erba
Dimethylformamide	$HCON(CH_3)_2$	Carlo Erba
Ethanol	C_2H_5OH	Carlo Erba
Hydrochloric acid	$C_{10}H_{14}O$	Carlo Erba
Sodium hydroxide	NaOH	Carlo Erba
Deionized water	H_2O	Milli-Q ultrapure water

3.4 New chitosan-grafted thymol coated on gold nanoparticles for control of cariogenic bacteria in the oral cavity.

3.4.1 Synthesis and characterization of CST (Chitosan-grafted-Thymol).

HCS (1g) was dissolved in 100 mL 1% w/v acetic acid solution. Thymol with various concentrations in 50 ml DMF was slowly dropped to the CS solution with

vigorously stirring. The assigned amount of formaldehyde was then slowly dropped into the CS-thymol solution according to mole ratio in Table 3.1. The mixture was stirred at 60 °C for 24 h. After that, 0.5M NaOH solution was added into the mixture to precipitation. The mixture was then filtered and the precipitate was washed with ethanol and distilled water, and dried at 60 °C to obtain CST product.

The structural characterizations of CST (Chitosan-grafted-Thymol) were determined by three characterization methods. The UV-vis spectra were obtained by scanning the wavelength from 200 to 800 nm by a BlueStar B spectrophotometer (Lab Tech, China). The ^{1}H-NMR spectra were determined by a JNM-ECZ-500R/S1 spectrometer (JEOL, Japan) at 500 MHz. D_2O/CF_3COOH was used to dissolve CST. The percentages of carbon, hydrogen, nitrogen of CS and its derivatives were determined using a FLASH 2000 elemental analyzer (Thermo Fisher Scientific, USA). The degree of substitution (%DS) determination of CST was calculated using data from ^{1}H NMR and EA.

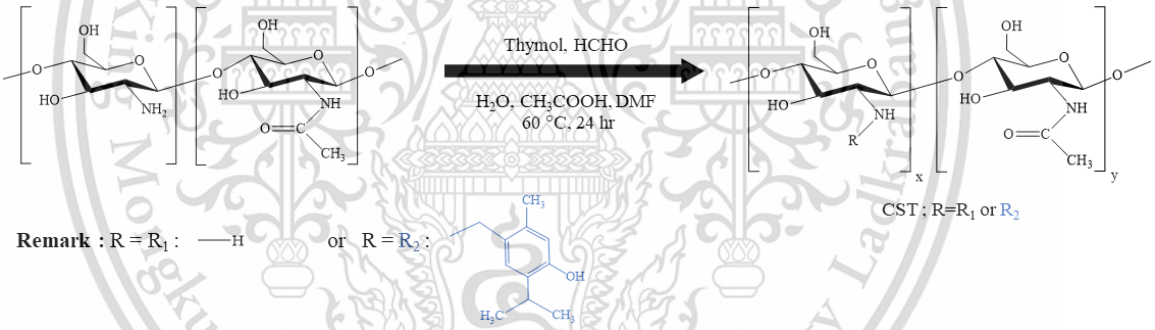

Figure 3.1 Schematic Illustration of the synthesis of CST.

Table 3.1 Mole ratio of Chitosan : Formaldehyde : Thymol

Mole ratio of HCS : Formaldehyde : Thymol	Chitosan (g)	Formaldehyde (g)	Thymol (g)
1.0 : 0.5 : 0.5	1	0.2147	0.3966
1.0 : 0.5 : 1.0	1	0.2147	0.7932
1.0 : 0.5 : 2.0	1	0.2147	1.5864
1.0 : 1.0 : 1.0	1	0.4293	0.7932
1.0 : 1.0 : 2.0	1	0.4293	1.5864

3.4.2 Synthesis of Gold Nanoparticles (AuNPs)

Deionized water (DI), 50 mmolar tetrachloroaurate trihydrate and 1% CST were pipetted at the assigned volume as shown in Table 3.2. The mixture was stirred for 3 minutes, before 2 ml sodium borohydride was rapidly added without stopping stirring causing color of the solution change from yellow-orange to red-wine. The mixture was further stirred for 10 min, and subsequently stored at room temperature for 24 h. Various ratios of the substances according to Table 3.2 were also repeated following the above procedure. The obtained solutions are called gold nanoparticle solutions (CST-AuNPs).

Table 3.2 Mole ratio of Gold (III) chloride trihydrate : CST : Sodium borohydride.

Gold (III) chloride trihydrate : CST : Sodium borohydride (mM)	10 mM $HAuCl_4 \cdot 3H_2O$ (ml)	0.1% w/v CST (ml)	$NaBH_4$ (ml)	DI Water (ml)
1.0 : 0.005 : 10	1	0.5	2	6.5
1.0 : 0.006 : 10	1	0.6	2	6.4
1.0 : 0.008 : 10	1	0.8	2	6.2
1.0 : 0.010 : 10	1	1.0	2	6.0
1.0 : 0.020 : 10	1	2.0	2	5.0
1.0 : 0.030 : 10	1	3.0	2	4.0
1.0 : 0.040 : 10	1	4.0	2	3.0
1.0 : 0.050 : 10	1	5.0	2	2.0

The absorption characteristics of gold nanoparticle solution were studied by ultraviolet-visible spectroscopy. The stability of CST-AuNPs was studied by Zeta potential. The size and particle morphology were studied by TEM. The crystallinity structure of the NPs was studied by XRD.

3.4.3 The stability of CST-AuNPs

1) Effect of pH: The solution of gold nanoparticles from section 3.4.2 at the appropriate condition (decided by colloidal stability and particle size) was placed into 5 beakers. The pH (measured by pH meter) of the solution in each beaker was then adjusted to 3, 5, 7, 9 and 11 by adding appropriate amount of 1M hydrochloric

acid or 1M sodium hydroxide solutions. The solutions were kept at room temperature for 24 h before analyzed by a UV-visible spectrophotometer and a zeta sizer.

2) Effect of ionic strength: The colloidal of gold nanoparticles from section 3.4.2 was chosen. Three types of salts as interference, including the mono–valent (NaCl), di–valent (Na_2SO_4) and tri–valent (Na_3PO_4) at 100, 50, 20, 10 and 1 mM were put into the gold nanoparticles colloidal. The observation of sedimentation was followed up for 7 days and the amount of sedimentation was relatively compared using UV-vis spectroscopy.

3) Effect of time: The colloidal of gold nanoparticles was followed up to observe sedimentation for 180 days and the amount of sedimentation was compared using UV-vis spectroscopy.

3.4.4 Antimicrobial assay: The antimicrobial activity of CS, CST and CST–AuNPs against *S. mutans* ATCC 25175 and *S. sobrinus* ATCC 33402 was evaluated by agar well diffusion method and macro–dilution method.

1) Agar well diffusion assay: The 10^4 CFU/mL inoculum was swapped onto Mueller–Hinton agar plates; afterward, well with the size of 5 mm was cut in the agar plate. Each well was aseptically filled up with 20 μL of CS, CST or CST–AuNPs as assigned. The plates were incubated at 37 °C for 24 h. 4% tween 80 was introduced as controls. The diameter of the inhibition zone around each well was measured and expressed in the mean diameter of the inhibition zone in millimeters (n = 3).

2) Minimum inhibitory concentration (MIC) and minimum bactericidal concentration (MBC) assay: MIC and MBC values were determined by broth macro–dilution assay. Colonies of the same morphological type were selected and transferred to 0.85% w/v sterile saline. To achieve the turbidity of a 0.5 McFarland standard inoculum was diluted with Brain Heart Infusion broth (BHI) 1:200 (approximately 5 x 10^5 CFU/mL). Each stock CS, CST or CST–AuNPs was dissolved with 4% w/v tween 80 with the final concentration ranging from 0.40–200 mg/L. Then, 50 μL adjusted *S. mutans* or *S. sobrinus* was added into each tube. After that the samples were incubated overnight at 37 ^{O}C for 24 h. MICs and MBCs were evaluated by no visible

growth of bacteria and lowest concentration of an antimicrobial agent that kills 99.9% of the initial bacterial population method, respectively.

3.5 Antimicrobial nanolayer films of carboxyethyl chitosan–grafted–chloroxylenol modified silver nanoparticles for enhanced surgical suture performance.

3.5.1 Synthesis and characterization of HCSX (High Mw Chitosan-g-Chloroxylenol) and LCSX (Low Mw Chitosan-g-Chloroxylenol)

A solution of high Mw CS or Low Mw CS (1g) was prepared by dissolving it in 100 mL 1% w/v acetic acid solution. Chloroxylenol, dissolved in 50 ml DMF, was then slowly dropped to the vigorously stirred CS solution. The assigned amount of formaldehyde was subsequently added dropwise into the CS-Chloroxylenol solution according to the mole ratio in Table 3.3. The resulting mixture was stirred at 60 °C for 24 h. After that, 0.5M NaOH solution was added into the mixture during time the precipitation was occurred. The precipitate was then filtered and washed with ethanol and distilled water. The precipitate was later dried at 60°C to obtain the CSX product.

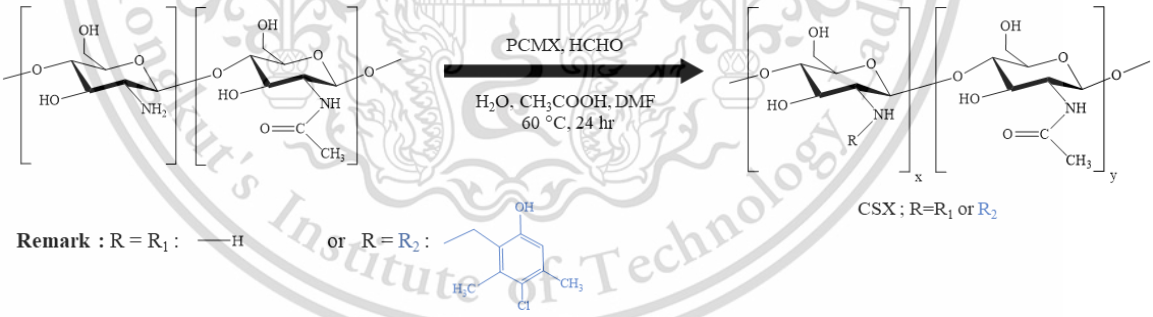

Figure 3.2 Schematic Illustration of the synthesis of CSX.

Table 3.3 Mole ratio of Chitosan : Formaldehyde : Chloroxylenol

Mole ratio of CS : Formaldehyde: Chloroxylenol	HCS (g)	LCS (g)	Formaldehyde (g)	Chloroxylenol (g)
1.0 : 0.5 : 1.0	1		0.2147	0.8269
1.0 : 0.5 : 2.0	1		0.2147	1.6538
1.0 : 1.0 : 1.0	1		0.4293	0.8269
1.0 : 1.0 : 2.0	1		0.4293	1.6538
1.0 : 1.0 : 4.0	1		0.4293	3.3076
1.0 : 1.0 : 1.0		1	0.4293	0.8269
1.0 : 1.0 : 2.0		1	0.4293	1.6538
1.0 : 1.0 : 4.0		1	0.4293	3.3076

The structural characterizations of CSX were determined by nuclear magnetic resonance (^{1}H-NMR), elemental analysis (EA) and UV-vis spectroscopy techniques. The UV-vis spectra were scanned from 200 to 800 nm by a BlueStar B spectrophotometer (Lab Tech, China). The ^{1}H-NMR spectra were determined by a JNM-ECZ-500R/S1 spectrometer (JEOL, Japan) at 500 MHz. D_2O/CF_3COOH was used to dissolve CSX. The degree of substitution (%DS) determination of CSX was calculated using data from ^{1}H NMR and EA.

3.5.2 Synthesis of HCECSX (High Mw Carboxyethylchitosan-grafted-Chloroxylenol) and LCECSX (Low Mw Carboxyethylchitosan-grafted-Chloroxylenol)

To improve the water-soluble properties of modified-CS, acrylic acid was introduced onto amino group of the modified-CS backbone. Firstly, the selected CSX (1 g) was dispersed in 100 mL distilled water. Acrylic acid was then added according to the mole ratio in Table 3.4. After adding acrylic acid, the temperature was raised to 60 ℃ for 48 h. The reaction was stopped by adding 10% w/v NaOH to adjust the pH to a range of 10–12. The resulting solution was then dialyzed against distilled water for a period of 3 days to purify it. The purified yield was then subjected to lyophilization.

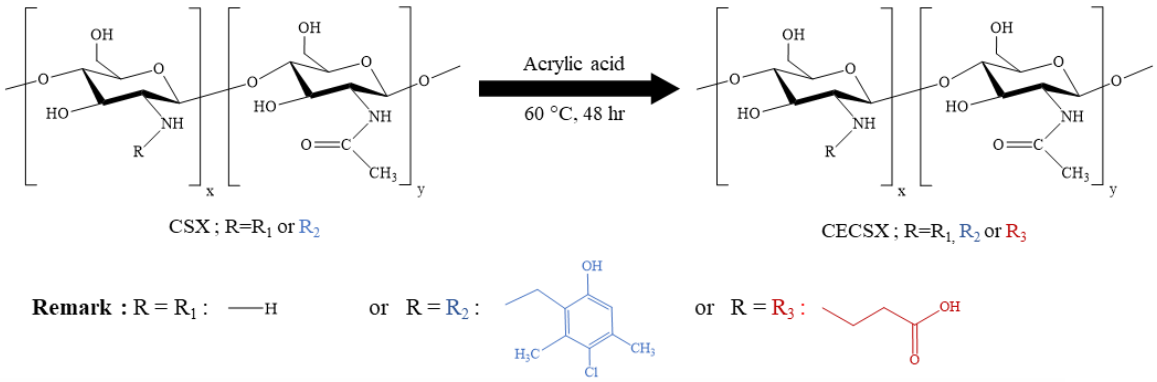

Figure 3.3 Schematic Illustration of the synthesis of CECSX.

Table 3.4 Mole ratio of CSX : Acrylic acid

Mole ratio of (H or L) CSX : Acrylic acid	HCSX (g)	LCSX (g)	Acrylic acid (g)
1.0 : 1.0	1	-	0.70
1.0 : 2.0	1	-	1.40
1.0 : 3.0	1	-	2.10
1.0 : 1.0	-	1	0.69
1.0 : 2.0	-	1	1.38
1.0 : 3.0	-	1	2.07

The structural characterizations of CECSX were determined by nuclear magnetic resonance (^{1}H NMR) and elemental analysis (EA). The degree of substitution (%DS) determination of CECSX was calculated using data from ^{1}H NMR and EA.

3.5.3 Synthesis of Silver Nanoparticles (AgNPs)

Deionized water (DI), 10 mM silver nitrate and 0.1% CECSX were pipetted at the assigned volume as shown in Table 3.5. The mixture was stirred for 3 minutes and subsequently 20 ml sodium borohydride was rapidly added without stopping stirring leading to the change of the solution color from clear to dark yellow. The mixture was further stirred for 10 min and subsequently stored at room temperature for 24 h. Various ratios of the substances according to Table 3.5 were also repeated following the above procedure. The obtained solutions are called silver nanoparticle solutions (CECSX-AgNPs).

Table 3.5 Mole ratio of Silver nitrate : CECSX : Sodium borohydride (100 ml)

Silver nitrate : CECSX : Sodium borohydride (mM)	10 mM $AgNO_3$ (ml)	0.1% w/v HCECSX (ml)	0.1% w/v LCECSX (ml)	$NaBH_4$ (ml)	DI Water (ml)
1.0 : 0.001 : 10	10	1	-	20	69
1.0 : 0.002 : 10	10	2	-	20	68
1.0 : 0.003 : 10	10	3	-	20	67
1.0 : 0.005 : 10	10	5	-	20	65
1.0 : 0.010 : 10	10	10	-	20	60
1.0 : 0.020 : 10	10	20	-	20	50
1.0 : 0.030 : 10	10	30	-	20	40
1.0 : 0.001 : 10	10	-	1	20	69
1.0 : 0.002 : 10	10	-	2	20	68
1.0 : 0.003 : 10	10	-	3	20	67
1.0 : 0.005 : 10	10	-	5	20	65
1.0 : 0.010 : 10	10	-	10	20	60
1.0 : 0.020 : 10	10	-	20	20	50
1.0 : 0.030 : 10	10	-	30	20	40

The absorption characteristics of silver nanoparticle solution were studied by ultraviolet-visible spectroscopy. The stability of HCECSX-AgNPs and LCECSX-AgNPs was studied by Zeta potential. The size and particle morphology were studied by TEM. The crystallinity structure of the NPs was studied by XRD.

3.5.4 Fabrication of Nanoparticle film on substrate

The various substates including woven and nonwoven textiles were used as substrate for nanoparticles coating. The glass slide was used to represent the surface used in the Layer-by-Layer deposition technique. PDAD/PSS were used to modified glass slide's surface (hydrophobic surface) before being immersed in the NPs solution.

1) Preparation of PDDA/PSS Films: The glass substrate was washed with dishwashing liquid and then ultra-sonicated, first in EtOH followed by DI water. The cleaned substrate was then blown to dry with hot air.

Poly(diallydimethylammonium chloride) (PDADMAC)/ Poly (sodium 4-styrenesulfonate) (PSS) multilayers were assembled on cleaned glass slide. PDADMAC/PSS films were assembled by repeatedly sequential dipping of the substrate in PDADMAC(10mM)/NaCl(1M) and PSS(10mM)/NaCl(1M) aqueous solutions for 5 min each with water rinsing in between each deposition step until five layers were obtained to gain positively charged film on the slide glass (Primer).

2) Preparation of AgNPs films on glass substrate: Glass slide with five layers of PDADMAC/PSS film were immersed in various concentration of HCECSX-AgNPs and LCECSX-AgNPs solutions for 24 hr. After that, the adhesion ability of the AgNPs film was evaluated by intensity of UV-vis spectroscopy.

- ***Study on the effect of salt in AgNPs solution on film adhesion:*** Glass slides with five layers of PDADMAC/PSS film were immersed in HCECSX-AgNPs and LCECSX-AgNPs solutions with various concentrations of NaCl, i.e. 5, 10, 25, 50 mM. After 24 hr, the adhesion ability of the AgNPs film was evaluated by intensity of UV-vis spectroscopy.
- ***Study on the effect of pH on film adhesion:*** Glass slides with five layers of PDADMAC/PSS film were immersed in HCECSX-AgNPs and LCECSX-AgNPs solutions after adjust pH to 5, 7 and 9. The adhesion ability of the AgNPs film was evaluated by intensity of UV-Vis spectroscopy.
- ***Study on the effect of time on film adhesion:*** Glass slides with five layers of PDADMAC/PSS film were immersed in HCECSX-AgNPs and LCECSX-AgNPs solutions with an appropriate concentration of NaCl. The adhesion ability of the AgNPs film was evaluated by intensity of UV-vis spectroscopy at 1, 3, 5, 10,15, 20, 30, 40, 50, 60, 90 and 120 minutes.
- ***Study on the number of layer:*** Glass slides with five layers of PDADMAC/PSS film were alternatively immersed in HCECSX-AgNPs or LCECSX-AgNPs solutions with optimized time in the previous section and 5 min of PDADMAC solution to obtain the number of

layers 1, 3, 5, 7, 9 and 11. The film's adhesion was measured by the intensity of UV-vis spectroscopy.

3) Preparation of AgNPs on substrate

The optical conditions determined from the previous experiments were employed to coat various surgical suture materials including cotton, polyamide, and polypropylene following the abovementioned procedure.

3.5.5 Antimicrobial assay

Agar well diffusion assay: The 10^4 CFU/mL inoculum was swapped onto Mueller–Hinton agar plates; afterward, well with the size of 5 mm was cut in the agar plate. Each well was aseptically filled up with 20 μL of CS, HCECSX, LCECSX HCECSX–AgNPs or LCECSX–AgNPs as assigned. The plates were incubated at 37 °C for 24 h. 4% tween 80 was introduced as controls. The diameter of the inhibition zone around each well was measured and expressed in the mean diameter of the inhibition zone in millimeters (n = 3).

Minimum inhibitory concentration (MIC) and minimum bactericidal concentration (MBC) assay: MIC and MBC values were determined by broth macro–dilution assay. Colonies of the same morphological type were selected and transferred to 0.85% w/v sterile saline. To achieve the turbidity of a 0.5 McFarland standard inoculum was diluted with Brain Heart Infusion broth (BHI) 1:200 (approximately 5 x 10^5 CFU/mL). Each stock CS, HCECSX, LCECSX HCECSX–AgNPs or LCECSX–AgNPs was dissolved with DI water with the final concentration ranging from 0.40–200 mg/L. Then, 50 μL adjusted *E. coli* and *S. aureus* were added into each tube. After that the samples were incubated overnight at 37 $^{\circ}$C for 24 h. MICs and MBCs were evaluated by no visible growth of bacteria and lowest concentration of an antimicrobial agent that kills 99.9% of the initial bacterial population method, respectively.

Antimicrobial Test for Metallized Sutures (*In vitro* time-kill study): A time-kill study is an essential microbiological method for evaluating an antimicrobial activity of test material. Neat cotton, polyamide, and polypropylene fibers and all treated cotton, polyamide, and polypropylene fibers were prepared to test against

microorganisms cultured in MHB at 37 °C for 18 h. After that, the concentration of each bacterial solution was adjusted to 0.5 McFarland standard solution, which equals 1.5×10^8 CFU/ml. This resulted in 5×10^5 CFU/ml in MHB. Each sample contained 3 mL of an inoculum that had been diluted to 5×10^5 CFU/mL and was continuously turbulent at 37 °C for 0, 1, 3, 6, and 24 hours. At each time point, 20 µL of each inoculum was taken out and refilled with regular saline solution. Finally, 10 µL of each serial dilution was taken out and dropped onto MHB agar that had been sterilized in a Petri dish. After incubating overnight at 37 °C, the number of bacterial colonies was totalled and compared to the control culture by measuring the CFU/ml values. The percentage of bacterial reduction was obtained by the following equation.

$$\text{Bacterial reduction (\%)} = \frac{N_{control} - N_{specimen}}{N_{control}} \times 100$$

Where:

$N_{control}$ is the number of colonies in the control (CFU/ml)

$N_{specimen}$ is the number of colonies in the specimens (CFU/ml)

Chapter 4

New chitosan-grafted thymol coated on gold nanoparticles for control of cariogenic bacteria in the oral cavity

4.1 Results and discussion

4.1.1 Synthesis and characterization of CST (Chitosan-g-Thymol)

The Mannich reaction was employed in the experiment to attach thymol onto the side chain of chitosan. This process involves the amino group of chitosan reacting with formaldehyde to form an electrophilic imine compound ($-N=CH_2$), which can subsequently react by inserting a phenol group at the para position to produce secondary amines or benzylamine. As a result, thymol could be grafted onto chitosan *via* a carbene bridge.

The synthesis mechanism of CST can be seen in Figure 4.1. The protonation of formaldehyde at oxygen double bonds (=O) resulting in Methylideneoxidanium (positively charged of O), then Methylideneoxidanium will reacts with the amine group ($-NH_2$) of chitosan to form $-NH_2^+$ and then $-NH_2^+$ is deprotonated back to amine, while the hydroxyl group (-OH) of CH_2 connected to $-NH_2^+$ is protonated to form Oxoniumyl ion ($-H_2O^+$) and then dehydration of H_2O to form Iminium ion. After that, while thymol react with Iminium ion, the positive charge on the Iminium ion will disappear. The double bond of the Iminium ion then breaks to form a single bond between $-CH_2-$ connected to -NH- of chitosan and carbon of thymol. The alcohol group (-OH) of thymol becomes positively charged (unstable). The positively charge turn back into the aromatic ring, where there is a resonance within the aromatic ring.

The structural characterizations of CST were determined by three characterization methods including UV-vis spectroscopy, ^{1}H Nuclear Magnetic Resonance and Elemental analyzer. The degree of substitution (%DS) determination of CST was calculated using data from ^{1}H NMR and EA.

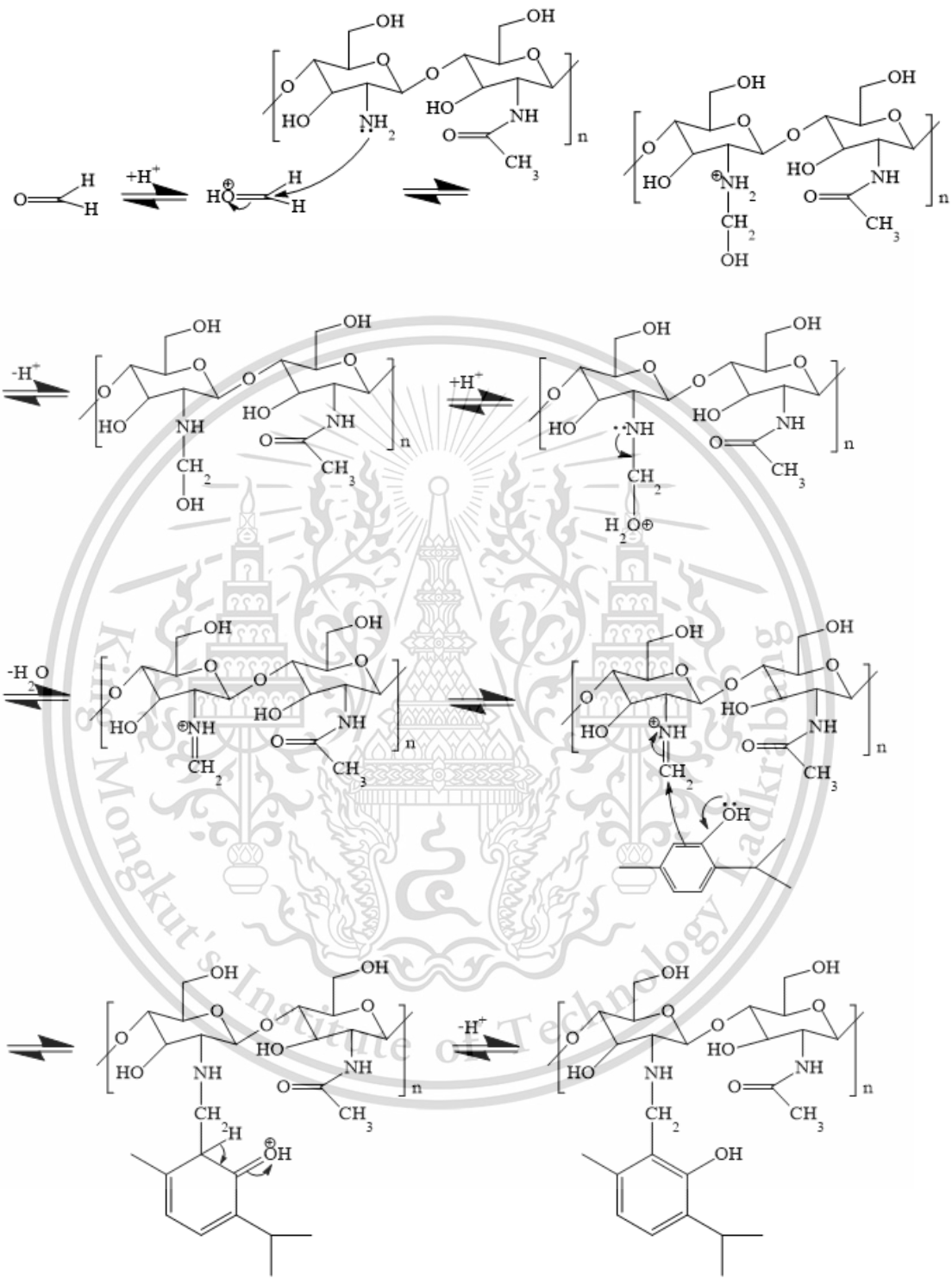

Figure 4.1 The synthesis mechanism of CST.

4.1.1.1 UV-vis spectroscopy

Figure 4.2 illustrates the absorption spectra of chitosan, CST, thymol, and the combination of chitosan with thymol. Thymol exhibited distinct broad peaks at 276 and 282 nm, whereas the chitosan spectra showed an absence of observable peaks within the 250 to 350 nm range. In contrast, the CST spectra displayed broad peaks at 281 nm, indicating a bathochromic shift compared to thymol. This shift provides supporting evidence for the covalent bonding of thymol to the chitosan structure. Consequently, the findings suggest that thymol was effectively grafted onto the chitosan backbone.

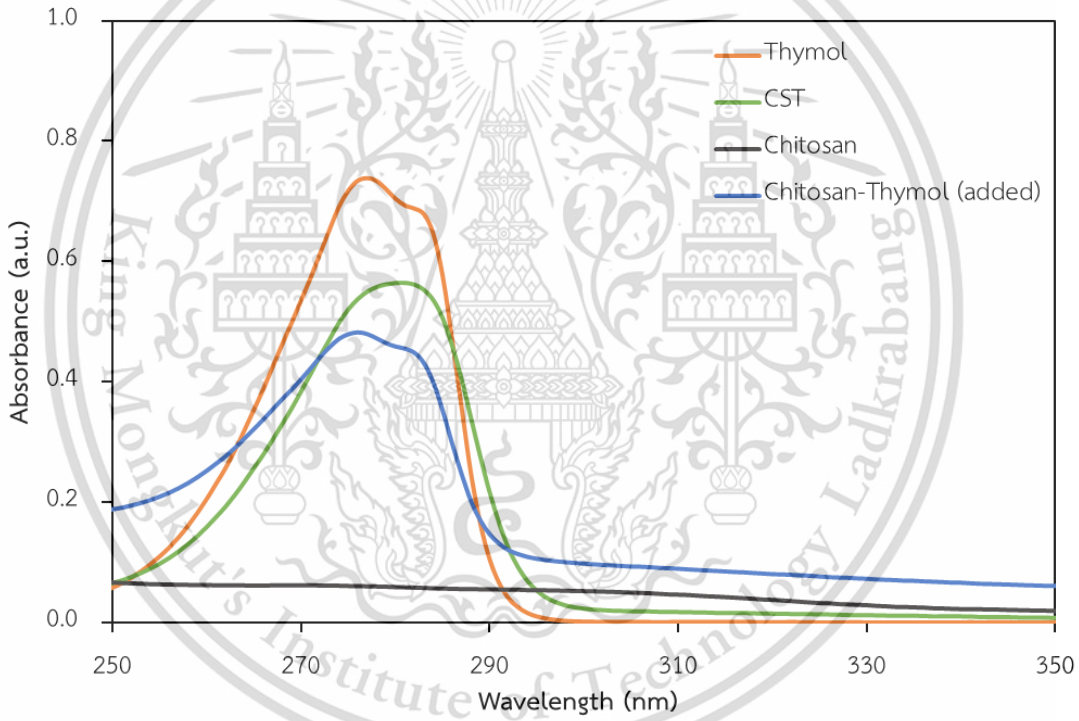

Figure 4.2 UV-vis spectra of chitosan, thymol, CST and chitosan combined with thymol.

4.1.1.2 Proton nuclear magnetic resonance (^{1}H NMR)

To graft thymol onto the chitosan side chain, the Mannich reaction was employed. In this reaction, an amino group of chitosan reacts with formaldehyde to form an electrophilic imine compound (-N=CH_2). Subsequently, this compound reacts with the phenol group introduced at the para position, resulting in the formation of secondary amines or benzylamine. This process effectively grafts thymol onto chitosan *via* a carbene bridge. The CST was structurally characterized using ^{1}H NMR, as

illustrated in Figure 4.3. In the chitosan spectra, characteristic peaks were observed at 1.86 and 2.97 ppm, corresponding to H_7 and H_2, respectively. Peaks in the range of 3.25 to 4.02 ppm were assigned to H_3-H_6 and H_2'-H_6'. In the CST spectra, characteristic chitosan peaks were retained, and new peaks at 1.00 and 2.15 ppm were observed, corresponding to the proton signals of the methyl group of thymol (H_f and H_b), respectively. Furthermore, doublet peaks around 6.74 and 7.10 ppm, attributed to the aromatic protons of thymol (H_c and H_d), were also evident. H_c with a coupling constant (J) of 6.2 Hz and H_d with a coupling constant (J) of 6.7 Hz indicate long-range couplings in the aromatic ring of thymol, suggesting that H_c and H_d are in ortho positions.

These observations provide strong evidence that thymol was successfully grafted onto chitosan through the Mannich reaction. The degree of substitution of CST was calculated using Equation 1, based on data from ^{1}H NMR. The results, corresponding to various ratios of chitosan and thymol, are presented in Table 4.1. The additional ^{1}H NMR results, obtained at various ratios of thymol and formaldehyde, are shown in Appendix A.

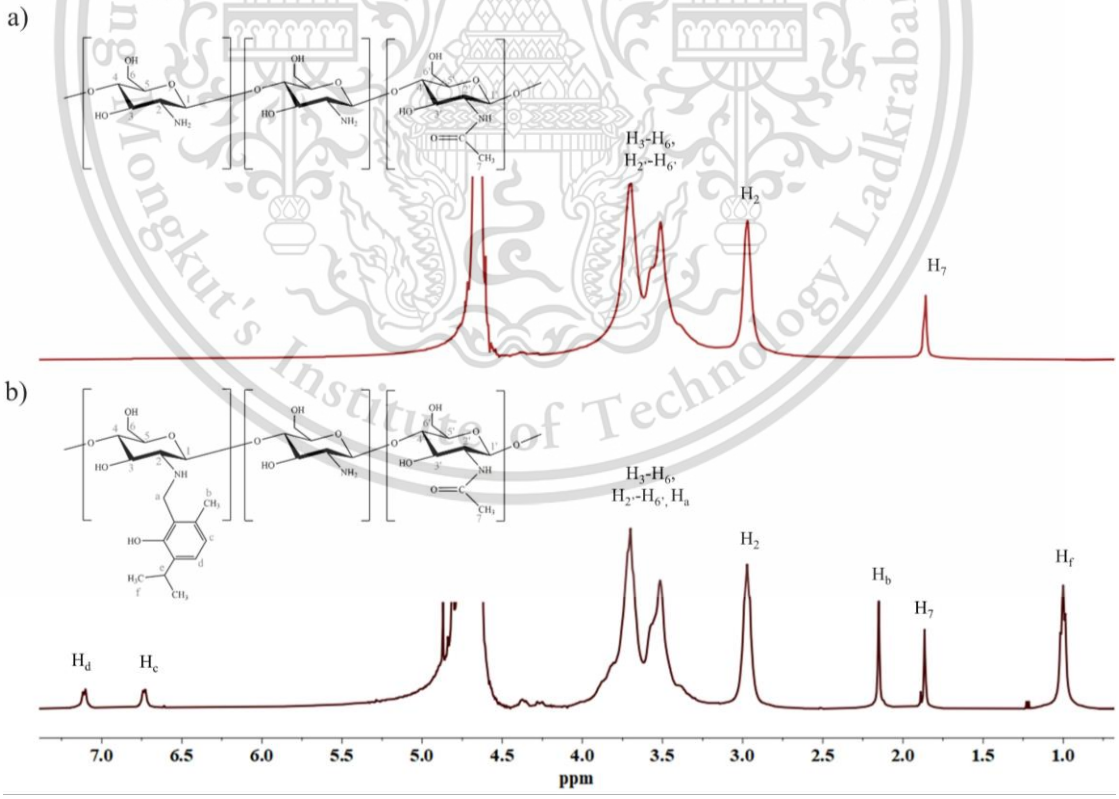

Figure 4.3 ^{1}H NMR spectra of a) chitosan and b) CST (Mole ratio of Chitosan : Formaldehyde : Thymol 1 : 0.5 :1) in CF_3COOH/D_2O.

The degree of substitution determination of CST was calculated using the following equation 1

$$\%DS_{NMR} = \frac{\left(H_f/6\right)}{H_2} \times 100 \qquad \text{eq.1}$$

Where:

$\%DS_{NMR}$ is the degree of substitution percentage

H_f is the integral area of protons at δ 1.00 ppm

H_2 is the integral areas of CS proton at δ 2.97 ppm

Table 4.1 The degree of substitution ($\%DS_{NMR}$) determination of CST calculated from ^{1}H NMR

Mole ratio of Chitosan : Formaldehyde : Thymol	The degree of substitution (%)
1.0 : 0.5 : 0.5	4.3%
1.0 : 0.5 : 1.0	9.8%
1.0 : 0.5 : 2.0	10.0%
1.0 : 1.0 : 1.0	16.2%
1.0 : 1.0 : 2.0	15.2%

According to the experiment, it was observed that increasing the amount of thymol beyond 1 mole ratio during the synthesis did not elevate the degree of substitution of thymol ($\%DS_{NMR}$). This lack of enhancement can be attributed to the exhaustion of aldehyde content in the reaction. Therefore, adding more than 1 mole ratio of thymol did not yield a higher %DS. Moreover, it is also difficult to eliminate excess thymol from the product. Additionally, increasing the aldehyde content in the synthesis process results in an increase in the crosslinking reaction. While this can indeed raise the %DS, it also makes the CST difficult to dissolve and renders it unsuitable for use as a stabilizer for gold nanoparticles.

4.1.1.3 Elemental analysis (EA)

The results of the elemental analysis shown in Table 4.2. The degree of substitution determination of CST using data from Elemental Analysis ($\%DS_{EA}$) was calculated using the following equation 2.

$$\%DS_{EA} = \left(\frac{\left(\frac{C}{N}\right)_D - \left(\frac{C}{N}\right)_O}{n} \right) \times \frac{14}{12} \times 100 \qquad \text{eq.2}$$

Where:

$\%DS_{EA}$ is the degree of substitution percentage obtained from elemental analysis data

$(C/N)_D$ is the carbon to nitrogen mass ratios of the chitosan derivative

$(C/N)_O$ is the carbon to nitrogen mass ratios of the original chitosan

N is the number of carbon introduced to the amino group

Table 4.2 The degree of substitution ($\%DS_{EA}$) determination of CST calculated from Elemental Analysis (EA).

Sample	Elemental content (%)			$\%DS_{EA}$
	N	C	H	
Chitosan	7.23	39.49	6.66	
Thymol	0	77.57	9.22	
CST 1.0 : 0.5 : 1.0	6.60	41.79	7.27	9.23

According to the elemental analysis results, the higher C/N ratio in CST compared to unmodified chitosan signifies the incorporation of additional carbon atoms into the chitosan structure during the reaction. This suggests that a significant portion of the chitosan has been modified with the addition of another carbon-containing group onto the chitosan backbone, while a substantial amount of the original CS is still present. The data from elemental analysis after calculation also revealed that the degree of substitution value ($\%DS_{EA}$) was 9.2%.

4.1.2 Synthesis of gold nanoparticles using CST as stabilizing agent (CST-AuNPs)

CST as a stabilizing agent is essential during the synthesis of nanoparticles (NPs) to inhibit the agglomeration of NPs-NPs by adsorbing onto their surface. CST-AuNPs were synthesized using a straightforward and quick chemical method. This synthesis process involves a chemical reduction using sodium borohydride ($NaBH_4$) as the reducing agent. In the presence of CST serving as the stabilizing agent, Au^{3+} ions are reduced to Au^0, resulting in the formation of stable AuNPs. The study also explored the impact of different CST concentrations on the synthesis of AuNPs, with concentrations ranging from 0.006% to 0.030% w/v being investigated. Visual observations and absorption characteristics of AuNPs stabilized with various CST concentrations were shown in Figure 4.4. Notably, the AuNPs in the solution exhibited a color change from vivid blue to dark red as the CST concentration increased, attributed to nucleation growth. Furthermore, an increase in CST concentrations resulted in a blue-shift in the absorption spectra, a phenomenon associated with surface plasmon resonance. λ_{max} of gold nanoparticle colloidal with concentrations ranging from 0.006% to 0.030% w/v displayed a single peak as shown in Table 4.3.

However, using both lower and higher concentrations of stabilizing agents can result in the precipitation of AuNPs. When there is insufficient stabilizing agent, nanoparticles may grow uncontrollably, leading to the formation of larger particles or aggregates that precipitate due to gravitational settling. Conversely, an excess of stabilizing agent can result in polymer chains adsorbing onto multiple particles, effectively bridging them together. This process causes aggregation and precipitation [53]. Therefore, such conditions are unsuitable for the synthesis of AuNPs.

To determine the concentration of CST-AuNPs, the stock colloidal CST-AuNP solution was diluted threefold with ultrapure water, and the absorbance intensity was measured at λ_{max} = 502 nm using UV-vis spectrometry. Beer's law, along with an extinction coefficient based on particle diameter (ε = 7.19 × 10^9 M^{-1} cm^{-1} for CST-AuNPs with a particle size of 2.41 nm), was utilized for the calculation. The extinction coefficient for CST-AuNPs was determined using the equation ln ε = 1.4418 lnD + 18.955, where D represents the diameter in nanometers (nm) [54]. Consequently, the concentration of CST-AuNPs was found to be 3.637 nanomolar [nM].

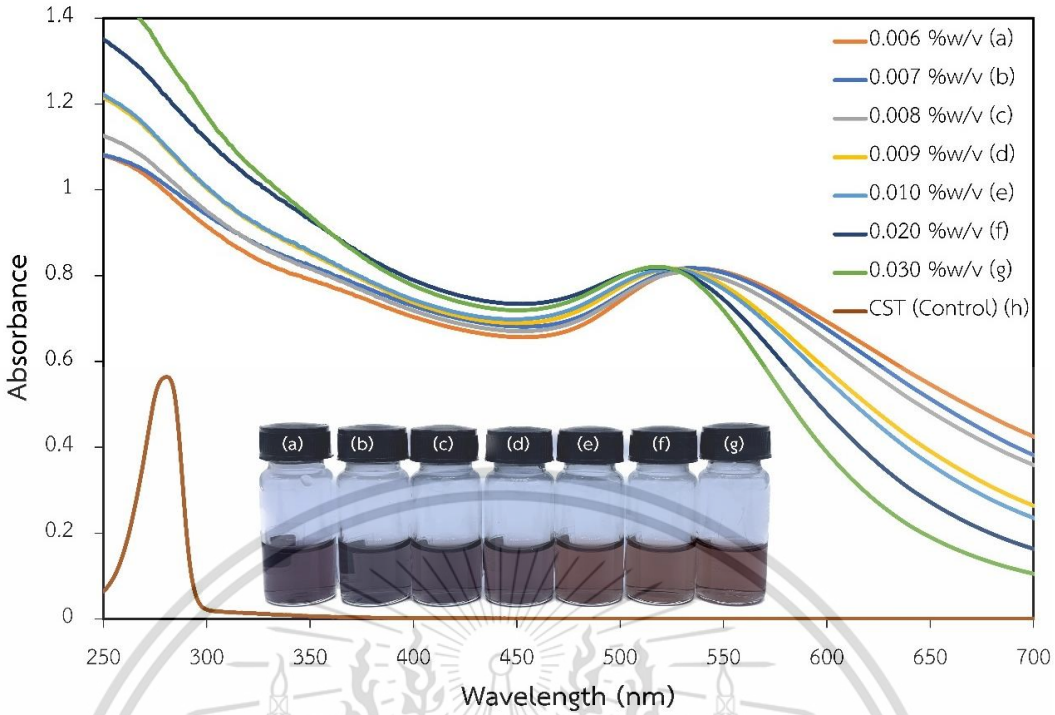

Figure 4.4 The visual observation and absorption spectra of chitosan–grafted–thymol coated on gold nanoparticles with various concentration of chitosan–grafted–thymol (a) 0.006 %w/v, (b) 0.007 %w/v, (c) 0.008 %w/v, (d) 0.009 %w/v, (e) 0.010 %w/v, (f) 0.020 %w/v (g) 0.030 %w/v and CST as control on the synthesis step.

Table 4.3 λ_{max} of gold nanoparticle colloidal

Concentration of CST (%)	λ_{max} (nm)
0.004	precipitated
0.005	precipitated
0.006	535
0.007	535
0.008	533
0.009	526
0.010	524
0.020	520
0.030	518
0.040	Precipitated
0.050	Precipitated

To study the stability of AuNPs, a zeta potential analyzer was employed. The zeta potential of CST coated on gold nanoparticles with various concentration of CST from 0.006 to 0.030 %w/v was shown in Figure 4.5 and zetapotential value was shown in Table 4.4. CST-AgNPs show negative charge in basic pH due to phenolic hydroxyl groups of thymol are acidic with a lower pKa. In basic conditions (pH 8-10), the phenolic group can lose a proton and become negatively charged ($-O^-$).

At lower CST concentrations, the zeta potential values are more negative, suggesting a stable dispersion due to strong electrostatic repulsion between particles. Increasing the concentration of CST leads to a higher ionic strength, which compresses the electrical double layer and results in a reduced zeta potential due to the shorter Debye length. However, the stability of the AuNPs is mainly due to steric stabilization rather than electrostatic stabilization. The polymer chains of CST creating a physical barrier that prevents the nanoparticles from aggregation.

Typically, dispersions with zeta potentials less negative than -30 mV or more positive than +30 mV are considered moderate stable[55]. The results indicate that the as-synthesized CST-AuNPs at all concentrations possess a negative potential charge, with values less negative than -30 mV at a pH of 9. Therefore, CST-AuNPs can be dispersed stably, as the negative potential charge prevents aggregation between nanoparticles-nanoparticles. This allows for the synthesis of a stable nanoparticle colloid in the aqueous phase.

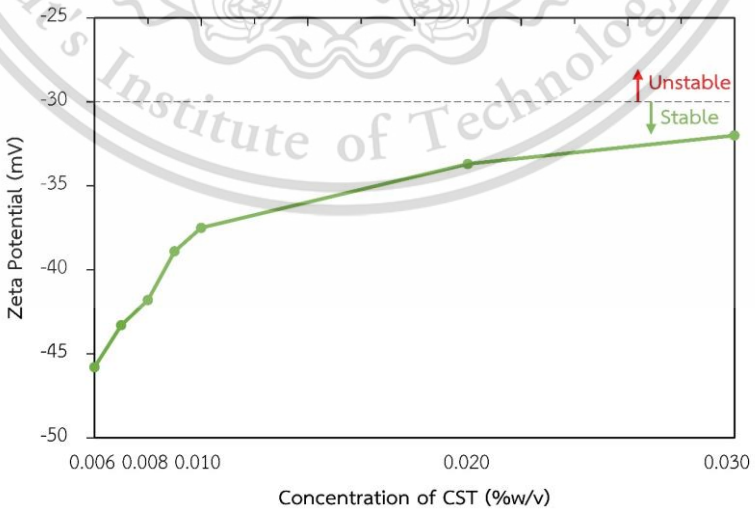

Figure 4.5 Zeta potential of CST coated on gold nanoparticles with various concentration of CST from 0.006 to 0.030 %w/v.

Table 4.4 The zetapotential value of CST-AuNPs

Concentration of CST (%)	Zetapotential (mV)
0.006	-45.8
0.007	-43.3
0.008	-41.8
0.009	-38.9
0.010	-37.5
0.020	-33.7
0.030	-32.0

The XRD patterns of CST-AuNPs are shown in Figure 4.6. Distinct peaks at specific 2θ values correspond to the standard Bragg reflections for AuNPs, confirming their successful synthesis. The identified peaks are associated with the (111), (200), (220), and (311) planes of the face-centered cubic (FCC) lattice of gold. The diffraction peak at a 2θ value of 38.1, corresponding to the (111) plane[56], suggests that the AuNPs have a preferred growth orientation in this direction. The (111) plane is often associated with the lowest surface energy, which is a favorable growth direction for nanoparticles due to energy minimization.

The results indicate that zero valent gold (Au^0), the metallic form of gold, was successfully synthesized. Furthermore, the CST capped AuNPs exhibit a crystalline structure, consistent with literature reports.

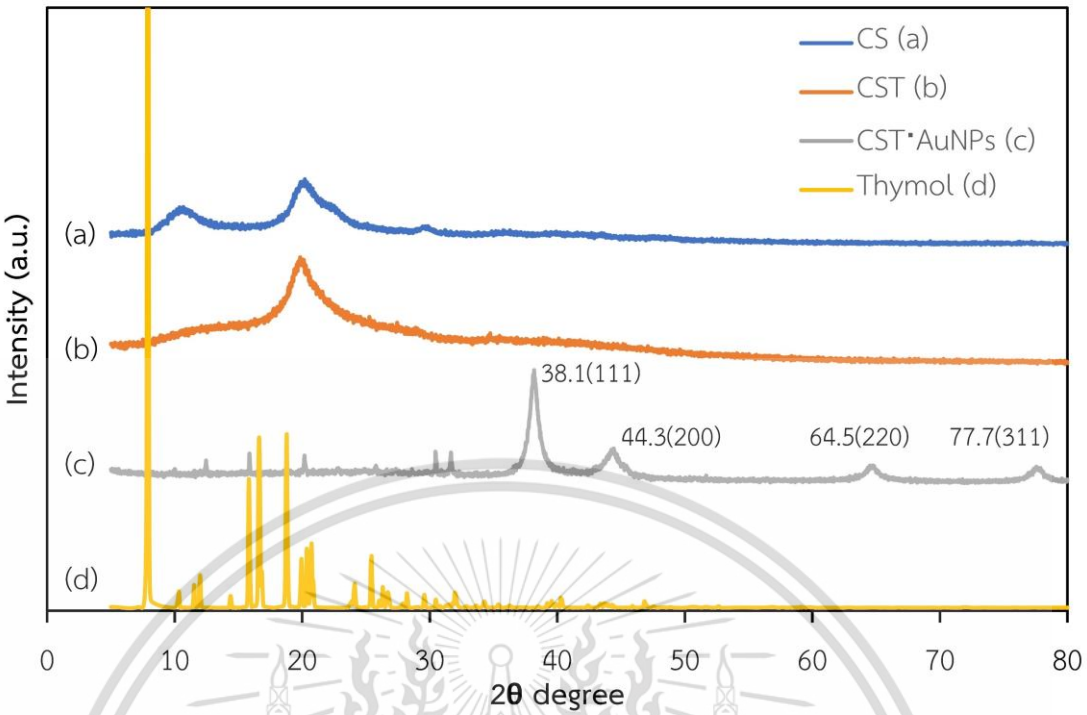

Figure 4.6 XRD pattern of (a) chitosan (b) chitosan–grafted–thymol (c) chitosan–grafted–thymol coated on gold nanoparticles and (d) thymol.

TEM analysis was used to investigate the size and morphology of the particles, as shown in Figure 4.7. This analysis studied the impact of varying CST concentrations on the preparation of AuNPs. During the synthesis step, the concentration of $HAuCl_4 \cdot 3H_2O$ was consistently maintained at 1 mM, while the CST concentration varied from 0.006 to 0.02% w/v under different conditions. Particle sizes of the AuNPs were found to range from 1.50 to 5.10 nm under these conditions. The particle size does not show significant variation with different CST concentrations (from 0.008 to 0.02% w/v), suggesting that the synthesis process is robust and not overly sensitive to changes in CST concentration. An optimal CST concentration of 0.020% w/v was identified for AuNP synthesis, yielding particle sizes between 2.41 and 3.30 nm at a pH of 9, with a zeta potential value of -33.7 mV. The observation supports the role of CST as a stabilizing agent, facilitating good dispersion of AuNPs. Stabilization is vital for preventing aggregation and maintaining the colloidal stability of the nanoparticles in solution.

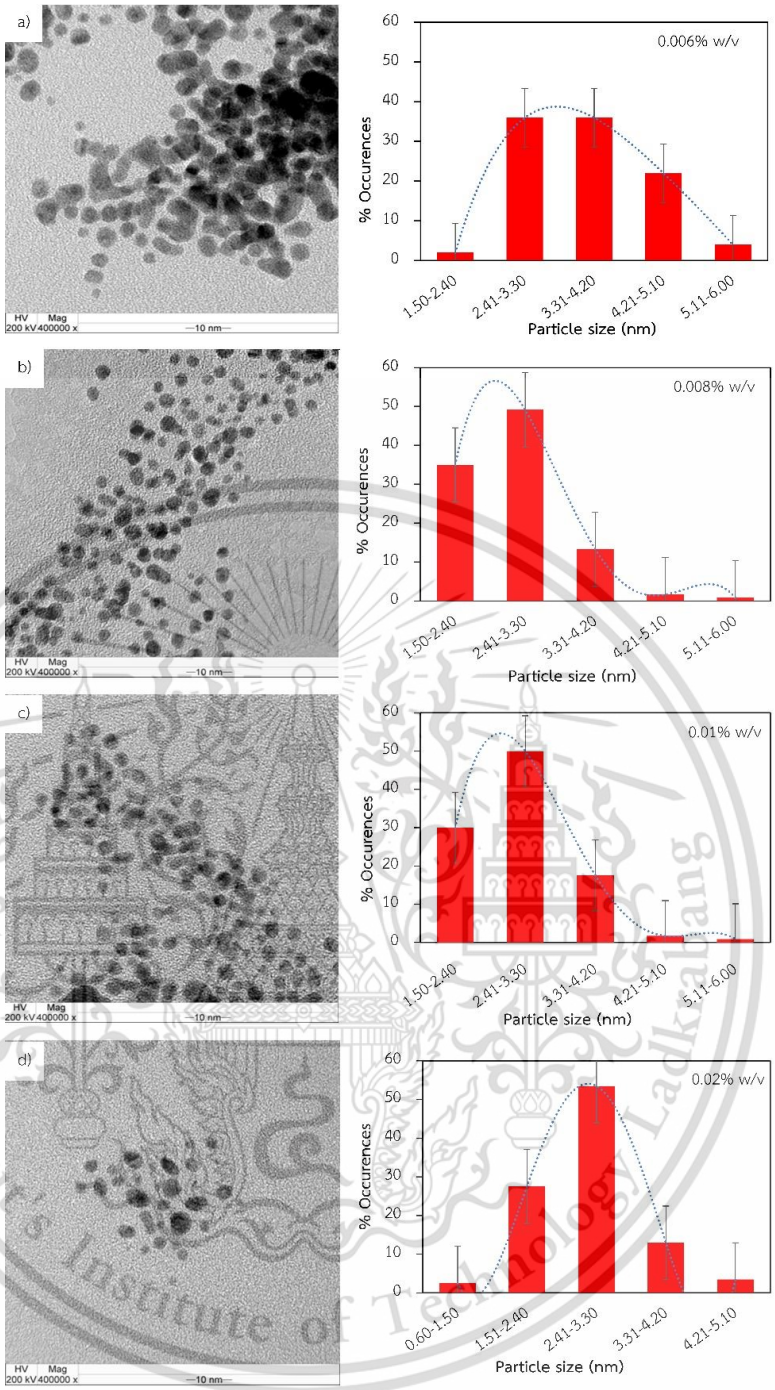

Figure 4.7 TEM images and size distribution of chitosan–grafted–thymol coated on gold nanoparticles at the CST concentration of (a) 0.006% w/v (b) 0.008% w/v (c) 0.01% w/v (d) 0.02% w/v.

4.1.3 The stability of CST-AuNPs

After the synthesis of CST-AuNPs, the stability of CST-AuNPs in various conditions was also assessed. The $CST_{0.020\%w/v}$-AuNPs were selected as the optimal

condition and served as a representative sample for the investigation. The selection of the optimal condition was determined based on the size and size distribution of the nanoparticles as analyzed by TEM, and Zeta potential value of the AuNPs colloidal.

1) Effect of pH: The stability of CST-AuNPs under various pH conditions provides important insights into their behavior. The solubility of CST under acidic conditions (pH < 5), due to the protonation of amino groups on the chitosan backbone, significantly influences the stability of AuNPs conjugated with CST. Therefore, it was imperative to explore the impact of different pH values on the stability of CST-AuNPs.

The UV-visible absorbance at a λ_{max} of 520 nm for CST-AuNPs at pH levels ranging from 3 to 11 was shown in Figure 4.8. The CST-AuNPs were dispersible at pH levels below 5 and above 7, with precipitation observed at pH 7. The addition of $NaBH_4$ resulted in a solution with a pH of 9, where the CST-AuNPs were well-dispersed, consistent with findings from various studies [57, 58].

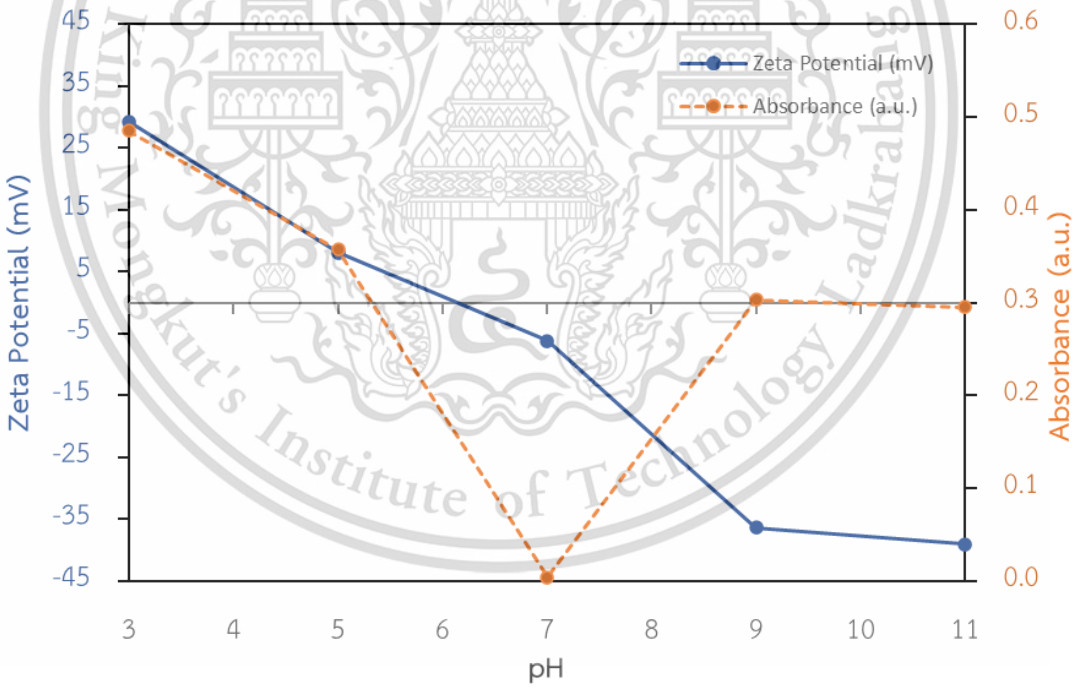

Figure 4.8 Effect of pH on the stability of CST-AuNPs.

The CST-AuNPs exhibit good dispersion at a basic pH of 9, with no significant impact on stability upon further pH increase. However, when the pH shifted to 7, precipitation of all particles was observed. This phenomenon might be attributed to the disruption of the electrostatic repulsion of the negatively charged BO_3^- ions and

the lack of charge on the deprotonated CST (with a zeta potential value approaching zero), leading to the precipitation of AuNPs. In contrast, at a more acidic condition, the amino groups of CST were protonated, resulting in a positive charge (and a higher zeta potential value), which facilitated the good dispersion of AuNPs.

2) Effect of ionic strength: The effect of ionic strength on the stability of CST-AuNPs was demonstrated through the UV-visible absorbance at λ_{max} of 520 nm of CST-AuNPs as the function of salt concentration and type, as presented in Figure 4.9. The result reveal that ionic strength is a crucial parameter influencing their stability. The study examined the stability of CST-AuNPs in relation to various salt concentrations and types, including NaCl (monovalent), Na_2SO_4 (divalent), and Na_3PO_4 (trivalent). It was observed that the stability of CST-AuNPs decreases as salt concentration increases. The variation in charge among monovalent, divalent, and trivalent salts significantly impacts the ionic strength, thereby affecting electrostatic repulsions between charged nanoparticles and consequently influencing stability and precipitation of nanoparticles. This occurrence is attributed to the reduction in electrostatic repulsion between CST and AuNPs due to the varying ionic strengths provided by these salts.

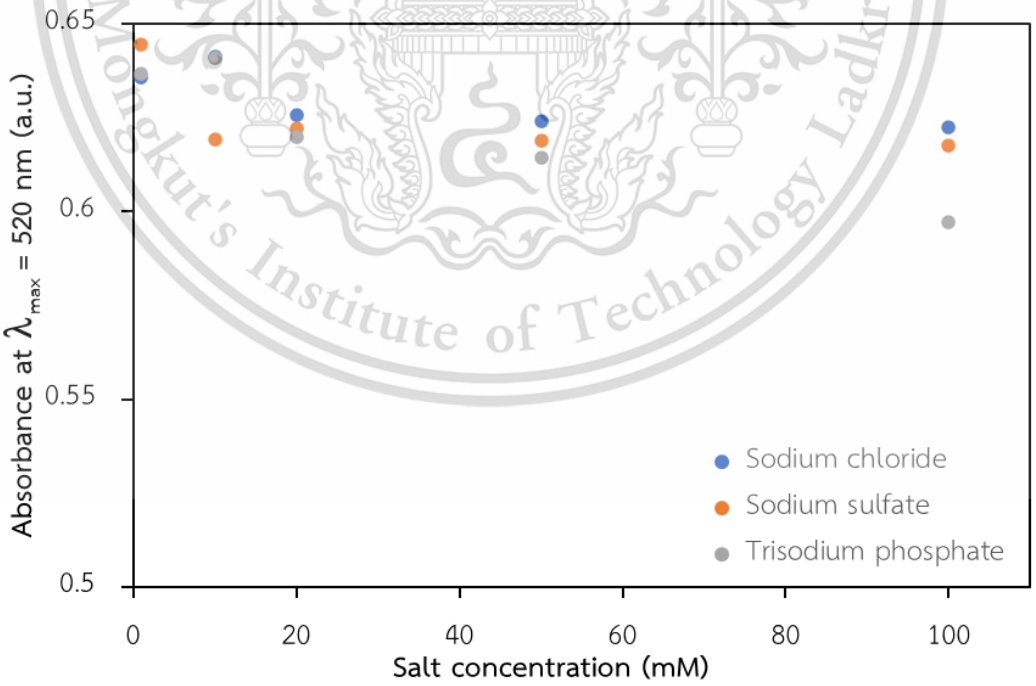

Figure 4.9 Effect of ionic strength on the stability of CST-AuNPs.

Monovalent salts yield lower ionic strength, resulting in weaker charge screening and gradual nanoparticle precipitation, often necessitating higher concentrations to induce this effect, which corresponds to higher UV intensity values. In contrast, divalent salts exhibit moderate ionic strength and more effectively reduce electrostatic repulsions, leading to quicker precipitation at comparatively lower concentrations. Trivalent salts possess the highest ionic strength, providing robust charge screening and inducing rapid nanoparticle aggregation and precipitation even at minimal concentrations, associated with lower UV intensity values.

3) Effect of time: The effect of time onto the stability of CST–AuNPs was shown in Figure 4.10. The UV-visible absorbance at a λ_{max} of 520 nm for CST-AuNPs was observed at various time points, ranging from 0 to 180 days. CST-AuNPs exhibit long-term stability (over three months) at pH 9. This long-term stability is advantageous for applications that require extended nanoparticle shelf life or performance duration.

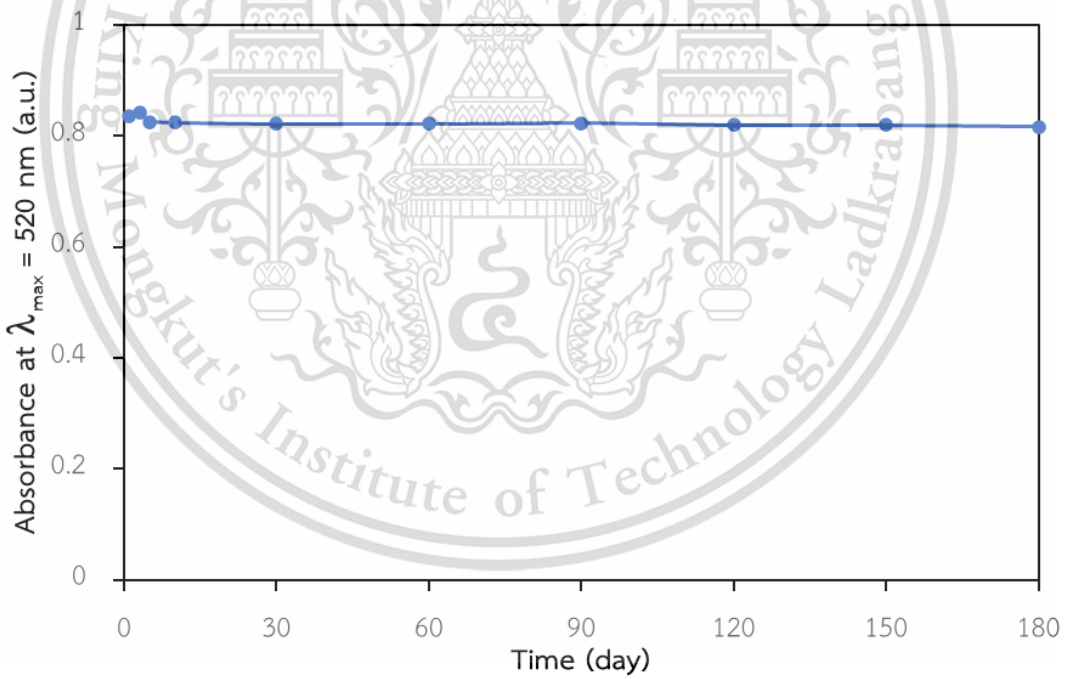

Figure 4.10 Effect of time on the stability of CST-AuNPs

4.1.4 Antimicrobial assay

1) Agar well diffusion assay: The antibacterial activity of chitosan, CST and CST–AuNPs was evaluated using the agar well diffusion method, as shown in Figure 4.11. chitosan, CST or CST–AuNPs were mixed with 4% tween 80 as controls to enhance stability in the solution and prolong the settling time during the antimicrobial test. 4% tween 80, used as a control, had no effect on antibacterial activity. chitosan and CST, on their own, are not antibacterial. This is attributed to their large polymer structure, which prevents them from spreading in water, the primary matrix of agar and culture media.

CST–AuNPs demonstrated significant antibacterial action against a majority of the pathogenic bacteria tested. The choice of capping agent during the synthesis process greatly impacts the nanoparticles' subsequent antimicrobial activity, particularly against *S. mutans* ATCC 25175 and *S. sobrinus* ATCC 33402. Specifically, the nanoparticles inhibited *S. mutans* with a clear zone of 15.90 mm and *S. sobrinus* with a clear zone of 14.25 mm. The observation suggests that AuNPs exhibit enhanced antibacterial properties when CST coated to their surface. The interaction between CST and the surface of AuNPs could be affecting bacterial membranes or interfering with essential bacterial processes, leading to their inhibition.

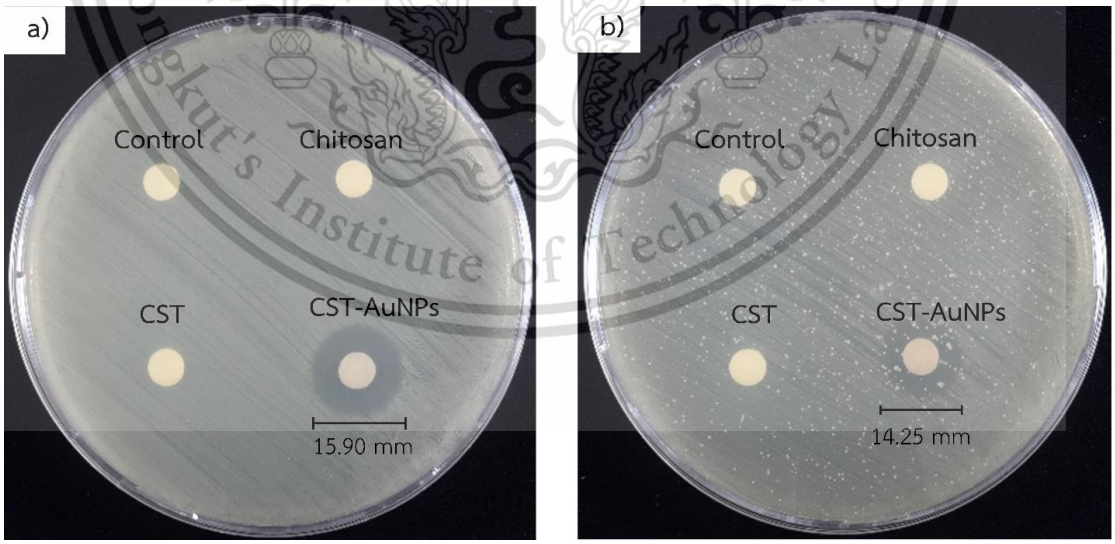

Figure 4.11 Bacterial inhibition photographs of chitosan, chitosan–grafted–thymol and chitosan–grafted–thymol coated on gold nanoparticles and control against using agar well diffusion method (a) *S. mutans* and (b) *S. sobrinus*.

2) Minimum inhibitory concentration (MIC) and minimum bactericidal concentration (MBC) assay: The antibacterial effectiveness of chitosan, CST and CST–AuNPs against *S. mutans* and *S. sobrinus* was evaluated through Minimum Inhibitory Concentration (MIC) and Minimum Bactericidal Concentration (MBC) assays as shown in Table 4.5. Chitosan showed MIC and MBC values of 100 against both *S. mutans* and *S. sobrinus*. The introducing of hydrophobic group on chitosan backbone will enhance antimicrobial activity [13, 59]. Thymol [13, 46, 59], a well-known hydrophobic group with antimicrobial properties, is expected to enhance the antimicrobial activity of chitosan after being grafted to the chitosan backbone, resulting in the production of CST. CST showed MIC and MBC values of 50 against both *S. mutans* and *S. sobrinus*.

Moreover, CST coated on AuNPs (CST–AuNPs) enhances antibacterial properties. CST–AuNPs exhibit MIC and MBC values of 25 mg/L and 100 mg/L, respectively, against *S. mutans*. Meanwhile, for *S. sobrinus*, the MIC and MBC values were recorded at 100 mg/L and 200 mg/L, respectively. These results demonstrate the antibacterial properties of CST–AuNPs against both bacterial strains, underscoring the significance of integrating thymol into the chitosan backbone to enhance its antimicrobial activity.

Table 4.5 MICs and MBCs of chitosan, chitosan–grafted–thymol and chitosan–grafted–thymol coated on gold nanoparticles against *S. mutans* and *S. sobrinus*.

Synthesis materials	***S.mutans* ATCC 25175**		***S. sobrinus* ATCC 33402**	
	MIC (mg/L)	MBC (mg/L)	MIC (mg/L)	MBC (mg/L)
chitosan	100	100	100	100
CST	50	50	50	50
CST–AuNPs	25	100	100	200

4.2 Conclusions

The synthesis of Chitosan-g-Thymol (CST) and its subsequent utilization in the formation of gold nanoparticles (CST-AuNPs) was successfully achieved through the Mannich reaction. Structural characterizations of CST were confirmed using UV-vis

spectroscopy, ^{1}H NMR, and Elemental Analysis, with the UV-vis spectra revealing a bathochromic shift indicative of thymol's covalent bonding to chitosan. The ^{1}H NMR data further supported the successful grafting of thymol onto chitosan at a mole ratio of chitosan: formaldehyde: thymol of 1.0: 0.5: 1.0 with a degree of substitution ($\%DS_{NMR}$) of 9.8%. The elemental analysis also confirmed the grafting, with a degree of substitution value ($\%DS_{EA}$) of 9.2%.

The stability of AuNPs is significantly impacted by the excellent characteristics of CST. The electrostatic characteristics of CST were primarily attained by the stability of the AuNPs through electrostatic repulsion. The synthesized CST-AuNPs exhibited stability across various pH levels, ionic strengths, and over extended periods. The average particle size of the AuNPs ranged between 2.41 and 3.30 nm, with predominantly spherical morphology.

The AuNPs displayed significant antibacterial activity against *S. mutans* ATCC 25175 and *S. sobrinus* ATCC 33402 when CST was coated on their surfaces. This study highlights the potential of CST coated on AuNPs surfaces as promising antimicrobial agents, particularly against cariogenic bacteria. The integration of thymol into the chitosan backbone plays a crucial role in enhancing its antimicrobial properties.

Chapter 5

Antimicrobial nanolayer films of carboxyethyl chitosan–grafted–chloroxylenol modified silver nanoparticles for enhanced surgical suture performance

5.1 Results and discussion

5.1.1 Synthesis and characterization of HCSX (High Mw Chitosan-g-Chloroxylenol) and LCSX (Low Mw Chitosan-g-Chloroxylenol)

Numerous studies have highlighted the antimicrobial properties of chitosan and its derivatives. While chitosan alone possesses antibacterial activity, but its effectiveness can be enhanced by incorporating various active functional groups such as thymol [20], catechol [59, 60], β-cyclodextrin [61], N-halamine [12], and phenolic acid [13]. Each of these additions contributes to improving the antimicrobial efficacy of chitosan derivatives.

In the experiment, the Mannich reaction was employed to attach chloroxylenol onto the amino group of chitosan. Chitosan's amino group reacts with formaldehyde, forming an electrophilic imine compound ($-N=CH_2$), which then reacts by inserting a phenol group at the para position to produce secondary amines or benzylamine. As a result, chloroxylenol could be grafted onto chitosan *via* a carbene bridge.

The synthesis mechanism of CSX is illustrated in Figure 5.1. Initially, formaldehyde undergoes protonation at oxygen double bonds (=O) resulting in the formation of Methylideneoxidanium (positively charged of O). Subsequently, Methylideneoxidanium reacts with the amine group ($-NH_2$) of chitosan to form $-NH_2^+$ and then $-NH_2^+$ is deprotonated back to amine form. Meanwhile, the hydroxyl group (-OH) of $-CH_2-$ connected to $-NH_2^+$ is protonated to form Oxoniumyl ion ($-H_2O^+$), which subsequently undergoes dehydration to form Iminium ion. Following this, chloroxylenol reacts with Iminium ion, resulting in the disappearance of the positive charge on the Iminium ion. The double bond of the Iminium ion then breaks to form a single bond between $-CH_2-$

connected to -NH- of chitosan and carbon of chloroxylenol. This process leaves the alcohol group (-OH) of chloroxylenol with a positively charged, rendering it unstable, which then undergoes a return to the aromatic ring, where resonance occurs within the aromatic ring, as described in the CST section of topic 4.1.1.

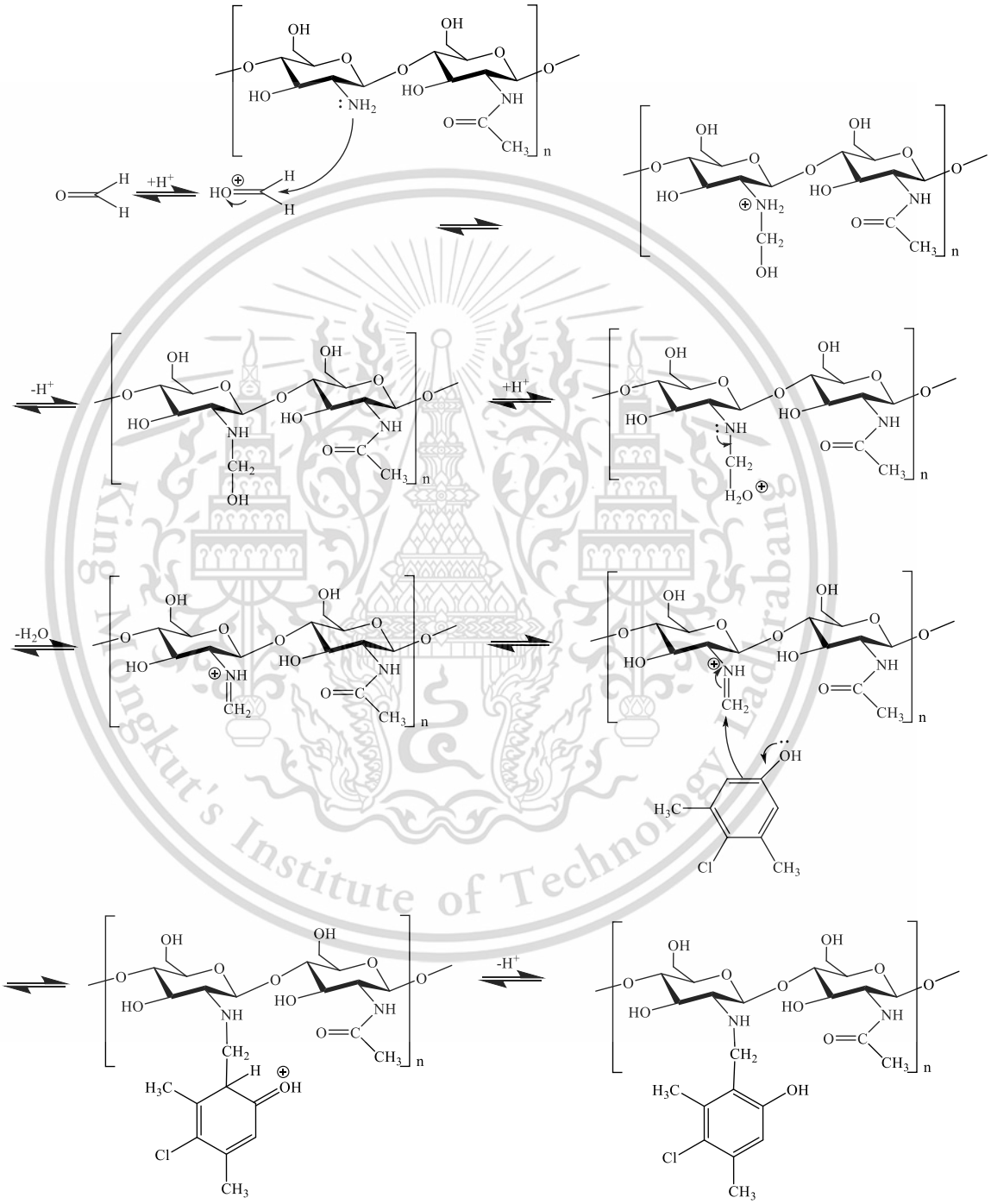

Figure 5.1 Synthesis mechanism of CSX.

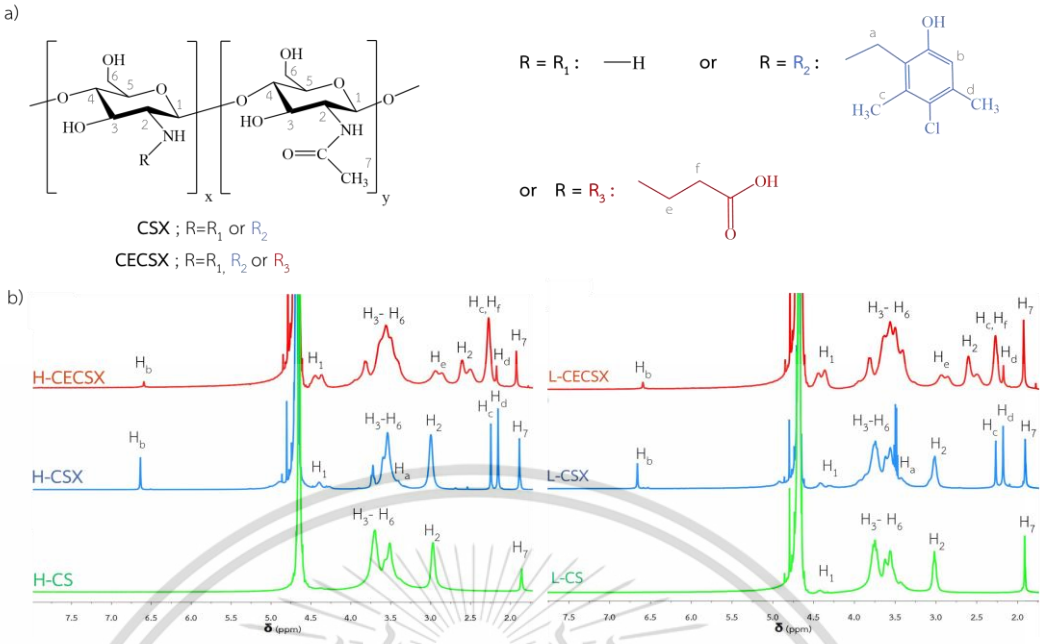

Figure 5.2 ^{1}H NMR spectra of chitosan, CSX in D2O/CF_3COOH and CECSX in D_2O.

In the experiment, chloroxylenol was grafted onto the side chain of chitosan through the Mannich reaction. A secondary amine or benzylamine is produced when the amino group of chitosan combines with formaldehyde to form an electrophilic imine (-N=CH_2). This product can then react by adding a phenol group at the para position, allowing the grafting of chloroxylenol onto chitosan *via* a methylene bridge. The structural characteristics of HCSX 1:1:2 and LCSX 1:1:2, as determined by ^{1}H NMR, are displayed in Figure 5.2 (other ratios are provided in Appendix A). The characteristic peaks corresponding to H_7 and H_2 in chitosan structure were assigned at 1.86 and 2.97 ppm, respectively, and the characteristic peaks of H_3-H_6 were assigned within the range of 3.25 – 4.00 ppm.

Regarding CSX, it retains the characteristic peaks of chitosan and reveals two additional peaks at 2.27 and 2.18 ppm, corresponding to the protons of the methyl group of chloroxylenol (H_c and H_d), respectively. Additionally, the aromatic protons of chloroxylenol (H_b) displayed distinct peaks at 6.66 ppm. These findings confirm the successful grafting of chloroxylenol onto chitosan *via* Mannich reaction. The degree of substitution of chloroxylenol (%DS_{NMR}) on the chitosan backbone was calculated using Equation 3, utilizing data from ^{1}H NMR. The calculated results are presented in Table 5.1.

$$\%DS_{NMR} = \frac{H_{c,d} / 6}{H_2} \times 100 \qquad \text{Eq.3}$$

where:

$\%DS_{NMR}$ is the degree of substitution percentage obtained from ^1H NMR

$H_{c,d}$ and H_2 are the integral areas of protons indicated in Figure 5.2

Table 5.1 The degree of substitution (%DS) determination of CSX calculated from ^1H NMR and Elemental analysis (Mole ratio of chitosan: formaldehyde: chloroxylenol).

Sample	Elemental Content (%)			$\%DS_{EA}$	$\%DS_{NMR}$
	N	C	H		
HCS	7.23	39.49	6.66	-	-
LCS	7.25	39.86	6.71	-	-
HCSX 1:0.5:1	7.46	40.834	7.075	0.15	2.67
	7.42	40.708	6.674	0.31	
HCSX 1:0.5:2	7.15	41.009	6.948	3.55	5.16
	7.31	41.318	6.541	2.47	
HCSX 1:1:1	6.972	41.048	7.048	5.52	6.16
	6.821	40.921	6.675	6.97	
HCSX 1:1:2	6.964	44.068	7.012	11.23	9.50
	6.939	43.819	6.657	11.06	
HCSX 1:1:4	7.2567	44.6825	6.806	9.02	9.33
	7.1524	43.9815	6.6687	8.91	
LCSX 1:1:1	6.64	42.40	6.64	11.33	7.66
	6.57	41.81	6.99	11.07	
LCSX 1:1:2	6.36	42.65	6.82	15.48	15.83
	6.31	42.54	6.34	15.95	
LCSX 1:1:4	7.01	45.70	6.72	13.12	14.16
	6.99	45.69	6.72	13.25	

According to the experiment, it was found that when more chloroxylenol is added in the synthesis step, the degree of substitution of chloroxylenol does not increase due to the depletion of aldehyde content in the reaction. Therefore, increasing the chloroxylenol content by more than 2 mol did not result in an increase in %DS. Moreover, it is also difficult to clear excess chloroxylenol from the reaction. In addition, increasing the aldehyde content in the synthesis increases the crosslinking reaction. While increasing the aldehyde content elevates the %DS, it renders the resulting CSX difficult to dissolve and unsuitable for use as a stabilizer of silver nanoparticles.

In the elemental analysis results, the C/N ratio of CSX surpassed that of chitosan, indicating the presence of additional carbon atoms after reaction. The analysis showed a degree of substitution value ($\%DS_{EA}$) of 11.14% for HCSX 1:1:2 and 15.72% for LCSX 1:1:2, as determined using Equation 4.

$$\%DS_{EA} = \frac{\left(\frac{C}{N}\right)_D - \left(\frac{C}{N}\right)_O}{n} \times \frac{14}{12} \times 100 \qquad \text{Eq. 4}$$

where:

$\%DS_{EA}$ is the degree of substitution percentage obtained from elemental analysis data

$(C/N)_D$ is the carbon to nitrogen mass ratios of the chitosan derivative

$(C/N)_O$ is the carbon to nitrogen mass ratios of the original chitosan

n is the number of carbons introduced to the amino group

5.1.2 Synthesis of HCECSX (High Mw Carboxyethylchitosan-grafted-Chloroxylenol) and LCECSX (Low Mw Carboxyethylchitosan-grafted-Chloroxylenol)

In the experiment, chitosan was modified with chloroxylenol to obtain CSX as described in topic 5.1.1, the Michael addition reaction was utilized to attach acrylic acid onto the amino group of CSX, resulting in the formation of CECSX (carboxyethylchitosan-grafted-chloroxylenol).

The Michael addition involves the nucleophilic attack of the CSX on the ß-carbon of acrylic acid, which is part of an **α**, ß -unsaturated carbonyl system, leading to the formation of a new carbon-carbon bond. This chemical process occurs in three stages; initially, the nucleophile attaches to the ß-carbon of the carbonyl and then transfers a proton to oxygen. Finally, enolates resulting from this process undergo a 1,4 addition from carboxyethylchitosan tautomerize. The entire reaction mechanism, as depicted in Figure 5.3, demonstrates the nucleophilic addition and the formation of the CECSX as the outcomes of this nucleophilic addition reaction [62].

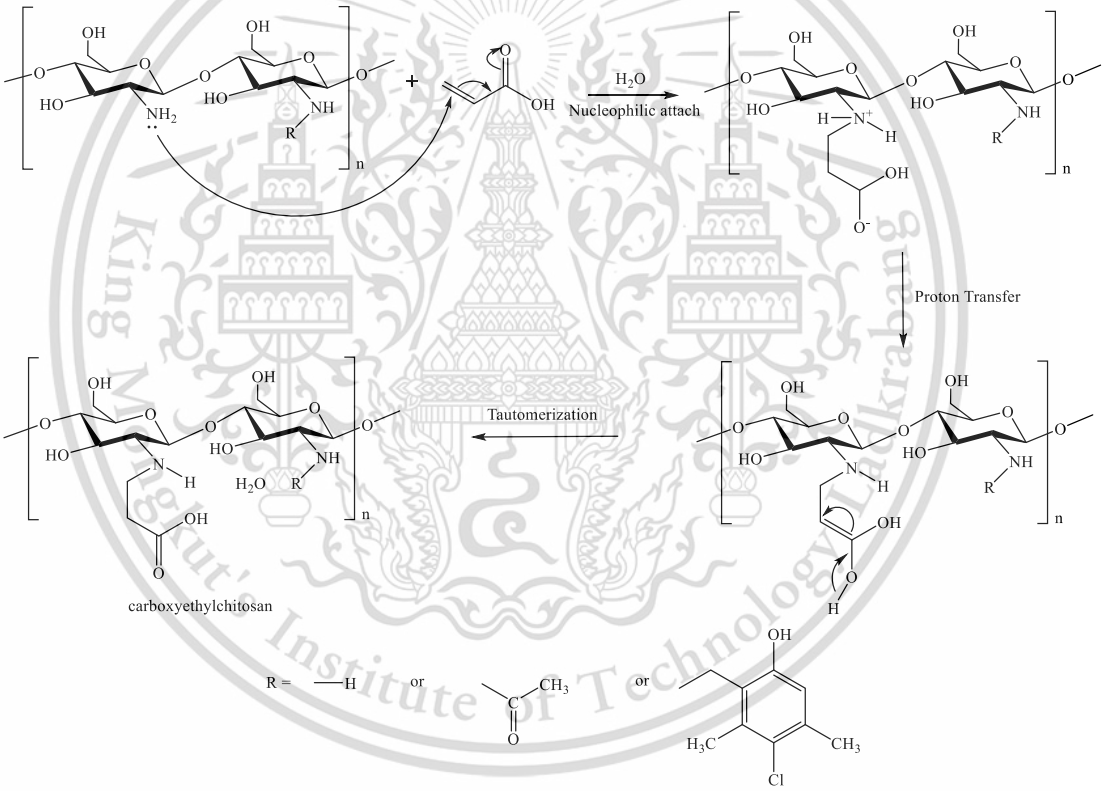

Figure 5.3 Synthesis mechanism of CECSX.

The optimum conditions for CSX (HCSX 1:1:2 and LCSX 1:1:2) were modified with acrylic acid *via* the Michael addition reaction to increase water solubility. ^{1}H NMR was used to structurally characterize the CECSX as shown in Figure 5.2.

The carboxyethyl group was affixed onto the amino group of chitosan, resulting in new signals at 2.94 and 2.18 ppm, assigned to H_e and H_f of the methylene group from the acrylic acid segment. Additionally, the signal at 2.3 ppm, corresponding to H_c of chloroxylenol, overlaps with the signal of H_f from acrylic acid [16, 62]. The degree of substitution of acrylic acid (%DS_{AA}) for HCESX and LCECSX is presented in Table 5.2 and was calculated from the ^{1}H NMR data using Equation 5.

$$\%DS_{AA} = \frac{\left(\frac{H_e}{2}\right)}{H_2} \times 100 \qquad \text{Eq. 5}$$

where:

%DS_{AA} is the degree of substitution percentage obtained from ^{1}H NMR

H_e and H_2 are the integrals areas of protons indicated in Figure 5.2

Table 5.2 The degree of substitution (%DS_{AA}) determination of acrylic acid on CECSX structure calculated from ^{1}H NMR.

Sample	%DS_{AA}
HCECSX 1:1	Not soluble in water
HCECSX 1:2	45
HCECSX 1:3	42
LCECSX 1:1	23
LCECSX 1:2	33
LCECSX 1:3	36

Using a mole ratio of acrylic acid to CSX (CSX: acrylic acid = 1:1), which is insufficient, results in HCECSX being insoluble in water and LCECSX being partially soluble in water. According to the literature, the optimal mole ratio is 1:2, where chitosan completely dissolves in water. Increasing the amount of acrylic acid to more than 2 moles per 1 mole of CSX does not affect the solubility of chitosan. Therefore, the optimal condition selected for the synthesis of both HCECSX and LCECSX was 1:2.

The UV-vis spectra of chitosan, HCECSX, LCECSX, and chloroxylenol are presented in Figure 5.4. It was observed that the chitosan spectrum lacked any peaks between 250 and 350 nm. In contrast, the CECSX spectra exhibited broad peaks at 286 nm, aligning with the aromatic structure of chloroxylenol. The peak displayed a red shift in comparison to the standalone PCMX, which exhibited a broader peak ranging from 279 to 284 nm. These findings suggest that chloroxylenol was covalently bonded to the chitosan backbone.

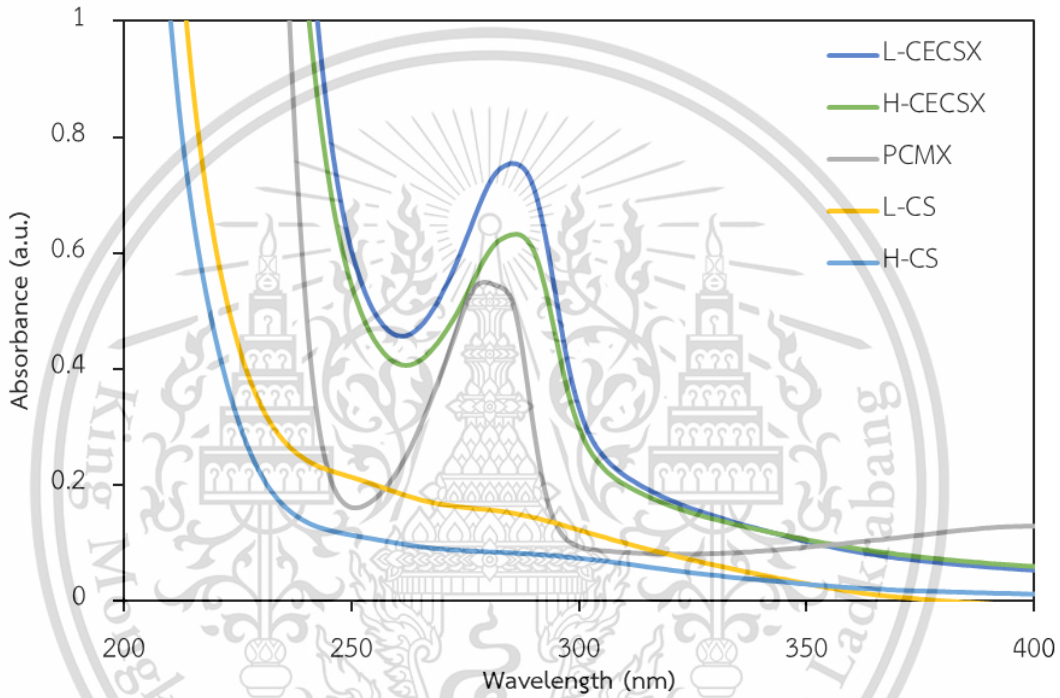

Figure 5.4 UV–vis spectra of HCECSX, LCECSX, high and low molecular weight chitosan and chloroxylenol (PCMX).

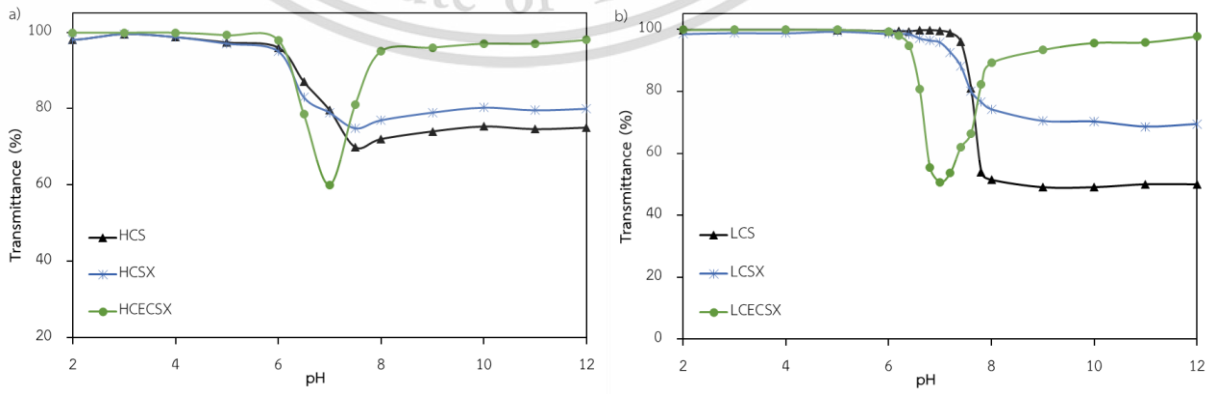

Figure 5.5 pH dependent of the water-solubility of high and low molecular weight chitosan, HCECSX and LCECSX.

Additionally, the acrylic acid modification of CSX enhanced its water solubility. To assess the water solubility, turbidity measurements of chitosan, CSX and CECSX were conducted at 600 nm. Chitosan and CSX typically dissolves well in a pH range of 1-6 but tend to become turbid and partially precipitate at pH levels greater than 6 for high molecular weight type and 6.5 for low molecular weight type due to the deprotonation of ammonium groups ($-NH_3^+$) to form amino groups ($-NH_2$). CSX exhibits less turbidity than chitosan due to interference from PCMX, a hydrophobic substance capable of disrupting crystallization and aggregation behavior.

As shown in Figure 5.5, CECSX exhibits good solubility and maintains a clear solution over a wide range of acid pH values, However, it shows initial turbid point at pH 6 due to the loss of protons from the carboxylic group (-COOH) to the amino group ($-NH_2$), forming $-NH_3^+$ and $-COO^-$, generating a zwitterion. Nevertheless, increasing the pH allows for redissolution, attaining total dissolution at a pH 8. This occurrence is due to deprotonation, resulting in the creation of $-COO^-$ and $-NH_2$ groups. The results indicate the successful bonding of acrylic acid onto the CSX backbone, enhancing its water solubility.

5.1.3 Synthesis of silver nanoparticles (HCECSX-AgNPs and LCECSX-AgNPs)

Carboxyethylchitosan-g-chloroxylenol (CECSX-AgNPs) were synthesized by chemical reduction method using $NaBH_4$, as described in topic 3.5.3. The mole ratio of silver nitrate: CECSX: $NaBH_4$ was shown in Table 3.5. HCECSX or LCECSX was used as stabilizing agent during the reduction of Ag^+ ions to Ag^0, facilitating the binding of this agent onto the surface of AgNPs to obtain stable AgNPs. The stability of the AgNPs solution in different HCECSX or LCECSX concentrations, ranging from 0.001% to 0.030% was assessed using a UV-vis spectrometer and a zeta potential analyzer. Visual observations and absorption spectra are displayed in Figure 5.6.

The absorption spectra exhibit a red shift due to the surface plasmon resonance phenomenon, which relates to the visual observation of a color change from dark yellow to light yellow with increasing CECSX concentration. Optimal conditions were selected based on λ_{max}, particle size, and the film adhesion ability of the nanoparticles. A concentration of 0.005% was chosen as optimal for synthesizing AgNPs for both HCECSX and LCECSX. The extinction spectrum for all conditions of HCECSX-AgNPs and LCECSX-AgNPs displayed a single peak, as depicted in Table 5.3.

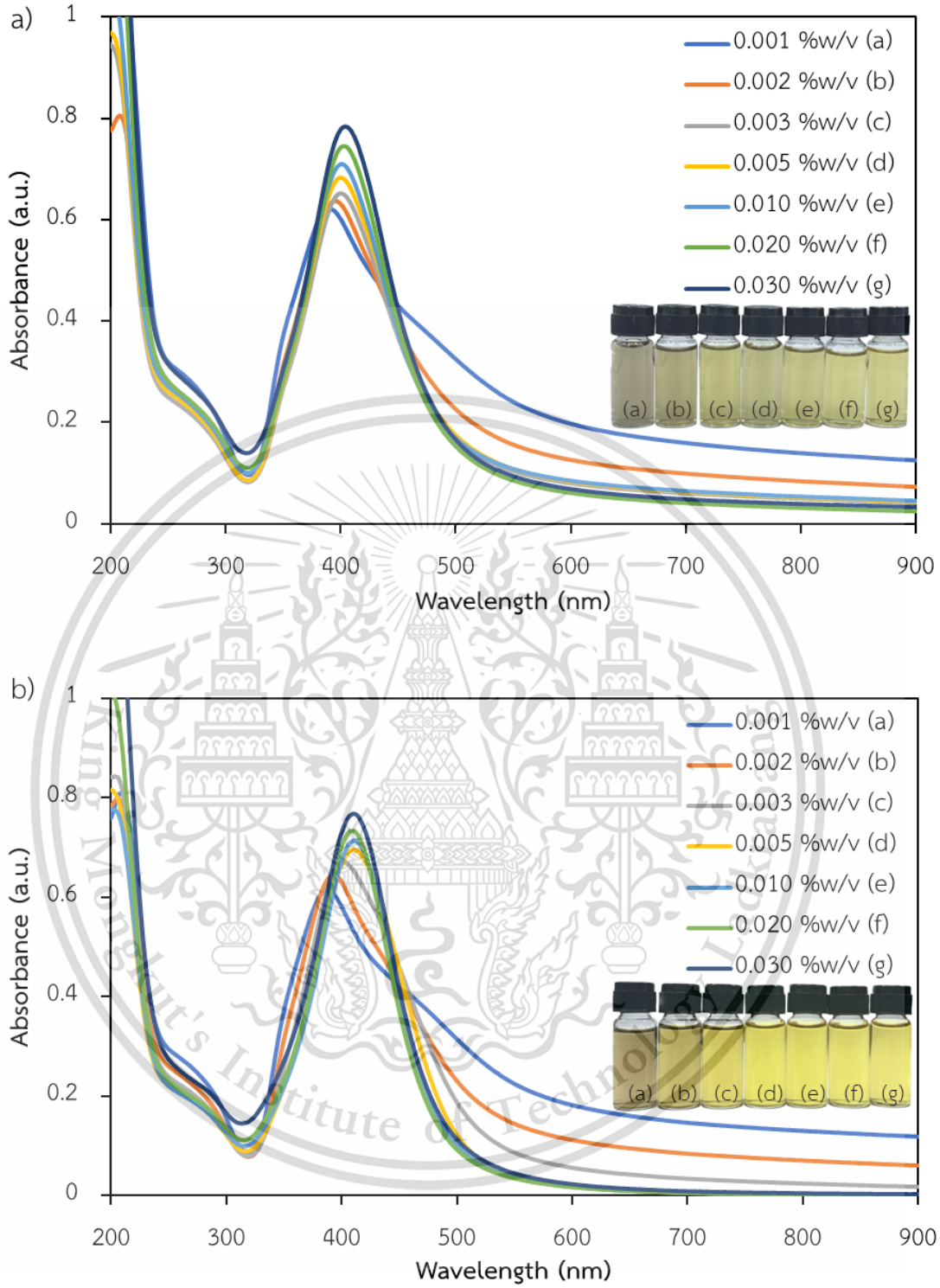

Figure 5.6 The visual observation and absorption spectra of a) HCECSX-AgNPs b) LCECSX-AgNPs with various concentration of HCECSX and LCECSX from 0.001-0.030 %w/v on the synthesis step.

Table 5.3 λ_{max} of CECSX-AgNPs colloidal

CECSX concentration (%)	λ_{max} of HCECSX (nm)	λ_{max} of LCECSX (nm)
0.001	402	387
0.002	404	394
0.003	401	402
0.005	400	411
0.010	400	411
0.020	395	410
0.030	391	411

The trends in zeta potential are depicted in Figure 5.7, and the specific zeta potential values are shown in Table 5.4, indicating that the as-synthesized HCECSX-AgNPs and LCECSX-AgNPs possess a negative charge at pH 9. This negative charge helps prevent aggregation of the AgNPs in the aqueous phase. According to the literature, nanoparticles exhibit moderate stability in a dispersion medium if the zeta value is above +30 mV or below -30 mV [55, 63]. However, exceptions exist where AgNPs maintain stability in solutions with a zeta potential less than ±30 mV, as observed with certain hydrophilic polymers like agar and PVA [64]. In the case of CECSX, the stability of AgNPs is facilitated by solubility of CECSX and the steric effects attributed to its modified positions. These aspects promote enhanced dispersion of polymer chains within the medium, effectively inhibiting the aggregation of AgNPs in the aqueous phase, even with a zeta potential lower than ±30 mV.

HCECSX-AgNPs tend to exhibit a higher zeta potential compared to LCECSX-AgNPs due to their longer polymer chains, which allow for more extensive surface coverage and increased surface charge on the nanoparticles. The enhanced steric stabilization and higher charge density, due to the greater availability of amino groups for protonation in high MW chitosan, contribute to increased electrostatic repulsion between nanoparticles. This phenomenon prevents aggregation more effectively, resulting in a higher zeta potential.

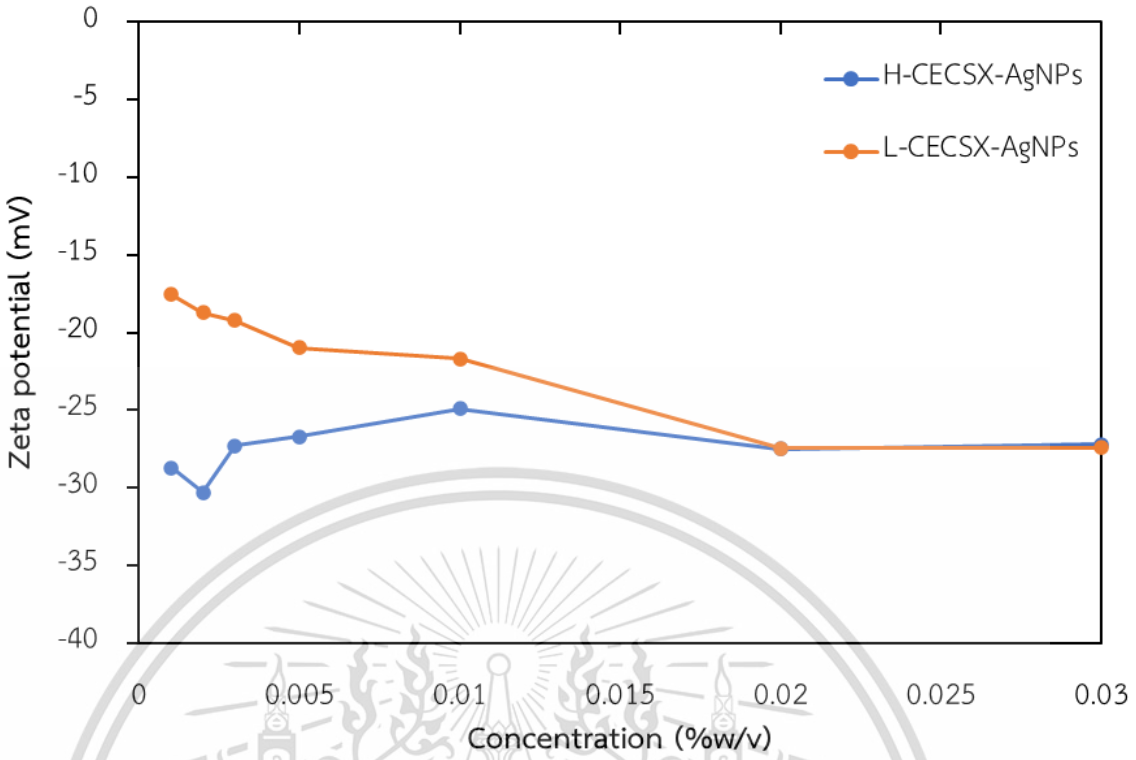

Figure 5.7 Zeta potential of HCECSX-AgNPs and LCECSX-AgNPs with various concentration of HCECSX or LCECSX from 0.001 to 0.030 %w/v.

Table 5.4 The zetapotential value of HCECSX-AgNPs and LCECSX-AgNPs

Concentration (%)	Zeta potential of HCECSX-AgNPs (mV)	Zeta potential of LCECSX-AgNPs (mV)
0.001	-28.7	-17.53
0.002	-30.3	-18.7
0.003	-27.3	-19.23
0.005	-26.7	-20.97
0.010	-24.9	-21.7
0.020	-27.5	-27.47
0.030	-27.2	-27.43

The particle size and shape were evaluated using TEM analysis. The TEM image demonstrates that both HCECSX-AgNPs and LCECSX-AgNPs are effectively dispersed in aqueous environments, exhibiting a nano size spherical shape. The particle size of AgNPs, capped with varying concentrations of HCECSX and LCECSX (0.003, 0.005, and

0.010% w/v), was found to range from 0.80 to 10.80 nm. The TEM images and size distributions of HCECSX-AgNPs and LCECSX-AgNPs are displayed in Figures 5.8 and 5.9, respectively.

The optimal concentrations of HCECSX and LCECSX for synthesizing AgNPs were determined to be 0.005% w/v. The average particle sizes were found to be 5.8±3.1 nm for HCECSX-AgNPs and 4.8±2.4 nm for LCECSX-AgNPs. These results suggest that CECSX, when prepared under basic conditions, acts effectively as a stabilizing agent, ensuring that the AgNPs remain suitably dispersed.

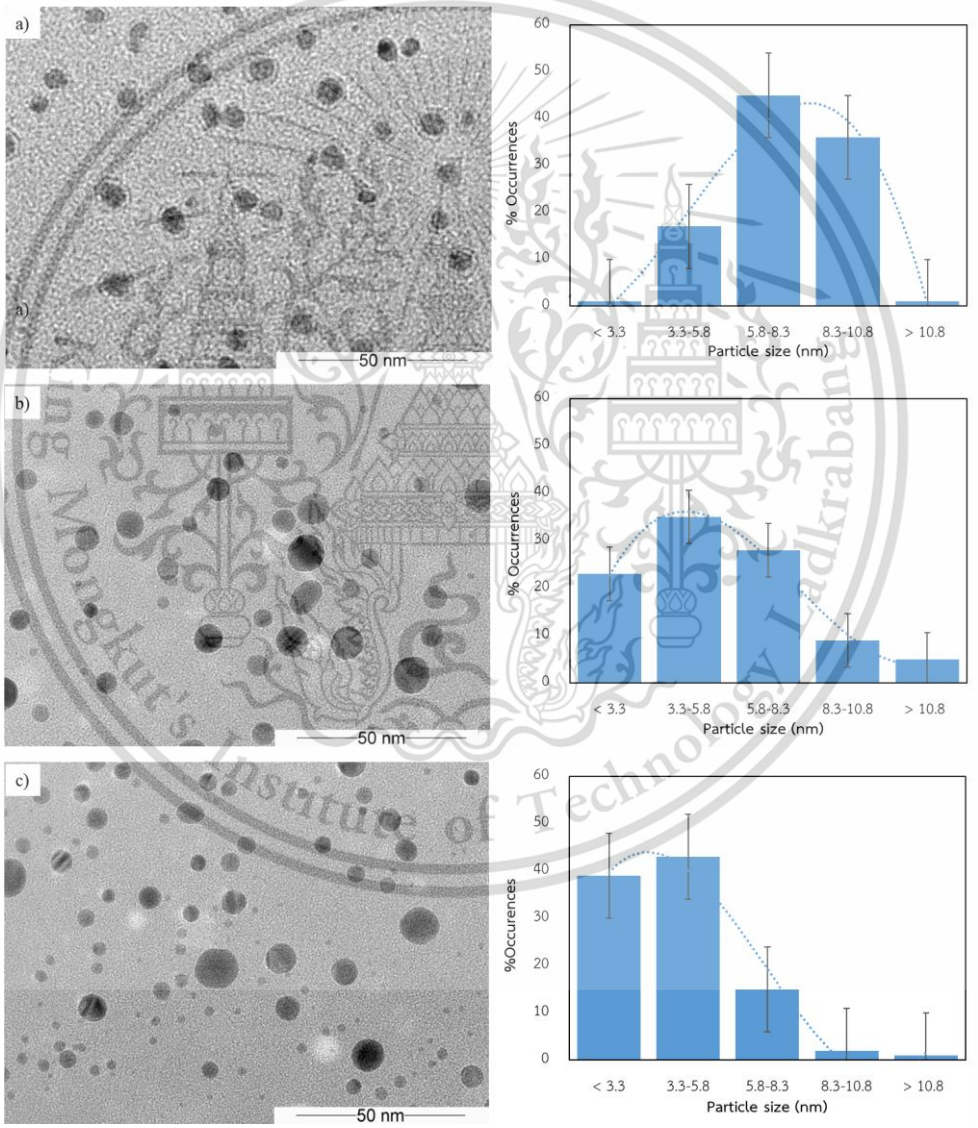

Figure 5.8 TEM images and size distribution of HCECSX-AgNPs at the HCECSX concentration of (a) 0.003% w/v (b) 0.005% w/v (c) 0.010% w/v.

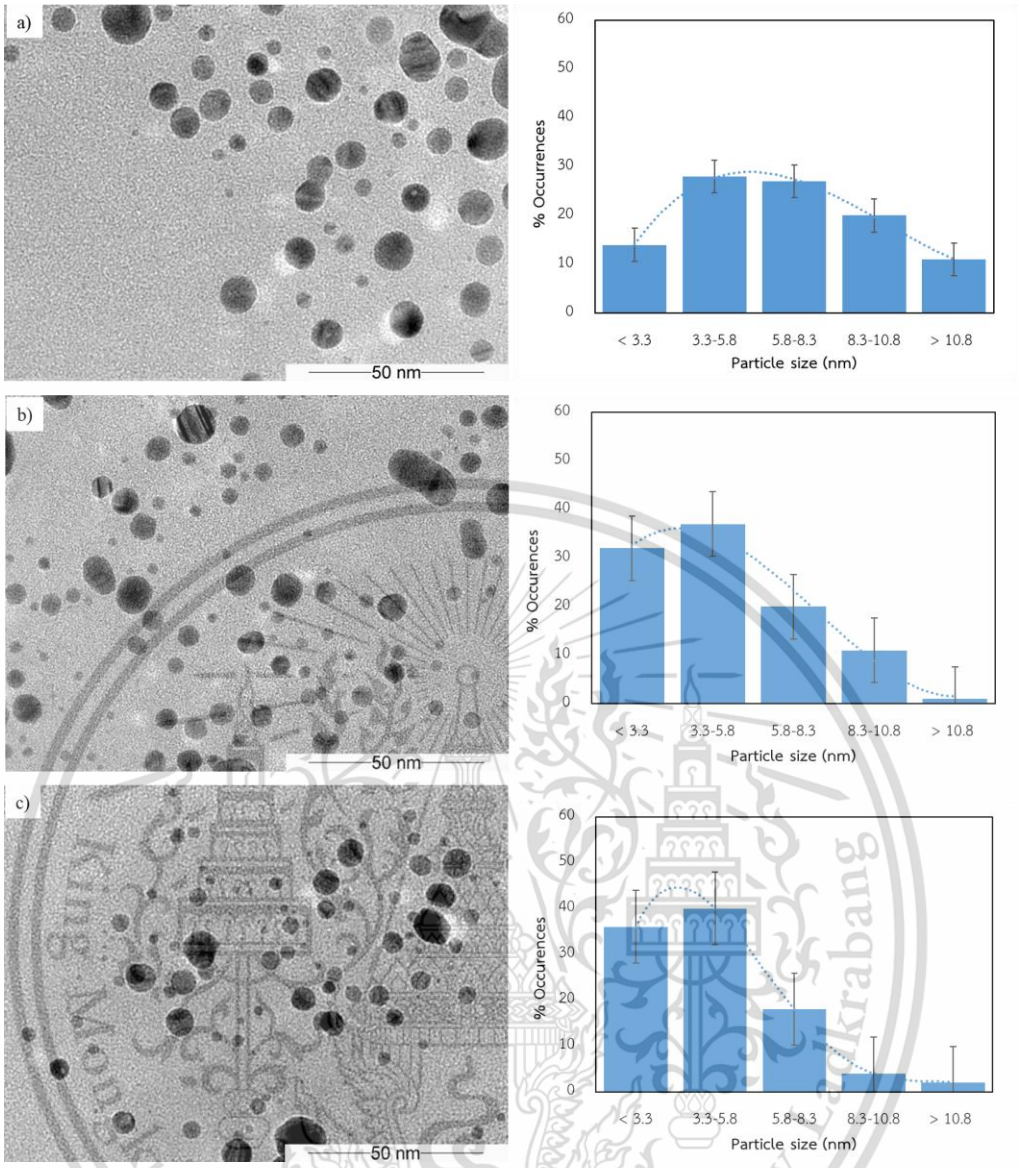

Figure 5.9 TEM images and size distribution of LCECSX-AgNPs at the LCECSX concentration of (a) 0.003% w/v (b) 0.005% w/v (c) 0.010% w/v.

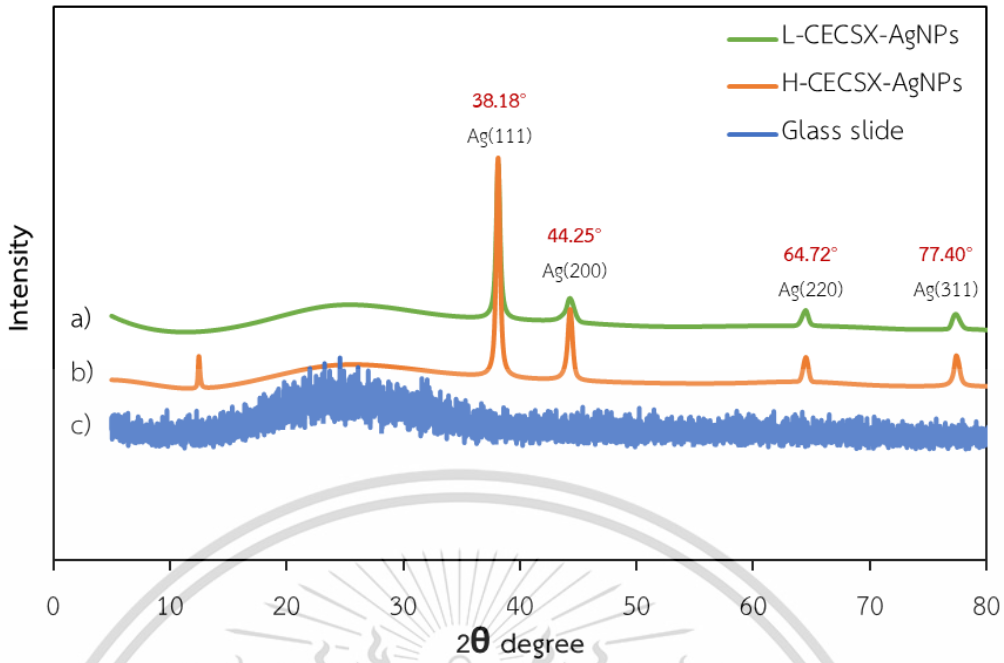

Figure 5.10 XRD pattern of a) chitosan–grafted–HCECSX coated on silver nanoparticles and b) chitosan–grafted–LCECSX coated on silver nanoparticles and c) glass slide as substrate.

The crystalline nature of the nanoparticles was analyzed using XRD measurements, with corresponding patterns illustrated in Figure 5.10, affirming the successful synthesis of HCECSX-AgNPs and LCECSX-AgNPs. Notably, both HCECSX-AgNPs and LCECSX-AgNPs displayed four remarkable peaks, aligning with characteristic Bragg reflections. The face centered cubic (FCC) lattice's 2θ (Bragg reflections) values were identified as 38.18(111), 44.25(200), 64.72(220), and 77.40(311), signifying the nanoparticles' spherical geometry and crystalline character (JCPDS card no: 65-2871). A pronounced diffraction at the 38.18 peak highlights the preferred growth orientation of zero-valent silver in the (111) direction. These findings confirm that the capping of AgNPs with HCECSX and LCECSX aligns with existing literature[65].

5.1.4 Layer by Layer deposition of silver nanoparticles film fabrication on substrate

The suitable condition of the layer-by-layer method will be studied through the glass surface before actually being used in film formation on the suture materials. The prepared silver nanoparticles stabilized with HCECSX/LCECSX were then used for the fabrication of silver nanoparticle/PDADMAC composite thin films using LbL self-

assembly method. The fundamental principle of LbL film formation relies on the attraction between oppositely charged components. The LbL film was built up by the electrostatic interaction between negatively charged silver nanoparticles and positively charged PDADMAC. The adhesion ability of HCECSX-AgNPs and LCECSX-AgNPs nanolayer films, with varying concentrations of HCECSX and LCECSX ranging from 0.001% to 0.030%, was evaluated using UV-vis absorption intensity after immersion in an AgNPs solution for 24 hours. The visual observations and absorption spectra are displayed in Figure 5.11, with the corresponding λ_{max} for each concentration listed in Table 5.5. The films showed a striking color due to the nanoparticle's adsorption. The color will brighten up when using higher concentrations of stabilizer during the NPs synthesis process due to a reduction in the particle size of NPs. The assembly of nanoparticles showed a yellow color due to the surface plasmon resonance (SPR) of the conduction electron.

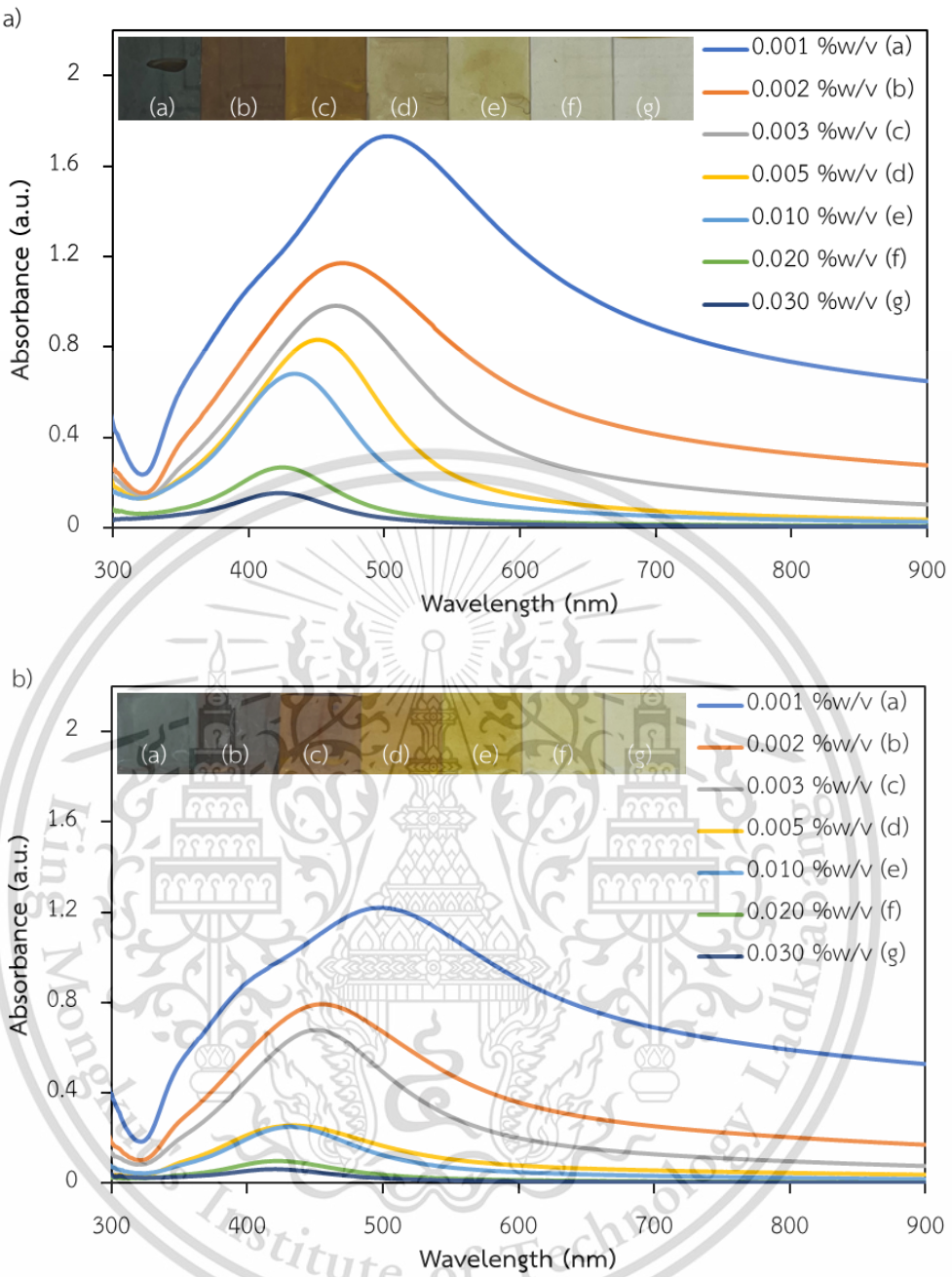

Figure 5.11 absorption spectra of a) HCECSX-AgNPs on glass substrate b) LCECSX-AgNPs on glass substrate with various concentration.

Table 5.5 λ_{max} of CECSX-AgNPs on glass slide films.

Concentration (%)	λ_{max} of HCECSX (nm)	λ_{max} of LCECSX (nm)
0.001	503	499
0.002	469	454
0.003	464	451
0.005	451	434
0.010	433	431
0.020	424	422
0.030	423	419

The optimum HCECSX-AgNPs and LCECSX-AgNPs concentrations (0.005 % w/v) for the synthesis of AgNPs would be the best conditions for LbL film growth. CECSX at the optimal concentration of 0.005% w/v was selected based on considerations of colloidal particle stability, nanoparticle size, and film adhesion to the surface.

To investigate the effect of controlling LbL growth, the growth of the silver nanoparticle composite thin films was monitored using UV–vis spectroscopy and AFM, with a focus on key factors including ionic strength, pH, time, and number of layers. These four fundamental parameters are typically studied when a new type of polyelectrolyte multilayer (PEM) thin film is proposed.

Effect of pH on film adhesion

To fabricate nanolayer films, a pH of 9 was selected to take advantage of the negative charges under basic conditions following the synthesis of AgNPs. All conditions of the CECSX-AgNPs film adhered well to the glass surface, according to Figure 5.11. Furthermore, CECSX-AgNPs at the optimal concentration (0.005 %w/v) were selected to study the impact of both basic and acidic conditions. The adhesion of CECSX-AgNPs to the film surface was investigated, as shown in Figure 5.12. Since the surface of the nanoparticles is largely negatively charged, the results showed that raising the pH value above 9 had little effect on the adhesive capabilities of the film. On the other hand, the film's adhesive ability decreased when the pH was changed to neutral or acidic conditions because the surface of the nanoparticles lost its negative charge.

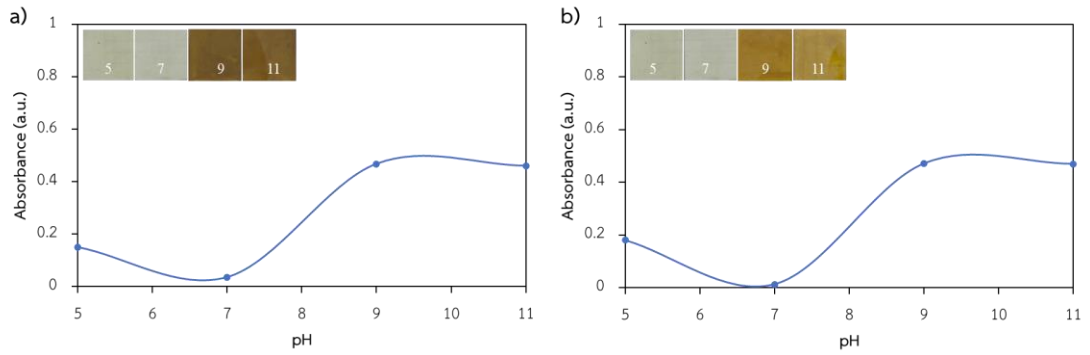

Figure 5.12 The effect of pH on preparing each layer of film at 0.005 %w/v of CECSX a) HCECSX-AgNPs b) LCECSX-AgNPs.

Effect of time on film adhesion

The effect of time on film preparation steps was tested under optimum conditions for HCECSX-AgNPs and LCECSX-AgNPs (0.005 % w/v) to estimate the appropriate duration for growing each film layer. The experiment revealed that immersing each layer of film for a period of 10 minutes for HCECSX-AgNPs and 15 minutes for LCECSX-AgNPs was sufficient. Specifically, immersing the CECSX-AgNPs film for this duration resulted in complete adhesion of the nanoparticles to the film layer. However, prolonging the immersion time did not improve nanoparticles film adhesion. The effect of time on the film preparation steps is shown in Figure 5.13.

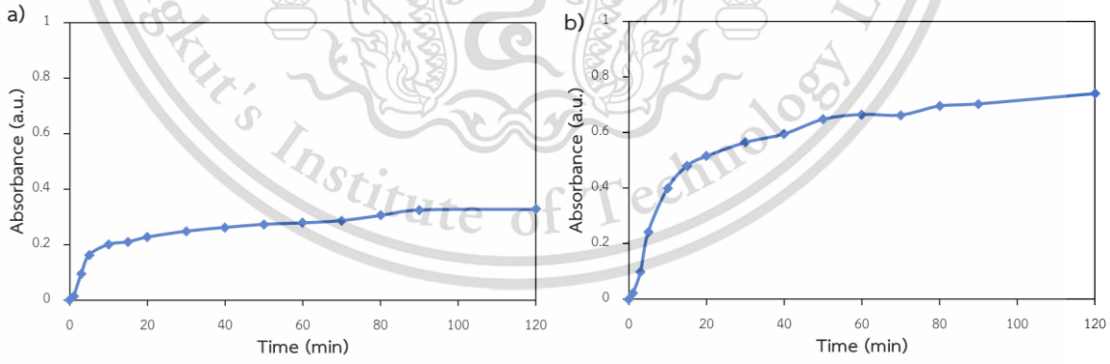

Figure 5.13 The effect of time on preparing each layer of film at 0.005 %w/v of CECSX a) HCECSX-AgNPs b) LCECSX-AgNPs.

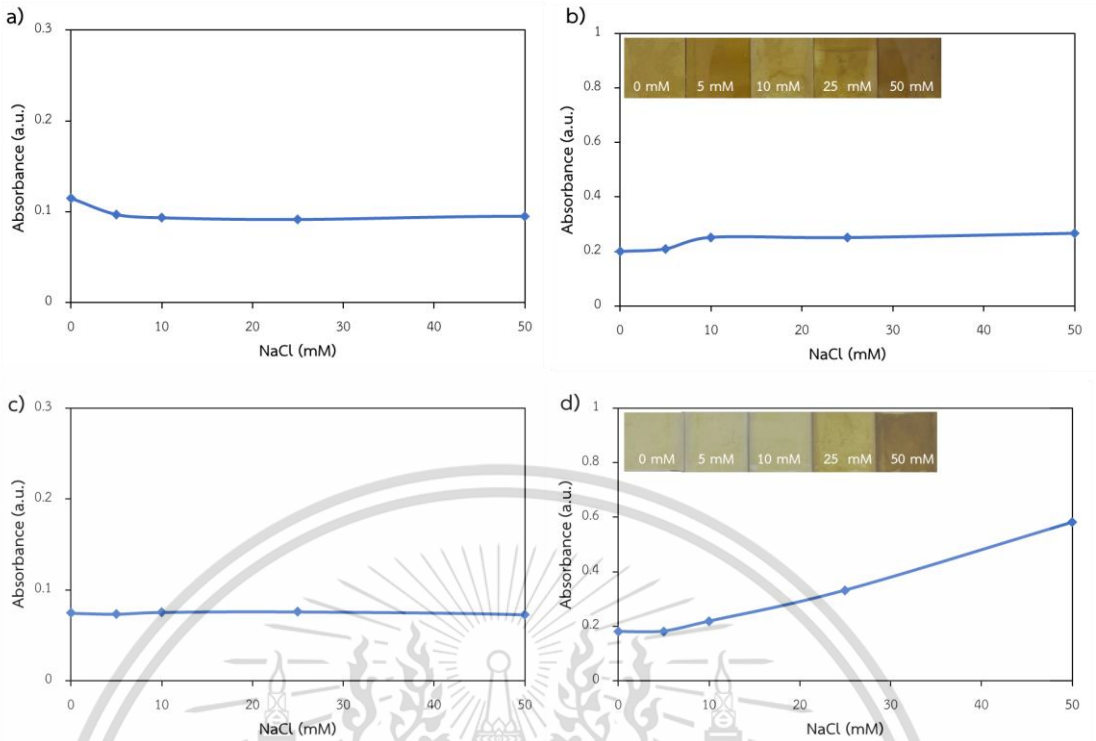

Figure 5.14 Absorption spectra of on preparation steps at 0.005 %w/v of CECSX a) HCECSX-AgNPs solution b) 1 layer of HCECSX-AgNPs film on glass substrate c) LCECSX-AgNPs solution d) 1 layer of LCECSX-AgNPs film on glass substrate, with NaCl from 0-50 mM.

Effect of ionic strength on film adhesion

The various concentrations of NaCl ranging from 0 to 50 mM were added to the as-synthesized CECSX-AgNPs solutions to evaluate their impact of ionic strength. NaCl concentration served as a parameter that enhances the formation of the film by reducing the attraction between polyelectrolytes. The absorption spectra of AgNPs solutions, the visual observation, and one-layer AgNPs film on glass substrate with various concentrations of NaCl are shown in Figure 5.14 with (a, b) for HCECSX and (c, d) for LCECSX. According to the experimental results, both scenarios -no addition of salt, and addition of 50 mM NaCl- exhibited the same surface adhesion ability. However, the addition of salt can greatly improve the adhesion performance of the film on the surface. The optimum salt concentration for film preparation was determined to be 50 mM, demonstrating the ability to enhance the film adhesion without inducing the solution precipitation. NaCl increases the ionic strength of the nanoparticle dispersion, resulting in a higher nanoparticle density within the absorption

layer. This leads to reduced electrostatic repulsion between nanoparticles, thereby strengthening the adherence of the nanoparticles to the surface. A comparison of CECSX-AgNPs films as a function of number of layers, with and without NaCl addition, is illustrated in the subsequent section.

Effect of number of film layer

The effect of the number of layers was studied in relation to the optimum concentration of NaCl in the previous section. Visual observation and absorption spectra of CECSX-AgNPs films with 0 and 50 mM NaCl as a function of the number of layers are shown in Figure 5.15 (a, b) for HCECSX and (c, d) for LCECSX. The number of layers was investigated ranging from 3 to 11 layers. The results revealed that the growth of film adhesion at 50 mM NaCl showed the appropriate condition. An increase in the number of layers corresponded to an increase in UV-visible absorbance intensity. The enhancement in absorbance values at λ_{max} for each layer of HCECSX-AgNPs and LCECSX-AgNPs are shown in Figure 5.15 (e) and (f), respectively.

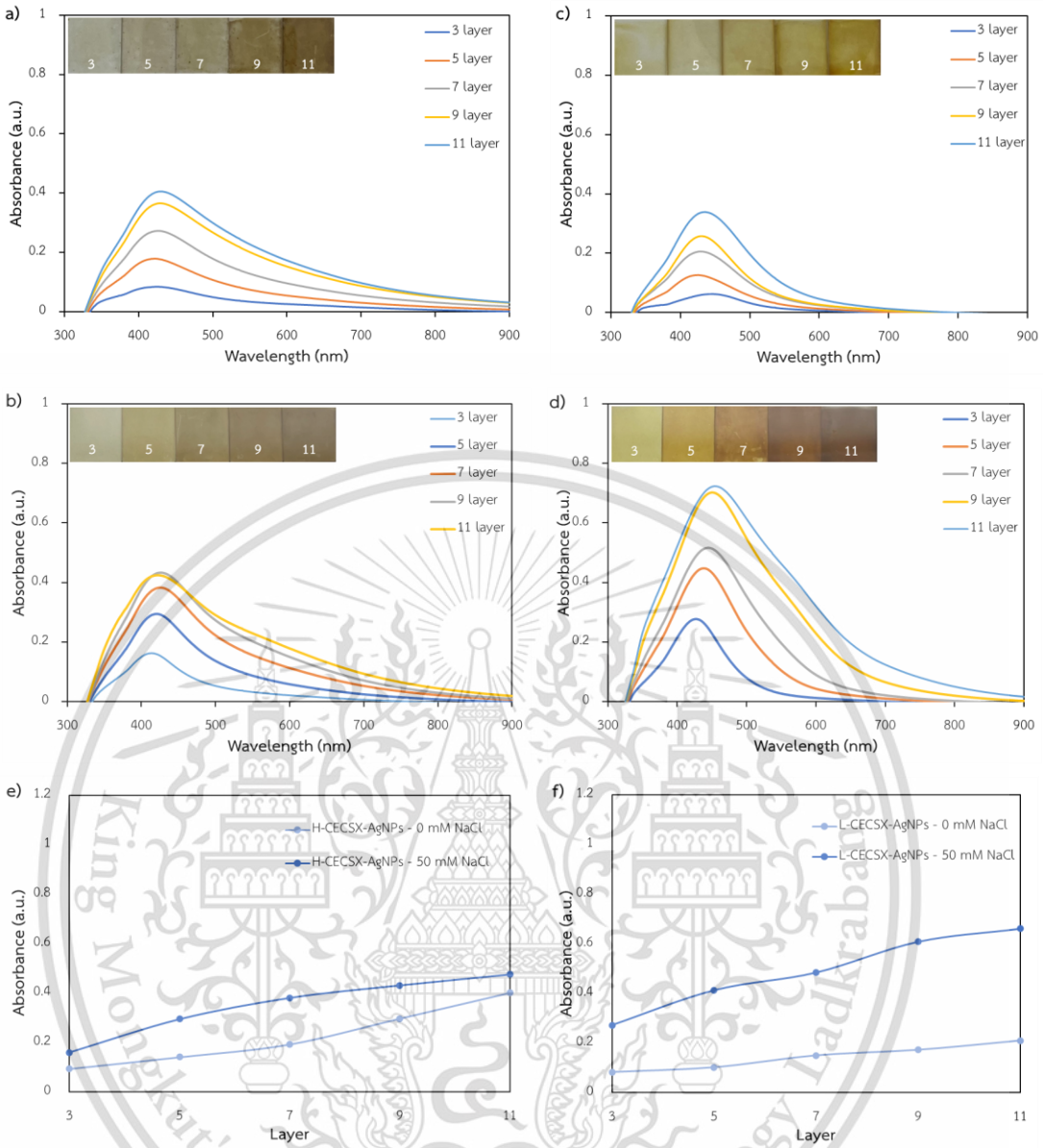

Figure 5.15 Absorption spectra of a) HCECSX-AgNPs with 0 mM NaCl b) HCECSX-AgNPs with 50 mM NaCl c) LCECSX-AgNPs with 0 mM NaCl d) LCECSX-AgNPs with 50 mM NaCl, as a function of layer. e) λ_{max} in each layer of a and b f) λ_{max} in each layer of c and d.

Number of layer	H-CECSX-AgNPs		RMS Roughness (nm)	L-CECSX-AgNPs		RMS Roughness (nm)
	Two dimensional (scanned at 1 μm)	Three dimensional (scanned at 5 μm)		Two dimensional (scanned at 1 μm)	Three dimensional (scanned at 5 μm)	
5	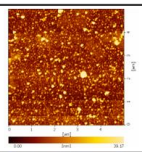	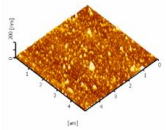	8.27	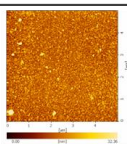	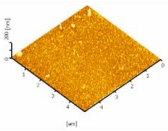	5.11
7	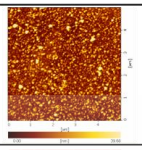	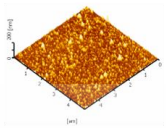	8.91	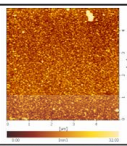	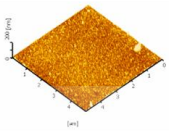	6.01
9	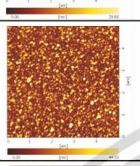	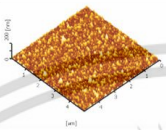	9.28	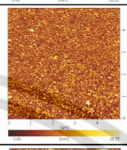	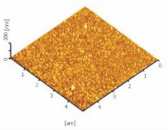	6.19
11	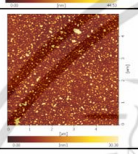	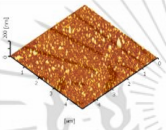	7.04	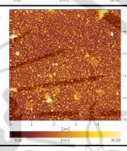	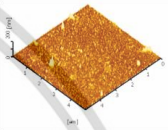	6.79

Figure 5.16 AFM images of HCECSX-AgNPs/PDADMAC and LCECSX AgNPs/PDADMAC multilayer films as the function of number of layers.

AFM images in Figure 5.16 clearly showed that HCECSX-AgNPs/PDADMAC and LCECSX-AgNPs/PDADMAC composites contain an interconnection network structure with isolated individual silver nanoparticles. During the LbL process, the electrostatic force between anionic AgNPs and cationic PDADMAC contributes to the formation of aggregates. These AgNPs counteract van der Waals interactions, leading to closely-packed aggregations and consequently resulting in a smoother surface of the LbL films. This aggregation causes the AgNPs to arrange themselves randomly and kinetically within the LbL films. Root-mean-square (RMS) roughness values, as determined from AFM images at 5, 7, 9, and 11 layers, were calculated to be 8.27, 8.91, 9.28, and 7.04 for HCECSX-AgNPs, and 5.11, 6.01, 6.19, and 6.79 for LCECSX-AgNPs, respectively. Increased roughness values result in the creation of a larger surface area with higher surface energy, potentially contributing to the development of hydrophobic surfaces. It can also make surfaces difficult to wet with polar liquids such as water (the contact angle of the neat suture materials and AgNPs-coated suture materials is shown in Figure 5.17). From the morphology obtained by the AFM technique, it was found that

nanolayer films could be formed, resulting in uniform coloration of the suture materials.

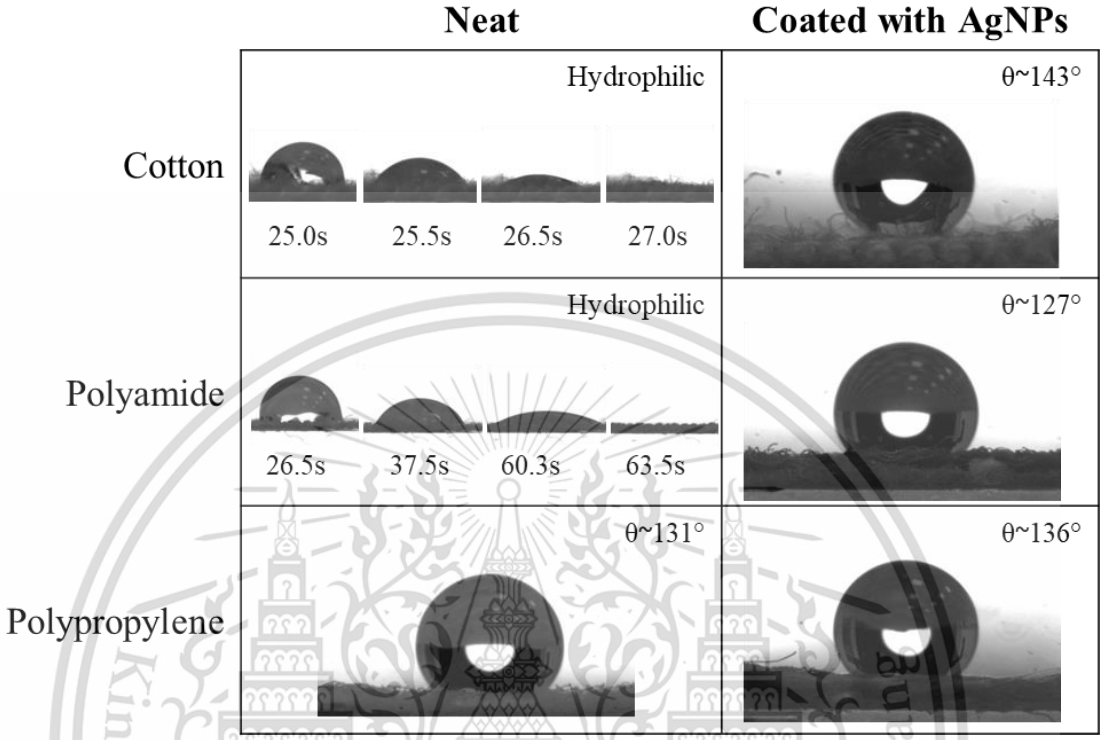

Figure 5.17 Contact angle of neat suture materials and AgNPs coat on suture materials.

The optimal conditions determined from the study of the layer-by-layer method on glass surface were selected for application to suture materials. HCECSX-AgNPs and LCECSX-AgNPs, as synthesized at pH 9, 50 mM NaCl and 9 layers, were selected to fabricate LbL films on three kinds of suture materials including cotton, polyamide, and polypropylene. Visual observation of HCECSX-AgNPs/PDADMAC and LCECSX-AgNPs/PDADMAC coating on cotton, polyamide, and polypropylene are shown in Figure 5.18. From visual observation with the naked eye, the color of the suture material surface has clearly changed from opaque white to yellowish brown demonstrating that silver nanoparticles are adhered to the suture material surface. To further verify the development of silver nanoparticles on the three types of suture materials, elemental data of the nanoparticles were investigated using FESEM/energy dispersive X-ray spectrometer (EDS). The EDS images of cotton, polyamide, and polypropylene covered with silver nanoparticles are also shown in Figure 5.19. The

EDS measurements revealed the presence of Ag element on all tested types of suture materials. These observations collectively support the conclusion that silver nanoparticles were effectively deposited onto various suture materials, including cotton, polyamide, and polypropylene, through a well-defined LbL process.

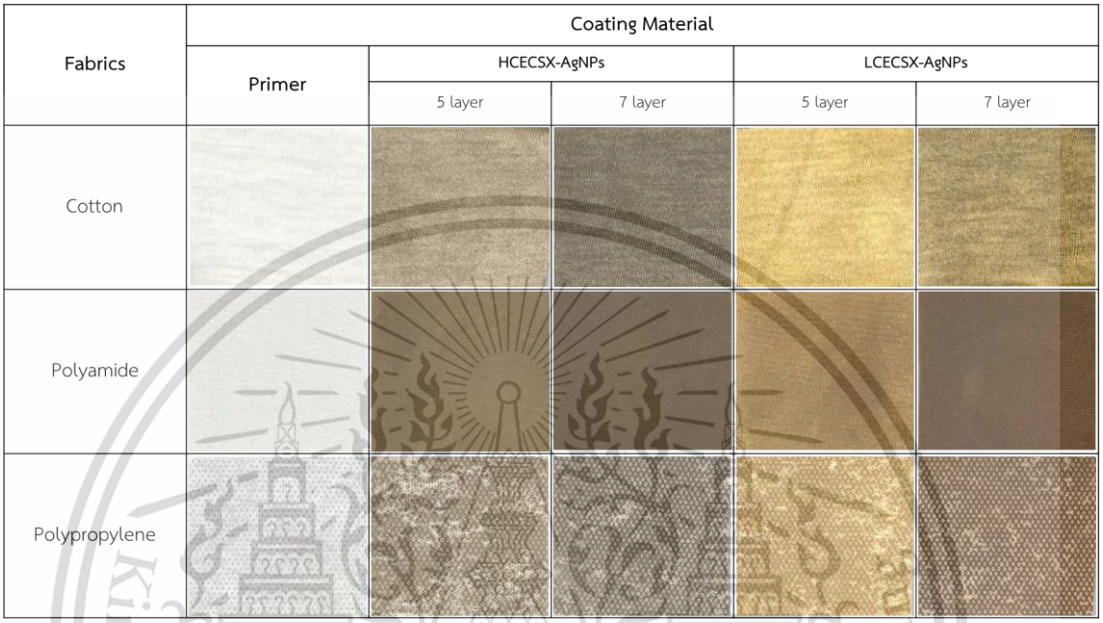

Figure 5.18 Visual observation of HCECSX-AgNPs/PDADMAC and LCECSX-AgNPs/PDADMAC coat on cotton, polyamide, and polypropylene by LbL method.

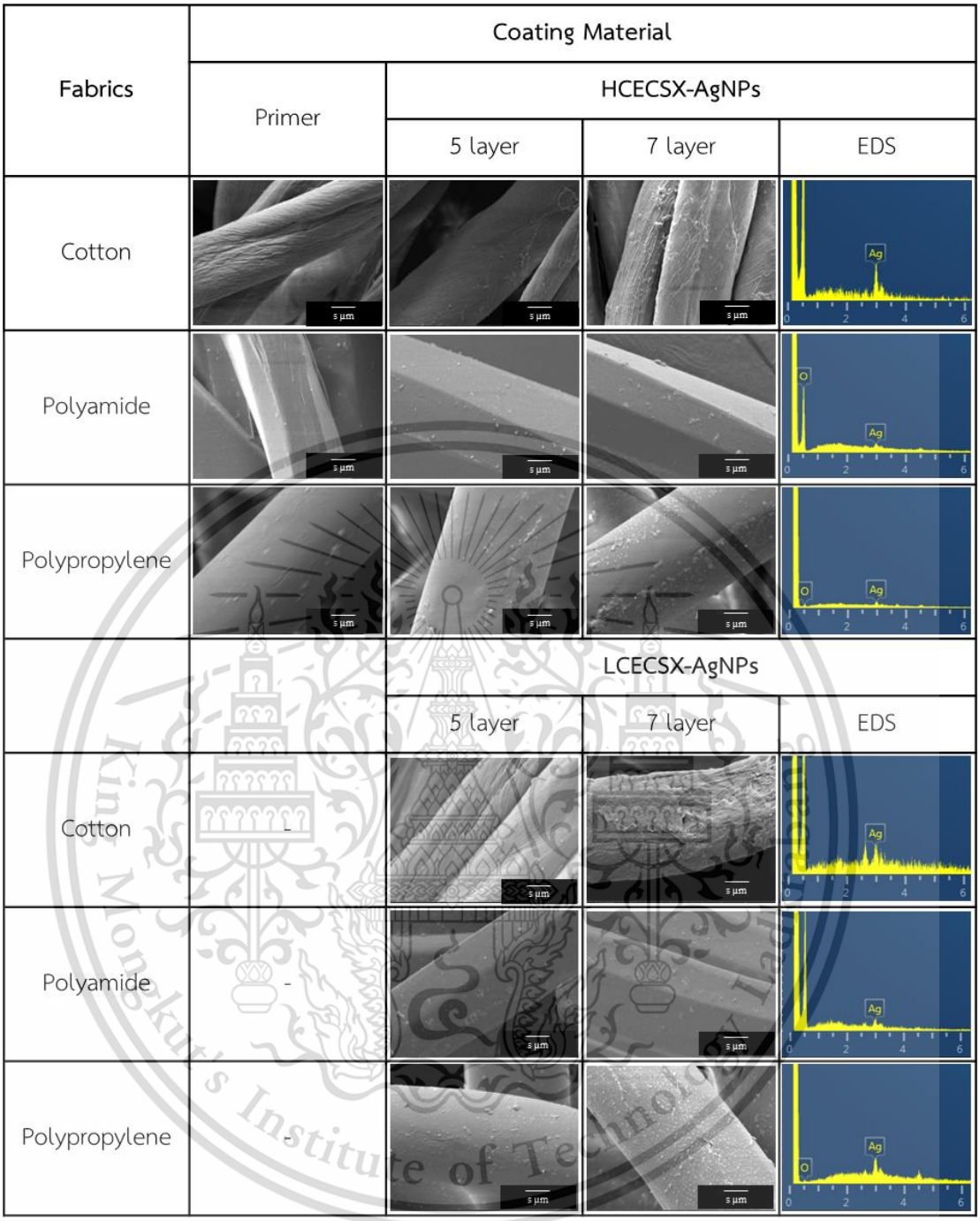

Figure 5.19 FESEM image and EDS of HCECSX-AgNPs/PDADMAC and LCECSX-AgNPs/PDADMAC coat on cotton, polyamide, and polypropylene by LbL method.

5.1.5 Antimicrobial assay

1) Minimum inhibitory concentration (MIC) and minimum bactericidal concentration (MBC) assay

The antibacterial action of HCS, LCS, HCSX, LCSX, HCECSX, LCECSX, HCECSX-AgNPs and LCECSX-AgNPs was determined as MIC and MBC values (see Table 5.6). The impact of incorporating PCMX into the chitosan structure was examined under a pH of 4. The findings showed that both high (HCSX) and low (LCSX) molecular weight CSX demonstrated enhanced activity compared to CS. The increased hydrophobicity of chitosan enables it to interact more effectively with the bacterial cell membrane's hydrophobic regions, facilitating membrane disruption and boosting antimicrobial activity [13, 20, 59]. This indicates that the addition of PCMX groups to the chitosan structure leads to enhanced antibacterial properties against both *S. aureus* and *A. baumannii*. However, for E. coli, the addition of PCMX groups to the chitosan structure does not affect antibacterial properties. This indicates that antimicrobial properties depend on the microbial strain and environmental conditions, further complicating the enhancement process.

Additionally, under neutral condition (pH 6.5-7), the results indicated that both high (HCECSX) and low (LCECSX) molecular weight exhibited antibacterial activity against the provided bacteria as reported in Table 5.6 as evidenced by their MIC and MBC values. In contrast, HCS, LCS and CECS (carboxyethylchitosan without grafting with PCMX) were ineffective against bacteria due to precipitation, rendering them ineffective. As evidenced in the literature, water-soluble chitosan derivatives are better dispersed in aqueous solutions, enabling a more even distribution of the antimicrobial agent [62, 66-68]. LCECSX demonstrated the most powerful antibacterial effect against both gram-positive and gram-negative strains under neutral conditions, while HCECSX show antibacterial properties against only against S. aureus. However, antibacterial properties at higher concentrations of HCECSX should be studied. Remarkably, at its isoelectric point in neutral pH, CECSX carries both negative (COO^-) and positive charges (NH_3^+). This dual charge feature allows it to inhibit a broad spectrum of bacteria, encompassing both gram-negative and gram-positive species.

Table 5.6 MIC and MBC values of HCS, LCS, HCSX, LCSX, HCECSX, LCECSX, HCECSX-AgNPs and LCECSX-AgNPs by microdilution method in neutral condition.

Synthesis materials	*E. coli* ATCC25922		*S. aureus* ATCC25923		*A. baumanii* ATCC19606	
	MIC (mg/L)	**MBC** (mg/L)	**MIC** (mg/L)	**MBC** (mg/L)	**MIC** (mg/L)	**MBC** (mg/L)
pH = 4.0						
HCS	200	200	200	400	50	50
LCS	200	200	200	200	100	100
HCSX	200	200	100	200	25	50
LCSX	200	200	100	200	50	100
pH = 6.5 – 7.0						
HCS[a]	ND	ND	ND	ND	ND	ND
LCS[a]	ND	ND	ND	ND	ND	ND
HCSX[a]	ND	ND	ND	ND	ND	ND
LCSX[a]	ND	ND	ND	ND	ND	ND
HCECS[b]	ND	ND	ND	ND	-	-
HCECSX	ND	ND	400	400	ND	ND
LCECSX	400	>400	200	400	400	>400
HCECSX-AgNPs	ND	ND	25	25	3.125	3.125
LCECSX-AgNPs	25	25	12.5	25	1.56	1.56

[a] = Precipitation stage

[b] = Antimicrobial resistant up to 0.5 %w/v

ND = Not detected

- = Not studied

Moreover, many research projects have focused on metallic nanoparticles, which have been employed as powerful antibacterial agents[65, 69]. Based on our proposed methodology, HCECSX-AgNPs and LCECSX-AgNPs possess the potential to demonstrate strong antibacterial activity. CECSX-AgNPs, carrying both negative and positive surface charges, can adhere to microbial layers, compromising their structural stability and function. In gram-positive bacteria, the negative charge of CECSX primarily engages with the thicker peptidoglycan layer. On the other hand, gram-negative bacteria have a thinner peptidoglycan layer and an outer membrane, predominantly

interact with the positive charge of CECSX on the AgNPs surface. This interaction disrupts the outer membrane, increasing its permeability, which subsequently leads to the bacteria's death [70]. Hence, CECSX may be used as an antibacterial agent in a range of biological applications by being coated on the surface of AgNPs.

Although HCECSX-AgNPs show effectiveness against E. coli, it is probably due to factors such as limited diffusion, weaker interactions with bacteria, slower release kinetics of silver nanoparticles, and bacterial resistance mechanisms. However, HECESX-AgNPs at higher concentrations or under more acidic conditions may exhibit better antibacterial activity because the positive charge from $-NH_3^+$ groups may interact with the bacterial cell wall, increasing its permeability. Therefore, optimizing the molecular weight and other properties of chitosan is crucial for enhancing its efficacy as an antimicrobial substance against bacteria.

2) Antimicrobial test for metallized suture materials (*In vitro* time-kill study)

***In vitro* time-kill study:** *In vitro* bacterial reduction of AgNPs/PDADMAC films on the three kinds of suture materials were evaluate against both gram-positive and gram-negative pathogens. The effectiveness of antibacterial coatings on suture materials significantly depends on the material substrate[71]. This indicates that the suture material properties, such as porosity, absorbency, and chemical composition, are crucial in determining the antibacterial coating's success. The embedding of AgNPs in suture materials operates through a mechanism observed in *in vitro* time-kill studies, where silver ions (Ag^+) are released into a solution [72]. In the presence of water or oxygen, AgNPs undergo oxidation, leading to electron loss from the silver atoms on the nanoparticles' surface, with the released electrons being accepted by oxygen or other environmental electron acceptors. The released silver ions then interact with bacterial cell membranes, causing structural damage and increased permeability. Inside the microbial cell, silver ions attach to proteins and DNA, disrupting vital cellular activities, ultimately leading to the cell's demise. The *in vitro* bacterial reduction of CECSX-AgNPs/PDADMAC films on various suture materials against *E. coli*, *S. aureus* and *A. baumannii* at 6 and 24 hr are shown in Table 5.7 for HCECSX-AgNPs and Table 5.8 for LCECSX-AgNPs. The bacterial reduction of CECSX-AgNPs coated on various suture materials against *E. coli*, *S. aureus* and *A. baumannii* at each time point over a 24-hour period is shown in Figure 5.20 for HCECSX-AgNPs and Figure 5.21 for LCECSX-AgNPs.

The variation in the antibacterial activity of silver nanoparticles across different suture materials can be ascribed to multiple factors and may not be directly comparable due to variations in thickness, fiber content, and density. For LCECSX-AgNPs, cotton's higher porosity and absorbency compared to polyamide and polypropylene play an important role. In addition, cotton and polyamide with hydrophilic properties, further facilitates the adherence and penetration of AgNPs [59], amplifying its antibacterial efficacy. Conversely, polypropylene [73] fabrics, generally being smoother and less fibrous, may offer limited surface area for the attachment of silver nanoparticles, potentially reducing their effectiveness in inhibiting bacterial activity.

However, in the case of high molecular weight chitosan. Overall, it was found that HCECSX harder to cover the surface area of all types of suture materials, lead to a reduction in its antimicrobial activity. But in the case of polypropylene, HCECSX-AgNPs could form a more continuous and uniform coating on the surface. This uniformity can provide a more effective barrier against bacterial adherence and colonization. Unlike the case of using low molecular weight chitosan, polypropylene exhibited the best antibacterial activities.

Table 5.7 Antibacterial property of HCECSX-AgNPs coated on various suture materials against *E. coli*, *S. aureus* and *A. baumannii.*

Sample	Contact time (hr)	Bacterial reduction					
		E. coli		*S. aureus*		*A. baumannii*	
		%	Log	%	Log	%	Log
HCECSX-AgNPs-cotton	6	46.00	0.27	31.97	0.17	69.60	0.52
	24	28.26	0.14	59.18	0.38	26.02	0.13
HCECSX-AgNPs-polyamide	6	49.00	0.29	59.56	0.39	78.90	0.68
	24	29.89	0.15	14.29	0.07	30.61	0.16
HCECSX-AgNPs-polypropylene	6	99.98	3.63	99.99	4.33	99.99	4.04
	24	29.89	0.15	43.54	0.250	34.69	0.19

Table 5.8 Antibacterial property of LCECSX-AgNPs coated on various suture materials against *E. coli*, *S. aureus* and *A. baumannii.*

Sample	Contact time (hr)	Bacterial reduction					
		E. coli		*S. aureus*		*A. baumannii*	
		%	Log	%	Log	%	Log
LCECSX-AgNPs-cotton	6	99.99	3.82	99.97	3.57	99.99	4.30
	24	90.22	1.00	98.36	1.78	93.47	1.18
LCECSX-AgNPs-polyamide	6	99.63	2.43	99.99	3.94	99.74	2.58
	24	92.12	1.10	99.01	2.00	89.23	0.96
LCECSX-AgNPs-polypropylene	6	94.00	1.22	83.07	0.77	94.00	1.22
	24	33.70	0.17	28.57	0.15	37.76	0.20

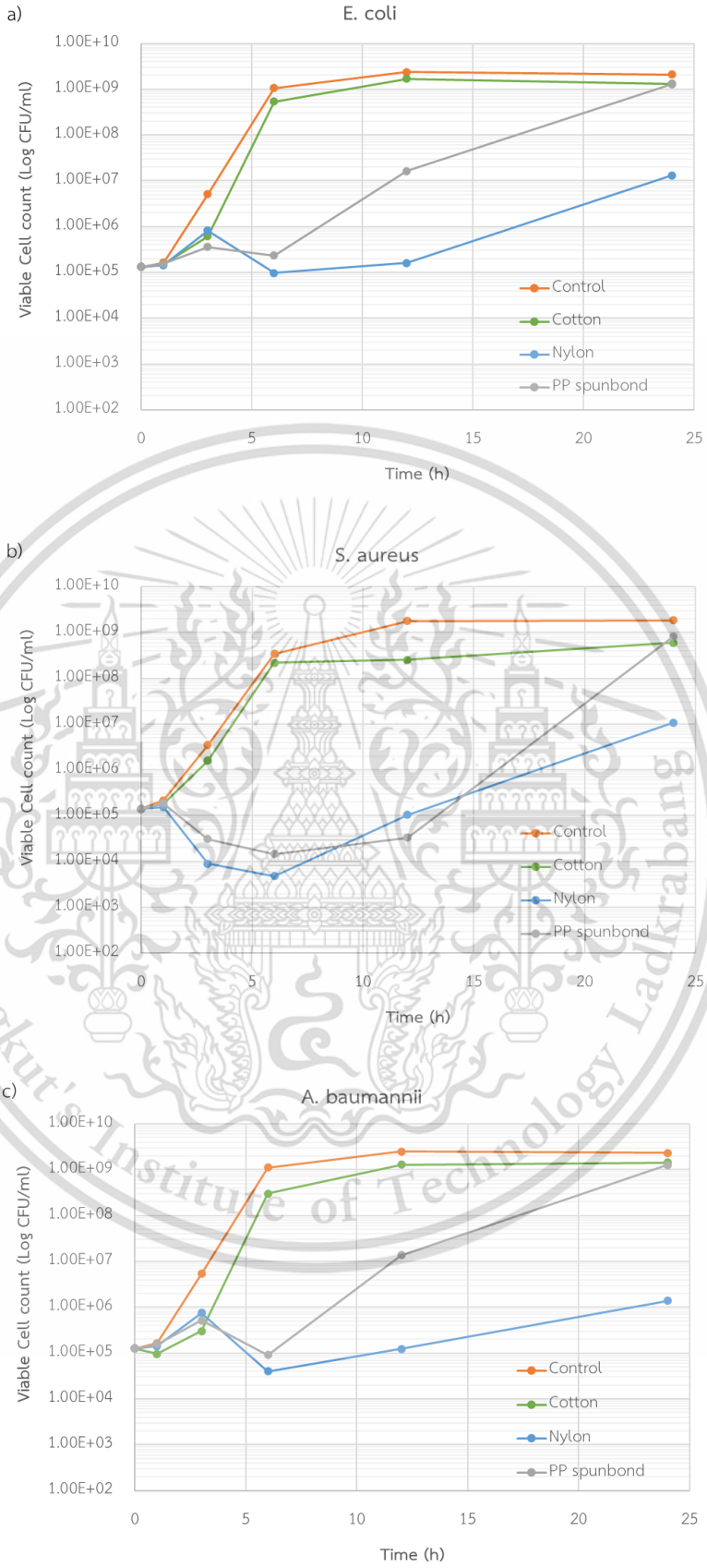

Figure 5.20 Antimicrobial bacterial reduction of HCECSX-AgNPs coat on cotton, polyamide and polypropylene against a) *E. coli*, b) *S. aureus* and c) *A. baumannii*.

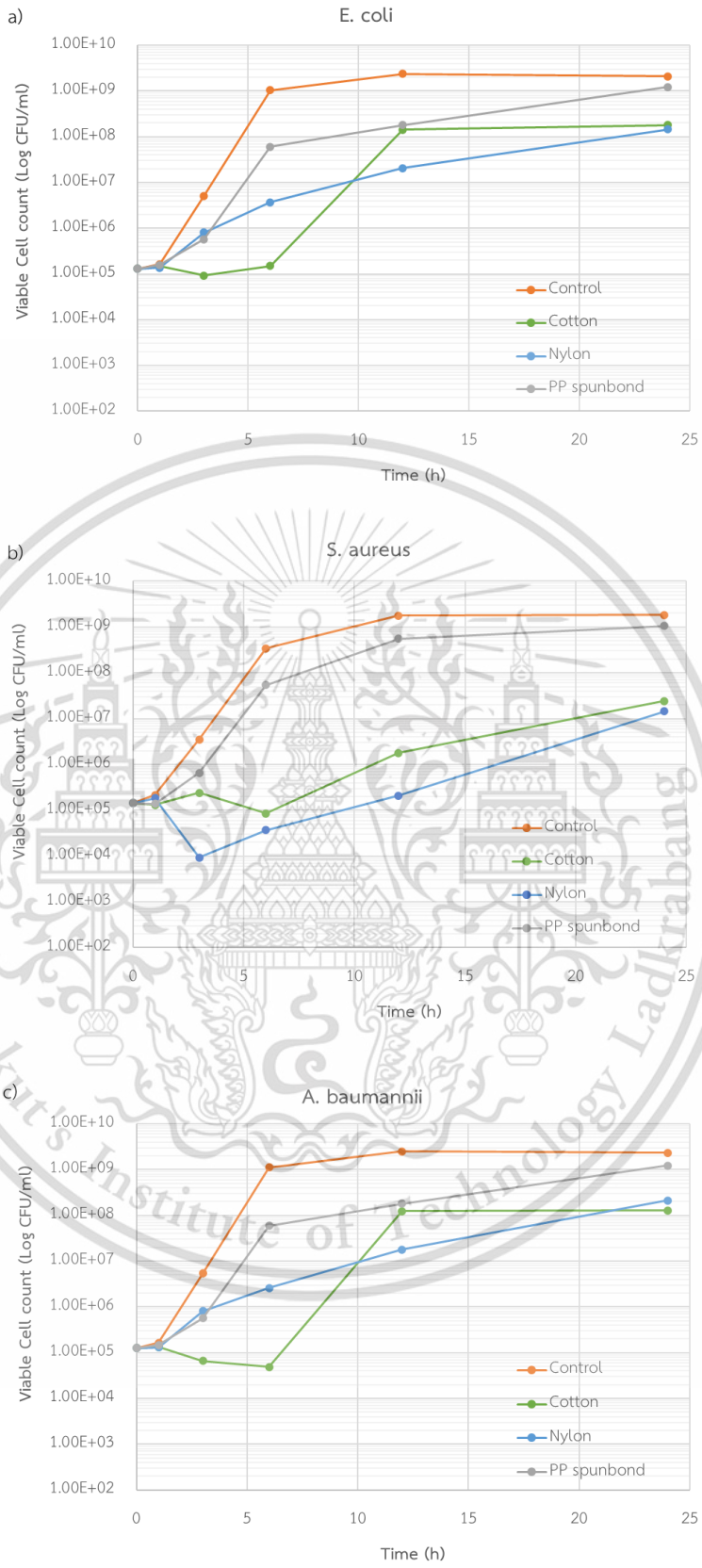

Figure 5.21 Antimicrobial bacterial reduction of LCECSX-AgNPs coat on cotton, polyamide and polypropylene against a) *E. coli*, b) *S. aureus* and c) *A. baumannii*.

5.2 Conclusions

This part of research explored the development of suture materials with enhancing antibacterial properties using water-soluble chitosan derivatives coating on AgNPs surfaces. Both high and low molecular weight chitosan served as synthetic precursors. HCECSX and LCECSX were synthesized by two step procedures. Initially, chloroxylenol was grafted onto the chitosan backbone through the Mannich reaction to obtain HCSX and LCSX, followed by further reacting acrylic acid with HCSX and LCSX through the Michael reaction to improve water solubility. Structural characterization of modified-CSs was achieved by ^{1}H NMR, UV-vis spectroscopy and elemental analysis.

AgNPs was synthesized using a simple chemical reduction method in the presence of $NaBH_4$, using HCECSX and LCECSX as stabilizing agents. Excellent HCECSX and LCECSX characteristics make AgNPs stabilize relatively efficiently through electrostatic repulsion forces. The particles of HCECSX-AgNPs and LCECSX-AgNPs were found to be well dispersed and mostly spherical in shape, with nanosizes smaller than 10.8 nm.

The HCECSX-AgNPs and LCECSX-AgNPs were applied as coating on suture materials include cotton, polyamide and polypropylene using layer-by-layer method. The primary electrostatic interaction between anionic CECSX-AgNPs and cationic PDADMAC led to the growth of nanolayer films on the suture materials. Notably, HCECSX-AgNPs, applied on polypropylene, demonstrated more than 99.98% reduction against all of the tested bacteria. Similarly, LCECSX-AgNPs, applied on cotton, demonstrated over 99.99% reduction, while LCECSX-AgNPs, applied on polyamide, exhibited over 99.63% reduction, both against all of the tested bacteria. This coating of CECSX on AgNP's surface potentially constitutes an important new alternative material for antimicrobial surgical sutures.

References

1. Li, Y., et al. 2023. "Advances, challenges, and prospects for surgical suture materials." *Publisher.* 168: 78-112.
2. Mehmet Orhan, D.K., Cem Gunessoglu. 2007. "Use of tricosan as antibacterial agent in textile." *Publisher.* 32: 114-118.
3. Chaganti, S., et al. 2023. "Comparison of bacterial colonization on absorbable non-coated suture with Triclosan- or Chlorhexidine-coated sutures: a randomized controlled study." *Publisher.* 27(18): 8371-8383.
4. Wang, D., et al. 2022. "The toxicity and antibacterial effects of Povidone-Iodine irrigation in fracture surgery." *Publisher.* 14(9): 2286-2297.
5. Su, C., et al. 2020. "Antibacterial Properties of Functionalized Gold Nanoparticles and Their Application in Oral Biology." *Publisher.* 2020: 5616379.
6. Martins, A.F., et al. 2014. "Antimicrobial activity of chitosan derivatives containing N-quaternized moieties in its backbone: a review." *Publisher.* 15(11): 20800-20832.
7. Khan, A. and K.A. Alamry. 2021. "Recent advances of emerging green chitosan-based biomaterials with potential biomedical applications: A review." *Publisher.* 506: 108368.
8. Chávez de Paz, L.E., et al. 2011. "Antimicrobial effect of chitosan nanoparticles on streptococcus mutans biofilms." *Publisher.* 77(11): 3892-5.
9. Shanmugam, A., K. Kathiresan, and L. Nayak. 2016. "Preparation, characterization and antibacterial activity of chitosan and phosphorylated chitosan from cuttlebone of Sepia kobiensis (Hoyle, 1885)." *Publisher.* 9: 25-30.
10. Saita, K., et al. 2020. "Dispersible chitosan particles showing bacteriostatic effect against Streptococcus mutans and their dental polishing effect." *Publisher.* 84(6): 1265-1273.
11. Goy, R.C., Britto, Douglas de and Assis, Odilio B. G. 2009. "A review of the antimicrobial activity of chitosan." *Publisher.* 19(3): 241-247.
12. Li, R., et al. 2013. "Antimicrobial N-halamine modified chitosan films." *Publisher.* 92(1): 534-539.
13. Wang, Y., et al. 2019. "The antioxidant and antimicrobial activities of different phenolic acids grafted onto chitosan." *Publisher.* 225: 115238.

14. Chalitangkoon, J. and P. Monvisade. 2019. "Dual pH/thermal-dependent coloring polymeric dye through Mannich reaction of chitosan: Synthesis and characterization." *Publisher.* 223: 115049.
15. Savetsakulanont, J., J. Chalitangkoon, and P. Monvisade. 2021. "Stimuli-responsive, self-healing, and injectable hydrogels with dual-crosslinked design from phenolphthalein-grafted N-carboxyethyl chitosan." *Publisher.* 306(10): 2100287.
16. Chalitangkoon, J., A. Ronte, and P. Monvisade. 2023. "Carboxyethylation of chitosan-based polymeric dyes for potential pH-sensing applications." *Publisher.* 149: 105001.
17. Cai, R., et al. 2019. "Antibacterial activity and mechanism of thymol against Alicyclobacillus acidoterrestris vegetative cells and spores." *Publisher.* 105.
18. Marchese, A., et al. 2016. "Antibacterial and antifungal activities of thymol: A brief review of the literature." *Publisher.* 210: 402-14.
19. Tan, J., et al. 2021. "Human exposure and health risk assessment of an increasingly used antibacterial alternative in personal care products: Chloroxylenol." *Publisher.* 786: 147524.
20. Chittratan, P., et al. 2022. "New chitosan-grafted thymol coated on gold nanoparticles for control of cariogenic bacteria in the oral cavity." *Publisher.* 7(30): 26582-26590.
21. Chittratan, P., et al. 2024. "Antimicrobial nanolayer films of chloroxylenol–carboxyethylchitosan–modified silver nanoparticles for enhanced surgical suture performance." *Publisher.* 693: 133957.
22. Rajput, N. 2015. "Methods of preparation of nanoparticles-a review." *Publisher.* 7(6): 1806.
23. Jamkhande, P.G., et al. 2019. "Metal nanoparticles synthesis: An overview on methods of preparation, advantages and disadvantages, and applications." *Publisher.* 53: 101174.
24. Rajoriya, P., et al. 2021. "Green Silver Nanoparticles: Recent Trends and Technological Developments." *Publisher.* 29.
25. Gu, X., et al. 2021. "Preparation and antibacterial properties of gold nanoparticles: a review." *Publisher.* 19(1): 167-187.
26. Tao, C. 2018. "Antimicrobial activity and toxicity of gold nanoparticles: research progress, challenges and prospects." *Publisher.* 67(6): 537-543.

27. Huang, H., Q. Yuan, and X. Yang. 2004. "Preparation and characterization of metal-chitosan nanocomposites." *Publisher.* 39(1-2): 31-7.
28. Emam, H.E. 2019. "Arabic Gum as Bio-Synthesizer for Ag–Au Bimetallic Nanocomposite Using Seed-Mediated Growth Technique and Its Biological Efficacy." *Publisher.* 27(1): 210-223.
29. Yuan, C.-G., et al. 2017. "Green synthesis of gold nanoparticles using Citrus maxima peel extract and their catalytic/antibacterial activities." *Publisher.* 11(5): 523-530.
30. Brust, M., et al. 1995. "Synthesis and reactions of functionalised gold nanoparticles." *Publisher.* 16): 1655-1656.
31. Amina, S.J. and B. Guo. 2020. "A Review on the Synthesis and Functionalization of Gold Nanoparticles as a Drug Delivery Vehicle." *Publisher.* 15: 9823-9857.
32. Sánchez-López, E., et al. 2020. "Metal-Based Nanoparticles as Antimicrobial Agents: An Overview." *Publisher.* 10(2).
33. Tian, E.-K., et al. 2021. "Gold Nanoparticle: Recent Progress on Its Antibacterial Applications and Mechanisms." *Publisher.* 2021: 2501345.
34. Abbaszadegan, A., et al. 2015. "The Effect of Charge at the Surface of Silver Nanoparticles on Antimicrobial Activity against Gram-Positive and Gram-Negative Bacteria: A Preliminary Study." *Publisher.* 2015: 720654.
35. Harish Prashanth, K.V. and R.N. Tharanathan. 2007. "Chitin/chitosan: modifications and their unlimited application potential—an overview." *Publisher.* 18(3): 117-131.
36. Sahariah, P. and M. Másson. 2017. "Antimicrobial Chitosan and Chitosan Derivatives: A Review of the Structure–Activity Relationship." *Publisher.* 18(11): 3846-3868.
37. Gafri, H.F.S., et al. 2019. "Mechanism of bacterial adhesion on ultrafiltration membrane modified by natural antimicrobial polymers (chitosan) and combination with activated carbon (PAC)." *Publisher.* 35(3): 421-443.
38. Zheng, L.-Y. and J.-F. Zhu. 2003. "Study on antimicrobial activity of chitosan with different molecular weights." *Publisher.* 54(4): 527-530.
39. Jarmila, V. and E. Vavríková. 2011. "Chitosan derivatives with antimicrobial, antitumour and antioxidant activities--a review." *Publisher.* 17(32): 3596-607.
40. Yi, H., et al. 2005. "Biofabrication with Chitosan." *Publisher.* 6(6): 2881-2894.
41. BYJU'S. 2023. "Mannich Reaction Mechanism." *Publisher.*).

42. Wikipedia. 2023. "Michael reaction." *Publisher.*).
43. Nagoor Meeran, M.F., et al. 2017. "Pharmacological Properties and Molecular Mechanisms of Thymol: Prospects for Its Therapeutic Potential and Pharmaceutical Development." *Publisher.* 8: 380.
44. Escobar, A., et al. 2020. "Thymol bioactivity: A review focusing on practical applications." *Publisher.* 13(12): 9243-9269.
45. Mathela, C.S., K.K. Singh, and V.K. Gupta. 2010. "Synthesis and in vitro antibacterial activity of thymol and carvacrol derivatives." *Publisher.* 67(4): 375-80.
46. Khan, S.T., et al. 2017. "Thymol and carvacrol induce autolysis, stress, growth inhibition and reduce the biofilm formation by Streptococcus mutans." *Publisher.* 7(1): 49.
47. Huang, H. and X. Yang. 2004. "Synthesis of Chitosan-Stabilized Gold Nanoparticles in the Absence/Presence of Tripolyphosphate." *Publisher.* 5(6): 2340-2346.
48. Laghrib, F., et al. 2019. "Chemical synthesis of nanosilver on chitosan and electroanalysis activity against the p-nitroaniline reduction." *Publisher.* 845: 111-118.
49. Detsri, E. and J. Popanyasak. 2015. "Fabrication of silver nanoparticles/polyaniline composite thin films using Layer-by-Layer self-assembly technique for ammonia sensing." *Publisher.* 467: 57-65.
50. Wu, Y., et al. 2018. "Fabrication of cotton fabrics with durable antibacterial activities finishing by Ag nanoparticles." *Publisher.* 89(5): 867-880.
51. Dubas, S.T., P. Kumlangdudsana, and P. Potiyaraj. 2006. "Layer-by-layer deposition of antimicrobial silver nanoparticles on textile fibers." *Publisher.* 289(1-3): 105-109.
52. Augustine, R. and K. Rajarathinam. 2012. "Synthesis and characterization of silver nanoparticles and its immobilization on alginate coated sutures for the prevention of surgical wound infections and the in vitro release studies." *Publisher.* 2: 205-212.
53. Gallegos, M.J., et al. 2022. "Aggregation and gelation in a tunable aqueous colloid–polymer bridging system." *Publisher.* 157(11).
54. Detsri, E., P. Seeharaj, and C. Sriwong. 2018. "A sensitive and selective colorimetric sensor for reduced glutathione detection based on silver triangular nanoplates conjugated with gallic acid." *Publisher.* 541: 36-42.

55. Mirda, E., et al. 2021. "Synthesis of chitosan-silver nanoparticle composite spheres and their antimicrobial activities." *Publisher.* 13(22): 3990.
56. Krishnamurthy, S., et al. 2014. "Yucca-derived synthesis of gold nanomaterial and their catalytic potential." *Publisher.* 9(1): 627.
57. Adlim, A., Bakar, M. A. 2008. "Preparation of chitosan-gold nanoparticles: part 1 (of 2). Effect of reducing technique." *Publisher.* 8(2): 184-188.
58. Adlim, A. 2006. "Preparation of Chitosan-Stabilized Silver (Chi-Ag) Nanoparticles Using Different Reducing Agents And Techniques." *Publisher.* 12(3): 185-191.
59. Huang, X., et al. 2016. "Green synthesis of silver nanoparticles with high antimicrobial activity and low cytotoxicity using catechol-conjugated chitosan." *Publisher.* 6(69): 64357-64363.
60. Cao, W., et al. 2020. "Preparation and characterization of catechol-grafted chitosan/gelatin/modified chitosan-AgNP blend films." *Publisher.* 247: 116643.
61. El-Tahlawy, K., M. Gaffar, and S. El-Rafie. 2006. "Novel method for preparation of β-cyclodextrin/grafted chitosan and it's application." *Publisher.* 63: 385-392.
62. Ibrahim, H.M., M. Mostafa, and N.G. Kandile. 2020. "Potential use of N-carboxyethylchitosan in biomedical applications: Preparation, characterization, biological properties." *Publisher.* 149: 664-671.
63. Kumar, A. and C.K. Dixit, *3 - Methods for characterization of nanoparticles*, in *Advances in nanomedicine for the delivery of therapeutic nucleic acids*, S. Nimesh, R. Chandra, and N. Gupta, Editors. 2017, Woodhead Publishing p. 43-58.
64. Verkhovskii, R., et al. 2019. "Physical properties and cytotoxicity of silver nanoparticles under different polymeric stabilizers." *Publisher.* 5(3): e01305.
65. Kalaivani, R., et al. 2018. "Synthesis of chitosan mediated silver nanoparticles (Ag NPs) for potential antimicrobial applications." *Publisher.* 2(1): 30-35.
66. Song, J., et al. 2020. "Preparation and characterization of arginine-modified chitosan/hydroxypropyl methylcellose antibacterial film." *Publisher.* 145: 750-758.
67. Awode, A.U., et al. 2020. "Fabrication of trichlorovinylsilane-modified-chitosan film with enhanced solubility and antibacterial activity." *Publisher.* 77(11): 5811-5824.
68. Qin, C., et al. 2006. "Water-solubility of chitosan and its antimicrobial activity." *Publisher.* 63(3): 367-374.

69. Prabhu, S. and E.K. Poulose. 2012. "Silver nanoparticles: mechanism of antimicrobial action, synthesis, medical applications, and toxicity effects." *Publisher.* 2(1): 32.
70. Shrivastava, S., et al. 2007. "Characterization of enhanced antibacterial effects of novel silver nanoparticles." *Publisher.* 18(22): 225103.
71. Gawish, S., et al. 2017. "Effect of Mordant on UV Protection and Antimicrobial Activity of Cotton, Wool, Silk and Nylon Fabrics Dyed with Some Natural Dyes." *Publisher.* 8.
72. Paternò, G.M., et al. 2021. "The Impact of Bacteria Exposure on the Plasmonic Response of Silver Nanostructured Surfaces." *Publisher.*).
73. Goli, K.K., et al. 2013. "Generation and properties of antibacterial coatings based on electrostatic attachment of silver nanoparticles to protein-coated polypropylene fibers." *Publisher.* 5(11): 5298-306.

Appendices

Appendix A

ACS OMEGA

http://pubs.acs.org/journal/acsodf

Article

New Chitosan-Grafted Thymol Coated on Gold Nanoparticles for Control of Cariogenic Bacteria in the Oral Cavity

Pakawat Chittratan, Jongjit Chalitangkoon, Karn Wongsariya, Arjnarong Mathaweesansurn, Ekarat Detsri,* and Pathavuth Monvisade*

Cite This: *ACS Omega* 2022, 7, 26582−26590

Read Online

ACCESS | Metrics & More | Article Recommendations | Supporting Information

ABSTRACT: Chitosan-grafted thymol (CST) coated on gold nanoparticles has been synthesized and characterized for the design of antimicrobial materials. CST was synthesized via adapting the Mannich reaction, and it acted as the capping agent for the synthesis of gold nanoparticles (AuNPs). The grafting of thymol onto the side chain of chitosan has provided a degree of substitution value ($\%DS_{NMR}$) of 10.0%, calculated by nuclear magnetic resonance spectroscopy. UV−visible spectrometry and elemental analysis were used to confirm the successful synthesis of CST through adapting the Mannich reaction. The appropriate concentration of CST for AuNP synthesis was found to be 0.020% w/v. A red-wine colloidal AuNP solution of 2.41−3.30 nM particle size exhibits a strong surface plasmon resonance at 502 nm, which shows negative charges at pH = 9 of −36.37 mV. This result evidenced that the AuNPs showed electrostatic repulsion and CST played a role as a capping agent to provide a good dispersion and stability state. CST coated on the AuNP surface was successfully utilized for the control of cariogenic bacteria in the oral cavity. The results obtained from this study show that the tuning of the capping agent used in the synthesis step strongly influences the latter antimicrobial activity of the nanoparticles against *Streptococcus mutans* ATCC 25175 and *Streptococcus sobrinus* ATCC 33402 activity, with an inhibition zone of 15.90 and 14.25 mm, respectively. The average minimum inhibitory concentration values against *S. mutans* ATCC 25175 and *S. sobrinus* ATCC 33402 were found to be 25 and 100 mg/L, respectively, whereas the minimum bactericidal concentration values were 100 and 200 mg/L, respectively.

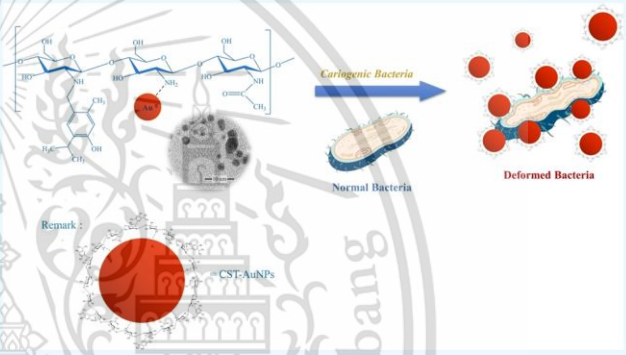

1. INTRODUCTION

Some oral infections including cavities, gingivitis, and periodontal disease are common from childhood to adulthood. Cavities are one of the most common oral infections caused by the bacteria *Streptococcus mutans* (*S. mutans*) and *Streptococcus sobrinus* (*S. sobrinus*), one of the principal cariogenic dental biofilm inhabitants that feeds on sugary, sticky foods, and beverages. *S. mutans* and *S. sobrinus* secrete glucosyltransferase on its cell wall, which allows the bacteria to produce polysaccharides from sucrose. These sticky polysaccharides are responsible for the bacteria's ability to aggregate with one another and adhere to tooth enamel.[1,2] To prevent the oral infections, daily brushing, flossing, and the use of appropriate mouthwash can significantly reduce the number of oral bacteria. Three different types of clinically used and most frequently studied antiplaque agents are sodium fluoride, ampicillin, and chlorhexidine.[1,3] However, some inherent issues of these antiplaque agents could not be avoided such as brown staining of the teeth and tongue, an unpleasant taste, enhanced supragingival calculus formation, and rarely painful desquamations of the oral mucosa all of which have led to the search for new formulations. Recently, gold nanoparticles (AuNPs) have been proposed as an antimicrobial agent to prevent the oral infections.[4−6] Most of the published work has mainly focused on the preparation of AuNPs conjugated with antibiotics, antimicrobial peptides, and ligands[4,7−12] in order to enhance the antibacterial abilities. AuNPs with smaller sizes have various benefits in antibiotic delivery such as regulating size and morphology, high-density surface ligands, and delivery without losing drugs which protects them from destruction. Darabpour et al.,[13] developed AuNPs using the chemical reduction technique and immobilized methylene blue onto AuNP surface. The particle sizes of AuNPs and zeta potential were found to be 85 nm and +32 mV, respectively. AuNPs conjugated with methylene blue demonstrated important photoinactivation across *Staphylococcus aureus* (*S. aureus*) biofilms. A reduction of greater than $5\log_{10}$ CFU was found.

Received: May 5, 2022
Accepted: July 11, 2022
Published: July 19, 2022

https://doi.org/10.1021/acsomega.2c02776
ACS Omega 2022, 7, 26582−26590

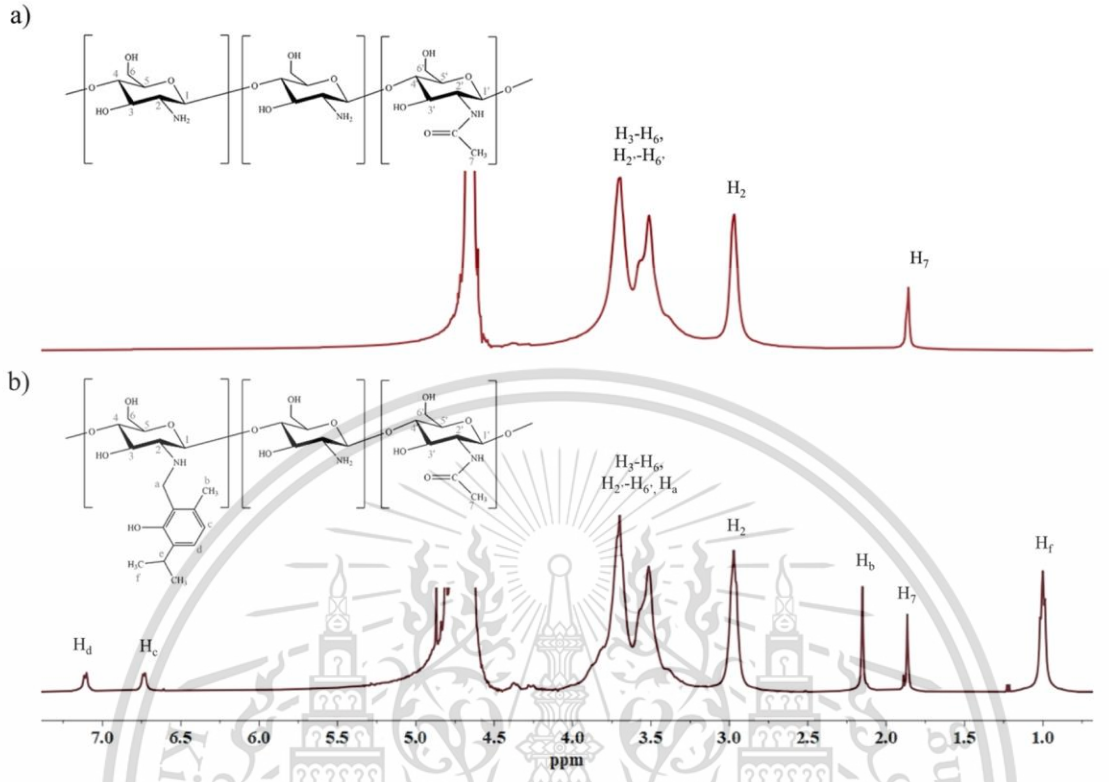

Figure 1. ^{1}H NMR spectra of (a) chitosan and (b) CST in CF_3COOH/D_2O.

Singh et al.,[14] explored the aqueous extract of *C. sativa* to synthesized AuNPs without any additional reducing and capping agents. The synthesized AuNPs were crystalline with an average diameter of 12−18 nm and showed bactericidal effects against *Pseudomonas aeruginosa* and *Escherichia coli*. Jiang and co-workers[15] fabricated AuNPs with 4,6-diamino-2-pyrimidinethiol in order to kill *Escherichia coli* ATCC11775 (*E. coli*) with multidrug-resistance Gram-negative bacteria efficiency to induce drug resistance to a much smaller degree than conventional antibiotics.

In this research, we have performed synthesis and characterization of chitosan-grafted thymol (CST) on the AuNP surface for antimicrobial activities in the oral cavity. It is well known that chitosan[16−19] and thymol[20−22] are most frequently used for antimicrobial and antiplaque agents. Chitosan has received much more attention as a chemical agent for mouthwashes that provides clinical benefits for plaque control. Chitosan is a linear polysaccharide composed of randomly distributed β-linked D−glucosamine and N−acetyl−D−glucosamine. The protonated amino groups upon chitosan chains interact with bacterium cell walls negatively charged, disrupting them and providing microbial death. Various methods have been tried to improve its antibacterial activity either by a physical or chemical strategy. Chemical modification requires introducing new groups onto the backbone by reacting with hydroxyl or with amino groups such as saccharization, alkylation, acylation, quaternization, and metallization.[23−27] These modifications bring chitosan a better antibacterial activity and expand its application as well with *S. aureus* and *E. coli*. However, there are a few research studies on the effects of chitosan derivatives against *S. mutans* and *S. sobrinus* especially for oral application. For this reason, the objective was to designed chitosan modified with thymol via adapting the Mannich reaction to enhance the antimicrobial properties and use them as a capping agent for AuNP synthesis. Many characterization techniques, such as UV−visible spectrometry, X-ray diffraction (XRD), transmission electron microscopy (TEM), zeta potential analyzer elemental analysis (EA), and ^{1}H NMR, were used to confirm the successful synthesis of CST and AuNPs. Finally, CST coated on gold nanoparticles was applied as the antimicrobial agent to control the growth of bacteria in oral application.

2. EXPERIMENTAL SECTION

2.1. Chemicals. High-molecular-weight chitosan (320,000 Da) was purchased from Eland Co., Ltd. (Bangkok, Thailand). The percentage of degree of deacetylation (%DD) of chitosan (CS) is 85%. Formaldehyde (HCHO: 37% w/w), hydrochloric acid (HCl), and sodium hydroxide (NaOH) were purchased form Carlo Erba (Italy). Thymol ($C_{10}H_{14}O$), gold(III) chloride trihydrate ($HAuCl_4{\cdot}3H_2O$), and sodium borohydride ($NaBH_4$) were acquired from Sigma-Aldrich Germany. All chemicals are of analytical reagent grade (AR grade) and used without further purification. Ultrapure deionized water (Milli−Q ultrapure water) with a resistivity of 18.2 MΩ cm at 25 °C was used for preparing all chemical solutions.

2.2. Preparation of CST. CST was synthesized by a well-described method through the Mannich reaction adapted from our previous research.[28] The preparation steps can be summarized as follows: chitosan (1 g) was dissolved in 100 mL of 1% w/v acetic acid solution under vigorous stirring. Then, 0.7932 g of thymol dissolved in 10 mL of dimethylformamide and 0.2147 g of formaldehyde were slowly dropped into chitosan solution and stirred at 60 °C for 24 h. After that, 0.5 M of fresh NaOH solution was added into the solution mixture for precipitation. The mixture was then

https://doi.org/10.1021/acsomega.2c02776
ACS Omega 2022, 7, 26582−26590

Scheme 1. Schematic Illustration of the Synthesis of (a) CST and (b) CST Coated on the Gold Nanoparticle Surface

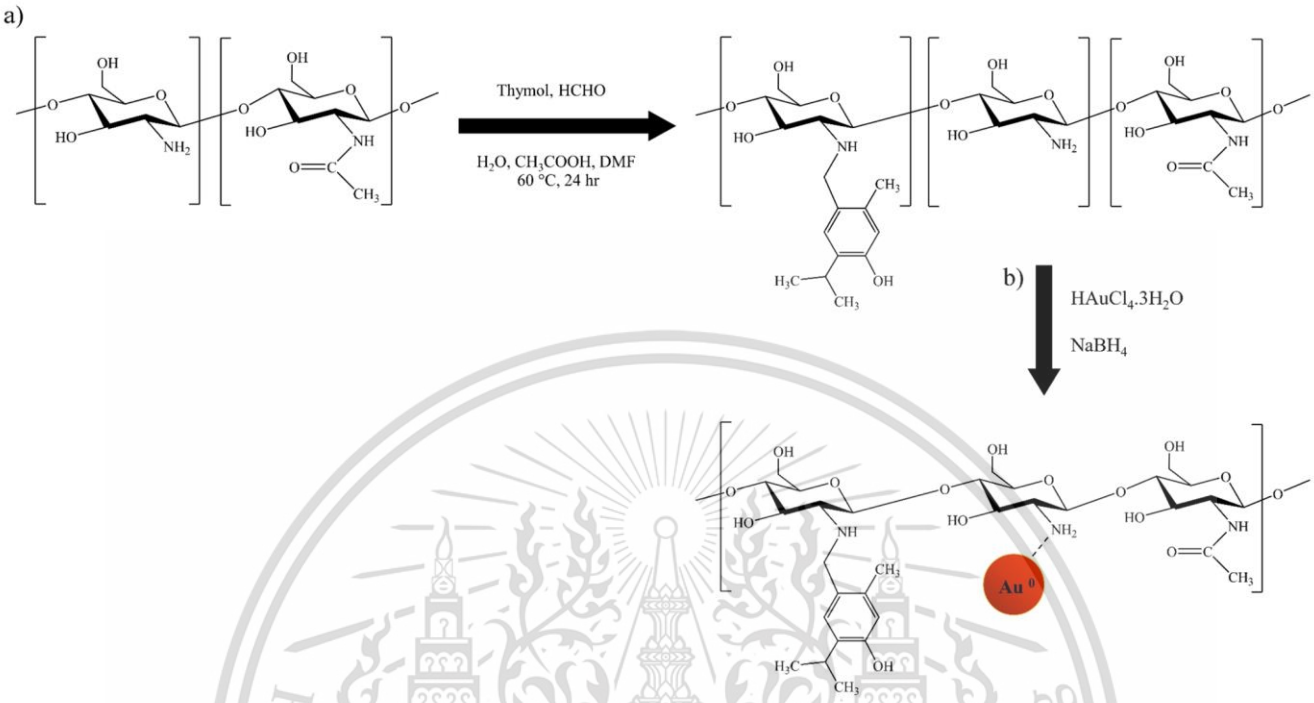

filtered using filter paper and washed with ethanol and distilled water. The precipitate was dried at 60 °C to obtain a CST product.

The structural characterization of CST was performed by ^{1}H NMR, EA, and UV−vis spectroscopy techniques. The UV−vis spectra were scanned from 200−800 nm using a BlueStar B spectrophotometer (Lab Tech, China). The ^{1}H NMR spectra were determined using a JNM-ECZ-500R/S1 spectrometer (JEOL, Japan) at 500 MHz. D_2O/CF_3COOH was used to dissolve CST. The degree of substitution (%DS) determination of CST was calculated using ^{1}H NMR and EA followed eqs 1 and 2, respectively.

$$\%DS_{NMR} = \frac{\left(\frac{H_f}{6}\right)}{H_2} \times 100 \quad (1)$$

where %DS is the degree of substitution percentage, and H_f and H_2 are the integral areas of protons indicated in Figure 1.

$$\%DS_{EA} = \left(\frac{\left(\frac{C}{N}\right)_D - \left(\frac{C}{N}\right)_O}{n}\right) \times \frac{14}{12} \times 100 \quad (2)$$

where $\%DS_{EA}$ is the degree of substitution percentage obtained from EA data; $(C/N)_D$ is the carbon to nitrogen mass ratios of the chitosan derivative; and $(C/N)_O$ is the carbon to nitrogen mass ratios of the original chitosan.

2.3. Synthesis of CST Coated on Gold Nanoparticles. AuNPs were synthesized by chemical reduction using CST and $NaBH_4$ as the capping and reducing agents, respectively. Briefly, 10 mL of 10 mM $HAuCl_4{\cdot}3H_20$ was mixed with 0.1% w/v of CST. Then, an aliquot of 0.5 mL $NaBH_4$ (50 mmol/L) was rapidly added to a solution mixture under stirring for 10 min at 25 °C. The color of the solution was changed rapidly from light yellow to red-wine immediately. The stirring process was continued for 30 min to complete reduction and homogenization. Finally, the dark red solution of CST−AuNPs with pH 9.0 was obtained. The synthesized solution was purified with a dialysis tube and stored at 4 °C in a refrigerator for 24 h before further use.

To estimate the concentration of CST−AuNPs, the stock colloidal CST−AuNP solution was diluted three times using ultrapure water, and the absorbance intensity was measured at λ_{max} = 502 nm using UV−vis spectrometry. The concentration of CST−AuNPs was 3.637 nanomolar [nM] calculated using Beer's law according to the extinction coefficient on particle diameter ($\varepsilon = 7.19 \times 10^9$ M^{-1} cm^{-1} for the particle size of CST−AuNPs = 2.41 nm). For references, the extinction coefficient for CST−AuNPs is calculated using the following equation of $\ln \varepsilon = 1.4418 \ln D + 18.955$ and D is the diameter in nanometer (nm).[29]

2.4. Characterization. Ultraviolet−visible (UV−vis) absorption spectra of AuNPs were measured using a double-beam UV1800 (Shimadzu, China) spectrophotometer with a 1 cm path length quartz cuvette. All the measurements were repeated at least three times. The morphology, particle size, and distribution of AuNPs were photographed using a transmission electron microscope (TEM, JEM−2010 model, JEOL Co., Ltd. Japan) at an accelerating voltage of 200 kV. Zeta potential of NPs was measured using a Nano ZS− Malvern instrument, England with a 633 nm helium−neon laser. An X-ray diffractometer was used to analyze the crystallographic structure of the NPs. The XRD patterns were recorded over a 2θ (Smartlab SE diffractometer, RIGAKU, Japan). pH of the synthesized solution was adjusted using a benchtop pH meter (Mettler)

2.5. Antimicrobial Assay. The antimicrobial activity of chitosan, CST, and CST−AuNPs against *S. mutans* ATCC 25175 and *S. sobrinus* ATCC 33402 was evaluated by the agar well diffusion method and macrodilution method.

2.5.1. Agar Well Diffusion Assay. The 10^4 CFU/mL of inoculum was swapped onto Mueller−Hinton agar plates;

https://doi.org/10.1021/acsomega.2c02776
ACS Omega 2022, 7, 26582−26590

afterward, a well with a size of 5 mm was cut in the agar plate. Each well was aseptically filled up with 20 μL of (a) Control: prepared by mixing 1% v/v CH_3COOH with 4% w/v of Tween80, (b) Chitosan: prepared by dissolving 1% w/v of chitosan pH 4.5 in control solution), (c) CST: prepared by dissolving 1% w/v of CST pH 4.5 in control solution, and (d) CST−AuNPs: prepared by dissolving pH 9.0 of AuNPs coated with $CST_{0.020\%w/v}$ mixed with 4% w/v of Tween80. The plates were incubated at 37 °C for 24 h. 4% of Tween 80 was introduced as controls. The diameter of the inhibition zone around each well was measured and expressed in the mean diameter of the inhibition zone in millimeters (n = 3).

2.5.2. Minimum Inhibitory Concentration (MIC) and Minimum Bactericidal Concentration (MBC) Assay. MIC and MBC values were determined by broth macrodilution assay. Colonies of the same morphological type were selected and transferred to 0.85% w/v of sterile saline. To achieve the turbidity of a 0.5 McFarland standard, inoculum was diluted with Brain Heart Infusion broth 1:200 (approximately 5×10^5 CFU/mL). Each stock as-synthesized chitosan, CST, and CST−AuNPs were dissolved in 4% w/v of tween 80 with the final concentration ranging from 0.40 to 200 mg/L. Then, 50 μL of adjusted *S. mutans* ATCC 25175 and *S. sobrinus* ATCC 33402 were added into each tube. After that, the samples were incubated overnight at 37 °C for 24 h. MICs and MBCs were evaluated by no visible growth of bacteria and lowest concentration of an antimicrobial agent that kills 99.9% of the initial bacterial population method, respectively.

3. RESULTS AND DISCUSSION

3.1. Synthesis and Characterization of CST. To graft thymol onto the chitosan side chain, the Mannich reaction was used in the experimental step. An amino group of chitosan can react with formaldehyde to form an electrophile imine compound (−N═CH_2) and then react with attached by introducing at the para position of the phenol group to yield secondary amines or benzylamine. Thus, chitosan could be grafted with thymol through the carbene bridge. The synthesis pathway of CST is shown in Scheme 1a. The product was structurally characterized by ^{1}H NMR as shown in Figure 1. The chitosan spectra showed characteristic peaks at 1.86 and 2.97 ppm assigned to H_7 and H_2, respectively. The peaks at 3.25−4.02 ppm were assigned to H_3−H_6 and $H_{2'}$−$H_{6'}$. In terms of CST, it showed a characteristic peak of chitosan and found new peaks at 1.00 and 2.15 ppm which correspond to protons of the methyl group of thymol (H_f and H_b), respectively. Moreover, the doublet peaks around 6.74 and 7.10 ppm of aromatic protons of thymol (H_c and H_d) were also observed, respectively. Thus, it was indicated that thymol was successfully grafted onto chitosan through the Mannich reaction. The degree of substitution of CST was 10.0%, as calculated from the ^{1}H NMR data. For EA results, the C/N ratio of CST was higher than that of chitosan, indicating that additional carbon atoms existed after the reaction. The data also revealed that the degree of substitution value ($\%DS_{EA}$) was 9.2% (Table S1, Supporting Information).

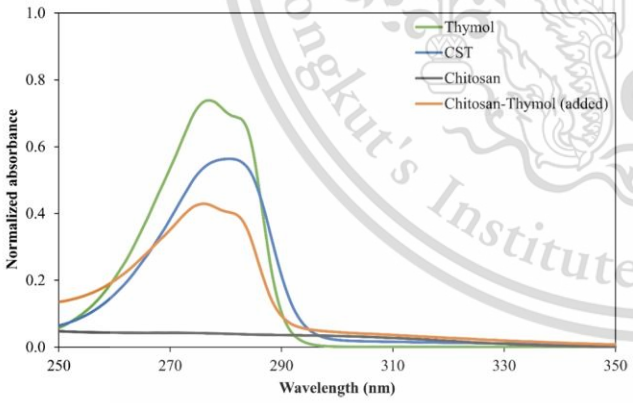

Figure 2. UV−vis spectra of CST, chitosan, thymol, and chitosan mixed with 0.05% w/v thymol in 0.1 M HCl solution.

The UV−vis spectra of chitosan, CST, thymol, and chitosan mixed thymol are displayed in Figure 2. It was found that the chitosan spectrum did not show any peak ranging from 250 to 350 nm while CST spectra exhibited broad peaks at 281 nm corresponding to the aromatic structure of thymol. Comparison with the spectra of chitosan mixed thymol which showed absorption peaks at 276 and 282 nm, corresponding to the characteristic peak of thymol, the CST spectra showed a red shift phenomenon implying chemical modification on thymol molecules.[30] The results suggested that thymol was grafted onto the chitosan backbone.

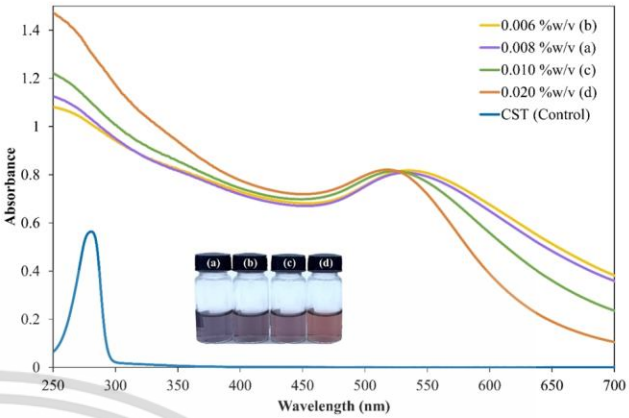

Figure 3. Visual observation and absorption spectra of CST coated on gold nanoparticles with various concentrations of CST (a) 0.006%w/v, (b) 0.008%w/v, (c) 0.010%w/v, and (d) 0.020%w/v and CST as the control on the synthesis step.

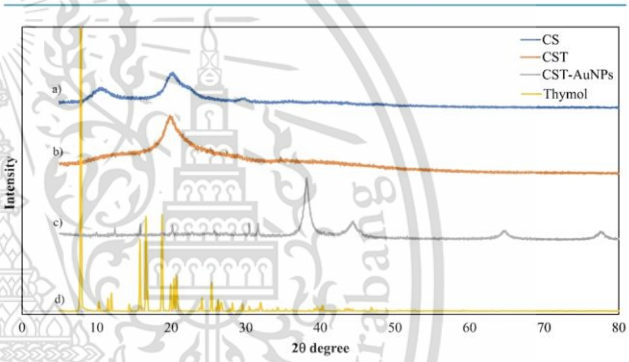

Figure 4. XRD pattern of (a) chitosan, (b) CST, (c) CST coated on gold nanoparticles, and (d) thymol.

3.2. Synthesis and Characterization of CST Coated on the Gold Nanoparticle Surface. Our main motivation in this work was to produce AuNPs using CST as the capping agent. The capping agent is needed to prevent the growth of the nanoparticles (NPs). This process occurs during the

https://doi.org/10.1021/acsomega.2c02776
ACS Omega 2022, 7, 26582−26590

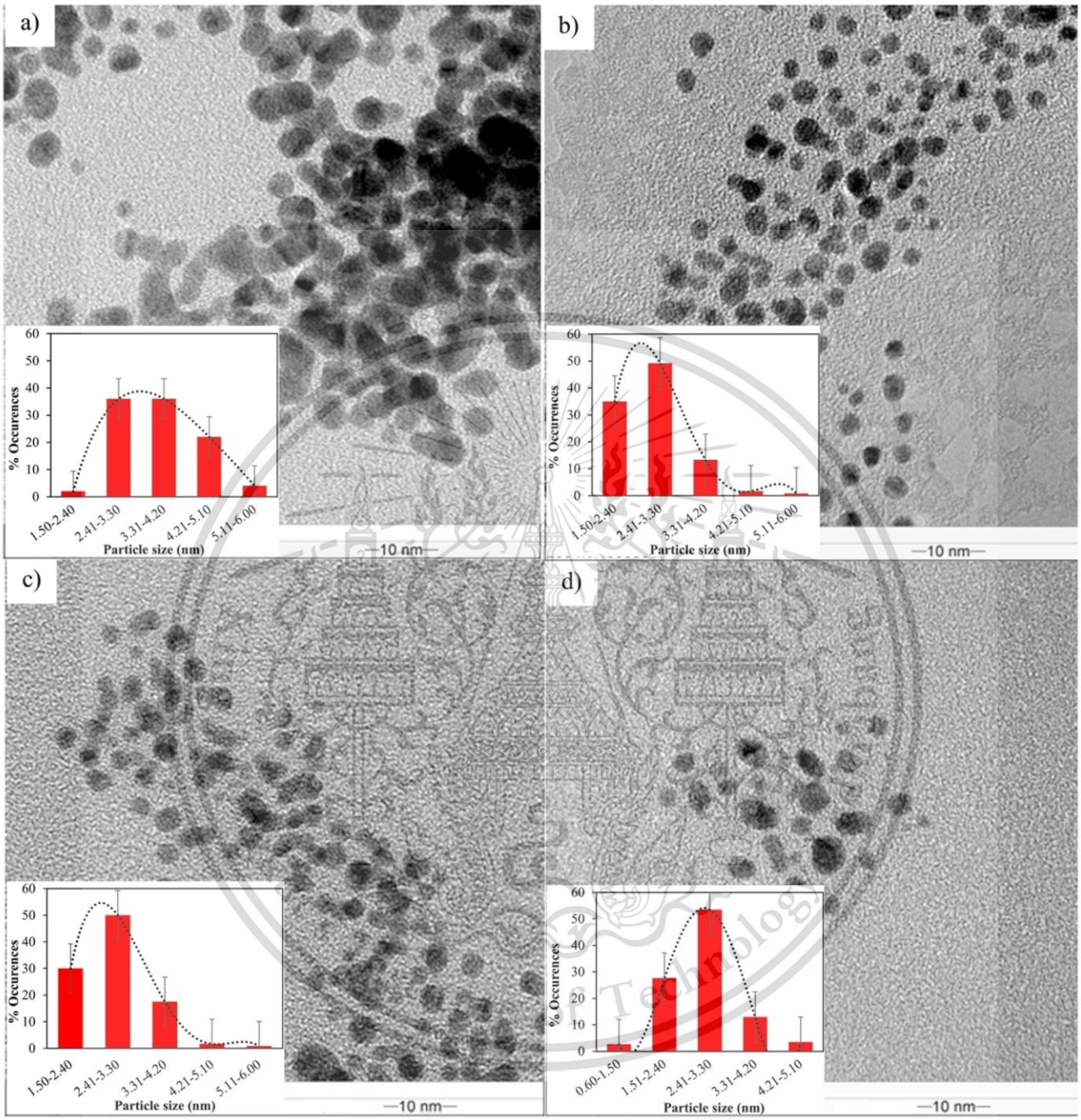

Figure 5. TEM images and size distribution of CST coated on gold nanoparticles at a CST concentration of (a) 0.006% w/v, (b) 0.008% w/v, (c) 0.01% w/v, and (d) 0.02% w/v.

formation of the NPs when a capping agent adsorbs at the NP surface. In the present case, CST-modified AuNPs were synthesized according to a very simple and rapid chemical method as shown in Scheme 1b. The synthesis of AuNPs with CST can be achieved through chemical reduction with $NaBH_4$ as a reducing agent. Au^{3+} ions were reduced to Au^0 in the presence of CST as a capping agent obtaining stable AuNPs. A zeta potential analyzer has been used to clarify the stability of NPs. Zeta potential analysis (Figure S1, Supporting Information) demonstrated that the as-synthesized CST−AuNPs had negative potential (pH = 9), which can prevent nanoparticle−nanoparticle aggregation and be dispersed from each other in the aqueous phase.

To study the influence of CST concentration for AuNP synthesis, four different CST concentrations of 0.006, 0.008, 0.010, and 0.020% w/v were used for investigation. The visual observation and absorption characteristics of various concentrations of AuNPs stabilized with CST are shown in Figure 3. The AuNPs formed in the solution, through nucleation growth, displayed a characteristic of vivid blue to dark red color when the concentration of CST increased from 0.006−0.020% w/v. Indeed, when the concentration of CST increased from 0.006−0.020%, the absorption spectra shifted to blue-

https://doi.org/10.1021/acsomega.2c02776
ACS Omega 2022, 7, 26582−26590

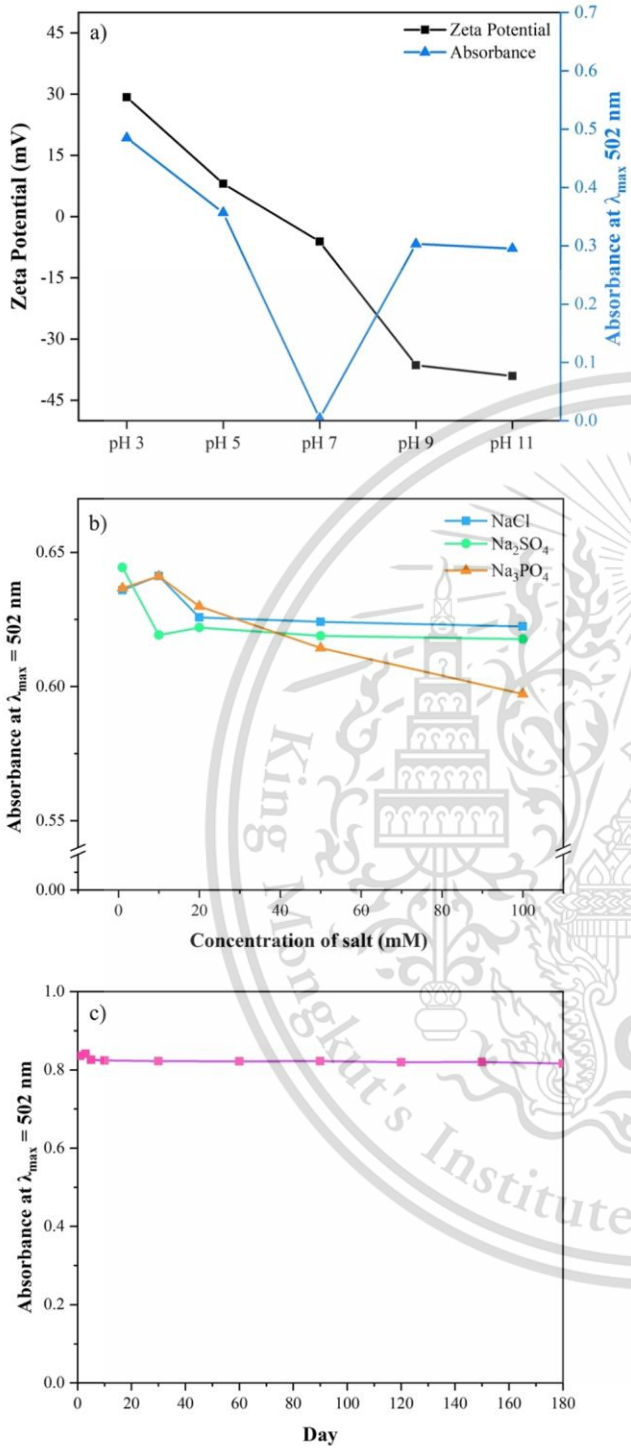

Figure 6. Effect of (a) pH, (b) ionic strength, and (c) time on the stability of CST coated on gold nanoparticles.

shift due to the surface plasmon resonance phenomenon. The extinction spectrum of $CST_{0.020\%w/v}$ − AuNPs exhibited a single peak around 502 nm with the zeta potential at pH 9 of −33.8 mV.

To further confirm the successful formation of CST−AuNPs, XRD measurements were carried out in order to identify the crystallinity structure of the NPs, and corresponding XRD patterns are shown in Figure 4. CST−AuNPs

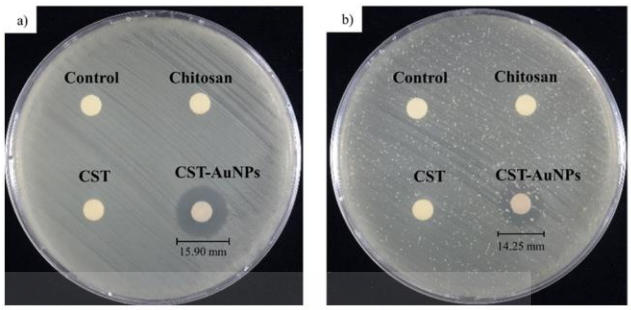

Figure 7. Bacterial inhibition photographs of chitosan, CST, and CST coated on gold nanoparticles and control against using the agar well diffusion method (a) *S. mutans* and (b) *S. sobrinus*.

Table 1. MICs and MBCs of Chitosan, CST, and CST Coated on Gold Nanoparticles against *S. mutans* and *S. sobrinus*

synthesis materials	*S.mutans* ATCC 25175		*S. sobrinus* ATCC 33402	
	MIC (mg/L)	MBC (mg/L)	MIC (mg/L)	MBC (mg/L)
chitosan	100	100	100	100
CST	50	50	50	50
CST−AuNPs	25	100	100	200

exhibited four distinct peaks corresponding to standard Bragg reflections. The 2θ (Bragg reflections) values are 38.1(111), 44.3(200), 64.5(220), and 77.7(311) of the face centered cubic (FCC) lattice. The potent diffraction at 38.1 peak shows that the preferred growth orientation of zero valent gold was fixed in the (111) direction.[31] These experimental observations clearly demonstrate that AuNP capping with CST was found to be in agreement with the literature report.[8]

To examine the size and particle morphology, TEM analysis was performed. As shown in Figure 5, the effect of CST concentration onto the preparation of AuNPs has been studied. The concentration of $HAuCl_4{\cdot}3H_2O$ was kept constant at 1 mM in the synthesis step, and different batches were prepared with CST concentration increasing from 0.006 to 0.02% w/v. The TEM images show that AuNPs are nanosize in shape and well dispersed in aqueous media. The particle size of AuNP capping with different CST concentrations from 0.006 to 0.02% w/v was found in the range of 1.50−5.10 nm. The particle size of CST−AuNPs was found to be not statistically significant different. The appropriate concentration of CST for AuNP synthesis was found at 0.020%w/v showing a particle size of 2.41−3.30 nM. This observation suggested that CST played a role as a stabilizing agent to provide a good dispersion state of the AuNPs.

3.3. Stability of CST Coated on the Gold Nanoparticle Surface. The stability of CST−AuNPs under various conditions was also investigated. The results are shown in Figure 6. It is well known that chitosan was soluble under acid conditions due to the protonation of amino groups on the chitosan backbone. The derivatives of CST could be dissolved under acid conditions at about pH < 5. The pH values of the CST would affect the interaction of AuNPs conjugated with CST. Therefore, it was necessary to investigate the effect of pH values on the stability of CST−AuNPs. Figure 6a shows the UV−visible absorbance at λ_{max} of 502 nm of CST−AuNPs when varying pH from 3−11. CST−AuNPs could be dispersed

https://doi.org/10.1021/acsomega.2c02776
ACS Omega 2022, 7, 26582−26590

Table 2. Comparison of Antibacterial Properties of Metallic Nanoparticles

method	microorganism	inhibition zone (mm)	MIC (mg/L)	MBC (mg/L)	ref.
peptide (extracted from Vespa orientalis waspvenom) −AuNPs	*S. mutans*	14.71	18.78	32	34
chitosan gel − AuNPs	*S. mutans*	8.56			35
lycopene − AgNPs	*S. aureus*	12			36
	S. mutans	12			
Aspergillus terreus IF0 − AuNPs	*E. coli*	13			37
	S. mutans	Not Active			
CST−AuNPs	*S. mutans* ATCC 25175	15.90	25	100	Present work
	S. sobrinus ATCC 33402	14.25	100	200	

in pH less than 5 and higher than 7 whereas the precipitation occurred at pH 7. As a result of the addition of $NaBH_4$, the pH solution was 9, and the solution was well dispersed, as reported in several studies.[32,33] Adjusting pH to basic range seemed to have no effect on their stability. When the pH was changed to acidity (pH 7), however, all particles precipitated. This could be because the electrostatic repulsion of negatively charged BO^{3-} has been destroyed, and deprotonated CST has no charge (zeta potential value near zero), causing AuNPs to precipitate. In a more acidic solution (pH 3), the amino groups of CST were protonated, making it more positively charged (corresponding to a higher zeta potential value) and causing AuNPs to have good dispersion.

Another important parameter for the stability of CST−AuNPs is ionic strength. The stability of CST−AuNPs as a function of salt concentration and salt type such as NaCl, Na_2SO_4, and Na_3PO_4 was investigated (Figure 6b). At low salt concentration, CST−AuNPs showed higher stability more than that at high concentration. The monovalent (Cl^-) and divalent (SO_4^{2-}) showed the slow precipitation of CST−AuNPs, while for trivalent (PO_4^{3-}), the CST−AuNP colloid tends to precipitate the fastest. The precipitation could be attributed to the lower of the electrostatic repulsion between CST and AuNPs and thus lead to the aggregation and sedimentation of AuNPs.

Figure 6c showed the effect of time onto the stability of CST−AuNPs. CST−AuNPs with pH 9 can be more stable more than 3 months.

3.4. Antimicrobial Assay. *3.4.1. Agar Well Diffusion Assay.* The antibacterial activity of CST−AuNPs was assessed by the agar well diffusion method. The results are shown in Figure 7. The CST−AuNPs showed good antibacterial activity against almost all pathogenic bacteria. The tuning of the capping agent used in the synthesis step strongly influences latter antimicrobial activity of the NPs against *S. mutans* ATCC 25175 and *S. sobrinus* ATCC 33402, with an inhibition clear zone of 15.90 and 14.25 mm against *S. mutans* and *S. sobrinus*, respectively. Indicated AuNPs show antibacterial properties when CST binds with the AuNP surface.

3.4.2. MIC and MBC Assay. The antibacterial activity of chitosan, CST, and CST−AuNPs against the bacterial strains was assessed by MIC and MBC. MIC and MBC values for CS, CST, and CST−AuNPs against *S. mutans* ATCC 25175 and *S. sobrinus* ATCC 33402 are shown in Table 1. The MICs and MBCs of CST−AuNPs against *S. mutans* ATCC 25175 were found to be 25 and 100 mg/L, respectively, while *S. sobrinus* ATCC 33402 was found to have an MIC and MBC of 100 and 200 mg/L, respectively. The report indicated that CST−AuNPs exhibited antibacterial activity against both bacterial species. Therefore, the modification of thymol into the backbone of chitosan was considered essential for antimicrobial activity enhancement.

Metallic nanoparticles have been widely studied and applied as an effective antibacterial agent. The antibacterial properties of modified metallic nanoparticles in the previous study are shown in Table 2. According to our proposed method, CST−AuNPs can be deemed to have potential with strong antimicrobial activity. CST coated on the AuNP surface can thus be employed as an antibacterial agent in a variety of biological applications.

4. CONCLUSIONS

A novel control of cariogenic bacteria in the oral cavity was made from a simple chemical reduction method using CST coated on the AuNP surface. The grafting of thymol onto the chitosan backbone was synthesized through adapting the Mannich reaction which provided degree of substitution values ($\%DS_{NMR}$) of 10.0%. Excellent properties of CST are very effective in stabilization of AuNPs. The electrostatic properties of CST were used to primarily provide the stabilization of the AuNPs by electrostatic repulsion. The particles of AuNPs were found to be well dispersed and mostly spherical in shape with an average particle size of 2.41−3.30 nm. The presence of AuNPs with CST enhanced bactericidal activity against *S. mutans* ATCC 25175 and *S. sobrinus* ATCC 33402. This CST coated on the AuNP surface potentially constitutes an important new weapon in the fight of cariogenic bacteria-related infection.

■ ASSOCIATED CONTENT

Supporting Information

The Supporting Information is available free of charge at https://pubs.acs.org/doi/10.1021/acsomega.2c02776.

Table S1: The elemental content of carbon, hydrogen, and nitrogen in chitosan, thymol, and CST calculated using EA and Figure S1: The zeta potential of CST coated on gold nanoparticles (pH 9) with various concentrations of CST (0.006, 0.008, 0.010, and 0.020% w/v) (PDF)

■ AUTHOR INFORMATION

Corresponding Authors

Ekarat Detsri − *Department of Chemistry, School of Science and Integrated Applied Chemistry Research Unit, School of Science, King Mongkut's Institute of Technology Ladkrabang, Bangkok 10520, Thailand;* orcid.org/0000-0001-8627-0631; Email: Ekarat.de@kmitl.ac.th

Pathavuth Monvisade − *Department of Chemistry, School of Science and Polymer Synthesis and Functional Materials*

Research Unit, School of Science, King Mongkut's Institute of Technology Ladkrabang, Bangkok 10520, Thailand; Email: Pathavuth.mo@kmitl.ac.th

Authors

Pakawat Chittratan − *Department of Chemistry, School of Science and Polymer Synthesis and Functional Materials Research Unit, School of Science, King Mongkut's Institute of Technology Ladkrabang, Bangkok 10520, Thailand*

Jongjit Chalitangkoon − *Department of Chemistry, School of Science and Polymer Synthesis and Functional Materials Research Unit, School of Science, King Mongkut's Institute of Technology Ladkrabang, Bangkok 10520, Thailand;* orcid.org/0000-0002-2836-125X

Karn Wongsariya − *Department of Biology School of Science, King Mongkut's Institute of Technology Ladkrabang, Bangkok 10520, Thailand*

Arjnarong Mathaweesansurn − *Department of Chemistry, School of Science and Applied Analytical Chemistry Research Unit, School of Science, King Mongkut's Institute of Technology Ladkrabang, Bangkok 10520, Thailand*

Complete contact information is available at: https://pubs.acs.org/10.1021/acsomega.2c02776

Notes

The authors declare no competing financial interest.

■ ACKNOWLEDGMENTS

This work has received funding support from the National Science, Research and Innovation Fund (NSRF), The Royal Golden Jubilee (RGJ) Ph.D. Programme (Grant No. PHD/0080/2559), and King Mongkut's Institute of Technology Ladkrabang (KMITL), grant number KREF016005. The authors would like to thank the Scientific Instruments Center, School of Science, King Mongkut's Institute of Technology Ladkrabang for supporting the instruments.

■ REFERENCES

(1) Liu, J.; Ling, J.-Q.; Zhang, K.; Huo, L.-J.; Ning, Y. Effect of Sodium Fluoride, Ampicillin, and Chlorhexidine on Streptococcus mutans Biofilm Detachment. *Antimicrob. Agents Chemother.* **2012**, *56*, 4532−4535.

(2) Al-Ahmad, A.; Wiedmann-Al-Ahmad, M.; Auschill, T. M.; Follo, M.; Braun, G.; Hellwig, E.; Arweiler, N. B. Effects of commonly used food preservatives on biofilm formation of Streptococcus mutans in vitro. *Arch. Oral Biol.* **2008**, *53*, 765−772.

(3) Thomas, A.; Thakur, S.; Mhambrey, S. Comparison of the antimicrobial efficacy of chlorhexidine, sodium fluoride, fluoride with essential oils, alum, green tea, and garlic with lime mouth rinses on cariogenic microbes. *J. Int. Soc. Prev. Community Dent.* **2015**, *5*, 302−308.

(4) Solanki, L. A.; Shantha Sundari, K. K.; Rajeshkumar, S. In-vitro Cytotoxicity Evaluation of Green Synthesized Gold Nanoparticles and Its Indigenous Mouthwash. *J. Pure Appl. Microbiol.* **2021**, *15*, 735−742.

(5) Solanki, L.; Shantha Sundari, K.; Muralidharan, N.; Jain, R. Antimicrobial effect of novel gold nanoparticle oral rinse in subjects undergoing orthodontic treatment: An ex-vivo study. *J. Int. Oral Health.* **2022**, *14*, 47−52.

(6) Ahrari, F.; Eslami, N.; Rajabi, O.; Ghazvini, K.; Barati, S. The antimicrobial sensitivity of Streptococcus mutans and Streptococcus sangius to colloidal solutions of different nanoparticles applied as mouthwashes. *Dent. Res. J. (Isfahan)* **2015**, *12*, 44−49.

(7) Chamundeeswari, M.; Sobhana, S. S. L.; Jacob, J. P.; Kumar, M. G.; Devi, M. P.; Sastry, T. P.; Mandal, A. B. Preparation, characterization and evaluation of a biopolymeric gold nanocomposite with antimicrobial activity. *Biotechnol. Appl. Biochem.* **2010**, *55*, 29−35.

(8) Franconetti, A.; Carnerero, J. M.; Prado-Gotor, R.; Cabrera-Escribano, F.; Jaime, C. Chitosan as a capping agent: Insights on the stabilization of gold nanoparticles. *Carbohydr. Polym.* **2019**, *207*, 806−814.

(9) Dykman, L. A.; Khlebtsov, N. G. Gold nanoparticles in biology and medicine: recent advances and prospects. *Acta Naturae* **2011**, *3*, 34−55.

(10) Regiel-Futyra, A.; Kus-Liśkiewicz, M.; Sebastian, V.; Irusta, S.; Arruebo, M.; Stochel, G.; Kyzioł, A. Development of Noncytotoxic Chitosan−Gold Nanocomposites as Efficient Antibacterial Materials. *ACS Appl. Mater. Interfaces* **2015**, *7*, 1087−1099.

(11) Abrica-González, P.; Zamora-Justo, J. A.; Sotelo-López, A.; Vázquez-Martínez, G. R.; Balderas-López, J. A.; Muñoz-Diosdado, A.; Ibáñez-Hernández, M. Gold nanoparticles with chitosan, N-acylated chitosan, and chitosan oligosaccharide as DNA carriers. *Nanoscale Res. Lett.* **2019**, *14*, 258.

(12) Su, C.; Huang, K.; Li, H.-H.; Lu, Y.-G.; Zheng, D.-L. Antibacterial Properties of Functionalized Gold Nanoparticles and Their Application in Oral Biology. *J. Nanomater.* **2020**, *2020*, No. 5616379.

(13) Darabpour, E.; Kashef, N.; Amini, S. M.; Kharrazi, S.; Djavid, G. E. Fast and effective photodynamic inactivation of 4-day-old biofilm of methicillin-resistant Staphylococcus aureus using methylene blue-conjugated gold nanoparticles. *J. Drug Deliv. Sci. Technol.* **2017**, *37*, 134−140.

(14) Singh, P.; Pandit, S.; Garnæs, J.; Tunjic, S.; Mokkapati, V. R.; Sultan, A.; Thygesen, A.; Mackevica, A.; Mateiu, R. V.; Daugaard, A. E.; Baun, A.; Mijakovic, I. Green synthesis of gold and silver nanoparticles from Cannabis sativa (industrial hemp) and their capacity for biofilm inhibition. *Int. J. Nanomed.* **2018**, *13*, 3571−3591.

(15) Zhao, Y.; Tian, Y.; Cui, Y.; Liu, W.; Ma, W.; Jiang, X. Small Molecule-Capped Gold Nanoparticles as Potent Antibacterial Agents That Target Gram-Negative Bacteria. *J. Am. Chem. Soc.* **2010**, *132*, 12349−12356.

(16) Chávez de Paz, L. E.; Resin, A.; Howard, K. A.; Sutherland, D. S.; Wejse, P. L. Antimicrobial effect of chitosan nanoparticles on streptococcus mutans biofilms. *Appl. Environ. Microbiol.* **2011**, *77*, 3892−3895.

(17) Costa, E. M.; Silva, S.; Costa, M. R.; Pereira, M.; Campos, D. A.; Odila, J.; Madureira, A. R.; Cardelle-Cobas, A.; Tavaria, F. K.; Rodrigues, A. S.; et al. Chitosan mouthwash: Toxicity and in vivo validation. *Carbohydr. Polym.* **2014**, *111*, 385−392.

(18) Uraz, A.; Boynueğri, D.; Özcan, G.; Karaduman, B.; Uç, D.; Şenel, S.; Pehlivan, S.; Öğüs, E.; Sultan, N. Two percent chitosan mouthwash: A microbiological and clinical comparative study. *J. Dent. Sci.* **2012**, *7*, 342−349.

(19) Liu, X.; Xia, W.; Jiang, Q.; Yu, P.; Yue, L. Chitosan oligosaccharide-N-chlorokojic acid mannich base polymer as a potential antibacterial material. *Carbohydr. Polym.* **2018**, *182*, 225−234.

(20) Khan, S. T.; Khan, M.; Ahmad, J.; Wahab, R.; Abd-Elkader, O. H.; Musarrat, J.; Alkhathlan, H. Z.; Al-Kedhairy, A. A. Thymol and carvacrol induce autolysis, stress, growth inhibition and reduce the biofilm formation by Streptococcus mutans. *AMB Express* **2017**, *7*, 49.

(21) Marchese, A.; Orhan, I. E.; Daglia, M.; Barbieri, R.; Di Lorenzo, A.; Nabavi, S. F.; Gortzi, O.; Izadi, M.; Nabavi, S. M. Antibacterial and antifungal activities of thymol: A brief review of the literature. *Food Chem.* **2016**, *210*, 402−414.

(22) Nagoor Meeran, M. F.; Javed, H.; Al Taee, H.; Azimullah, S.; Ojha, S. K. Pharmacological Properties and Molecular Mechanisms of Thymol: Prospects for Its Therapeutic Potential and Pharmaceutical Development. *Front. Pharmacol.* **2017**, *8*, 380.

(23) Chalitangkoon, J.; Monvisade, P. Dual pH/thermal-dependent coloring polymeric dye through Mannich reaction of chitosan: Synthesis and characterization. *Carbohydr. Polym.* **2019**, *223*, No. 115049.

(24) Wang, W.; Meng, Q.; Li, Q.; Liu, J.; Zhou, M.; Jin, Z.; Zhao, K. Chitosan Derivatives and Their Application in Biomedicine. *Int. J. Mol. Sci.* **2020**, *21*, 487.
(25) Yin, M.; Wang, Y.; Zhang, Y.; Ren, X.; Qiu, Y.; Huang, T.-S. Novel quaternarized N-halamine chitosan and polyvinyl alcohol nanofibrous membranes as hemostatic materials with excellent antibacterial properties. *Carbohydr. Polym.* **2020**, *232*, No. 115823.
(26) Yue, L.; Sun, D.; Mahmood Khan, I.; Liu, X.; Jiang, Q.; Xia, W. Cinnamyl alcohol modified chitosan oligosaccharide for enhancing antimicrobial activity. *Food Chem.* **2020**, *309*, No. 125513.
(27) Khan, A.; Alamry, K. A. Recent advances of emerging green chitosan-based biomaterials with potential biomedical applications: A review. *Carbohydr. Res.* **2021**, *506*, No. 108368.
(28) Chalitangkoon, J.; Monvisade, P. Synthesis of chitosan-based polymeric dyes as colorimetric pH-sensing materials: Potential for food and biomedical applications. *Carbohydr. Polym.* **2021**, *260*, No. 117836.
(29) Detsri, E.; Seeharaj, P.; Sriwong, C. A sensitive and selective colorimetric sensor for reduced glutathione detection based on silver triangular nanoplates conjugated with gallic acid. *Colloids Surf. A Physicochem. Eng. Asp.* **2018**, *541*, 36−42.
(30) Yu, S.; Du, J.; Zheng, Y.; Yan, L. Synthesis and characterization of carboxymethyl chitosan containing functional ultraviolet absorber substituent. *J. Appl. Polym. Sci.* **2007**, *106*, 4098−4103.
(31) Sneha, K.; Esterle, A.; Sharma, N.; Sahi, S. Yucca-derived synthesis of gold nanomaterial and their catalytic potential. *Nanoscale Res. Lett.* **2014**, *9*, 627.
(32) Adlim, A.; Bakar, M. A. Preparation of chitosan-gold nanoparticles: part 1 (of 2). Effect of reducing technique. *Indones. J. Chem.* **2008**, *8*, 184−188.
(33) Adlim, A. Preparation of Chitosan-Stabilized Silver (Chi-Ag) Nanoparticles Using Different Reducing Agents And Techniques. *J. Sains Tek.* **2006**, *12*, 185−191.
(34) Jalaei, J.; Layeghi-Ghalehsoukhteh, S.; Hosseini, A.; Fazeli, M. Antibacterial effects of gold nanoparticles functionalized with the extracted peptide from Vespa orientalis wasp venom. *J. Pept. Sci.* **2018**, *24*, No. e3124.
(35) Sámano-Valencia, C.; Martínez-Castañón, G. A.; Martínez-Gutiérrez, F.; Ruiz, F.; Toro-Vázquez, J. F.; Morales-Rueda, J. A.; Espinosa-Cristóbal, L. F.; Zavala Alonso, N. V.; Niño Martínez, N. Characterization and Biocompatibility of Chitosan Gels with Silver and Gold Nanoparticles. *J. Nanomater.* **2014**, *2014*, 1−11.
(36) Murthykumar, K.; Malaiappan, S.; Shanmugam, R. Antioxidant and antibacterial effect of lycopene mediated silver nanoparticle against Staphylococcus aureus and Streptococcus mutans- an In vitro study. *Plant Cell Biotechnol. Mol. Biol.* **2020**, *21*, 90−98.
(37) Priyadarshini, E.; Pradhan, N.; Sukla, L. B.; Panda, P. K. Controlled Synthesis of Gold Nanoparticles UsingAspergillus terreusIF0 and Its Antibacterial Potential against Gram Negative Pathogenic Bacteria. *J. Nanotechnol.* **2014**, *2014*, 1−9.

https://doi.org/10.1021/acsomega.2c02776
ACS Omega 2022, 7, 26582−26590

Appendix B

Colloids and Surfaces A: Physicochemical and Engineering Aspects 693 (2024) 133957

Contents lists available at ScienceDirect

Colloids and Surfaces A: Physicochemical and Engineering Aspects

journal homepage: www.elsevier.com/locate/colsurfa

Antimicrobial nanolayer films of chloroxylenol–carboxyethylchitosan–modified silver nanoparticles for enhanced surgical suture performance

Pakawat Chittratan [a,b], Ekarat Detsri [a,c,*], Jongjit Chalitangkoon [a,b], Arjnarong Mathaweesansurn [a,d], Pathavuth Monvisade [a,b]

[a] Department of Chemistry, School of Science, King Mongkut's Institute of Technology Ladkrabang, Bangkok 10520, Thailand
[b] Polymer Synthesis and Functional Materials Research Unit, School of Science, King Mongkut's Institute of Technology Ladkrabang, Bangkok 10520, Thailand
[c] Integrated Applied Chemistry Research Unit, School of Science, King Mongkut's Institute of Technology Ladkrabang, Bangkok 10520, Thailand
[d] Applied Analytical Chemistry Research Unit, School of Science, King Mongkut's Institute of Technology Ladkrabang, Bangkok 10520, Thailand

GRAPHICAL ABSTRACT

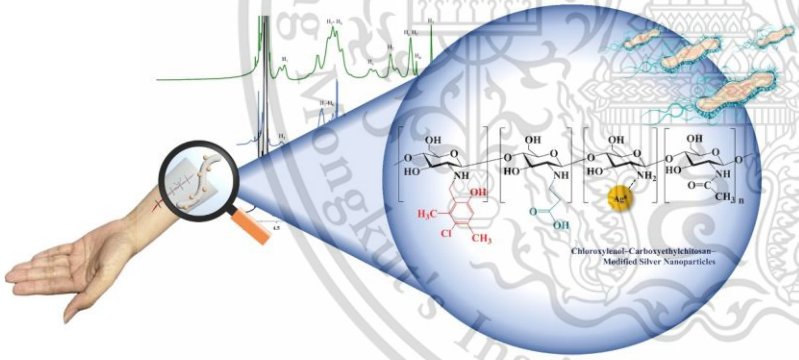

ARTICLE INFO

Keywords:
Chloroxylenol-carboxyethylchitosan
Silver nanoparticles
Surgical sutures
Layer-by-Layer
Pathogenic bacteria

ABSTRACT

Antimicrobial surgical suture materials incorporating chloroxylenol-carboxyethylchitosan-modified silver nanoparticles (CECSX-AgNPs) were successfully prepared using the Layer-by-Layer (LbL) deposition technique. Chitosan (CS) was covalently affixed with chloroxylenol as hydrophobic functional groups (PCMX), yielding chloroxylenol-chitosan (CSX) and later hydrophilic acrylic acid onto the CSX skeleton, providing a novel water-soluble antimicrobial agent of chloroxylenol-carboxyethylchitosan (CECSX). ^{1}H NMR confirmed the successful substitution of PCMX and acrylic acid onto CS, with $\%DS_{PCMX}$ and $\%DS_{AA}$ of 8.0 and 33.0, respectively. CECSX successfully stabilized AgNPs *via* the chemical reduction method, resulting in CECSX modified AgNPs. The colloidal solution exhibited a yellowish hue, spherical shape, monodispersity with an average particle size of 4.8 ± 2.4 nm, and a zeta potential value of −20.97 ± 0.03 mV. Minimum inhibitory concentration (MIC) values for

* Correspondence to: Department of Chemistry and Integrated Applied Chemistry Research Unit, School of Science, King Mongkut's Institute of Technology Ladkrabang, Bangkok 10520, Thailand.
E-mail addresses: 59605103@kmitl.ac.th (P. Chittratan), Ekarat.de@kmitl.ac.th (E. Detsri), Arjnarong.ma@kmitl.ac.th (A. Mathaweesansurn), Pathavuth.mo@kmitl.ac.th (P. Monvisade).

https://doi.org/10.1016/j.colsurfa.2024.133957
Available online 12 April 2024

CECSX-AgNPs against *E. coli* (ATCC25922), *S. aureus* (ATCC25923), and *A. baumanii* (ATCC19606) were determined as 25, 12.5, and 1.56 mg/L, respectively. Using the LbL deposition technique, CECSX-AgNPs were successfully deposited onto various suture materials including cotton, polyamide, and polypropylene. Remarkably, CECSX-AgNPs coated surgical sutures exhibited the highest bacterial reduction of 99.99 %. These findings underscore the efficacy of CECSX as a high-performance stabilizing agent for AgNPs production, providing outstanding antibacterial activity on diverse surgical suture materials and promoting the wound healing process.

1. Introduction

Sutures are important surgical medical devices used for sealing injured organs and tissues and fostering postoperative wound healing. Inadequate closure may potentially increase the risk of wound dehiscence, thereby creating a pathway for bacterial contamination. Historically, both systemic and localized antibiotic therapies have been employed to manage surgical-site infections [1]. Nowadays, suture functionalization with antibacterial agents is regarded as an alternate control strategy that counteracts cross–contamination and microbial proliferation. A variety of antibacterial agents are used in suture functionalization, including triclosan [2], chlorohexidine [2–4], and iodine [5]. Despite their effectiveness, these antimicrobial medications may induce allergies, skin irritation, and staining of surrounding tissues or clothing, particularly with iodine-containing solutions. In recent years, silver nanoparticles (AgNPs) have emerged as promising antimicrobial agents for coating sutures, owing to their exceptional attributes such as limited susceptibility to pathogen at surgical sites and extensive antimicrobial and antiviral properties [6]. Interestingly, the antimicrobial properties of AgNPs were found to be size- and shape-dependent [7]. Moreover, the conjugation of AgNPs with antibacterial agents has demonstrated notable antimicrobial effects. Despite these exceptional characteristics, there is a scarcity of literature on the utilization of biogenic agents modified AgNPs for suture coating. S. Yadav *et al.* [8] reported the antimicrobial properties of surgical sutures coated by propolis modified AgNPs. Propolis modified AgNPs exhibit a highly dispersed, mostly spherical morphology with a diameter of approximately 20 nm. Coated sutures displayed a clear zone of clearance where they were not observed with uncoated sutures. Significant differences were observed in zone of clearance for 1.8 ± 0.01 mm, 1.2 ± 0.03 mm, and 1.0 ± 0.06 mm against *S. aureus*, *E. coli*, and *A. niger*, respectively. S. T. Dubas *et al.* [9] fabricated surgical sutures by coating sodium alginate modified AgNPs. The antimicrobial properties of AgNPs against *S. aureus* were found to increase as the size of the nanoparticles (NPs) decreased. The % reduction of *S. aureus* was 76.82 %. Indeed, numerous studies suggested that AgNPs have exhibited significant extensive antimicrobial properties. Each research uniformly concurs on the assertion that not only size and shape but also surface characteristics of AgNPs play a pivotal role in their interactions with bacteria. To curtail the agglomeration and unrestrained growth of AgNPs, a stabilizing agent is required. This stabilizing agent prevents NPs aggregation through mechanisms of steric hindrance or electrostatic repulsion, simultaneously regulating particle growth dynamics [10].

Chitosan (CS) is a naturally occurring polysaccharide derived from the deacetylation of chitin [11]. Because of its chemical and physical properties, CS is becoming increasingly popular as a stabilizing agent in AgNP synthesis. CS contains amino and hydroxyl groups, which allow for electrostatic interactions with negatively charged nanoparticles, effectively preventing aggregation [12]. The ability of CS to polymer to encapsulate AgNPs also reduces their tendency to agglomerate, thereby enhancing their stability [13]. Furthermore, CS contains active functional groups that can be modified to improve properties such as antimicrobial activity [14–18] and water solubility [19–21]. The antibacterial activity of CS can be further enhanced by integrating some functional groups into its structure through chemical reactions involving hydroxyl or amino moieties [22–27]. Despite numerous studies aimed at enhancing the efficacy of CS in antimicrobial properties, challenges persist regarding its water solubility. Hence, our objective was to enhance the antimicrobial property of CS, while also aiming to improve its water solubility. Subsequently, the modified CS was utilized to fabricate antimicrobial surgical suture materials.

In the present study, a new antimicrobial agent was developed by incorporating AgNPs with CS derivatives and subsequently coated on the surface of a surgical suture. The strong antimicrobial effect of the CS-modified AgNPs can be enhanced by altering the surface charges of AgNPs to achieve stronger attractive force. To achieve this, the study focuses on two main objectives for altering the surface properties of CS. Firstly, chloroxylenol (PCMX) was covalently bonded to the CS backbone yielding chloroxylenol-chitosan (CSX). The incorporation of chloroxylenol as hydrophobic active functional groups onto the CS backbone represents a strategic enhancement to the antimicrobial activity of the materials. Secondly, hydrophilic acrylic acid was introduced to CSX to obtain chloroxylenol-carboxyethylchitosan (CECSX). The modification of acrylic acid brings CSX better water solubility affecting the higher antibacterial activity under neutral and basic conditions (pH 7–12) against pathogenic bacteria. Subsequently, the novel CECSX antimicrobial compound was used as a stabilizer in the synthesis of AgNPs to produce a highly stable colloidal and antimicrobial AgNPs solution (CECSX-AgNPs). Finally, using the advantages of Layer-by-layer (LbL) technique [28], CECSX-AgNPs were coated onto various suture materials to create multifunctional nanolayer films for antimicrobial sutures. The LbL technique based on the electrostatic interaction between the negatively charged CECSX–AgNPs and the positively charged poly(diallyldimethylammonium chloride) (PDADMAC) was employed to fabricate CECSX-AgNPs coating on surgical suture materials. The resulting CECSX-AgNPs coated surgical suture surfaces demonstrated outstanding antimicrobial properties against *E. coli* (ATCC25922), *S. aureus* (ATCC25923), and *A. baumanii* (ATCC19606), thereby highlighting the potential of this innovative approach to advance the field of medical materials and infection control.

2. Experimental

2.1. Chemicals and instruments

Low molecular weight CS powder of 50–190 kDa with 85 % degree of deacetylation, para-chloro-meta-xylenol (Chloroxylenol; PCMX), silver nitrate ($AgNO_3$), sodium borohydride ($NaBH_4$), poly(diallyldimethylammonium chloride) (PDADMAC) and poly (sodium 4-styrenesulfonate) (PSS) were purchased from Sigma-Aldrich Co., Ltd., USA. Acetic acid (CH_3COOH), acrylic acid ($C_3H_4O_2$), hydrochloric acid (HCl), formaldehyde (HCHO), and sodium hydroxide (NaOH) were purchased from Carlo Erba Co., Ltd., USA. All reagents were of analytical grade (AR grade) and were used as received without further purification. All stock solutions were prepared with deionized water (DI water) with a resistivity of 18.2 MΩ·cm at 25 °C obtained from Milli-Q® EQ 7000 ultrapure water system.

The absorbance spectra of the as-synthesized materials in a wavelength range of 200–700 nm were recorded using a UV–vis spectrophotometer (UV1800, Shimadzu Co., Ltd., Japan). The Zeta Potential analyzer (Nano ZS-Malvern Instrument Co., Ltd., England) was used to measure the surface zeta potential of NPs. Morphology of CECSX-AgNPs was observed using a Transmission Electron Microscope (TEM, JEM2100, JEOL Co., Ltd., Japan) at an accelerating voltage of 200 kV.

The crystalline phase of CECSX-AgNPs was characterized by X-ray diffractometer (XRD, RIGAKU Co., Ltd., Japan). Atomic Force Microscopy (AFM, SPA400 model, SEIKO Instruments Co., Ltd., Japan) was utilized to examine the surface morphology of nanolayer films. The morphology and appearance of AgNPs on suture materials were photographed by Field Emission Scanning Electron Microscope (FESEM, Quanta 250 FEG, FEI Co., Ltd., United States) and Energy Dispersive X-Ray Spectrometer (EDS, INCAx-act, 51-ADD001, Oxford, United Kingdom).

2.2. Synthesis of chloroxylenol-carboxyethylchitosan (CECSX)

CECSX was synthesized based on a modified two-step process [14], involving Mannich and Michael reactions. Firstly, chloroxylenol (PCMX) was chemically bonded to the chitosan (CS) structure *via* the Mannich reaction, forming chloroxylenol-chitosan (CSX). Low molecular weight CS powder of 5.28 mmol (1.00 g) was dissolved in 100 mL of 1 % w/v acetic acid and stirred overnight at room temperature until complete dissolution. Then 10.56 mmol (1.654 g) of chloroxylenol in 50 mL DMF was added immediately into the CS solution. Subsequently, 5.28 mmol (0.429 g) of formaldehyde was slowly added dropwise into the mixed solution under vigorous stirring. The reaction proceeded at 60 °C for 24 h. After the reaction completed, the mixture solution was terminated by adding 100 mL of 0.5 M NaOH. The precipitant was filtered using Whatman No. 40 and dried to obtain the CSX product, with yield 84.0 %.

Acrylic acid was then attached to the CSX backbone using Michael reaction to obtain CECSX. Briefly, 4.44 mmol (1.00 g) of CSX was suspended in 100 mL of distilled water. The solution was left to swell for 30 min under continuously stirred and followed by adding 8.88 mmol (0.64 g) of acrylic acid into CSX suspension. The mixture was vigorously stirred at 60 °C for 48 h. To terminate the reaction, 10 % w/v NaOH was rapidly added into the mixture solution for adjusting pH to 12. CECSX was purified using a dialysis membrane (Sigma-Aldrich Co., Ltd USA., molecular weight cut-off: 14,000 Da). The purified CECSX product was obtained after lyophilization and stored in a desiccator until further use. The synthesis resulted in a high yield of CECSX (84 %).

The absorption characteristics of CS, CSX, CECSX and PCMX were evaluated using a UV–vis spectrophotometer. 0.75 mg of CS, CSX, and CECSX were individually dissolved in 1.0 mL of 0.1 M HCl. Meanwhile, 0.02 mg of PCMX was dissolved in a slight amount of 5 % ethanol and then adjusted to a volume of 1.0 mL by adding 0.1 M HCl. The modified chitosan structure was characterized using ^{1}H NMR (JNM–ECZ–500 R/S1 spectrometer, JEOL Co. Ltd., Japan). Samples of 1 % w/v of CS and CSX were dissolved in CF_3COOH/D_2O (1/100 w/v), while 1 % w/v of

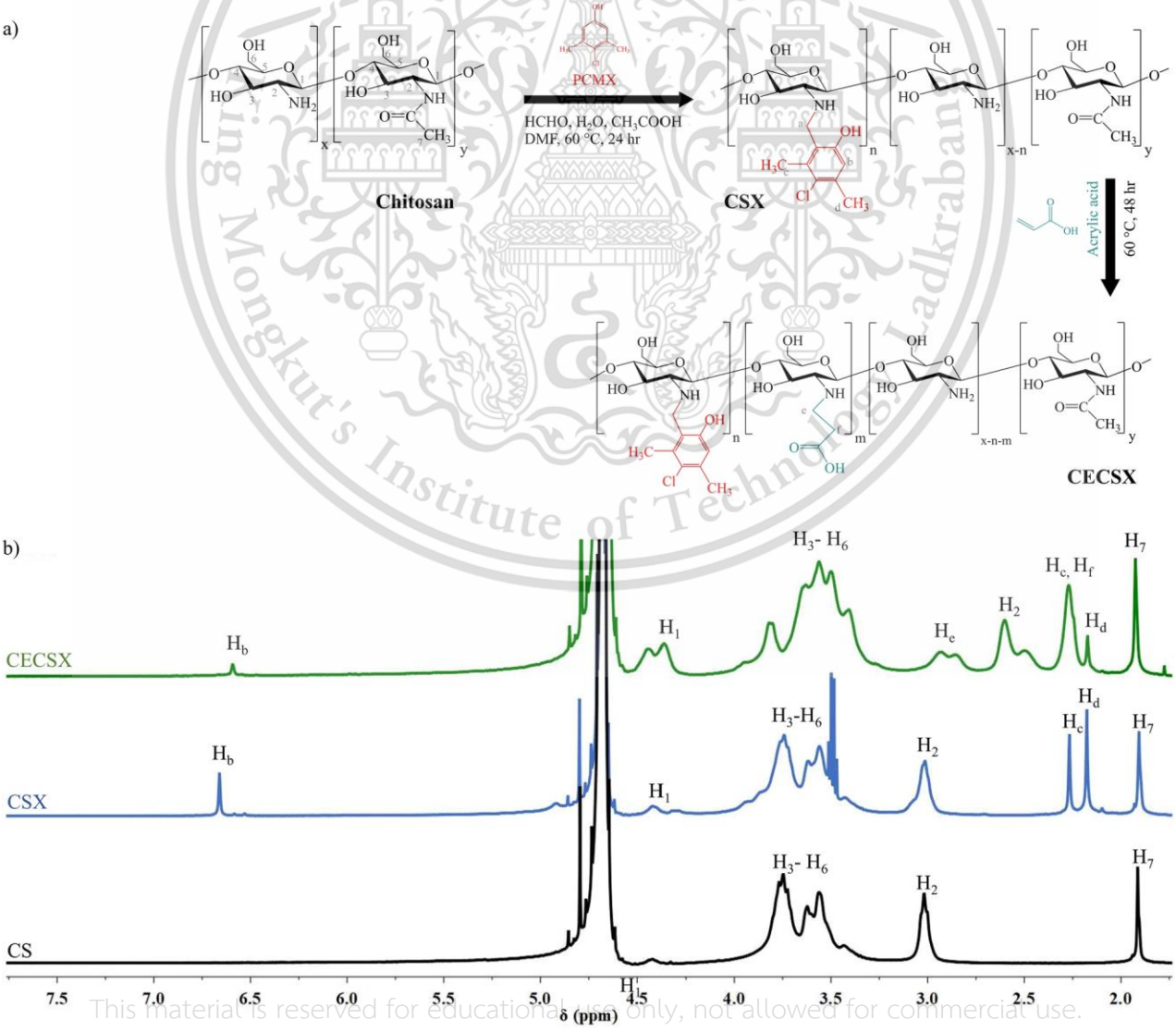

Fig. 1. (a) Synthesis scheme of CSX and CECSX, and (b) ^{1}H NMR spectra of CS and CSX in D_2O/CF_3COOH, and CECSX in D_2O.

CECSX was dissolved in D_2O. The degree of substitution of PCMX (%DS_{PCMX}) and acrylic acid (%DS_{AA}) on chitosan backbone structure was calculated using data from ^1H NMR spectra following the Eqs. (1) and (2), respectively.

$$\%DS_{PCMX} = \frac{H_b}{H_2} \times 100 \quad (1)$$

where: %DS_{PCMX} is the degree of substitution percentage obtained from ^1H NMR. H_b and H_2 are the integral areas of protons indicated in Fig. 1

$$\%DS_{AA} = \frac{\frac{H_e}{2}}{H_2} \times 100 \quad (2)$$

where: %DS_{AA} is the degree of substitution percentage obtained from ^1H NMR. H_e and H_2 are the integrals areas of protons indicated in Fig. 1

2.3. Synthesis of chloroxylenol-carboxyethylchitosan-modified silver nanoparticles (CECSX-AgNPs)

CECSX-AgNPs was synthesized based on chemical reduction method using CECSX and $NaBH_4$ as stabilizing agent and reducing agent, respectively. A typical procedure was as follows: 10 mL of 10 mM $AgNO_3$ solution and 0.3 mL of 0.1 % w/v CECSX were mixed homogenously in 6.7 mL of DI water. Then, 2 mL of 50 mM $NaBH_4$ solution was rapidly added and continuously stirred for 30 min. The mixture solution was immediately changed from clear to dark yellow color, indicating the formation of AgNPs. Different final CECSX concentrations of 0.003 % w/v, 0.005 % w/v, and 0.010 % w/v were also studied for the formation of CECSX-AgNPs. The excess $NaBH_4$ was removed using a dialysis tube with molecular weight cut-off 14,000 Da. Ultimately, the obtained CECSX-AgNPs product was stored in a dark amber glass container in a 4 °C refrigerator for further use. The concentration of CECSX-AgNPs was determined to be 5.1 nM using Beer-Lambert's law with an extinction coefficient (ε) of 1.63×10^9 M^{-1} cm^{-1} for an average AgNPs size of 4.8 ±2.4 nm. The equation, $\ln \varepsilon = 1.4418 \ln D + 18.955$, was employed to calculate ε based on the nanoparticle diameter (D) [29].

2.4. Nanolayer films of chloroxylenol-carboxyethylchitosan-modified silver nanoparticles assembly

To simulate CECSX-AgNPs nanolayer films built up on suture materials, glass slides were used as the primary substrates for the LbL deposition study. Firstly, glass slide substrates were coated with 10 mM of positively charged PDADMAC and subsequently 10 mM of negatively charged PSS solution for 5 layers to ensure good buildup of nanolayer films of CECSX-AgNPs assembly. The coatings of PDADMAC and PSS complexes were formed via electrostatic interaction on the surfaces of hydrophobic glass slides. Then, the 5th positively charged layer of PDADMAC glass slide substrates was immersed into CECSX-AgNPs solution for 5 min and rinsed with DI water to remove the excess of unbonded CECSX-AgNPs. The desired number of layers of CECSX-AgNPs nanolayer films was obtained by repeating self-assembling negatively charged CECSX-AgNPs solution and positively charged PDADMAC. When the outermost layer of the glass slide is formed by more hydrophilic PDADMAC, the positively charged balance of CECSX-AgNPs is more equilibrated. Although, PDADMAC [30,31] and PSS [32] seem to be highly toxic and may pose a definite threat to cells. However, certain low-concentration counterparts remain practically safe. To enhance the nanofilm adhesion ability, several films formation parameters including pH, time, ionic strength, and number of layers were studied. The best optimal conditions for CECSX-AgNPs nanofilms assembled were fabricated on surgical suture materials including cotton, polyamide, and polypropylene.

2.5. Antimicrobial assay

The Minimum Inhibitory Concentration (MIC) and Minimum Bactericidal Concentration (MBC) assays are employed to determine the lowest concentration of an antibacterial substance or agent required to visibly prevent bacterial growth and to identify the smallest concentration of an antibacterial agent needed to kill bacteria under specific conditions over a defined period, respectively. The MIC and MBC values were determined using a broth macro-dilution method. Initially, bacterial colonies were transferred to 0.85 % sterile saline to reach the turbidity level equivalent to a 0.5 McFarland standard. This bacterial suspension was then diluted with Mueller Hinton Broth (MHB) at a ratio of 1:200, resulting in a concentration of approximately 5×10^5 CFU/mL. The CS, CECSX, and CECSX-AgNPs with concentrations ranging from 0.78 to 400 mg/L were prepared by diluting with 0.1 % v/v CH_3COOH. Subsequently, 50 μL of each prepared pathogenic bacteria, including *E. coli* (ATCC25922), *S. aureus* (ATCC25923), and *A. baumanii* (ATCC19606), were added into the CS, CECSX, and CECSX-AgNPs test tube samples. All sample tubes were incubated at 37 °C overnight. The MIC and MBC values were determined as the lowest concentrations of the antimicrobial agents that resulted in the elimination of 99.9 % of the initial bacterial population, without any observable bacterial growth.

In vitro time-kill study: A time-kill method is an effective assay for evaluating antibacterial activity by measuring the effect of biologic compounds on bacterial growth. In this study, CECSX-AgNPs coated surgical sutures were cut into 3 cm-long samples. The microorganisms were cultivated in Mueller Hinton Broth (MHB) at 37 °C for a duration time of 18 h. Adjust the turbidity of the suspension to 0.5 McFarland by 0.85 % sterile NaCl standard solution (inoculum of 1.5×10^8 CFU/mL). The final inoculum was prepared at of 5×10^5 CFU/mL in MHB solution. A 3 cm-long CECSX-AgNPs coated surgical suture was dipped into 3 mL of bacterial suspensions under continuous agitation at a temperature of 37 °C. After these cultures were incubated, 20 μL of samples were collected at specified time intervals of 0, 1, 3, 6, and 24 h. Subsequently, the cultures solution was diluted 2-fold and dropped onto a petri dish containing MHB agar. All plates were then incubated at 37 °C for 24 h. Different bacterial colonies were observed on all the plates. Data were analyzed by determining the percent reduction of microbial growth compared to control samples in CFU/mL, which can be calculated using the following Eqs. (3) and (4).

$$\text{Percent of bacterial reduction } (\%) = \frac{(A - B) \times 100}{A} \quad (3)$$

$$\text{Log of bacterial reduction} = \log_{10}\frac{A}{B} \quad (4)$$

where: A = the number of viable microorganisms before coated (CFU/mL), B = the number of viable microorganisms after coated (CFU/mL)

3. Results and discussion

3.1. Characterizations of chloroxylenol-carboxyethylchitosan

Firstly, chloroxylenol (PCMX) was chemically attached to the chitosan (CS) structure using the Mannich reaction to obtain chloroxylenol-chitosan (CSX). The presence of hydrophobic PCMX junctions on the CS backbone significantly enhances antibacterial properties. Introducing hydrophobic moieties into the CS structure can also enhance its interaction with the lipid components of bacterial membranes. This modification can disrupt the membrane's integrity, causing leakage of cellular contents and ultimately leading to bacterial cell death [14]. As depicted in Fig. 1a., PCMX was chemically attached to the CS structure through a methylene bridge between the ortho position of PCMX and the amino group of CS. The ^1H NMR (Fig. 1b) spectrum of CSX revealed new peaks at 2.27 and 2.18 ppm, corresponding to the methyl groups of PCMX (H_c and H_d, respectively). Additionally, the aromatic proton (H_b) appeared

at 6.66 ppm. These observations confirm the successful covalent attachment of PCMX onto the chitosan backbone with a degree of substitution (%DS) of 9. To enhance the water solubility of CSX, carboxyethylation was carried out through the Michael reaction between acrylic acid and CSX to produce chloroxylenol-carboxyethylchitosan (CECSX). In comparison to the ^{1}H NMR spectrum of CSX, CECSX exhibited a new peak around 2.9 ppm, assigned to the methylene proton H_e. Furthermore, a broad peak overlapping with H_c was observed at 2.3 ppm corresponding to H_f [19,21]. Nevertheless, the peaks corresponding to H_b and H_d of the PCMX moiety remained in the same positions, indicating that PCMX remained covalently bonded to the CS. The %DS values for acrylic acid and PCMX in CECSX were determined to be 33 and 8, respectively.

To further confirm the successful synthesis of CECSX, a series of experiments for comparison were designed and conducted. In the UV–vis spectra results (Fig. 2a), CSX exhibited a distinctive single peak at 287 nm, whereas no such peak was observed in the CS spectrum. Notably, this peak was shifted to a higher wavelength when compared to the free PCMX, which displayed a broader peak ranging from 279 to 284 nm. This shift confirms the covalent bonding between PCMX and CS [14,33]. In the case of the CECSX spectrum, it displayed the same maximum absorption peak as CSX, indicating that the carboxyethylation of CSX did not impact the PCMX moiety of the product. Fig. 2b illustrates the water-solubility characteristics of CS, CSX, and CECSX over a broad pH range, as measured by their transmission at 600 nm [19,34]. CS and CSX were generally soluble within a pH range of 1–6 but tended to become cloudy and partially precipitate when the pH exceeded 6.5. This phenomenon can be attributed to the deprotonation of ammonium groups ($–NH_3^+$) to amino groups ($–NH_2$). Notably, CSX exhibited a higher transmittance value, possibly owing to the interruption of crystallization and aggregation by the presence of the PCMX moiety in CSX. In the case of CECSX, it demonstrated solubility in acidic solutions and exhibited poor solubility at pH 6.2 due to its isoelectric point. However, it could be redissolved with an increase in pH and achieved complete dissolution at a pH of 8. This behavior resulted from deprotonation, leading to the formation of –COOH and $–NH_2$ groups. The enhanced water solubility of CECSX has potential for use in a variety of applications, including the synthesis of AgNPs using an acid–free condition for dissolving CS.

3.2. *Characterizations of chloroxylenol-carboxyethylchitosan-modified AgNPs*

The CECSX-modified AgNPs were synthesized through the chemical reduction of $AgNO_3$ with a $NaBH_4$ solution. CECSX acted as the stabilizing agent for controlling size and shape by inhibiting nanoparticles overgrowth and preventing their aggregation. CECSX could be adsorbed on the surface of AgNPs, possibly through interaction *via* the coordinate bond of Ag (sp orbital) and the carboxylate groups of CECSX. The visual observation and absorption spectra of CECSX-AgNPs are shown in Fig. 3a. The color of the colloidal solution changed from colorless to dark yellow immediately after Ag^+ ions were reduced to Ag^0 to obtain AgNPs coated with CECSX. Visual observation revealed a characteristic color change in CECSX-AgNPs from dark yellow to pale yellow, displaying the strong surface plasmon resonance (SPR) characteristic at 402, 411, and 412 nm, when the synthesized concentration of $AgNO_3$ was kept constant at 1 mM and the concentration of CECSX varied from 0.003 % w/v, 0.005 % w/v, and 0.010 % w/v, respectively. The red shift phenomenon in the SPR of CECSX-AgNPs in the synthesized nanoparticles is probably due to the dielectric constant of CECSX surrounding nanoparticles. According to the reports in the literature [35], the SPR spectrum of AgNPs, which use CECSX as the stabilizing agent, was found in agreement with each AgNPs production method.

To examine the size distribution and surface morphology of CECSX-AgNPs, TEM analysis was conducted, as shown in Fig. 3b-d. When using CECSX concentrations of 0.003 % w/v, 0.005 % w/v, and 0.010 % w/v, the particle sizes of CECSX-AgNPs were found to have a narrow size distribution ranging of 7.2 ± 3.5 nm, 4.8 ± 2.4 nm, to 4.8 ± 2.9 nm, respectively. The CECSX-AgNPs are spherical-like shapes and are effectively dispersed in aqueous environments. We note that the particle size of CECSX-AgNPs is relatively small compared to others, suggesting the strong coordinate bond of Ag^+ occupation on the $–NH_3^+$ and $–COO^-$ groups of the chitosan derivatives. We also observe that CECSX can effectively serve as a stabilizing agent for AgNPs preparation under basic conditions. Furthermore, the stability of CECSX-AgNPs colloidal solution at various CECSX concentrations was characterized using a zeta potential analyzer. The stability of the colloidal particles is expressed by the zeta potential (ζ), which quantifies the electric potential of the nanoparticles. The ζ of as-synthesized CECSX-AgNPs at CECSX concentrations of 0.003 % w/v, 0.005 % w/v, and 0.010 % w/v were negatively charged at −19.23, −20.97 and −21.70, respectively. This negative charge ζ is essential for binding with carboxylate functional groups of CECSX on nanoparticles. According to the literature [13,36], nanoparticles with high stability and dispersibility have ζ greater than +30 mV or less than −30 mV. Our observation revealed that the ζ of CECSX-AgNPs are less than ±30 mV. Although, despite the lower ζ, the nanoparticles are now stabilized by the steric effect of CECSX, leading to more stable nano colloidal suspensions.

To confirm the successful synthesis of CECSX-AgNPs, XRD measurement was carried out to identify the crystallographic structure of the nanoparticles. The XRD patterns of the synthesized CECSX-AgNPs are dispicted in Fig. 4. Four intense diffraction peaks corresponding to typical Bragg reflections were observed in the synthesized CECSX-

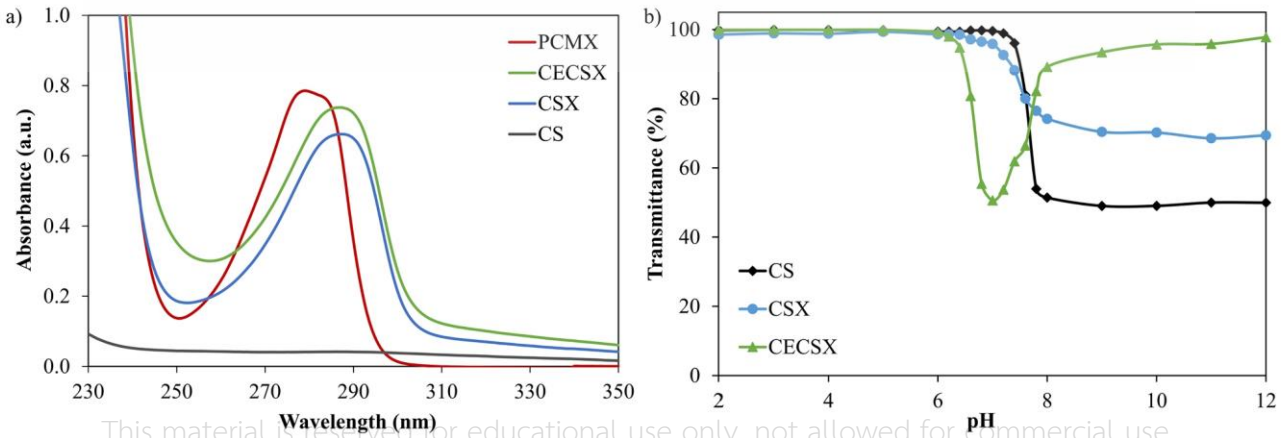

Fig. 2. (a) UV–vis spectra of 0.75 mg/mL of CS, CSX, CECSX and PCMX in 0.1 M HCl, and (b) pH dependent of the 0.75 mg/mL water-solubility of CS, CSX and CECSX in water.

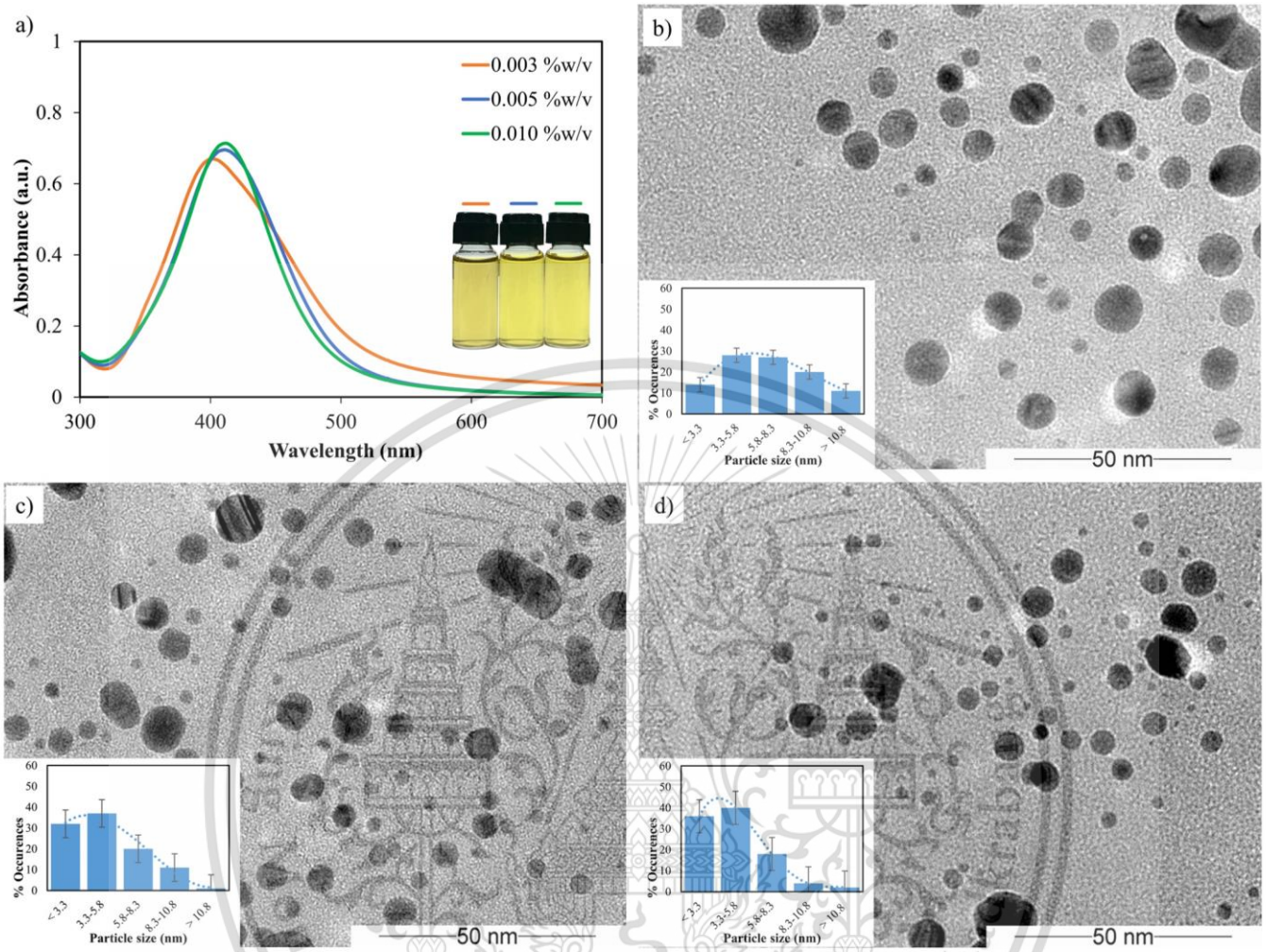

Fig. 3. (a) Absorption spectra with the corresponding photographs and (b-d) TEM images and size distribution of colloidal CECSX-AgNPs with various CECSX concentrations of 0.003 %w/v, 0.005 %w/v and 0.010 %w/v.

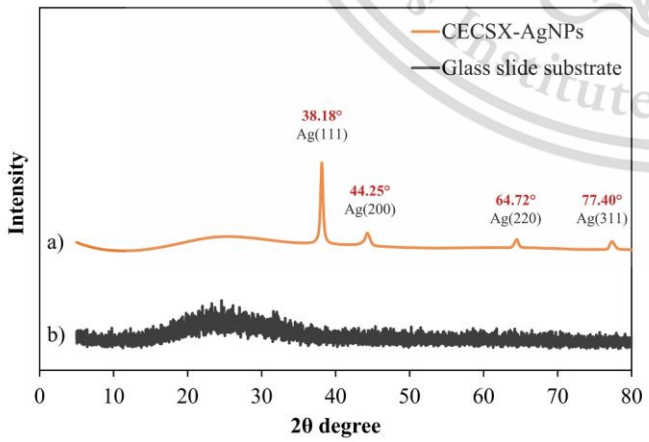

Fig. 4. XRD patterns of a) CECSX-AgNPs coated on glass slide substrate and b) glass slide substrate.

AgNPs. The XRD pattern exhibited 2θ (Bragg reflections) values of 38.18° (111), 44.25° (200), 64.72° (220), and 77.40° (311) corresponding to a spherical structure of face-centered cubic (FCC) lattice. These observations suggested that the crystalline structure of CECSX-AgNPs is in agreement with JCPDS card nos. 65–2871 [37]. The resulting XRD pattern clearly demonstrated that the stabilization of CECSX under reaction conditions caused the silver ions to be reduced to Ag^0 with no peaks of any other impurity crystalline phases visible in the pattern [38].

3.3. *Nanolayer films assemblies of chloroxylenol-carboxyethylchitosan-modified AgNPs*

The aim of this work was the deposition of CECSX-AgNPs onto cotton, polyamide, and polypropylene surgical suture materials using Layer-by-layer (LbL) self-assembly technique by taking advantage of electrostatic interaction between oppositely charged species of negatively charged CECSX-AgNPs and positively charged of PDADMAC. PDADMAC, being a strong polyelectrolyte, possesses a high linear charge density, which enhances the perennial binding of negatively charged CECSX-AgNPs. Glass slides were used as the primary substrates for the fundamental study of nanoparticle adhesion. The surface growth of CECSX-AgNPs with various CECSX concentrations of 0.003 %w/v, 0.005 %w/v, and 0.010 %w/v for synthesized AgNPs were shown in Fig. 5a. The nanolayer films displayed a striking yellow color, confirming the adhesion of CECSX-AgNPs onto the glass slides substrate. In the presence of CECSX, the formation of AgNPs generated a Surface Plasmon Resonance (SPR) characteristic in the range of 450–480 nm. The SPR absorption intensity of AgNPs decreased with the increasing concentrations of CECSX from 0.003 % to 0.010 %w/v. This is probably

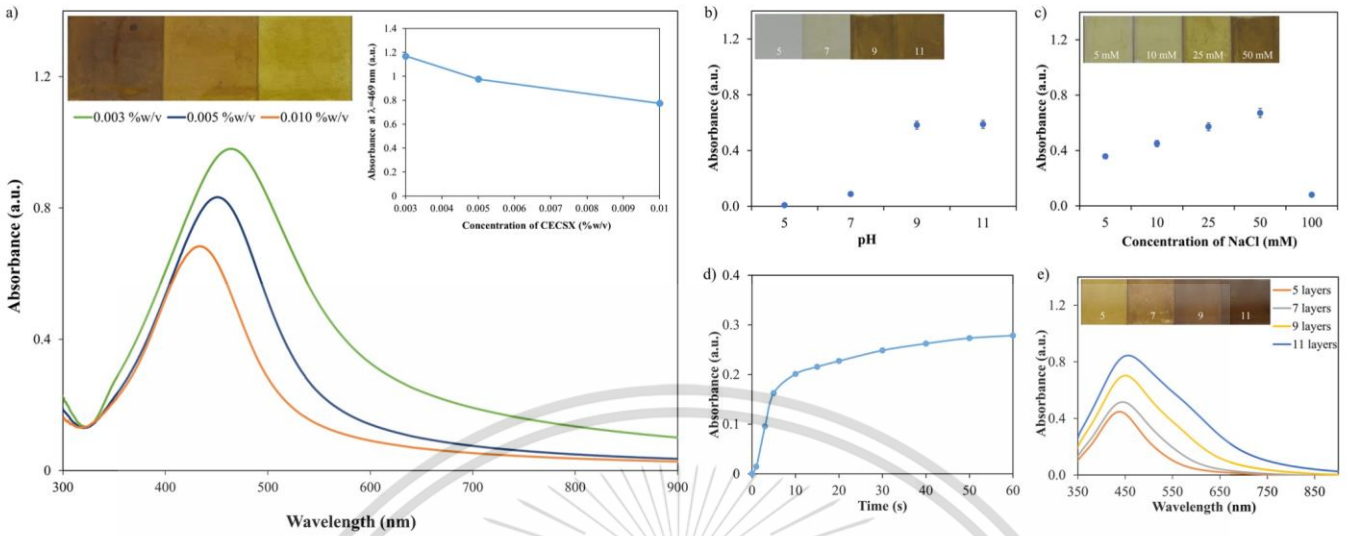

Fig. 5. Nanolayered films buildup of CECSX-AgNPs (a) Absorption spectra of AgNPs as the different CECSX stabilizing concentration, (b) Effect of pH, (c) Effect of NaCl ionic strength concentration, (d) Effect of Adsorption time, and (e) Effect of number of layers.

the result of higher electrostatic charges and higher electrostatic repulsion between nanoparticles, leading to a low packing of nanoparticles.

To achieve high adhesion of CECSX-AgNPs onto the glass slide substrate, the experimental conditions influencing the adsorption of nanoparticles based on LBL assembled technique were investigated. The LbL parameters affecting nanofilms growth including pH, time, ionic strength, and the number of layers were investigated. For the optimization of each parameter, 0.005 % w/v of CECSX stabilized AgNPs was chosen to investigate the adhesion of AgNPs onto the glass slide substrate surface. The growth of CECSX-AgNPs nanolayer films was monitored by UV–vis spectrophotometer. As shown in Fig. 5b, the pH effect of CECSX-AgNPs on the LbL adhesion was investigated at pH values of 5, 7, 9, and 11. It was observed that at pH 9, CECSX-AgNPs exhibited sufficient strong adhesion onto the glass slide substrate. Further increase in pH did not lead to any increase in the film adhesion properties. In contrast, when the pH of CECSX-AgNPs was adjusted to neutral or acidic medium, the film adhesion ability performed less effectively due to the loss of the negative charge on the nanoparticle surface. Another important aspect of the LbL adsorption of CECSX-AgNPs is ionic strength. As shown in Fig. 5c, colloidal CECSX-AgNPs were mixed with various concentrations of NaCl of 5, 10, 25, 50, and 100 mM. In this study, for the lowest salt concentrations (5, 10, and 25 mM), the LbL build-up was shown in a constant linear fashion. At 50 mM NaCl concentration, the CECSX-AgNPs adhesion response reached a maximum probably because strong charge density ensures strong film growth, thus providing an excellent bonding candidate. In contrast, at 100 mM NaCl concentration, CECSX-AgNPs were precipitated. Therefore, 50 mM of NaCl concentration was selected to enhance the adhesion of CECSX-AgNPs growth onto the substrate. Another optimization of CECSX-AgNPs film buildup was performed on adsorption time (Fig. 5d). The glass slides were immersed in CECSX-AgNPs solutions for various durations ranging from 1 to 60 min. Immersing the CECSX-AgNPs film for 10 min resulted in complete adhesion of the nanoparticles to the film layer. Extending the immersion time did not lead to a significant enhancement in adhesion. Finally, to improve the adhesion efficiency of CECSX-AgNPs nanolayer films, the study of the number of layers is imperatively carried out. The increase in the number of layers as the function of absorbance was shown in Fig. 5e. It is evident that after a few layers are deposited, the absorbance increases steadily with each layer of deposition because the amount of CECSX-AgNPs being deposited for each dipping cycle is constant. The morphology and smoothness of nanolayer film assemblies of CECSX-AgNPs at the different number of layers were also investigated. The AFM images shown in Fig. 6 present the surface topography of the CECSX-AgNPs nanolayer films, implying that the CECSX-AgNPs/PDADMAC composite leads to closely packed aggregations with Van der Waals interactions. The root-mean-square (RMS) roughness values of CECSX–AgNPs with 5, 7, 9, and 11 layers were measured at 5.11, 6.01, 6.19, and 6.79 nm, respectively. The RMS roughness values increased with the number of layers due to the accumulation of imperfections with each additional layer. Increasing the roughness value results in the creation of a larger surface area with higher surface energy, which can contribute to the development of hydrophobic surfaces. For reference, the contact angle of suture-coated CECSX-AgNPs was also explored in this study and shown in Supporting Information Fig. S1. Normally, cotton and polyamide are hydrophilic materials. However, following treatment with CECSX-AgNPs, these materials transform into a hydrophobic state. The contact angle of CECSX-AgNPs coated on cotton and polyamide reached 127° and 143°, respectively. In the case of polypropylene, which inherently possesses hydrophobic properties, the contact angle was altered from 131° to 136° after the deposition of CECSX-AgNPs.

The goal of this research was to deposit colloidal CECSX-AgNPs onto surgical suture materials using the LbL self-assembly technique to improve antimicrobial activities. The negatively charged CECSX-AgNPs colloidal solution was immobilized onto three kinds of surgical sutures including cotton, polyamide, and polypropylene. To control LBL growth, the advantage of the electrostatic interaction between negatively charged CECSX-AgNPs can then be self-assembled into a nano thin film in the sequence with positively charged PDADMAC. The best optimum conditions for on nanolayer film assemblies of CECSX-AgNPs, including CECSX-AgNPs pH 9, 50 mM NaCl ionic strength, 10 min of adhesion time, and 11 layers were chosen to fabricate nanolayer films onto suture materials. Moreover, the surface morphology of CECSX-AgNPs obtained by the AFM implied that the surface was smooth and uniform, which can be useful in the suture coating process. In Fig. 7, the FESEM images of three kinds of surgical sutures including cotton, polyamide, and polypropylene coated with CECSX-AgNPs are shown. It was found that CECSX-AgNPs were deposited with high-density coating on the suture surface. The deposited CECSX-AgNPs with tunable SPR endow the cotton, polyamide, and polypropylene surgical sutures with abundant color. Optimistic colors were observed revealing a change in the surgical sutures surface color to yellowish brown on cotton and brownish on both polyamide, and polypropylene. Additionally, the results from EDS confirmed the presence of CECSX-AgNPs, which are well distributed on the surface of the surgical sutures. This result implies that the LbL

Number of layer	Morphological Evolution		RMS Roughness (nm)
	Two dimensional (scanned at 1 μm)	Three dimensional (scanned at 5 μm)	
5	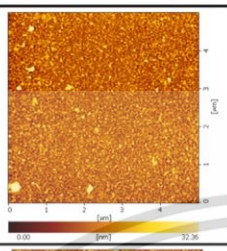	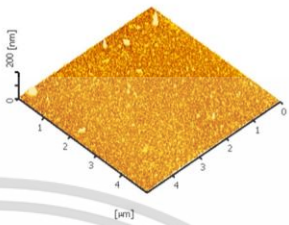	5.11
7	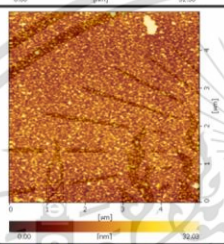	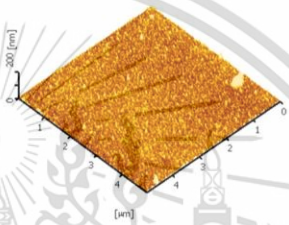	6.01
9	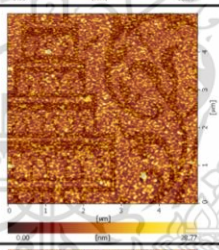		6.19
11	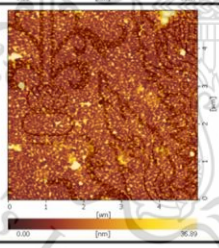	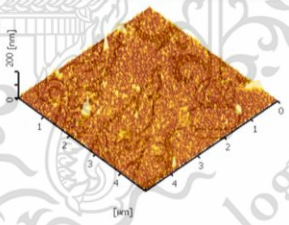	6.79

Fig. 6. AFM images of CECSX-AgNPs/PDADMAC multilayer films as the function of number of layers.

method, using the advantages of electrostatic interaction between negatively charged CECSX-AgNPs and positively charged PDADMAC, can be assembled onto the surfaces of cotton, polyamide, and polypropylene surgical sutures.

3.4. Antimicrobial assay

3.4.1. Minimum inhibitory concentration (MIC) and minimum bactericidal concentration (MBC) assay

The antibacterial activities of CS, CECSX, and CECSX-AgNPs were determined by microdilution method through MIC and MBC values, as shown in Table 1. MIC represents the lowest concentration at which bacterial growth was inhibited, while MBC signifies the lowest concentration causing bacterial cell death. The effect of introducing PCMX into the CS structure was studied at pH=4. The results indicated that CSX exhibited higher activity than CS, with MIC values improving from 200 to 100 mg/L against *S. aureus* (ATCC25923) and 100–50 mg/L against *A. baumannii* (ATCC19606), respectively. Increasing the hydrophobic properties of CS leads to better interaction with the hydrophobic regions of the bacterial cell membrane, aiding in membrane disruption and enhancing antimicrobial activity [14,16,18]. These results suggest that adding PCMX groups to the CS structure resulted in improved antibacterial properties against *S. aureus* (ATCC25923) and *A. baumanii* (ATCC19606).

Furthermore, under neutral conditions (pH=6.5–7.0), CECSX demonstrates superior antimicrobial activity compared to CS, CSX and carboxyethylchitosan (CECS). Prior to chemical structure modification, CS was precipitated in a neutral state of pH rendering it ineffective against various bacteria. To solve the insolubility of chitosan at neutral pH, water-soluble chitosan derivatives were synthesized to improve dispersion in an aqueous medium, enabling a more even distribution of the antimicrobial agent. It is evident that CECSX demonstrates the most potent antibacterial effect at neutral pH against *E. coli* (ATCC25922), *S. aureus* (ATCC25923), and *A. baumanii* (ATCC19606), with MIC values found to be 400, 200, and 400 mg/L, respectively. Due to their amphiphilic nature, the synthesized CECSX can operate with both hydrophobic and hydrophilic properties onto the polymer skeleton. The hydrophobic moieties of CECSX favorably interact with the hydrophobic regions of bacterial cell membranes, while the water–soluble components of CECSX improve the dispersion and solubility of CS in aqueous environments. As a results, CECSX can adhere to microbial cells causing cell lysis, or inhibit cell transduction. Notably, at its isoelectric point in

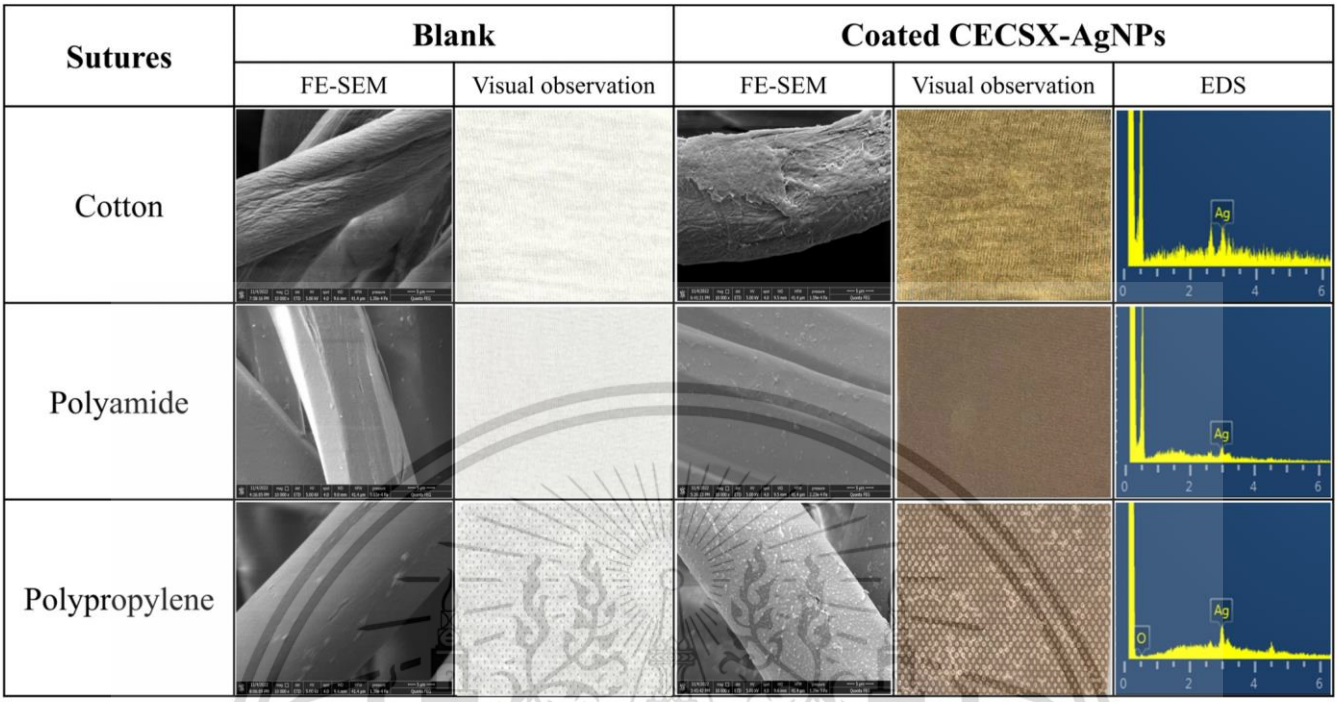

Fig. 7. FESEM images, visual observation, and EDS of CECSX-AgNPs/PDADMAC coated on cotton, polyamide, and polypropylene surgical sutures.

Table 1
MIC and MBC values of CS, CECSX, CECSX-AgNPs by microdilution method in acidic (pH=4.0) and neutral conditions (pH=6.5–7.0).

Synthesis materials	*E. coli* (ATCC25922)		*S.aureus* (ATCC25923)		*A. baumannii* (ATCC19606)	
	MIC (mg/L)	MBC (mg/L)	MIC (mg/L)	MBC (mg/L)	MIC (mg/L)	MBC (mg/L)
pH = 4.0						
CS	200	200	200	200	100	100
CSX	200	200	100	200	50	100
pH = 6.5–7.0						
CS[a]	ND	ND	ND	ND	ND	ND
CSX[a]	ND	ND	ND	ND	ND	ND
CECS[b]	ND	ND	ND	ND	-	-
CECSX	400	>400	200	400	400	>400
CECSX-AgNPs	25	25	12.5	25	1.56	1.56

ND = Not detected
- = Not studied
[a] = Precipitation stage
[b] = Antimicrobial resistant up to 0.5 %w/v

neutral pH, CECSX possesses both negative charges (COO^-) and positive charges (NH_3^+). This dual charge characteristic enables it to inhibit a wide range of bacteria, including both gram-negative and gram-positive species.

Moreover, numerous research studies have focused on the antimicrobial activity using AgNPs. AgNPs with CS derivatives have been utilized as potent antibacterial agents. However, the antibacterial activity of nanoparticles is influenced by various factors, including size, shape, surface charges, and functionalization [7,39]. Therefore, CECSX-AgNPs which possess both functionalized negatively and positively surface charges and small particle sizes can adhere to microbial surface layers and disrupt their structural integrity and functions. In gram-positive bacteria, the negative charges of CECSX on the AgNPs surface primarily interact with the thicker peptidoglycan layers, resulting in an MIC value of 12.5 mg/L against *S. aureus* (ATCC25923). Conversely, gram-negative bacteria have both an outer membrane and thin peptidoglycan layers. The positively charges of CECSX on the AgNPs surfaces primarily interact with and disrupt their outer membrane, increasing permeability and leading to eventual cell death [40]. These results in MIC values were found to be 25 mg/L and 1.56 mg/L against *E. coli* (ATCC25922) and *A. baumanii* (ATCC19606), respectively. Based on these observations, CECSX-stabilized AgNPs can be used as an antibacterial agent for microorganisms.

3.4.2. *In vitro time-kill study*

Antimicrobial agents on strains of microorganisms of CECSX-AgNPs coated on cotton, polyamide, and polypropylene surgical sutures dependent on time were determined by the time-kill assay, as shown in Table 2. For *E. coli* (ATCC25922), *S. aureus* (ATCC25923) and *A. baumanii* (ATCC19606) microorganisms, CECSX-AgNPs coated on cotton, polyamide, and polypropylene surgical sutures provided better antibacterial performance. CECSX-AgNPs coated on cotton and polyamide showed the highest % of bacterial reduction of 99 %, while CECSX-AgNPs coated on polypropylene had a maximum efficiency of 94 % bacterial reduction. At 6 and 24 h in the *in vitro* time-kill conditions, we observed that *E. coli* (ATCC25922), *S. aureus* (ATCC25923), and *A. baumanii* (ATCC19606) were not significantly affected by

Table 2
Time-kill assay of CECSX-AgNPs coated cotton, polyamide, and polypropylene surgical sutures against *E. coli* (ATCC25922), *S. aureus* (ATCC25923) and *A. baumannii* (ATCC19606).

CECSX-AgNPs coated surgical sutures	Contact time (hr)	Bacterial reduction					
		E. coli (ATCC25922)		*S.aureus* (ATCC25923)		*A. baumannii* (ATCC19606)	
		%	Log	%	Log	%	Log
Cotton	6	99.99	3.82	99.97	3.57	99.99	4.30
	24	90.22	1.00	98.36	1.78	93.47	1.18
Polyamide	6	99.63	2.43	99.99	3.94	99.74	2.58
	24	92.12	1.10	99.01	2.00	89.23	0.96
Polypropylene	6	94.00	1.22	83.07	0.77	94.00	1.22
	24	33.70	0.17	28.57	0.15	37.76	0.20

bacterial reduction. CECSX-AgNPs cause bacterial damage by oxidizing in the presence of oxygen or in an aqueous environment to form silver ions (Ag^+ ions). Electrons are lost from the surface of AgNPs to oxygen or other electron acceptors in the environment. The interaction between Ag^+ ions and bacterial cell membranes results in enhanced permeability and structural damage. The essential functions of microbial cells are disrupted and lead to cell death when silver ions bind to the proteins and DNA in cells.

3.5. Comparison of antibacterial properties with other reported suture materials

Other reported suture materials have been extensively researched and utilized for their potent antibacterial efficacy. A comparison of the antibacterial properties of these materials with previous studies is presented in Table 3. Additionally, a comparative assessment of various colloidal AgNPs is provided in Supporting Information Table S1. In our proposed method, CECSX-AgNPs display significant potential by demonstrating robust antimicrobial activity. Coating the surface of AgNPs with CECSX enhances their functionality as antibacterial agents. Notably, CECSX, serving as a stabilizing agent, proves suitable for synthesizing of AgNPs, making them versatile for a wide range of applications, both in solution and as coating on surgical sutures.

Table 3
Comparison of antibacterial properties of other reported suture coating materials.

Suture coating materials	Microorganisms	MIC (mg/L)	MBC (mg/L)	Ref.
Tricosan	*E. coli*	0.5	-	[41]
	S. aureus	0.025	1	[42]
Menadione	*S. aureus* (ATCC 29213)	16	256	[43]
	S. aureus (ATCC 33591)	8	256	
Totarol	*S. aureus* (ATCC 25923)	64	128	[44]
Eugenol	*S. mutans* (ATCC25171)	250	1000	[45]
SiO_2-CaO-P_2O_5-AgNPs composite	*E. faecalis*	2.5	5	[46]
Securidaca Inappendiculate modified AgNPs	*E. coli*	2	4	[47]
	S. aureus	4	8	
Sodium alginate modified AgNPs	*E. coli* (ATCC 12228)	10	-	[48]
	S. aureus (ATCC6538-P)	12.5	-	
TiO_2-Ag^+	*S. aureus* (ATCC 29213)	2	4	[49]
	E. faecalis (ATCC 29212)	2	4	
Methicillin modified AgNPs	*S. aureus*	11.25	22.50	[50]
CECSX modified AgNPs	*E. coli* (ATCC25922)	25	25	Present work
	S. aureus (ATCC25923)	12.5	25	
	A. baumannii (ATCC19606)	1.56	1.56	

4. Conclusions

In conclusion, surgical sutures design through the Layer-by-Layer assembled (LbL) of CECSX-modified silver nanoparticles (CECSX-AgNPs) exhibited superior antibacterial properties. Chloroxylenol-carboxyethylchitosan (CECSX) was synthesized by incorporating chloroxylenol (PCMX) and acrylic acid onto the chitosan (CS) backbone through Mannich and Michael reactions. The highest substitute values of 8.0 % and 33.0 % of PCMX and acrylic acid have shown great effectiveness as antibacterial and water-soluble properties over pH ranges of 2–12, respectively. CECSX was then incorporated into AgNPs and subsequently coated on the surgical sutures using the LbL technique. The CECSX-AgNPs coated sutures exhibited different antimicrobial activities depending on the type of surgical sutures. The finished CECSX-AgNPs coated cotton and polyamide surgical sutures provided the highest bacterial reduction at 99 %, while polypropylene surgical sutures demonstrated a maximum efficiency of 94 % bacterial reduction against *E. coli* (ATCC25922), *S. aureus* (ATCC25923), and *A. baumanii* (ATCC19606). This suggests that CECSX-AgNPs could serve as a promising alternative material for antimicrobial surgical sutures.

However, it is important to state a limitation of the study: while CECSX-AgNPs have demonstrated antimicrobial effectiveness against both gram-positive and gram-negative bacteria such as *E. coli*, *S. aureus*, and *A. baumanii*, their efficacy against other pathogenic bacteria i.e., *M. luteus*, *B. subtilis*, *S. epidermis*, and *S. lentus* has not been adequately investigated. This quandary warrants further investigation. Additionally, future studies should explore the clinical efficacy and cost-saving effectiveness of CECSX-AgNPs to provide a comprehensive understanding of their potential applications.

CRediT authorship contribution statement

Pakawat Chittratan: Writing – original draft, Methodology, Investigation, Data curation. **Arjnarong Mathaweesansurn:** Writing – review & editing. **Pathavuth Monvisade:** Writing – original draft, Supervision, Methodology, Funding acquisition, Conceptualization. **Ekarat Detsri:** Writing – review & editing, Visualization, Supervision, Data curation, Conceptualization, Formal analysis, Methodology. **Jongjit Chalitangkoon:** Investigation, Data curation.

Declaration of Competing Interest

The authors declare that they have no known competing financial interests or personal relationships that could have appeared to influence the work reported in this paper.

Data availability

No data was used for the research described in the article.

Acknowledgements

This work has received funding support from the National Science, Research and Innovation Fund (NSRF), Grant number RE-KRIS/FF66/55. The authors would like to thank the Scientific Instruments Center, School of Science, King Mongkut's Institute of Technology Ladkrabang for supporting the instruments.

Appendix A. Supporting information

Supplementary data associated with this article can be found in the online version at doi:10.1016/j.colsurfa.2024.133957.

References

[1] Y. Li, Q. Meng, S. Chen, P. Ling, M.A. Kuss, B. Duan, S. Wu, Advances, challenges, and prospects for surgical suture materials, Acta Biomater. 168 (2023) 78–112, https://doi.org/10.1016/j.actbio.2023.07.041.
[2] S. Chaganti, V. Kunthsam, S.Y. Velangini, K.J. Alzahrani, F.M. Alzahrani, I. F. Halawani, M. Alshahrani, H. Ashi, H.A. Baeshen, S. Patil, Comparison of bacterial colonization on absorbable non-coated suture with Triclosan- or Chlorhexidine-coated sutures: a randomized controlled study, Eur. Rev. Med. Pharmacol. Sci. 27 (2023) 8371–8383, https://doi.org/10.26355/eurrev_202309_33760.
[3] A. Thomas, S. Thakur, S. Mhambrey, Comparison of the antimicrobial efficacy of chlorhexidine, sodium fluoride, fluoride with essential oils, alum, green tea, and garlic with lime mouth rinses on cariogenic microbes, J. Int Soc. Prev. Community Dent. 5 (2015) 302–308, https://doi.org/10.4103/2231-0762.161759.
[4] J. Liu, J.-Q. Ling, K. Zhang, L.-J. Huo, Y. Ning, Effect of sodium fluoride, ampicillin, and chlorhexidine on *Streptococcus mutans* biofilm detachment, Antimicrob. Agents Chemother. 56 (2012) 4532–4535, https://doi.org/10.1128/AAC.00885-12.
[5] D. Wang, X. Huang, W. Lv, J. Zhou, The toxicity and antibacterial effects of Povidone-Iodine irrigation in fracture surgery, Orthop. Surg. 14 (2022) 2286–2297, https://doi.org/10.1111/os.13422.
[6] D.M. Syukri, O.F. Nwabor, S. Singh, S.P. Voravuthikunchai, Antibacterial functionalization of nylon monofilament surgical sutures through in situ deposition

of biogenic silver nanoparticles, Surf. Coat. Technol. 413 (2021) 127090, https://doi.org/10.1016/j.surfcoat.2021.127090.
[7] S. Agnihotri, S. Mukherji, S. Mukherji, Size-controlled silver nanoparticles synthesized over the range 5–100nm using the same protocol and their antibacterial efficacy, RSC Adv. 4 (2014) 3974–3983, https://doi.org/10.1039/C3RA44507K.
[8] G.D. Selvaraju, V.R. Umapathy, C. SumathiJones, M. Singh Cheema, D. R. Jayamani, R. Dharani, S. Sneha, M. Yamuna, E. Gayathiri, S. Yadav, Fabrication and characterization of surgical sutures with propolis silver nano particles and analysis of its antimicrobial properties, J. King Saud. Univ. Sci. 34 (2022) 102082, https://doi.org/10.1016/j.jksus.2022.102082.
[9] S.T. Dubas, S. Wacharanad, P. Potiyaraj, Tunning of the antimicrobial activity of surgical sutures coated with silver nanoparticles, Colloids Surf. Physicochem. Eng. Asp. 380 (2011) 25–28, https://doi.org/10.1016/j.colsurfa.2011.01.037.
[10] E. Detsri, J. Popanyasak, Fabrication of silver nanoparticles/polyaniline composite thin films using layer-by-layer self-assembly technique for ammonia sensing, Colloids Surf. Physicochem. Eng. Asp. 467 (2015) 57–65, https://doi.org/10.1016/j.colsurfa.2014.11.019.
[11] M. Rinaudo, Chitin and chitosan: properties and applications, Prog. Polym. Sci. 31 (2006) 603–632, https://doi.org/10.1016/j.progpolymsci.2006.06.001.
[12] V. Kulikouskaya, K. Hileuskaya, A. Kraskouski, I. Kozerozhets, E. Stepanova, I. Kuzminski, L. You, V. Agabekov, Chitosan-capped silver nanoparticles: a comprehensive study of polymer molecular weight effect on the reaction kinetic, physicochemical properties, and synergetic antibacterial potential, SPE Polym. 3 (2022) 77–90, https://doi.org/10.1002/pls2.10069.
[13] E. Mirda, R. Idroes, K. Khairan, T.E. Tallei, M. Ramli, N. Earlia, A. Maulana, G. M. Idroes, M. Muslem, Z. Jalil, Synthesis of chitosan-silver nanoparticle composite spheres and their antimicrobial activities, Polymers 13 (2021) 3990, https://doi.org/10.3390/polym13223990.
[14] P. Chittratan, J. Chalitangkoon, K. Wongsariya, A. Mathaweesansurn, E. Detsri, P. Monvisade, New chitosan-grafted thymol coated on gold nanoparticles for control of cariogenic bacteria in the oral cavity, ACS Omega 7 (2022) 26582–26590, https://doi.org/10.1021/acsomega.2c02776.
[15] W. Cao, J. Yan, C. Liu, J. Zhang, H. Wang, X. Gao, H. Yan, B. Niu, W. Li, Preparation and characterization of catechol-grafted chitosan/gelatin/modified chitosan-AgNP blend films, Carbohydr. Polym. 247 (2020) 116643, https://doi.org/10.1016/j.carbpol.2020.116643.
[16] X. Huang, Y. Pang, Y. Liu, Y. Zhou, Z. Wang, Q. Hu, Green synthesis of silver nanoparticles with high antimicrobial activity and low cytotoxicity using catechol-conjugated chitosan, RSC Adv. 6 (2016) 64357–64363, https://doi.org/10.1039/C6RA09035D.
[17] R. Li, P. Hu, X. Ren, S.D. Worley, T.S. Huang, Antimicrobial N-halamine modified chitosan films, Carbohydr. Polym. 92 (2013) 534–539, https://doi.org/10.1016/j.carbpol.2012.08.115.
[18] Y. Wang, M. Xie, G. Ma, Y. Fang, W. Yang, N. Ma, D. Fang, Q. Hu, F. Pei, The antioxidant and antimicrobial activities of different phenolic acids grafted onto chitosan, Carbohydr. Polym. 225 (2019) 115238, https://doi.org/10.1016/j.carbpol.2019.115238.
[19] J. Chalitangkoon, A. Ronte, P. Monvisade, Carboxyethylation of chitosan-based polymeric dyes for potential pH-sensing applications, J. Taiwan Inst. Chem. Eng. 149 (2023) 105001, https://doi.org/10.1016/j.jtice.2023.105001.
[20] J. Huaytragul, J. Chalitangkoon, P. Monvisade, N. Chotsaeng, Enhancing chitosan solubility in alcohol: water mixtures for film-forming systems releasing with turmeric extracts, J. Taiwan Inst. Chem. Eng. 123 (2021) 293–301, https://doi.org/10.1016/j.jtice.2021.05.020.
[21] H.M. Ibrahim, M. Mostafa, N.G. Kandile, Potential use of N-carboxyethylchitosan in biomedical applications: preparation, characterization, biological properties, Int. J. Biol. Macromol. 149 (2020) 664–671, https://doi.org/10.1016/j.ijbiomac.2020.01.299.
[22] M. Yin, Y. Wang, Y. Zhang, X. Ren, Y. Qiu, T.S. Huang, Novel quaternarized N-halamine chitosan and polyvinyl alcohol nanofibrous membranes as hemostatic materials with excellent antibacterial properties, Carbohydr. Polym. 232 (2020) 115823, https://doi.org/10.1016/j.carbpol.2019.115823.
[23] J. Song, H. Feng, M. Wu, L. Chen, W. Xia, W. Zhang, Preparation and characterization of arginine-modified chitosan/hydroxypropyl methylcellose antibacterial film, Int. J. Biol. Macromol. 145 (2020) 750–758, https://doi.org/10.1016/j.ijbiomac.2019.12.141.
[24] H. Tan, R. Ma, C. Lin, Z. Liu, T. Tang, Quaternized chitosan as an antimicrobial agent: antimicrobial activity, mechanism of action and biomedical applications in orthopedics, Int. J. Mol. Sci. 14 (2013), https://doi.org/10.3390/ijms14011854.
[25] N.A. Mohamed, M.W. Sabaa, A.H. El-Ghandour, M.M. Abdel-Aziz, O.F. Abdel-Gawad, Quaternized N-substituted carboxymethyl chitosan derivatives as antimicrobial agents, Int. J. Biol. Macromol. 60 (2013) 156–164, https://doi.org/10.1016/j.ijbiomac.2013.05.022.
[26] W. Tang, J. Wang, H. Hou, Y. Li, J. Wang, J. Fu, L. Lu, D. Gao, Z. Liu, F. Zhao, X. Gao, P. Ling, F. Wang, F. Sun, H. Tan, Review: application of chitosan and its derivatives in medical materials, Int. J. Biol. Macromol. 240 (2023) 124398, https://doi.org/10.1016/j.ijbiomac.2023.124398.
[27] M.W. Huh, I.-K. Kang, D.H. Lee, W.S. Kim, D.H. Lee, L.S. Park, K.E. Min, K.H. Seo, Surface characterization and antibacterial activity of chitosan-grafted poly (ethylene terephthalate) prepared by plasma glow discharge, J. Appl. Polym. Sci. 81 (2001) 2769–2778, https://doi.org/10.1002/app.1723.
[28] G. Decher, M. Eckle, J. Schmitt, B. Struth, Layer-by-layer assembled multicomposite films, COCIS 3 (1998) 32–39, https://doi.org/10.1016/S1359-0294(98)80039-3.
[29] E. Detsri, P. Seeharaj, C. Sriwong, A sensitive and selective colorimetric sensor for reduced glutathione detection based on silver triangular nanoplates conjugated with gallic acid, Colloids Surf. Physicochem. Eng. Asp. 541 (2018) 36–42, https://doi.org/10.1016/j.colsurfa.2018.01.016.
[30] D. Fischer, Y. Li, B. Ahlemeyer, J. Krieglstein, T. Kissel, In vitro cytotoxicity testing of polycations: influence of polymer structure on cell viability and hemolysis, Biomaterials 24 (2003) 1121–1131, https://doi.org/10.1016/s0142-9612(02)00445-3.
[31] T. McNerney, A. Thomas, A. Senczuk, K. Petty, X. Zhao, R. Piper, J. Carvalho, M. Hammond, S. Sawant, J. Bussiere, PDADMAC flocculation of Chinese hamster ovary cells: enabling a centrifuge-less harvest process for monoclonal antibodies, mAbs 7 (2015) 413–428, https://doi.org/10.1080/19420862.2015.1007824.
[32] L.J.D. Zaneveld, D.P. Waller, R.A. Anderson, C. Chany, II, W.F. Rencher, K. Feathergill, X.-H. Diao, G.F. Doncel, B. Herold, M. Cooper, Efficacy and safety of a new vaginal contraceptive antimicrobial formulation containing high molecular weight poly(sodium 4-styrenesulfonate), Biol. Reprod. 66 (2002) 886–894, https://doi.org/10.1095/biolreprod66.4.886.
[33] J. Chalitangkoon, P. Monvisade, Dual pH/thermal-dependent coloring polymeric dye through Mannich reaction of chitosan: synthesis and characterization, Carbohydr. Polym. 223 (2019) 115049, https://doi.org/10.1016/j.carbpol.2019.115049.
[34] J. Savetsakulanont, J. Chalitangkoon, P. Monvisade, Stimuli-responsive, self-healing, and injectable hydrogels with dual-crosslinked design from phenolphthalein-grafted N-carboxyethyl chitosan, Macromol. Mater. Eng. 306 (2021) 2100287, https://doi.org/10.1002/mame.202100287.
[35] Y. Wu, Y. Yang, Z. Zhang, Z. Wang, Y. Zhao, L. Sun, A facile method to prepare size-tunable silver nanoparticles and its antibacterial mechanism, Adv. Powder Technol. 29 (2018) 407–415, https://doi.org/10.1016/j.apt.2017.11.028.
[36] A. Kumar, C.K. DixitMethods for characterization of nanoparticles Woodhead Publishing , 3 , Advances in nanomedicine for the delivery of therapeutic nucleic acids (Eds.), S. Nimesh, R. Chandra, N. Gupta , in: 2017, in: 43–58, 10.1016/B978-0-08-100557-6.00003-1.
[37] X.Q. He, Y.Y. Cui, Y. Zhang, C.X. Yang, Fabrication of magnetic polydopamine@naphthyl microporous organic network nanosphere for efficient extraction of hydroxylated polycyclic aromatic hydrocarbons and p-nitrophenol from wastewater samples, J. Chromatogr. A 1651 (2021) 462347, https://doi.org/10.1016/j.chroma.2021.462347.
[38] R. Kalaivani, M. Maruthupandy, T. Muneeswaran, A. Hameedha Beevi, M. Anand, C.M. Ramakritinan, A.K. Kumaraguru, Synthesis of chitosan mediated silver nanoparticles (Ag NPs) for potential antimicrobial applications, Front. Med. 2 (2018) 30–35, https://doi.org/10.1016/j.flm.2018.04.002.
[39] Y. Sun, Y. Xia, Shape-controlled synthesis of gold and silver nanoparticles, Science 298 (2002) 2176–2179, https://doi.org/10.1126/science.1077229.
[40] S. Shrivastava, T. Bera, A. Roy, G. Singh, P. Ramachandrarao, D. Dash, Characterization of enhanced antibacterial effects of novel silver nanoparticles, Nanotechnology 18 (2007) 225103, https://doi.org/10.1088/0957-4484/18/22/225103.
[41] W. Zeng, W. Xu, Y. Xu, W. Liao, Y. Zhao, X. Zheng, C. Xu, T. Zhou, J. Cao, The prevalence and mechanism of triclosan resistance in Escherichia coli isolated from urine samples in Wenzhou, China, Antimicrob. Resist. Infect. Control. 9 (2020) 161, https://doi.org/10.1186/s13756-020-00823-5.
[42] M.T. Suller, A.D. Russell, Triclosan and antibiotic resistance in Staphylococcus aureus, J. Antimicrob. Chemother. 46 (2000) 11–18, https://doi.org/10.1093/jac/46.1.11.
[43] C.H. Yap, S.K. Lim, Y.L. Chan, C.F. Chee, S.T. Tay, Potential application of menadione for antimicrobial coating of surgical sutures, Biotechnol. Notes 4 (2023) 20–27, https://doi.org/10.1016/j.biotno.2023.02.001.
[44] J. Reinbold, A.-K. Uhde, I. Müller, T. Weindl, J. Geis-Gerstorfer, C. Schlensak, H.-P. Wendel, S. Krajewski, Preventing surgical site infections using a natural, biodegradable, antibacterial coating on surgical sutures, Molecules 22 (2017) 1570, https://doi.org/10.3390/molecules22091570.
[45] V.A. Carneiro, E.F. Furtado, R.M.B. Cavalcante, M.L. Silva, R.L. Silva, Q.C. Fidelis, F.E.A. Catunda Junior, Inhibition of Streptococcus mutans (ATCC 25175) biofilm formation on eugenol-impregnated surgical sutures, Afr. J. Microbiol. Res. 13 (9) (2019) 168–175, https://doi.org/10.5897/AJMR2018.9044.
[46] J.C. Kung, Y.J. Chen, Y.C. Chiang, C.L. Lee, Y.T. Yang-Wang, C.C. Hung, C.J. Shih, Antibacterial activity of silver nanoparticle (AgNP) confined mesoporous structured bioactive powder against Enterococcus faecalis infecting root canal systems, J. Non-Cryst. Solids 502 (2018) 62–70, https://doi.org/10.1016/j.jnoncrysol.2018.06.030.
[47] T.J. Jayeoye, F.N. Eze, O.O. Olatunde, S. Singh, J. Zuo, O.J. Olatunji, Multifarious biological applications and toxic Hg(2+) sensing potentiality of biogenic silver nanoparticles based on Securidaca inappendiculata hassk stem extract, Int J. Nanomed. 16 (2021) 7557–7574, https://doi.org/10.2147/ijn.s325996.
[48] R. Augustine, K. Rajarathinam, Synthesis and characterization of silver nanoparticles and its immobilization on alginate coated sutures for the prevention of surgical wound infections and the in vitro release studies, Int J. Nano Dimens 2 (2012) 205–212.
[49] V. Puca, T. Traini, S. Guarnieri, S. Carradori, F. Sisto, N. Macchione, R. Muraro, G. Mincione, R. Grande, The antibiofilm effect of a medical device containing TIAB on microorganisms associated with surgical site infection, Molecules 24 (2019) 2280, https://doi.org/10.3390/molecules24122280.
[50] M.A. Ansari, H.M. Khan, A.A. Khan, S.S. Cameotra, M.A. Alzohairy, Anti-biofilm efficacy of silver nanoparticles against MRSA and MRSE isolated from wounds in a tertiary care hospital, Indian J. Med. Microbiol. 33 (2015) 101–109, https://doi.org/10.4103/0255-0857.148402.

Appendix C

Synthesis and Characterization

C1. NMR of CST

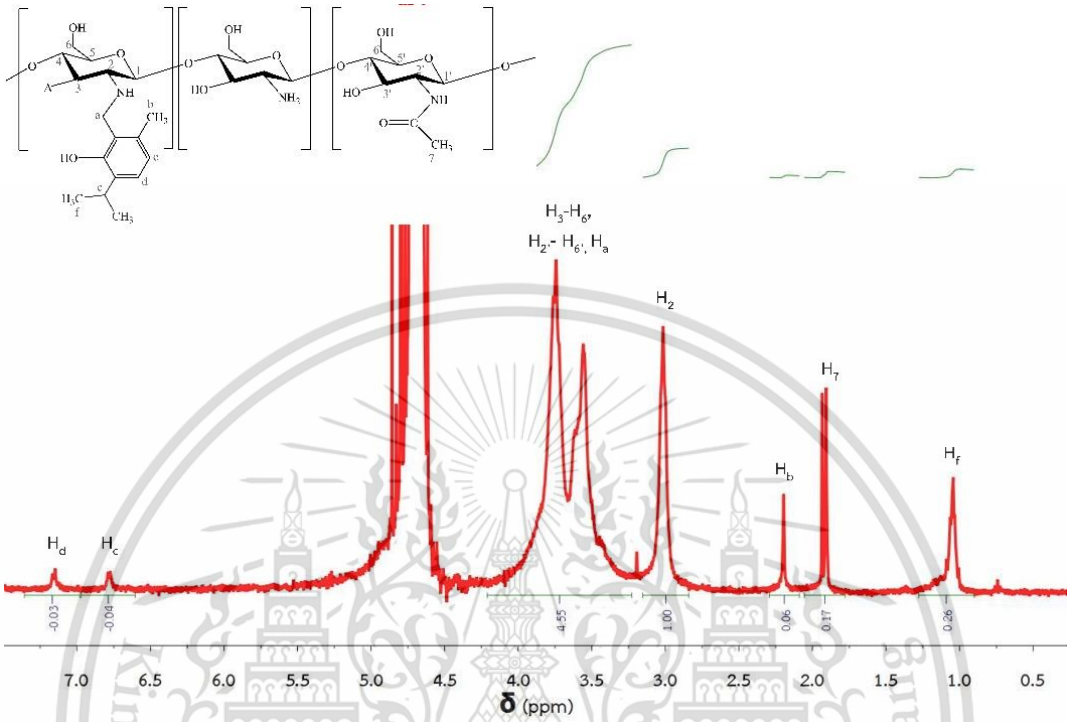

Figure C1 ^{1}H NMR spectra of CST 1.0 : 0.5 : 0.5 mol in CF_3COOH/D_2O.

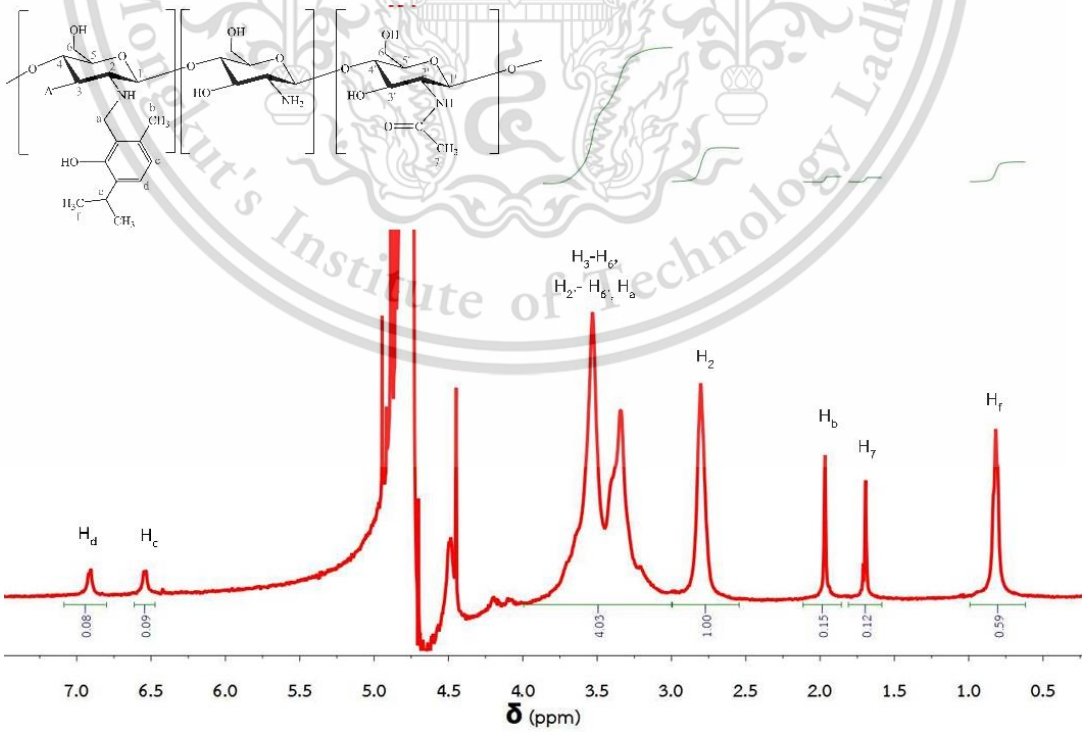

Figure C2 ^{1}H NMR spectra of CST 1.0 : 0.5 : 1.0 mol in CF_3COOH/D_2O.

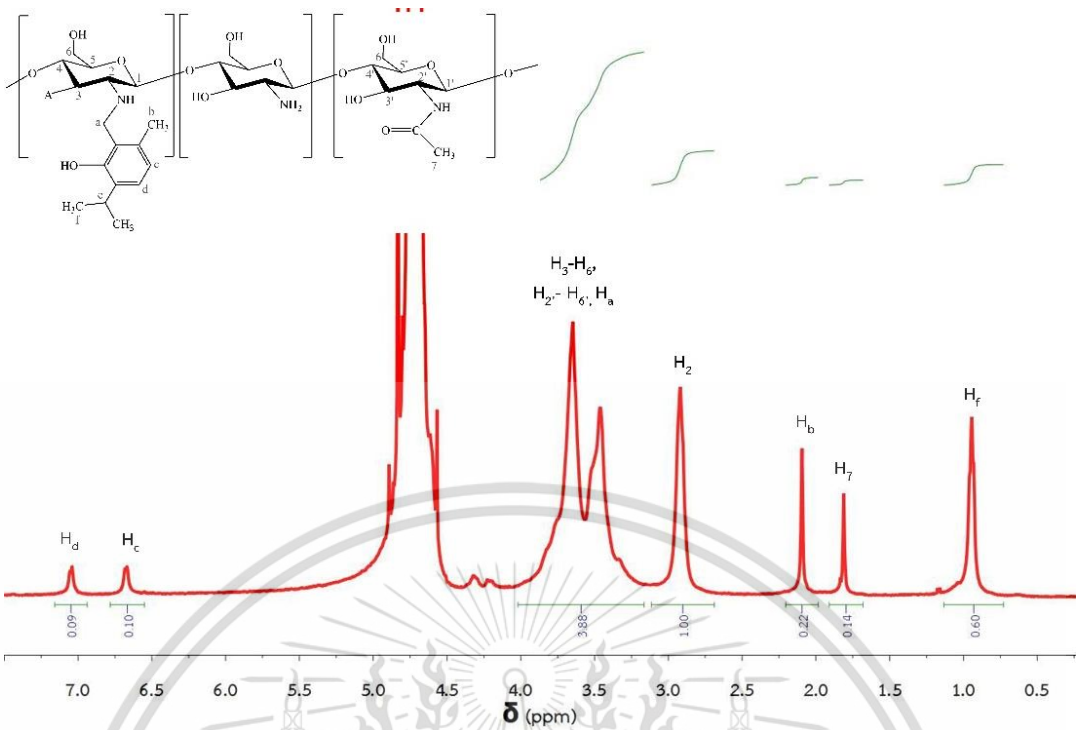

Figure C3 ^{1}H NMR spectra of CST 1.0 : 0.5 : 2.0 mol in CF_3COOH/D_2O.

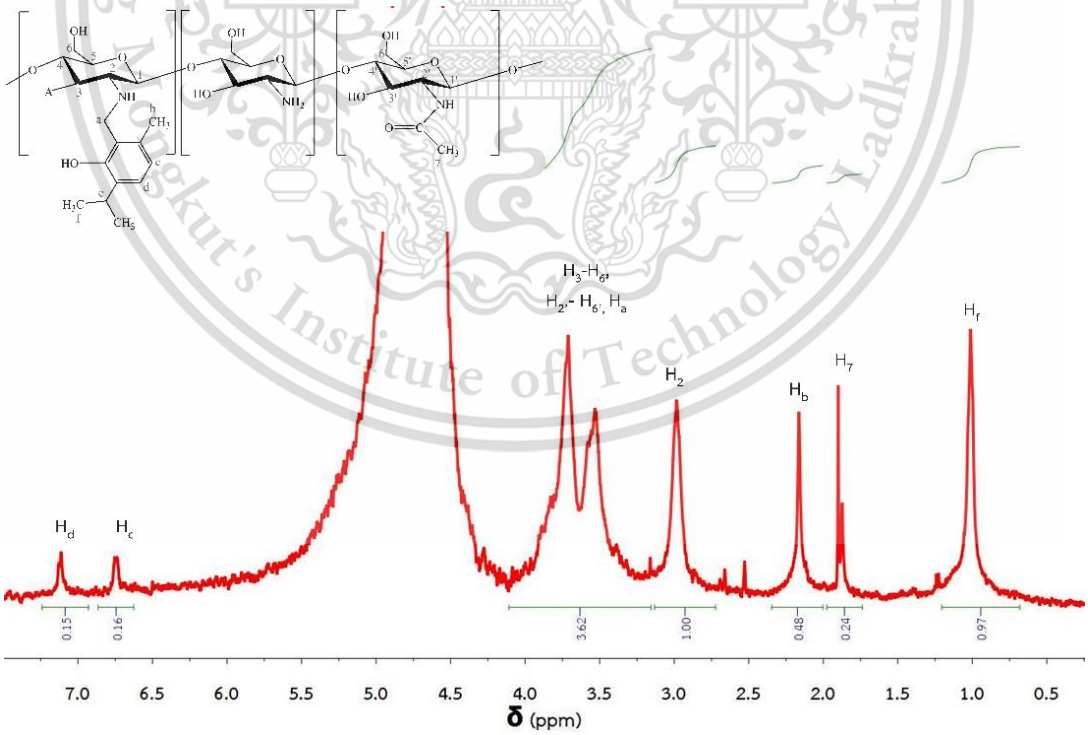

Figure C4 ^{1}H NMR spectra of CST 1.0 : 1.0 : 1.0 mol in CF_3COOH/D_2O.

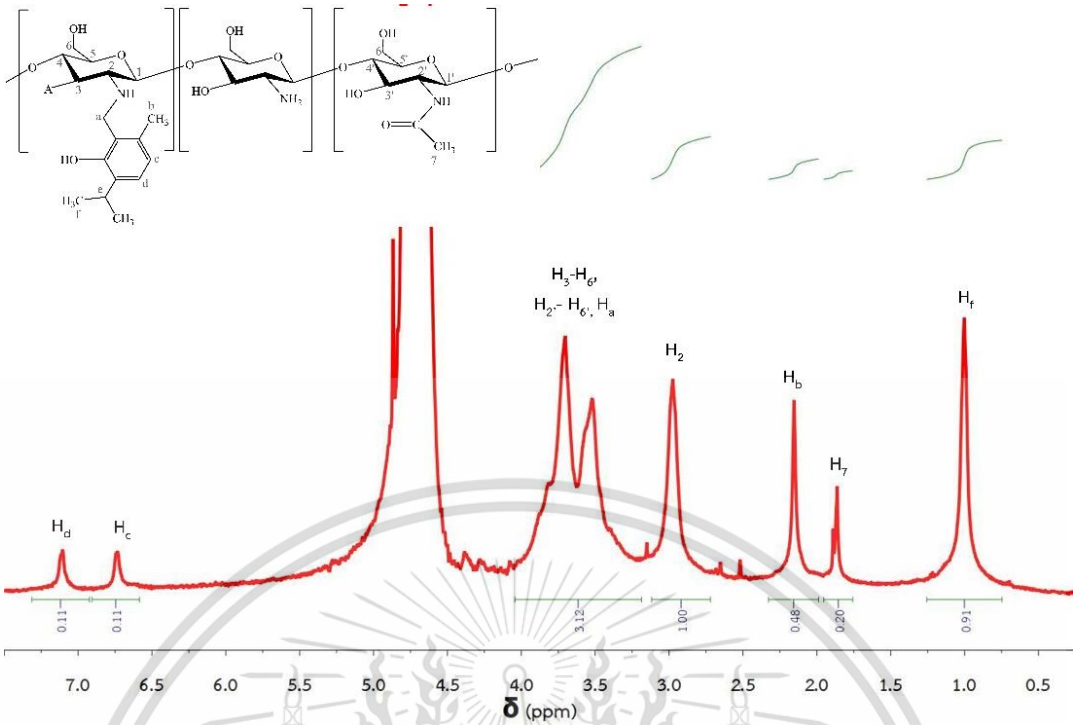

Figure C5 ^{1}H NMR spectra of CST 1.0 : 1.0 : 2.0 mol in CF_3COOH/D_2O.

The $\%DS_{NMR}$ can be obtained from the the peak area of the H_b position or H_f position as follows equations:

$$\%DS_{NMR} = \frac{H_b/3}{H_2} \times 100 \qquad \text{eq. C1}$$

$$\%DS_{NMR} = \frac{H_f/6}{H_2} \times 100 \qquad \text{eq. C2}$$

Table C1. Peak area of H_2, H_b and H_f in CST structure and $\%DS_{NMR}$ obtained from ^{1}H NMR.

Mole ratio of Chitosan : Formaldehyde : Thymol	H_2	H_b	H_f	%DS (H_b)	%DS (H_f)
1.0 : 0.5 : 0.5	1.00	0.06	0.26	2.0%	4.3%
1.0 : 0.5 : 1.0	1.00	0.15	0.59	5.0%	9.8%
1.0 : 0.5 : 2.0	1.00	0.22	0.60	7.3%	10.0%
1.0 : 1.0 : 1.0	1.00	0.48	0.97	16.0%	16.2%
1.0 : 1.0 : 2.0	1.00	0.48	0.91	16.0%	15.2%

C2. NMR of CSX

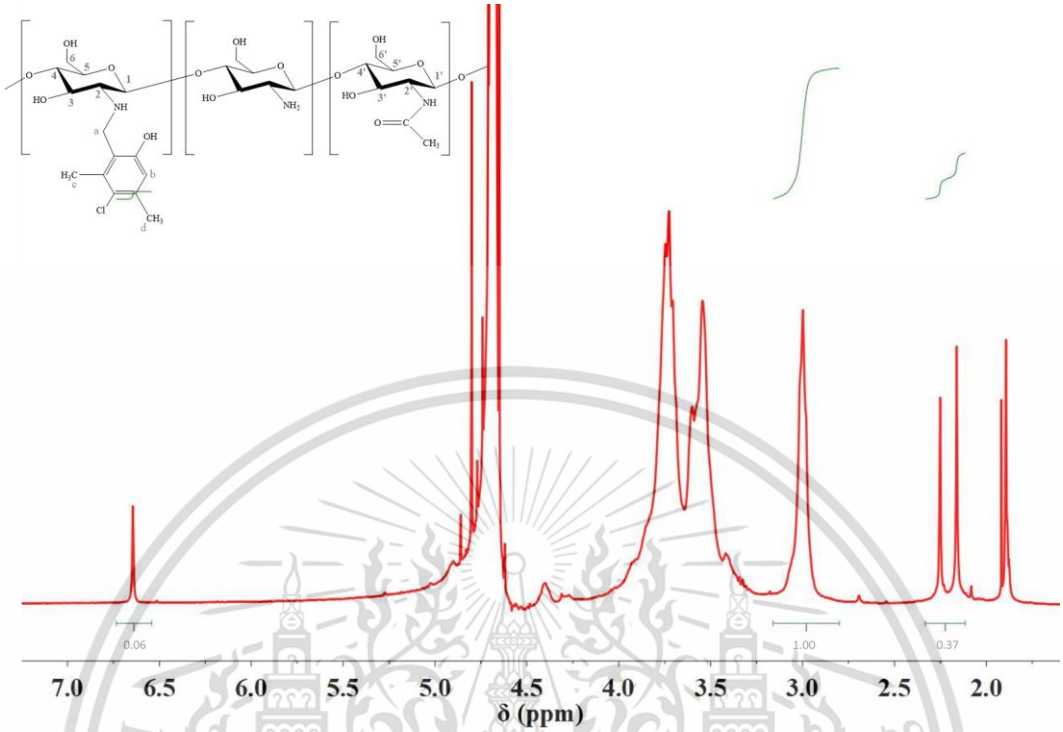

Figure C6 ^{1}H NMR spectra of HCSX 1.0 : 1.0 : 1.0 mol in CF_3COOH/D_2O.

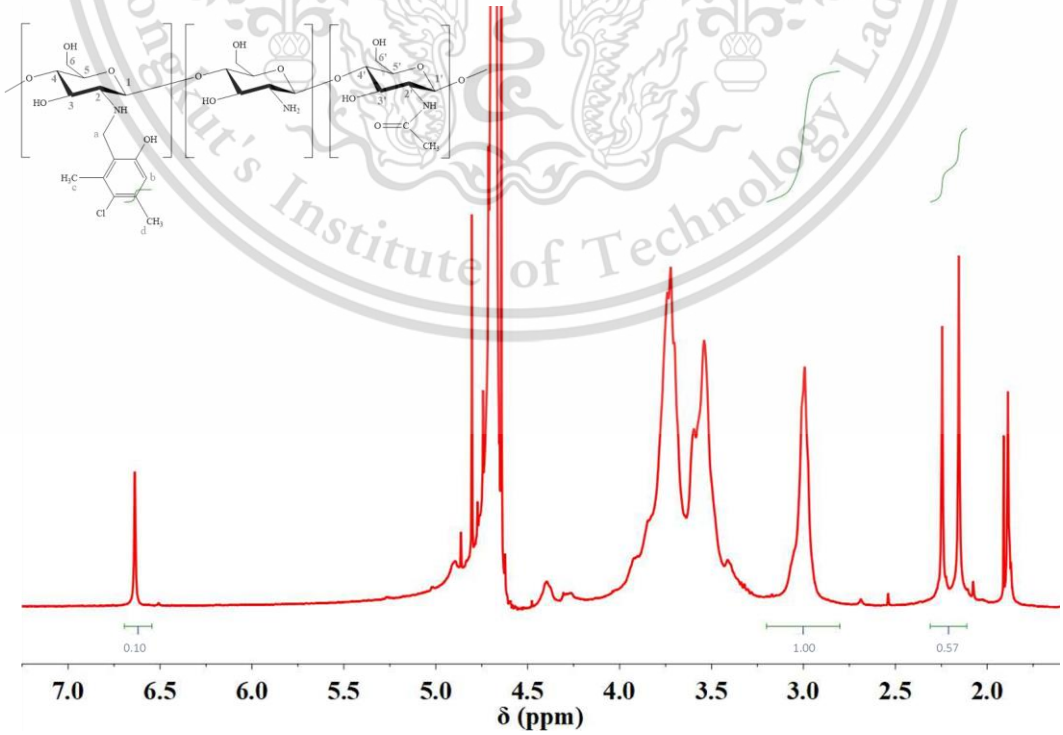

Figure C7 ^{1}H NMR spectra of HCSX 1.0 : 1.0 : 2.0 mol in CF_3COOH/D_2O.

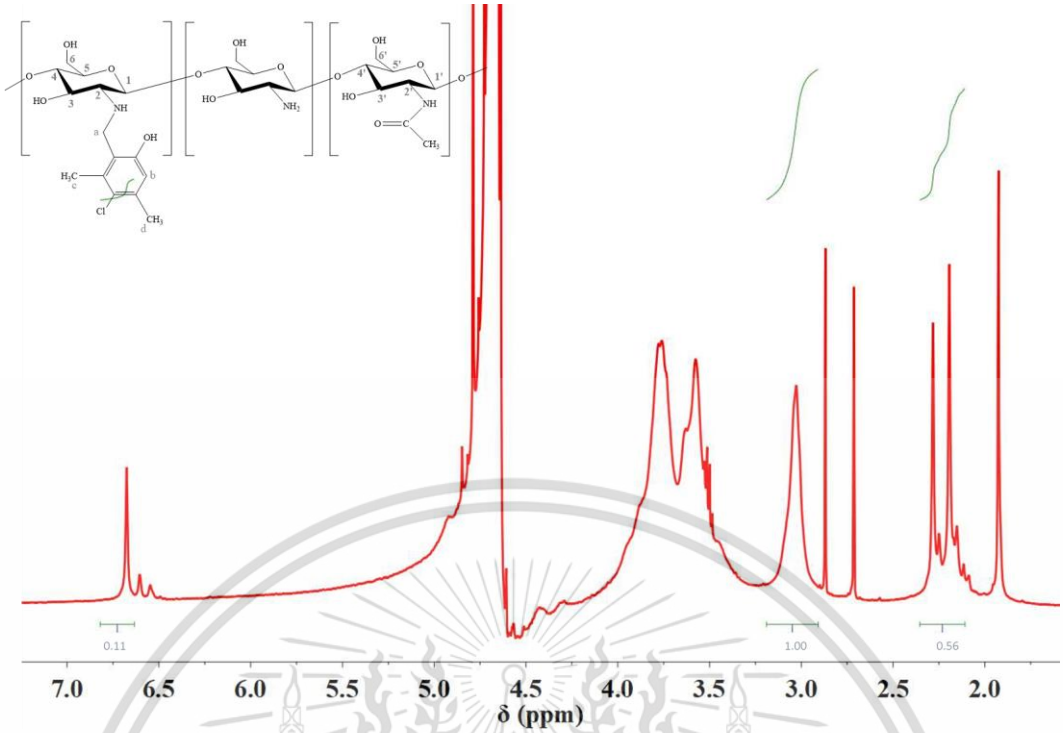

Figure C8 ^{1}H NMR spectra of HCSX 1.0 : 1.0 : 4.0 mol in CF_3COOH/D_2O.

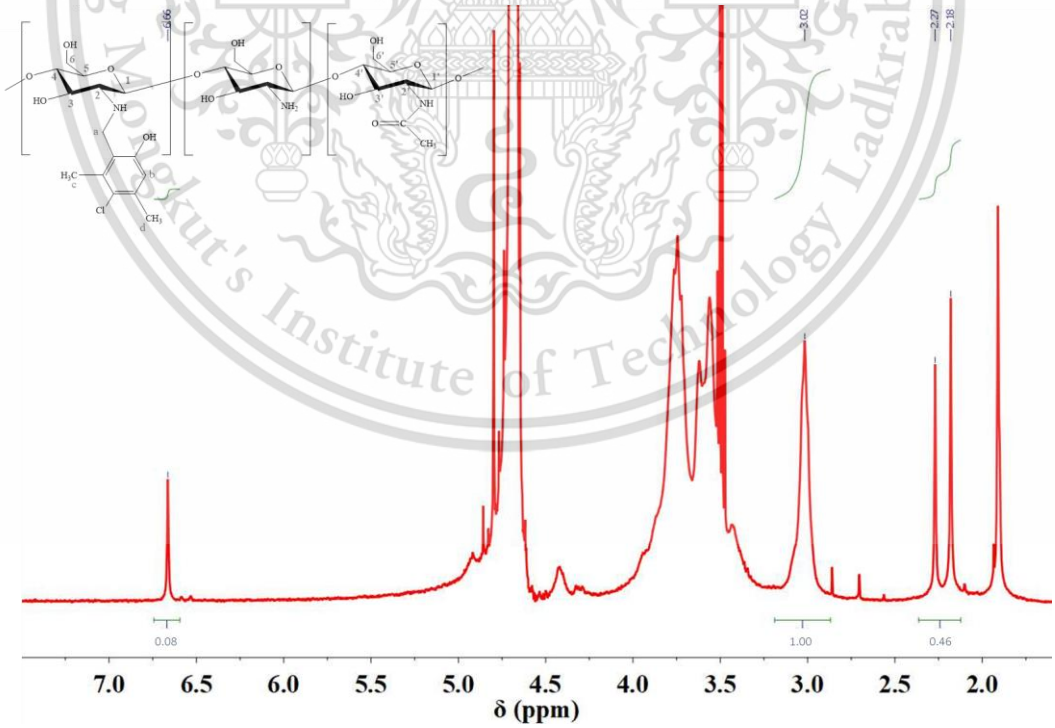

Figure C9 ^{1}H NMR spectra of LCSX 1.0 : 1.0 : 1.0 mol in CF_3COOH/D_2O.

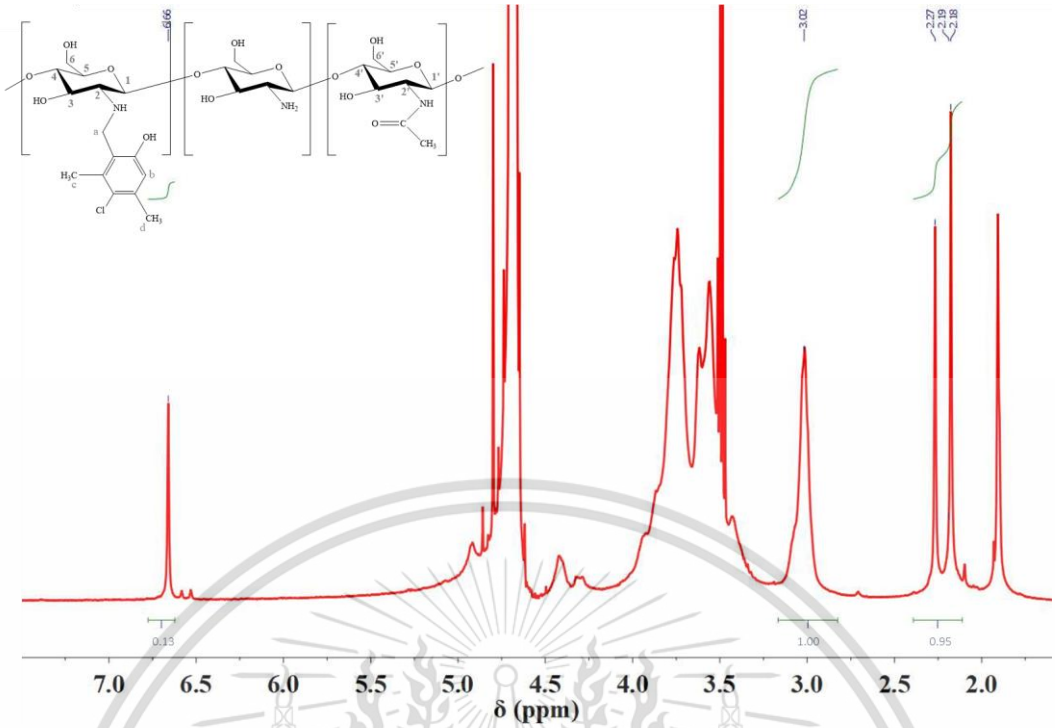

Figure C10 ^{1}H NMR spectra of LCSX 1.0 : 1.0 : 2.0 mol in CF_3COOH/D_2O.

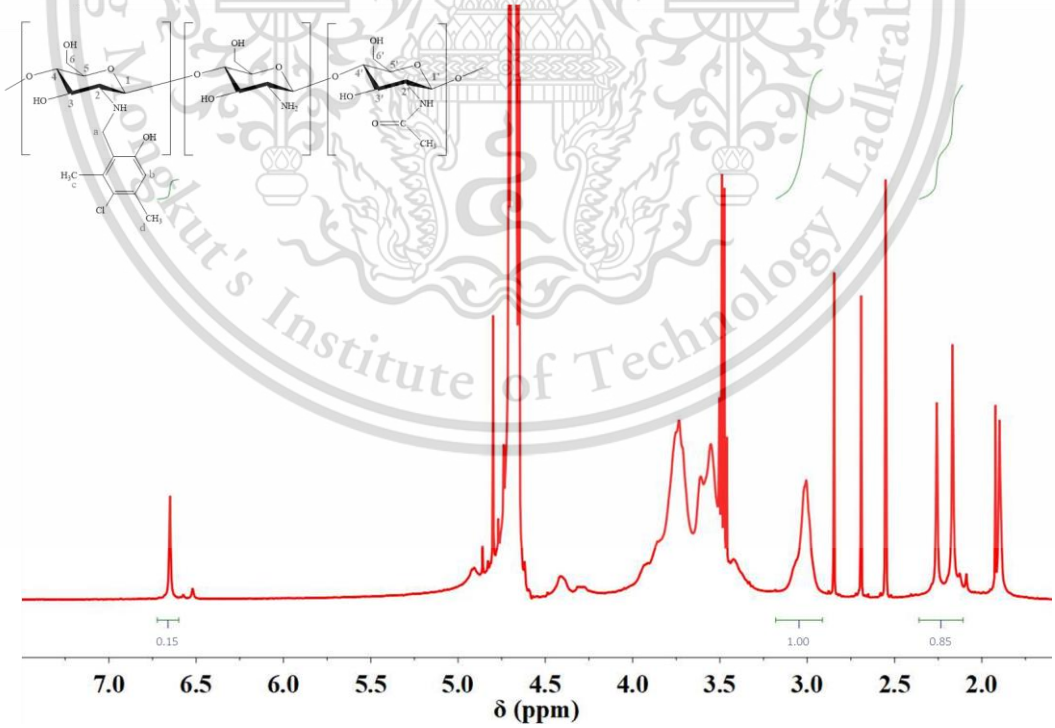

Figure C11 ^{1}H NMR spectra of LCSX 1.0 : 1.0 : 4.0 mol in CF_3COOH/D_2O.

The $\%DS_{NMR}$ can be obtained from the the peak area of the $H_{c,d}$ position or H_b position as follows equations:

$$\%DS_{NMR} = \frac{H_{c,d}/6}{H_2} \times 100 \qquad \text{eq. C3}$$

$$\%DS_{NMR} = \frac{H_b}{H_2} \times 100 \qquad \text{eq. C4}$$

Mole ratio of Chitosan : Formaldehyde : PCMX	H_2	$H_{c,d}$	H_b	**%DS ($H_{c,d}$)**	**%DS (H_b)**
HCSX					
1.0 : 1.0 : 1.0	1.00	0.37	0.06	6.2%	6.0%
1.0 : 1.0 : 2.0	1.00	0.57	0.10	9.5%	10.0%
1.0 : 1.0 : 4.0	1.00	0.56	0.11	9.3%	11.0%
LCSX					
1.0 : 1.0 : 1.0	1.00	0.46	0.08	7.7%	8.0%
1.0 : 1.0 : 2.0	1.00	0.95	0.13	15.8%	13.0%
1.0 : 1.0 : 4.0	1.00	0.85	0.15	14.2%	15.0%

Appendix D

Calculation of %DS, average molecular weight per repeating unit and %yield using data from ^{1}H-NMR spectra

In this section, methods for estimating %DS, average molecular weight per repeating unit, and %yield of each product were presented. Calculation was achieved using integration information from ^{1}H-NMR spectra.

D1. CST (Chitosan-g-thymol)

D1-1 Chitosan (High Mw): Before calculating average molecular weight per repeating unit of CST average molecular weight per repeating unit of CS used in the reaction was needed to be firstly determined. It should be mentioned again that CS is the product from deacetylation of chitin as illustrated in Figure D-1

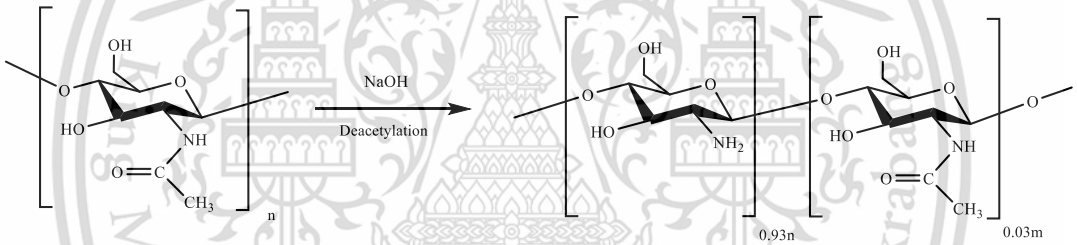

Figure D-1 Deacetylation reaction of chitin.

Therefore, average molecular weight per repeating unit of CS could be determined as equation D-1

Mw per repeating unit of CS = $(Mw_{acetyl}-(43 \times 0.93)) + (Mw_H \times 0.93)$ (D-1)

= (203-40) + (1x0.93)

= 164

D1-2 CST (1.0 : 0.5 : 1.0)

Average molecular weight per repeating unit of CS (1.0 : 0.5 : 1.0) could be determined as equation B-2

Mw per repeating unit of CST = $(Mw_{CS}-(Mw_H \times 0.10)) + (Mw_{Thymol} \times 0.10)$ (D-2)

= (164-1(0.10)) + (150.22x0.10)

= 179

%Yield

Determining theoretical weight of CST

$$W_{CST} = 1\ g\ CS\ x\ \frac{1molCS}{164gCS} \times \frac{179gCST}{1molCST} \quad (D\text{-}3)$$

$$= 1.09\ g$$

%Yield of products could be calculated by equation D-4:

$$\%Yield = \frac{Actual.Weight}{Theroretical.Weight} \times 100 \quad (D\text{-}4)$$

After the reaction. 1.12 g of product was obtained. Therefore,

$$\%Yield = \frac{0.92}{1.09} \times 100$$

$$= 84\ \%$$

D2. CSX (Chitosan-g-PCMX)

D2-1 High Mw Chitosan (see D1-1)

D2-2 HCSX

Average molecular weight per repeating unit of HCSX (1.0 : 1.0 : 2.0, $\%DS_{NMR}$=9.5%) could be determined as equation D-5

$$Mw\ per\ repeating\ unit\ of\ HCSX = (Mw_{CS}-(Mw_H \times 0.095)) + (Mw_{PCMX} \times 0.095) \quad (D\text{-}5)$$

$$= (164-(1x.095)) + (156.61x0.095)$$

$$= 179$$

%Yield

Determining theoretical weight of HCSX

$$W_{CST} = 1\ g\ CS\ x\ \frac{1molCS}{164gCS} \times \frac{179gCSX}{1molCSX} \quad (D\text{-}6)$$

$$= 1.09\ g.$$

%Yield of products could be calculated by equation D-4:

$$\%\text{Yield} = \frac{\text{Actual.Weight}}{\text{Theroretical.Weight}} \times 100$$

After the reaction. 0.89 g of product was obtained. Therefore,

$$\%\text{Yield} = \frac{0.89}{1.09} \times 100$$

$$= 81\%$$

D2-3 Low Mw Chitosan (LCS)

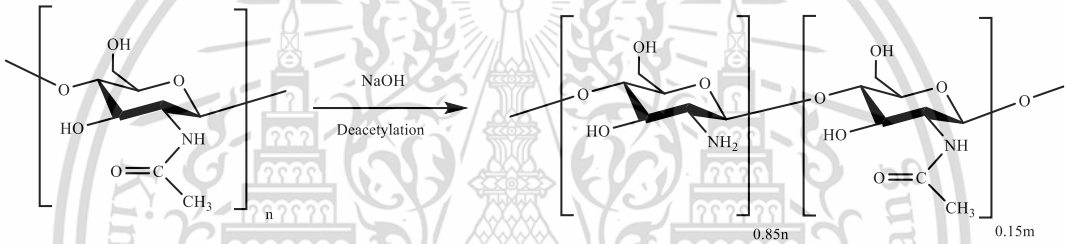

Figure D-2 Deacetylation reaction of chitin

Average molecular weight per repeating unit of LCS could be determined as equation D-7

Mw per repeating unit of CS $= (Mw_{acetyl}\text{-}(43 \times 0.85)) + (Mw_H \times 0.85)$ (D-7)

$= (203\text{-}36.55) + (1\text{x}0.85)$

$= 167$

D2-4 LCSX

Average molecular weight per repeating unit of LCSX (1.0 : 1.0 : 2.0, $\%DS_{NMR}$=15.8%) could be determined as equation D-8

Mw per repeating unit of LCSX $= (Mw_{CS}\text{-}(Mw_H \times 0.158)) + (Mw_{PCMX} \times 0.158)$ (D-8)

$= (167\text{-}(1\text{x}0.158)) + (156.61\text{x}0.158)$

$= 192$

%Yield

Determining theoretical weight of LCSX

$$W_{CSX} = 1\ g\ CS \times \frac{1molCS}{167gCS} \times \frac{192gCSX}{1molCSX}$$

$$= 1.14\ g$$

%Yield of products could be calculated by equation D-4:

$$\%Yield = \frac{Actual.Weight}{Theroretical.Weight} \times 100$$

After the reaction. 1.02 g of product was obtained. Therefore,

$$\%Yield = \frac{1.02}{1.14} \times 100$$

$$= 89\%$$

Author Biography

Name	Mr. Pakawat Chittratan
Date of Birth	30 June 1988
Address	41 M.2, Nongpaklong, Muang Nakhonpathom, Nakhonpathom, 73000
Education	(2010) Bachelor of Engineering, Petrochemicals and Polymeric Materials, The Faculty of Engineering and Industrial Technology, Silpakorn University (2014) Master of Science, Nanoscience and Nanotechnology, College of Nanotechnology, King Mongkut's Institute of Technology Ladkrabang

International Publications

1. Chittratan, P., et al., Antimicrobial nanolayer films of chloroxylenol-carboxyethyl-chitosan modified silver nanoparticles for enhanced surgical suture performance. Colloids and Surfaces A: Physicochemical and Engineering Aspects, 2024. 693: p. 133957.
2. Chittratan, P., et al., New chitosan-grafted thymol coated on gold nanoparticles for control of cariogenic bacteria in the oral cavity. ACS Omega, 2022. 7(30): p. 26582-26590.
3. Chittratan, P., et al., DFT-based computational investigation on functional monomer and solvent selection of molecularly imprinted polymers for recognition of chlorpyrifos organophosphate insecticide. Suranaree Journal of Science and Technology, 2020. 27(1): p. 1–6, 030003.
4. Chittratan, P., et al., Efficeincy improvement of triphenylamine-based organic dyes in DSSCs, an effects of linker moiety. *Advanced Materials Research*, 2013. 802: p. 257–261.

Conferences

1. Design and characterization of chitosan-grafted-thymol on gold nanoparticles for antimicrobial activity. Oral presentation in the Material Chemistry and Nanotechnology (MN) session of the Pure and Applied Chemistry International Conference 2022 (PACCON2022).